Dynamical models of the mammalian Target of Rapamycin network in ageing

Piero Dalle Pezze

Institute for Ageing and Health

Newcastle University

A thesis submitted in partial fulfilment of
the requirements for the degree of

Doctor of Philosophy

November 2012

Author

Piero Dalle Pezze
Institute for Ageing and Health,
Newcastle University,
United Kingdom

Supervisors

Dr Daryl P. Shanley
Institute for Ageing and Health,
Newcastle University,
United Kingdom

Professor Thomas B. L. Kirkwood
Institute for Ageing and Health,
Newcastle University,
United Kingdom

Examiners

Professor Boris N. Kholodenko
UCD Conway Institute of
Biomolecular and Biomedical Research,
University College Dublin,
Ireland

Dr Viktor I. Korolchuk
Institute for Ageing and Health,
Newcastle University,
United Kingdom

Declaration

I confirm that no part of the material offered has previously been submitted by me for a degree in this or any other University. Material generated through joint work has been acknowledged and the appropriate publications cited. In all other cases, material from the work of others has been acknowledged, and quotations and paraphrases suitably indicated.

I understand that the print version will be made available for consultation in the Library or a Library to which it has been issued on inter-library loan, though it will not be permitted to leave the Library in either case.

I understand that work deposited in the Newcastle University e-Thesis Repository will be accessible to a wide variety of people and institutions - including automated agents - via the Internet. An electronic copy of my thesis may also be included in the national British Library database of theses.

Date: 30 November 2012

Print Name: Piero Dalle Pezze

Abstract

The mammalian Target of Rapamycin (mTOR) kinase is a central regulator of cellular growth and metabolism and plays an important role in ageing and age-related diseases. The increase of *in vitro* data collected to extend our knowledge on its regulation, and consequently improve drug intervention, has highlighted the complexity of the mTOR network. This complexity is also aggravated by the intrinsic time-dependent nature of cellular regulatory network cross-talks and feedbacks. Systems biology constitutes a powerful tool for mathematically formalising biological networks and investigating such dynamical properties.
The present work discusses the development of three dynamical models of the mTOR network. The first aimed at the analysis of the current literature-based hypotheses of mTOR Complex 2 (mTORC2) regulation. For each hypothesis, the model predicted specific differential dynamics which were systematically tested by *in vitro* experiments. Surprisingly, no current hypothesis could explain the data and a new hypothesis of mTORC2 activation was proposed. The second model extended the previous one with an AMPK module. In this study AMPK was reported to be activated by insulin. Using a hypothesis ranking approach based on model goodness-of-fit, AMPK activity was *in silico* predicted and *in vitro* tested to be activated by the insulin receptor substrate (IRS). Finally, the last model linked mTOR with the oxidative stress response, mitochondrial regulation, DNA damage and FoxO transcription factors. This work provided the characterisation of a dynamical mechanism to explain the state transition from normal to senescent cells and the irreversibility of the senescent phenotype.

Keywords: ageing, systems biology, mathematical modelling, mTOR network, insulin signalling, AMPK, cellular senescence, oxidative-stress response, mitochondria, FoxO, Mfn2.

Acknowledgements

I would like to express my sincere gratitude to my supervisors Dr Daryl Shanley and Professor Thomas Kirkwood for selecting me for this project, believing in my ideas and work, and their continuous support. I have appreciated the opportunity to work in the Institute for Ageing and Health of Newcastle University very much. The work presented in this thesis was funded by the European Council 6th FP NoE LifeSpan for the first two years and then by the Graduate School of the Faculty of Medical Sciences, Newcastle University.

I want to thank our collaborators Annika Sonntag and Dr Kathrin Thedieck from the Department of Bioinformatics and Molecular Genetics, Freiburg University, Germany, for their *in vitro* experimental contribution and our discussions on TOR biology. A special thanks goes to Dr Glyn Nelson and Professor Thomas von Zglinicki from the Institute for Ageing and Health, Newcastle University, United Kingdom, for their *in vitro* experimental work and our discussions on cellular senescence in my last year of doctorate. I also thank Dr Glyn Nelson for his detailed reading of this thesis.

I would like to acknowledge all my colleagues and friends for believing in me and the support they have given me during my doctoral studies at Newcastle University.

Last but not least, I would like to express my deepest thank to my family, for their help and support in every moment of my life.

Table of Contents

List of Figures

List of Tables

Nomenclature

Ψm	Mitochondrial (mt) membrane potential.
4E-BP	4E-binding protein
AIC	Akaike information criterion
AMP	Adenosine monophosphate
AMPK	Adenosine monophosphate-activated protein kinase
ATP	Adenosine 5-triphosphate
BDNF	Brain-derived neurotrophic factor
BIC	Bayesian information criterion
CaMKIII	Calcium-calmodulin type III kinase
CR	Caloric restriction
CS	Cowden syndrome
CV	Coefficient of variance
DAP1	Death-associated protein 1
eEF2K	Eukaryotic elongation factor-2 kinase
EGF	Epidermal growth factor
eIF4A-G	Eukaryotic initiation factor 4A-G
EP	Evolutionary programming algorithm
EPO	Erythropoietin
FKBP	FK506-binding protein

FoxO	Forkhead box family, subclass O
GA	Genetic algorithm
GAB1	Grb2-associated binder 1
GAP	GAPase-activating protein
GAPDH	Glyceraldehyde-3-phosphate dehydrogenase
GDP	Guanosine diphosphate
GEF	Guanine nucleotide-exchange factors
GRB	Growth factor receptor-bound protein
GS	Glycogen syhthase
GSK-3	Glycogen syhthase kinase 3
GTP	Guanosine-5'-triphosphate
HIF	Hypoxia-inducible factor
HM	Hydrophobic motif
IGF	Insulin growth factor
IIS	Insulin and insulin-like signalling
IR	Insulin receptor
IRS	Insulin receptor substrate
JNK	c-Jun N-terminal kinase
LKB1	Liver kinase B1
LM	Levenberg-Marquardt algorithm
LV	Las Vegas methods
MC	Monte Carlo methods

MDM2	Murine double minute 2
MOTA	Mean optimal transformations analysis
mSIN1	Mammalian stress-activated protein kinase interacting protein 1
mtDNA	Mitochondrial DNA
mTOR	Mammalian target of Rapamycin
mTORC1	Mammalian target of Rapamycin complex 1
mTORC2	Mammalian target of Rapamycin complex 2
NF-κB	Nuclear factor kappa-light-chain-enhancer of activated B cells
NFL	p70-S6K-induced negative feedback loop
ODE	Ordinary differential equation
p.i.	Post-induction
p70-S6K	p70 ribosomal S6 kinase
PDK1	Phosphoinositide-dependent protein kinase 1
PGC-1α/β	Peroxisome proliferator-activated receptor-γ coactivator
PH	Pleckstrin homology
PI(3,4)P2	phosphatidylinositol (3,4)-bisphosphate
PI(3,4,5)P3	phosphatidylinositol (3,4,5)-trisphosphate
PI(4,5)P2	phosphatidylinositol (4,5)-bisphosphate
PI3K	Phosphoinositide 3-kinases
PIKK	Phosphatidylinositol kinases
PJS	Peutz-Jeghers syndrome
PKB	Protein kinase B, also Akt

PKC	Protein kinase C
PRAS40	Proline-rich Akt substrate of 40 kDa
PTEN	Phosphatase and tensin homologue
Raptor	Regulatory-associated protein of mTOR
Rheb	Ras-homolog enriched in brain
Rictor	Rapamycin-insensitive companion of mTOR
ROS	Reactive oxygen species
RSK	p90 ribosomal S6 kinase
SA	Simulated annealing algorithm
SBGN	Systems biology graphical notation
SBML	Systems biology markup language
SD	Steepest descent algorithm
SGK	Serum- and glucocorticoid-inducible kinase
SH3BP4	SH3 domain-binding protein 4
SIRT1	NAD-dependent deacetylase sirtuin-1
SREBP	Sterol regulatory element binding protein
TGF-β	Transforming Growth Factor β
TN	Truncated-Newton algorithm
TNF-α	Tumour necrosis factor α
TR	Trust region algorithm
TSC1/TSC2	Tuberous sclerosis complex
TSCS	Tuberous sclerosis complex syndrome

ULK1	Serine/threonine-protein kinase ULK1
VEGF	Vascular endothelial growth factor
VHL	Von Hippel-Lindau

Chapter 1

Introduction

1.1 Motivation

The insulin/insulin-like signalling and Target of Rapamycin (IIS/TOR) network is a central regulator of cellular growth and metabolism and plays an important role in ageing and age-related diseases. In response to metabolic stimuli such as insulin, nutrients or energy, a cascade of signalling events modulated by post-translational modifications, in particular phosphorylation, occurs to promote TOR activity. Once phosphorylated, TOR governs cellular processes essential for development and ultimately ageing, such as promotion of cell growth, proliferation and metabolism, improvement of mitochondrial function, and inhibition of autophagy and apoptosis. Hence, understanding the functional mechanisms of the IIS/TOR network is an essential component in extending our knowledge on ageing and age-related diseases.

The increase of *in vitro* data collected to extend our knowledge on its regulation and consequently improve drug intervention, has notably highlighted the complexity of the mTOR network. This complexity is also increased by the intrinsic time-dependent nature of cellular regulatory networks cross-talks and feedbacks. This high level of complexity found in many biological signalling pathways raised interest for systems biology in the scientific community. Systems biology constitutes a powerful tool for mathematically formalising biological networks and investigating their dynamical properties. In this work, the regulatory mechanisms of the mammalian TOR network were investigated in detail using a combined *in silico-in vitro* systems biology approach.

1.2 Objectives

In the first two years of my doctorate, I developed two computational models of the TOR signalling network that further our understanding of the influence of growth factors and nutrition on cellular decisions. Calibrated on immunoblot-based experimental data, provided by the team of Kathrin Thedieck, Freiburg University, Germany, these models were used to investigate and test hypotheses of activation of mTOR Complex 2 and AMPK. As mTOR and AMPK are important regulators of FoxO and autophagy, understanding their functional mechanism represents a crucial aspect in ageing.
In the last year of my doctorate, I developed a mathematical model which integrated knowledge from several biochemical processes of interest in ageing research. Through the interaction with the team of Professor Thomas Von Zglinicki, Institute for Ageing and Health, Newcastle University, UK, a new process-oriented modelling project was begun with the aim of combining behaviours of some of the most studied components in ageing research: insulin/TOR, ROS, FoxO and mitochondria. This work aimed to establish the first mathematical extended framework for cellular senescence. At this initial stage, my main objective was to formally provide a mechanism for explaining the transition of cell state from normal to senescent.
By investigating systems dynamics with detailed *in vitro* time-course experimental data and network modelling with a focus on functional outcomes at the cellular level, these projects contributed to a better understanding and opened new avenues for future research on TOR signalling in development and ageing and for therapies of age-related diseases.

1.3 Outline

This thesis follows a tree structure based on a TOR-focused introduction on ageing, insulin/TOR network and systems modelling, and three systems biology projects (see Figure 1.1).
In Chapter 2, a general introduction on ageing and the recent implications of TOR in ageing and age-related diseases are presented in order to contextualise

this work inside a theoretical framework.
In Chapter 3, the insulin/TOR network is discussed from a molecular biology perspective. In this chapter the upstream and downstream signalling pathways of both mTOR Complex 1 (mTORC1) and mTOR Complex 2 (mTORC2) are extensively described.
Chapter 4 introduces systems biology in the specific case of dynamical models optimised over experimental data sets as well as the most prominent analyses from dynamical systems theory. A review of the recent published mTOR mathematical models is proposed in order to link systems modelling with TOR biology.
Chapter 5 describes the differential investigation of three hypotheses of mTORC2 activation and the discovery of a new class I PI3K independent of p70-S6K-negative feedback loop, which promotes mTORC2 activity upon insulin stimulation. The article related to this work and published in Science Signalling is attached in Appendix A.
In Chapter 6, the previously described model was extended with the inclusion of AMPK regulation. Using a hypothesis ranking approach based on model goodness-of-fit, AMPK activity was *in silico* predicted and *in vitro* tested to be activated by the insulin receptor substrate (IRS) upon insulin stimulation. The article related to this work and published in FEBS Journal is attached in Appendix B.
Chapter 7 discusses a new mathematical model linking mTOR with the oxidative stress response, mitochondria regulation, DNA damage through FoxO transcription factors and Mfn2. This work provides the formalisation of a dynamical mechanism to explain the state transition from normal to senescent cells and their irreversibility.
Finally, a general conclusion of this thesis is presented in Chapter 8.

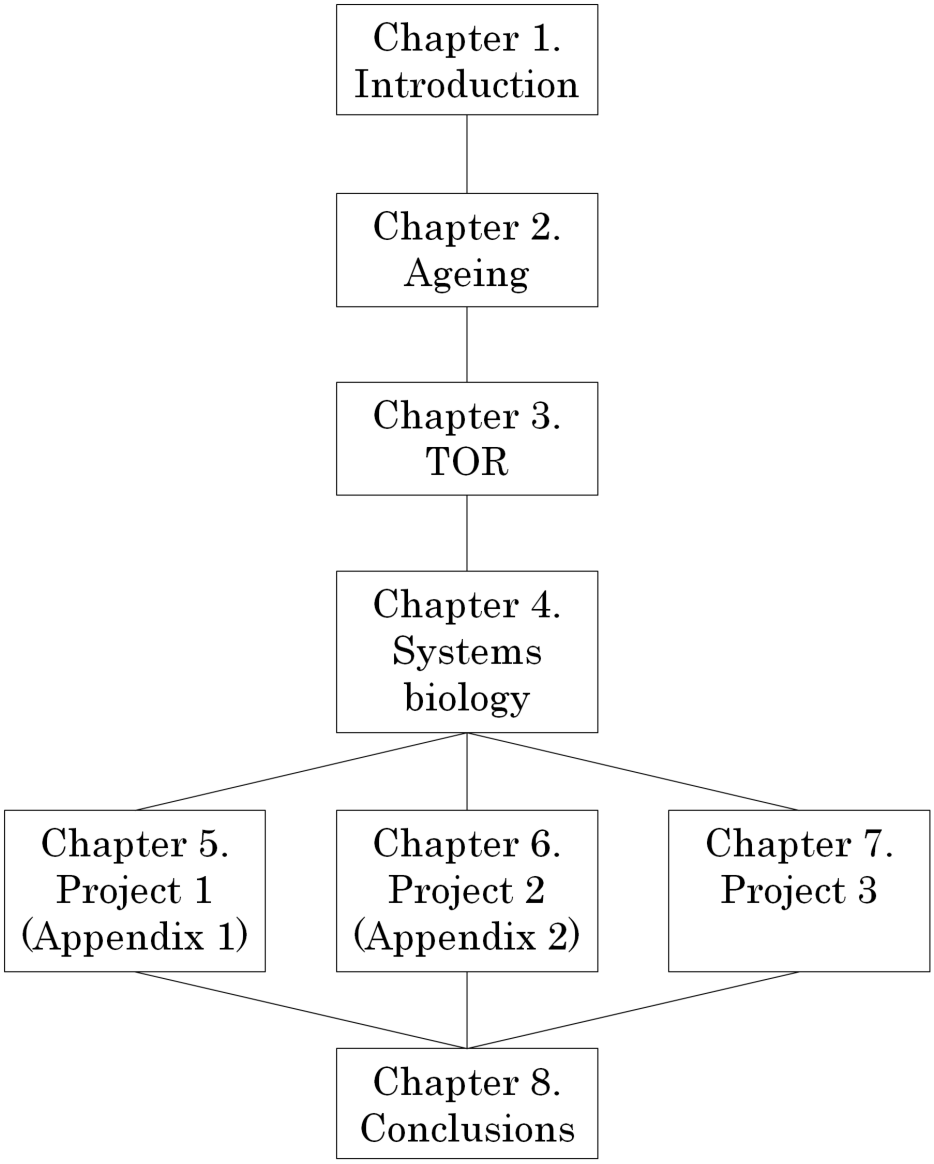

Figure 1.1: Thesis structure.

Chapter 2

TOR in ageing and age-related diseases

The process of ageing and its role in disease has intrigued mankind for centuries. Despite this, a clear understanding of why and how ageing occurs is still far from being achieved. Among the proposed ageing theories, the disposable soma theory is one of the most comprehensive, widely applicable and well established. In this theory the problem of allocating resources to remove or repair molecular damage is central. One of the key systems that responds to resource availability is the nutrient sensing network. This network is a widely conserved intracellular system that serves to detect nutrient availability and govern an appropriate cellular response. Many studies have shown that inhibition of this network by nutritional, pharmacological and genetic intervention extends lifespan in a wide range of organisms including yeast, worms, flies and rodents. Of particular interest is the finding that Rapamycin, which inhibits a key component of the nutrient sensing network, suitably named the target of Rapamycin (TOR), is effective in extending lifespan in a similar range of organisms. Rapamycin was originally discovered in Easter island and shown to inhibit growth and proliferation within the cell, and is widely used to prevent organ transplantation rejection. It is an established drug and as a candidate for pharmacological intervention aimed at prolonging lifespan and healthspan, and reducing the impact of age-related diseases.
This chapter presents a summary on the biology of ageing and age-related diseases with particular emphasis on TOR.

2.1 Theoretical foundations on ageing

This section introduces the theoretical foundations of this study through a *top-down* approach. Firstly, the disposable soma theory and the resource allocation problem are introduced. Secondly, the connection between this evolutionary theory of ageing and TOR-dependent cellular regulation is proposed.

2.1.1 The disposable soma theory

Ageing is a progressive loss of function accompanied by increasing mortality and decreasing fertility with age. The disposable soma theory [Finch and Kirkwood, 2000; Kirkwood, 1977, 1981; Kirkwood and Rose, 1991; Shanley and Kirkwood, 2000] considers the problem an organism faces in partitioning limited resources acquired from the environment between the physiological functions of maintenance/repair and reproduction. Investment in maintenance/repair will slow the rate of ageing whereas investment in reproduction is essential for producing offspring. The optimal decision that maximises Darwinian fitness will depend on the amount of resources available and on the environmental conditions but in general investment in maintenance/repair is inevitably less than required for indefinite survival and the accumulation of damage results in ageing. In the wild, life is constantly compromised by multiple extrinsic factors such as predators, food deprivation and temperature variability. In an unprotected environment, the risk of mortality is therefore high (see Figure 2.1A). Moreover, an organism is continuously challenged by internal damage, for instance due to injury, infections, diseases, malnutrition, toxins, oxidative stress, which must be repaired. Maintainance is crucial in order to preserve the soma in good enough condition for survival to ensure opportunities to reproduce. The physiological functions of repair and maintenance require a considerable amount of energy which has to be carefully allocated in the organism. This investment is compromised by the competing energy demand for reproduction which includes maintenance of the germline cells. As a consequence, the organism gradually degrades over time, becoming more susceptible to extrinsic and intrinsic risk factors, and ultimately dies.

2.1.2 The resource allocation problem

In the disposable soma theory, resource allocation is the key problem as resources are limited and maintenance is costly. In an organism, these resources are allocated among the physiological functions of growth, maintenance and repair, storage and reproduction [Kirkwood, 2008] (see Figure 2.1B). At the level of the organism, resource allocation is partially regulated by growth factors and nutrients, as variability in these two players significatively affects size and reproduction in *Caenorhabditis elegans*, *Drosophila melanogaster* and mice [Bass *et al.*, 2007; Holzenberger *et al.*, 2001; Selman *et al.*, 2009; Walker *et al.*, 2005; Zid *et al.*, 2009]. Similarly, at the level of the cell, resource allocation is regulated by growth factors, amino acids and energy [Laplante and Sabatini, 2012; Russell *et al.*, 2011; Sengupta *et al.*, 2010; Zoncu *et al.*, 2011]. In the cell, a key protein responsible for orchestrating resource allocation is the target of Rapamycin (TOR). Through resource availability, recognised by the cell as growth factors, nutrients and energy, TOR promotes cellular growth and proliferation, improves mitochondrial function increasing the amount of cellular energy, and inhibits conservative or recycling processes such as cell cycle arrest or autophagy [Dunlop and Tee, 2009; Inoki and Guan, 2006; Stanfel *et al.*, 2009; Yang and Guan, 2007; Zid *et al.*, 2009] (see Figure 2.1C). Therefore, understanding the regulation of TOR and its interacting partners represent a crucial step in furthering our knowledge of ageing and uncovering potential therapies for extending healthspan and lifespan.

2.1.3 Links between TOR, mitochondria and ROS

In response to growth factors and nutrients TOR regulates protein translation and mitochondrial function [Finley and Haigis, 2009; Kaeberlein, 2010; Kaeberlein *et al.*, 2007; Stanfel *et al.*, 2009]. TOR can affect mitochondria in multiple ways. TOR can directly inhibit mitochondrial autophagy (mitophagy) impeding the degradation of dysfunctional mitochondria [Lee *et al.*, 2012]. Conversely, TOR also regulates global mitochondrial function through mitochondrial biogenesis [Hock and Kralli, 2009].

There is substantial evidence on the link between mitochondria and reactive oxygen species (ROS). The majority of cellular ROS are generated as a by-product

of ATP production by the mitochondrial electric transport chain (ETC) during oxidative phosphorylation [Murphy, 2009]. The ETC activity can be measured by the mitochondrial membrane potential (see Figure 2.2). Interestingly, ROS are responsible for the damage of mitochondrial DNA (mtDNA) subunits [Shokolenko *et al.*, 2009] which would lead to a gradual dysfunction of the mitochondria ETC mechanism [Turrens, 2003]. Mitochondrial function would therefore enter a sub-optimal state characterised by low energy production (ATP) and high ROS generation. The establishment of this *vicious cycle* between ROS production and mitochondrial ETC activity may lead to catastrophic dynamical changes inside a cell [Turrens, 2003].
From this prospective, it is clear that the insulin/TOR signalling regulation of mitochondrial function is essential to understand in order to selectively intervene for improving cellular functions and health.

2.2 TOR-dependent interventions for extending lifespan

This section discusses two of the most well-known interventions for increasing lifespan in a TOR-dependent manner: caloric restriction and selective perturbation of TOR-dependent downstream partners.

2.2.1 Caloric restriction

Caloric Restriction (CR), defined as a reduction in calories without malnutrition, is the most well known nutritional intervention that leads to lifespan extension and prevention from various chronic diseases in protected environments [Gredilla and Barja, 2005; Kapahi *et al.*, 2010]. Although most studies report a positive effect for CR there are notable exceptions. In fact, CR was not found to extend lifespan or reduce the incidence of cancer in wild mice [Harper *et al.*, 2006] or rhesus monkeys [Mattison *et al.*, 2012]. Mutations in the insulin and insulin-like signalling pathway were the first genetic interventions confirmed to extend life in animals [Kenyon, 2010]. Both insulin signalling and amino acids activate TOR, and reduced TOR activity increases lifespan [Evans *et al.*, 2010; Kaeberlein and

Kapahi, 2009; Kapahi *et al.*, 2004; Laplante and Sabatini, 2012]. In yeast, both replicative[1] and chronological[2] lifespans increase when TOR1 and TOR2 genes are deleted or pharmacologically inhibited. In general, reduced TORC1 activity has been demonstrated to increase lifespan in several organisms including single-celled budding yeast *Saccharomyces cervisiae* [Wanke *et al.*, 2008], invertebrate nematode *Caenorhabditis elegans* and fruit fly *Drosophila melanogaster* [Zid *et al.*, 2009], mice [Anisimov *et al.*, 2010; Harrison *et al.*, 2009] and rhesus monkeys [Colman *et al.*, 2009]. The effects of CR in the mTOR pathway are a progressive reduction of the IGF/PI3K/Akt/mTOR signalling, and an increase in AMPK [Jiang *et al.*, 2008]. This results in an enhancement of autophagy activity which could therefore limit the progression of age-related diseases and promoting lifespan [Ravikumar *et al.*, 2010].

2.2.2 Intervention on TOR downstream targets

Another way to extend lifespan is by the regulation of TOR downstream targets or substrates, such as p70 ribosomal S6 kinase 1 (p70-S6K1) [Selman *et al.*, 2009] and 4E-binding protein 1 (4E-BP1) [Zid *et al.*, 2009]. These substrates promote the production of ribosomal proteins and ribosome biogenesis and a reduced production is associated with increased lifespan. In addition to the regulation of mRNA translation, ageing is also modulated by autophagy [Blagosklonny, 2010; Blagosklonny and Hall, 2009; Cuervo, 2008; Hansen *et al.*, 2008]. A reduction in TOR activity obtained by Rapamycin-induced inhibition or CR, stimulates the autophagy process. Through autophagy [Alvers *et al.*, 2009], non-vital and damaged components are destroyed and transformed into nutrients, extending lifespan. It is worth noting that, in contrast to yeast, in mammals TOR can be regulated in different ways in different tissues and thus, it is also important to understand the consequences of TOR inhibition within a specific tissue. In fact, inhibition of TORC1 may be beneficial in some tissues, but in contrast, may be detrimental to others [Russell *et al.*, 2011].

[1]Replicative lifespan counts the number of daughter cells generated by a mother cell prior to senescence [Mortimer and Johnston, 1959].

[2]Chronological lifespan measures the amount of time a cell can survive within the G0 phase (quiescence) of the cell cycle [MacLean *et al.*, 2001].

2.3 TOR in age-related diseases

In this section, the role of TOR in the most significant age-related diseases is outlined to provide an overview on the impact that TOR research could have on society by increasing both lifespan and healthspan.

2.3.1 Cancer

Mutations of important cell check-point proteins, such as the tumour suppressor PTEN or the oncogene protein Akt/PKB, as well as an elevated mTOR activity, are often discovered in many cancers. The interest of cancer research in mTOR is also related to the effects of the natural drug Rapamycin [Bjornsti and Houghton, 2004], which has been shown to extend lifespan in cancer-prone mice [Anisimov *et al.*, 2010]. Following Rapamycin treatment, cells tend to arrest their life-cycle at G1 phase because of insufficient cell growth input [Bjornsti and Houghton, 2004]. A pure Rapamycin treatment in cancer does not provide significant improvements because the drug only partially inhibits mTORC1 and does not affect mTORC2 [Janes and Fruman, 2010]. However, the adoption of radiotherapy or chemotherapy drugs administered in combination with Rapamycin has been shown to be more effective in cancer treatment [Rosner *et al.*, 2008]. Due to the limitation of Rapamycin, interest has increased in the study of cancer treatments by more specific TOR inhibitors, such as Torin and PP242 [Feldman *et al.*, 2009; Janes and Fruman, 2010; Laplante and Sabatini, 2012; Liu *et al.*, 2011]. mTOR is also responsible for the activation of the Vascular Endothelial Growth Factor (VEGF), a signalling pathway related to vasculogenesis, process in which new blood vessels are created, and angiogenesis, which is the growth of blood vessels from existing ones [Treins *et al.*, 2002]. This stimulation is essential for cancer maintenance and development of metastasis.

2.3.2 Diabetes and Obesity

Diabetes is a serious age-related disease and is affected by age-related increase in obesity. There are two forms of diabetes, Type 1 and Type 2, and both involve the mTOR signalling pathway. In the former, the destruction of pancreatic

β-cells leads to insufficient insulin production. As a consequence, glucose levels increase in blood and urine and patients need repeated administration of insulin, typically by injection [Lehuen *et al.*, 2010]. Type 2 diabetes is mostly connected to caloric excess and lack of physical activities, which are both associated with the elderly. Type 2 diabetes is associated with over activation of the mTOR pathway and the consequent insulin resistance and deficiency. One feature is an upregulation of mTOR due to amino acids which leads to a sustained p70-S6K-dependent negative feedback activation and consequent constitutive degradation of insulin receptor substrate (IRS1) [Dann *et al.*, 2007; Laplante and Sabatini, 2012; Tremblay *et al.*, 2007] (see Figure 3.2 for a conceptual map of the TOR network). Conversely, inhibition of mTORC1 activity with Rapamycin reduces the p70-S6K activity restoring the normal sensitivity of the IRS1/PI3K/Akt pathway. Type II diabetes is usually linked to obesity and TOR is also an important regulator of lipid synthesis [Laplante and Sabatini, 2012; Rosner *et al.*, 2008]. In hepatic cells mTOR exerts a role in the lipogenic gene expression by regulating the transcription factor sterol regulatory element binding protein 1c (SREBP-1c) [Peterson *et al.*, 2011]. Amino acids represent a key regulator of both mTORC1 and SREBP-1c. Recently, SREBP-1c has been found to be activated by protein kinase C β (PKCβ) [Yamamoto *et al.*, 2010], which is stabilised and phosphorylated by mTORC2 [Ikenoue *et al.*, 2008]. Therefore, a long-term continuous activity of mTORC1 and mTORC2 can determine insulin resistance and hepatic steatosis through IRS1 degradation and SREBP-1c activation.

2.3.3 Neurodegeneration

The mechanisms by which neurons lose their functionality are not yet completely understood. Interestingly, CR and inhibition of mTOR signalling have been proposed as possible candidates in order to protect neurons and reduce neuronal loss during ageing by promoting autophagy. These effects could limit and also reduce damage causing neurological disorders such as Alzheimer's, Parkinson's, Huntington's, Creutzfeldt-Jakob's and dementia diseases [Rosner *et al.*, 2008]. These neurodegenerative diseases are characterised by an accumulation of aggregated mutant proteins in the intracellular space. For example, Huntington's disease

presents polyglutamine (polyQ) expansion repeats; mutant forms of τ, a protein thought to contribute to neurofibrillary tangles, are discovered in Alzheimer's disease; whereas α-synuclein and β-amyloid mutants accumulate Parkinson's disease [Glick *et al.*, 2010; Levine and Kroemer, 2008]. Autophagy can potentially benefit these diseases by removing these aggregates. Rapamycin or Metformin treatment could be used to inhibit mTORC1 signalling and increase autophagy levels [Hara *et al.*, 2006; Komatsu *et al.*, 2006]. The role of autophagy in neurodegenerative diseases is also highlighted by the fact that, mice with deficiency of autophagy-related 5/7 proteins (Atg5, Atg7) increased the accumulation of mutant proteins in neurodegenerative diseases [Hara *et al.*, 2006; Komatsu *et al.*, 2006]. Finally, other important neuropsychiatric disorders, such as autism, epilepsy and mental retardation, are often linked to mutations of TSC genes, upstream of mTORC1 [Gomez *et al.*, 1999; Tee *et al.*, 2002]. Thus, an inhibition of mTOR may improve the impact of these diseases in affected patients.

2.3.4 Hamartoma syndromes

The Hamartoma syndromes represent genetic diseases characterised by benign tumours which grow in brain and various organs such as lungs, kidneys, skin and heart. Hamartoma syndromes include: tuberous sclerosis complex syndrome (TSCS), Cowden syndrome (CS) and Peutz-Jeghers syndrome (PJS) [Inoki *et al.*, 2005]. TSC syndrome is due to a mutation of either TSC1 or TSC2 which disrupts TSCs complex hyperactivating mTORC1. This hyperactive mTORC1 promotes cell over-growth and tumour formation in TSC patients [Umeoka *et al.*, 2008]. In CS patients, a mutated PTEN leaves activated PIP3 hyperstimulating mTORC1. As a consequence, PIP3 hyperactivates Akt/mTORC1 causing a dysregulation of cellular growth and proliferation [Pilarski, 2009]. A similar effect can be observed in PJS patients, due to a mutation of the protein LKB1 [Beggs *et al.*, 2010]. A mutation of LKB1 prevents the formation of AMPK and leaves activated mTORC1 even though in hypoxia conditions [Krymskaya and Goncharova, 2009]. Cells induced by a hyperactive mTORC1 grow larger, faster and with different structure than normal cells, increasing susceptibility to tumourigenesis. Rapamycin can be used for reducing tumour size by inhibiting mTORC1. To

reduce the risk of malignancy progression, it is also important to restrict the activity of the PI3K/Akt pathway directly by using PI3K inhibitor drugs, such as LY294002 or Wortmannin. Due to the crucial role of mTORC2 in the phosphorylation of Akt, new TOR specific inhibitors could improve the treatment of the Hamartoma syndromes.

2.4 Figures

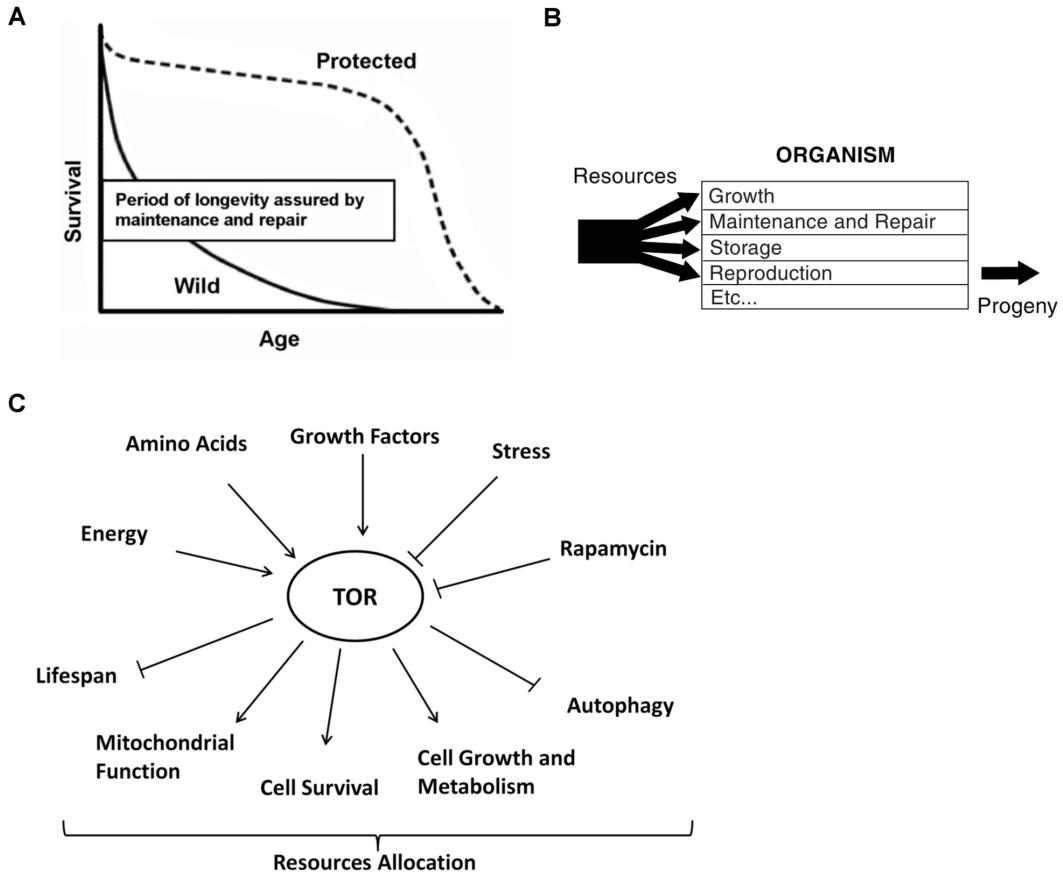

Figure 2.1: Disposable soma theory, resource allocation and TOR. (A) Lifespan differences between wild and protected environments. Adapted from [Kirkwood, 2008, Fig. 1]. (B) Resources allocation in the disposable soma theory of ageing [Kirkwood, 1977, 1981, 2008]. In this theory, the problem of resource allocation is crucial since resources are limited and maintenance is costly. Adapted from [Kirkwood, 2008, Fig. 3]. (C) TOR in ageing. In response to stimuli such as insulin or growth factors, amino acids, energy and stress, Target of Rapamycin (TOR) kinase governs numerous age-related cellular processes regulating the allocation of resources.

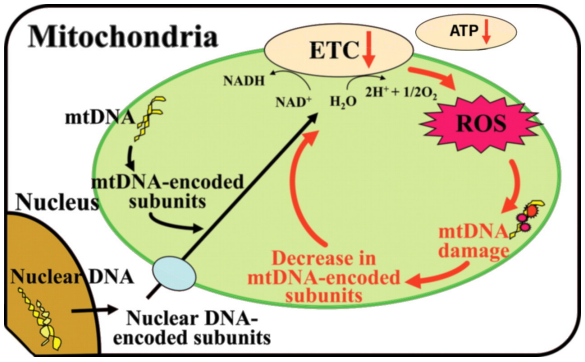

Figure 2.2: ROS production and mitochondrial dysfunction. Mitochondrial DNA (mtDNA) in combination with nuclear DNA encode proteins building the mitochondrial electron transport chain (ETC), whose activity can be measured by mitochondrial membrane potential. Through ETC, molecules of adenosine triphosphate (ATP) are synthesised and utilised by the cell as an energy supply. Aside from ATP production, mitochondrial ETC also produces reactive oxygen species (ROS) as a waste product. ROS accumulation, due to a lack of ROS detoxification, severely damages mtDNA subunits, establishing a vicious circle which decreases mitochondrial function, energy levels within the cell, and increases ROS production and mutated mtDNA. Adapted from [Tsutsui *et al.*, 2009, Fig. 1].

Chapter 3

mTOR network: an overview

TOR kinase is centrally located in a complex signalling network that responds to the availability of cellular resources. TOR is positively regulated by growth factors, nutrients and energy uptake. Through these signals, the kinase activates protein translation initiation and elongation mechanisms, regulates cell growth and metabolism, improves mitochondria function and transmits signals for cell survival. TOR-activated downstream targets inhibit apoptosis, autophagy and cell cycle arrest. Conversely, nutritional or energetic stress conditions negatively control TOR activity. The TOR network is further complicated by several feedback mechanisms that work at different time-scales and hamper a full understanding. This chapter presents details of TOR kinase and the two protein complexes containing TOR in mammals (mTOR) to place TOR in the network of related upstream and downstream signals.

3.1 mTOR, Rapamycin and AGC kinases

This section introduces the mammalian TOR kinase from a biochemical point of view and the first natural drug found to partially inhibit the kinase. A short introduction of the mTOR-dependent AGC kinases is also presented as useful background to understanding the complexity of mTOR network.

3.1.1 mTOR: kinase and complexes

The protein TOR was discovered in the early 1990s in genetic screens in yeast for the resistance to Rapamycin [Heitman *et al.*, 1991]. TOR1 and TOR2 in yeast and the single mammalian homolog mTOR which are present in two multi-protein complexes, mTORC1 and mTORC2, integrate upstream signals to regulate sev-

eral downstream processes.
The mammalian TOR, mTOR, is a serine/threonine protein kinase which belongs to the phosphatidylinositol kinase (PIKK) family in which the catalytic domain presents significant homology to that of other phosphoinositide 3-kinases (PI3Ks) although mTOR has protein rather that lipid targets. The protein mTOR is composed of five important components. From its N-terminus: a tandem HEAT domain involved in substrate binding; a FAT domain whose function is currently unknown; an FRB domain which provides a docking site for the ligand FKBP12; finally, there are the fundamental mTOR kinase domain and the FATC (FAT C-terminus) domain [Hay and Sonenberg, 2004; Wullschleger *et al.*, 2006]. The details of the FATC domain activity are still unknown.
The mTOR kinase represents a central regulator of eukaryotic growth and cell division when stimulated by nutrients and growth factors, energy signals and cellular stresses. mTOR was found to exist in two complexes named mTOR Complex 1 (mTORC1) and mTOR Complex 2 (mTORC2) which are structurally and functionally different (see Figure 3.1).
Whenever stimulated by amino acids and growth factors such as insulin, mTORC1 controls multiple cellular processes such as autophagy inhibition, mRNA translation, ribosome biogenesis, lipid storage and cell cycle progression. mTORC2 responds only to growth factors and serves to regulate actin polymerisation and promotes the phosphorylations of Akt/PKB and serum- and glucocorticoid-inducible kinase 1 (SGK1). In contrast to mTORC1, the role and the interactions of mTORC2 within the cell still remains mostly unknown.

3.1.2 The natural drug Rapamycin

Rapamycin was discovered in Easter Island and is an immunosuppressant drug used to prevent organ rejection in transplants [Saunders *et al.*, 2001]. It is the first drug to have been shown to extend lifespan in a mammal [Harrison *et al.*, 2009]. Also, it has been shown to have significant anti-proliferative properties which made it an interesting drug candidate in cancer research [Rao *et al.*, 2004; Vignot *et al.*, 2005].
Rapamycin binds with a protein named FK506-binding protein 12 kDa (FKBP12)

[Choi *et al.*, 1996] which associates directly with TOR, altering its normal kinase activity, ultimately resulting in cell growth arrest [Evans *et al.*, 2010]. When bound to the FRB domain of mTOR by FKBP12 protein, Rapamycin blocks some of the physiological functions of mTOR by inhibiting part of the mTOR autophosphorylation. This intrinsic mTOR activity is fundamental for mTOR to modulate signals to its substrates. Interestingly, the activity of both mTOR and Rapamycin are highly preserved among eukaryotes. Of particular interest in ageing is the fundamental role of TOR in the regulation of autophagy, a key process responsible for the degradation of cytosolic components.

3.1.3 mTOR-dependent regulation of AGC kinases

The mTOR network contains several important kinases belonging to the AGC family of approximately 60 kinases. In the context of the mTOR network, the most important AGC kinases are PDK1, Akt/PKB [McManus *et al.*, 2004; Mora *et al.*, 2004], p70 ribosomal S6 kinase (p70-S6K) [Volarevic and Thomas, 2001], p90 ribosomal S6 kinase (RSK) [Williams *et al.*, 2000], serum- and glucocorticoid-inducible kinase (SGK1) [Jacinto and Lorberg, 2008] and protein kinase C (PKC) [Newton, 2003]. AGC kinases are characterised by three important phosphorylation sites, whose activation provides differential functionality. A partial activation of the kinase is achieved by phosphorylation at the activation loop, also called T-loop, in the kinase domain. This phosphorylation enables conformational change in the protein structure which exposes the kinase hydrophobic motif (HM), located in a C-terminal tail region, on the protein surface. Phosphorylation at this region determines a full activation of the AGC kinase and further functionality [Pearce *et al.*, 2010]. The third and least characterised phosphorylation site or region is the turn motif phosphate which is also located in the protein tail. Its function is to stabilise the phosphorylation of the kinase by sheltering the hydrophobic motif from dephosphorylation [Hauge *et al.*, 2007; Pearce *et al.*, 2010].

3.2 Upstream signalling pathways of mTOR

Multiple signalling pathways have a regulatory influence on the mTOR Complexes 1 and 2. This section presents the four major inputs of mTOR: growth factors, amino acids, energy and hypoxia. The most important cross-talks from these signals to other pathways are also mentioned.

3.2.1 The insulin insulin-like signalling pathway

Insulin and insulin-like signalling (IIS) is mediated at the cell membrane by a specific insulin receptor (IR). In the presence of insulin molecules on the external membrane surface, the insulin receptor is auto-phosphorylated at several tyrosine residues transmitting the signal in the internal membrane surface. Among several proteins activated by IR, the insulin receptor substrate (IRS) is crucial in the IIS pathway. The IRS binds with phosphoinositide 3-kinase (PI3K) forming a complex which enables the production of phosphatidylinositol (3,4,5)-trisphosphate (PI(3,4,5)P3) from phosphatidylinositol (4,5)-bisphosphate (PI(4,5)P2) or phosphatidylinositol (3,4)-bisphosphate (PI(3,4)P2) through phosphorylation at the membrane surface [Polak and Hall, 2009]. The activity of PtdIns(3,4,5)P3 is negatively controlled by phosphatase and tensin homolog (PTEN) and SH2-containing inositol phosphatase (SHIP), which convert the PI(3,4,5)P3 in the form of PI(4,5)P2 and PI(3,4)P2 respectively. Upon insulin or insulin-like stimuli, phosphoinositide-dependent kinase-1 (PDK1) and Akt, also known as Protein Kinase B (PKB), relocalise from the cytoplasm to the membrane surface and their Pleckstrin Homology (PH) domain binds with PI(3,4,5)P3 molecules [Polak and Hall, 2009]. This binding exerts a conformational change in Akt/PKB which is necessary to enable PDK1 to phosphorylate Akt at T308 at the T-loop [Biondi, 2004; Garcia-Martinez and Alessi, 2008; Kobayashi and Cohen, 1999; Mao *et al.*, 2008a; McManus *et al.*, 2004; Mora *et al.*, 2004; Toker and Newton, 2000]. Once phosphorylated at T308, Akt affects the integrity of the tuberous sclerosis complex (TSC1/TSC2) by phosphorylating TSC2 at S924 and T1518 [Inoki *et al.*, 2002; Potter *et al.*, 2002]. Whereas TSC1 mainly serves for the stabilisation of the TSC1/TSC2 complex, TSC2 presents a GAPase Activating Protein (GAP) domain which controls GTPase activity of mTORC1 activator

Ras-homolog enriched in brain (Rheb). Therefore, TSC2 switches off Rheb by hydrolysing Rheb activator guanosine-5'-triphosphate (GTP) to guanosine diphosphate (GDP), whereas guanine nucleotide-exchange factors (GEFs) reverse this reaction by freeing GDP molecules from the GTPase and thus promoting GTP formation and consequent GTP-bound Rheb activation. Whenever TSC1/TSC2 complex is disrupted, GTP-bound Rheb is free to bind with mTOR Complex 1 (mTORC1) at the lysosomal surface, mediating the insulin signalling [Huang and Manning, 2008]. Regarding mTORC2, it is known that the complex is sensitive to growth factors, such as insulin, but little is known about how this activation happens. Insulin stimulation has been shown to be responsible for the phosphorylation of Rictor at T1135, even when Rictor is not associated with mTOR, as this phosphorylation was inhibited upon Wortmannin treatment [Boulbes *et al.*, 2010]. Recent studies have shown the presence of a positive feedback from TSC1/TSC2 to mTORC2, whereas a direct association between the dimer and mTORC1 is not known. These authors showed that the heterodimer could positively regulate mTORC2 in a Rheb-independent manner [Huang *et al.*, 2008; Rosner *et al.*, 2008; Sparks and Guertin, 2010]. These studies used Akt-S473 (see Section 3.4.1), which is dependent on the p70-S6K-dependent negative feedback loop (see Section 3.3.2), as a marker of mTORC2, instead of a specific direct readout of mTORC2 activity. Although several speculations of mTORC2 activation have been proposed, a comprehensive study of the modalities of mTORC2 activation has yet to be conducted and this will be the subject presented in Section 5 (see Figure 3.2).

3.2.2 The amino acids signalling pathway

Amino acids such as Leucine, Tryptophan and Phenylalanine [Christie *et al.*, 2002; Taylor, 2009; Thedieck and Hall, 2009] play a crucial role in regulating the mTOR network and mTORC1 activation, although surprisingly the mechanisms are still mostly unknown. Recent studies have revealed the presence of new Rag proteins which are necessary for the mTORC1 activation by amino acids [Kim *et al.*, 2008] (see Figure 3.2). Rag proteins are a family of four small GTPases, RagA, RagB, RagC and RagD, belonging to the Ras family. Rags associate as

heterodimers formed by RagA or RagB, with RagC or RagD [Kim *et al.*, 2008; Sancak *et al.*, 2008]. mTORC1 and Rags associate in the presence of amino acids, in particular leucine. Rags do not directly activate mTORC1, but allow mTORC1 to bind with Rheb which is necessary for mTORC1 activation. Interestingly, a more recent study [Sancak *et al.*, 2010] based on mass spectrometry analysis, has discovered the presence of a complex named Ragulator. Whenever stimulated by amino acids, Ragulator is responsible for the mTORC1 translocation to the lysosomal surface and the subsequent association between mTORC1 and the heterodimer Rags. Once mTORC1 localises to the lysosomal surface, an insulin stimulation can enhance mTORC1 activation by promoting the binding between GTP-bound Rheb and mTORC1. This synchronised confluence of the insulin and amino acids signalling pathways on the lysosomal surface could explain why insulin/IGF stimulation without amino acids is not sufficient for the activation of mTORC1 [Drummond *et al.*, 2008; Sancak *et al.*, 2010]. Conversely, in the absence of amino acids mTORC1 localises to the cytoplasm [Kalender *et al.*, 2010]. Therefore, amino acids are essential for activating Ragulator which transfers mTORC1 to the lysosomal compartment and binds it with its activator Rheb.

Little information is known about how amino acids regulate the Rag GTPase proteins. Durán *et al.* [2012], from the lab of Hall, recently focused on glutamine, an amino acid involved in cell growth and metabolised through glutaminolysis to produce α-ketoglutarate. The authors reported that glutamine combined with leucine activated Rag GTPase complex and promoted lysosomal translocation and activation of mTORC1 by enhancing glutaminolysis and α-ketoglutarate production. Another recent study showed that SH3 domain-binding protein 4 (SH3BP4) negatively regulates Rag GTPase complex by binding to the inactive form of the complex under amino acids starvation conditions. Once bound to SH3BP4, Rag GTPase complex is unable to switch state and therefore to interact with and activate mTORC1. This leads to an inhibition of mTORC1 activity in a Rag GTPase-dependent manner [Kim *et al.*, 2012].

Amino Acids were also shown to partially activate mTORC2 and its readout Akt-S473 indirectly via class I PI3K [Jacinto *et al.*, 2004; Tato *et al.*, 2011] although the detail of this connection is still unclear.

3.2.3 The energy signalling pathway

Another important regulator of mTOR is the energy signalling pathway [Thedieck and Hall, 2009]. The main component of this signalling cascade is Adenosine Monophosphate-activated Protein Kinase (AMPK). AMPK is a trimeric complex formed by α, β and γ subunits, which are necessary to maintain protein stability and function. AMPK is directly regulated by the tumour suppressor Liver Kinase B1 (LKB1). LKB1 is activated under energy or nutrient stress conditions and acts as a growth and proliferation suppressor. In adipocyte cells, LKB1 is negatively regulated via the androgen receptor, whereas positively via oestrogen receptor alpha [McInnes *et al.*, 2012]. When in a complex with the proteins STRAD and MO25, active LKB1 phosphorylates the AMPK-α subunit activation loop under conditions of energy stress, and this is sufficient for AMPK activation [Shackelford and Shaw, 2009]. LKB1 is of clinical importance as it plays a key role in maintaining cell polarity and lack of LKB1 is associated with Peutz- Jeghers syndrome and other forms of cancer.
AMPK is an energy level sensor. Whenever the number of AMP molecules is much greater than ATP, the cell is in a low-energy status. In response to energy stress, AMPK becomes active in order to maintain energy homoeostasis in cell metabolism. Under such energy-stress conditions, the γ subunit of AMPK binds directly with AMP molecules and undergoes a conformational change, becoming activated. Once activated, AMPK phosphorylates the unit TSC2 of the TSC1/TSC2 complex at T1271 and S1387, increasing the dimer GTPase activity [Inoki *et al.*, 2005, 2003]. In addition, active AMPK phosphorylates the mTORC1 scaffold protein Raptor at S722 and S792, inhibiting it [Gwinn *et al.*, 2008]. Therefore, AMPK negatively controls mTORC1 through TSC1/TSC2 upregulation and Raptor inhibition (see Figure 3.2).

3.2.4 The hypoxic signalling pathway

Hypoxia, which is referred to as a condition of low levels of oxygen, plays a role in the TOR network. Activated mTORC1 promotes the transcription of Hypoxia-inducible factor 1 (HIF-1) heterodimeric complex (see Figure 3.2). HIF-1 is differentially regulated depending on hypoxic or normoxic conditions in the

cell. Under hypoxic conditions HIF-α binds with HIF-β and the dimer then migrates from the cytosol to the nucleus and induces transcription of genes required for cellular adaptive response to hypoxic stress [Déry *et al.*, 2005], such as erythropoietin (EPO), p300 and POLII [Maxwell, 2005]. HIF-1 also promotes glucose metabolism [Huang *et al.*, 2004; Ke and Costa, 2006] and angiogenesis by activating the Vascular Endothelial Growth Factor (VEGF) pathway [Gray *et al.*, 2005; Klimova and Chandel, 2008]. Interestingly, HIF-1 activates the transcription of the two genes Redd1 and Redd2 which inhibit mTOR in a TSC1/TSC2-dependent manner [Brugarolas *et al.*, 2004; McCarthy, 2004], thereby providing a negative feedback loop. citetBrugarolas2004 showed that Redd1/2 is required for down-regulating mTORC1 by promoting TSC1/TSC2 activity in a hypoxia-dependent and energy-independent manner. The hypoxic signalling pathway through mTORC1 also involves the protein Bnip3 which has been shown to be enhanced by HIF-1α subunit, under hypoxia conditions [Wouters and Koritzinsky, 2008]. Bnip3 inhibits the GTP form of Rheb, directly reducing mTORC1 activation. In addition, Bnip3 was demonstrated to positively regulate autophagy [Bellot *et al.*, 2009]. Instead, in case of normoxic conditions, HIF-1 is rapidly hydroxilated by EGLN1/PHD1 and EGLN2/PHD2 at several prolines. Once HIF-1 is hydroxilated, the interaction with Von Hippel-Lindau (VHL) is facilitated, increasing HIF-1 ubiquitination and proteasomal degradation [Déry *et al.*, 2005; Maxwell, 2005].

3.2.5 Other signalling pathways

In addition to mTOR other kinases in the network have an important role. Among these, Akt and IRS are potentially the two most important examples. Akt plays a direct role in glucose metabolism by phosphorylating and inhibiting Glycogen Synthase Kinase 3 (GSK-3). GSK-3 phosphorylates and inhibits Glycogen Synthase (GS), which is involved in the synthesis of glycogen from glucose [Embi *et al.*, 1980]. Akt also controls other cellular processes, such as cell survival and proliferation. Through phosphorylation, Akt enhances the oncogene protein murine double minute 2 (MDM2), an E3 ubiquitin ligase and the main repressor of p53, and deactivates FoxO. By inhibiting FoxO and p53 activity, the apoptotic

signalling cascade composed of Bim-Bcl-2-Bax is repressed, thereby favouring cell survival. Akt deactivates several genes, such as Wee1, p27Kip1, p21Cip, which are involved in cell cycle arrest. Through these inhibitions, Akt promotes cell proliferation.
IRS has multiple activity when stimulated by growth factors. Besides propagating the insulin signalling by binding with PI3K (see Section 3.2.1), IRS binds to Growth factor receptor-bound protein 2 (GRB2) and GRB10, which are involved in the Epidermal Growth Factor (EGF) pathway. In more detail, GRB2 and GRB10 activate the signalling cascade SOS-Ras-MEK1/2-Erk, which has several crosstalk connections with the insulin signalling pathway (see Figure 3.2).

3.3 Interacting partners of mTORC1

Several signalling pathways have been shown to interact with mTORC1 and our expanding knowledge of the mTOR network is uncovering new modalities of intervention in ageing and age-related diseases. In this section, the most important interacting partners and downstream target kinases of mTORC1 are presented.

3.3.1 Rheb, FKBP38 and PRAS40

Rheb is a small GTPase protein belonging to the Ras superfamily of G-proteins. Rheb is activated (GTP-bound Rheb) by GEFs and inactivated (GDP-bound Rheb) by TSC2 GAPase domain [Huang and Manning, 2008]. Rheb is fundamental to provide a full activation of mTORC1 and thus to activate cell growth mechanisms. Moreover, Rheb over-expression was found to correlate with an increase in p70-S6K1 and 4E-BP1 phosphorylation in Drosophila [Stocker *et al.*, 2003], which indicates that mTORC1 activity is connected to an activated Rheb.
FKBP38, or FKBP8, is a member of the FK506-binding protein (FKBP) family which includes FKBP12. FKBP12 binds to Rapamycin, interacts with the FRB domain of mTOR within the complex mTORC1 and leads to inhibition. FKBP38 is a mitochondrial membrane protein which associates with mTORC1 in a similar way to that of the complex FKBP12 and Rapamycin. Unlike FKBP12, FKBP38 does not require Rapamycin in order to form a complex with mTORC1. After

binding with FKBP38, mTORC1 is not able to propagate signals to its downstream targets. In-vitro assays demonstrated that FKBP38 competed with the complex FKBP12-Rapamycin for binding with the FRB domain of mTOR in mTORC1 [Bai *et al.*, 2007]. Like the complex FKBP12-Rapamycin, FKBP38 only interacts with mTORC1 and does not show any binding with mTORC2. Furthermore, it was shown that the activated GTP-bound form of Rheb decreased the binding of FKBP38 with mTOR in mTORC1 *in vitro*, thus relieving the inhibition of mTORC1.

The Proline-rich Akt Substrate of 40 kDa (PRAS40) is a protein able to bind to the Raptor subunit of mTORC1. PRAS40 is directly phosphorylated by Akt/PKB at T246 and by mTORC1 at S183, S202/3, S212, S221. The phosphorylation by Akt/PKB results in a conformational change in mTORC1-bound PRAS40 which enables mTORC1 to subsequently phosphorylate PRAS40 and disrupt the complex [Nascimento and Ouwens, 2009; Nascimento *et al.*, 2010; Thedieck *et al.*, 2007; Wang *et al.*, 2007]. The dissociation of PRAS40 and mTORC1 permits mTORC1 to interact with the GTP form of Rheb, becoming activated. Therefore, the insulin pathway acts as a double activator of mTORC1 firstly by activating Rheb and secondly by separating mTORC1 from its inhibitor PRAS40 [Thedieck and Hall, 2009; Thedieck *et al.*, 2007; Wang *et al.*, 2007].

3.3.2 The downstream substrate p70-S6K

Among the numerous mTORC1 substrates, the two best studied are the kinase p70-S6K1 (p70-S6 kinases) and the 4E-binding protein 1 (4E-BP1). Following stimulation by growth factors and amino acids, mTORC1 phosphorylates p70-S6K1 which phosphorylates its numerous substrates, inducing protein translation. Among these substrates are the Programmed Cell Death 4 (PDCD4), the S6 ribosomal protein [Heinonen *et al.*, 2008], the eukaryotic Initiation Factor 4B (eIF4B) which is known to associate with eIF3 and the eukaryotic Elongation Factor-2 Kinase (eEF2K) which activates its substrate eEF2, promoting the elongation phase of protein synthesis. A reduced p70-S6K1 activity has been shown to extend lifespan in mice [Selman *et al.*, 2009].

p70-S6K1 belongs to the AGC protein kinases family and has several phospho-

rylation sites [Jacinto and Lorberg, 2008]. mTORC1 phosphorylates p70-S6K1 at T389 and S371. In order to become fully activated, p70-S6K1 requires an additional phosphorylation at T229 by PDK1. p70-S6K1 plays an important role in the mTOR signalling pathway not only as translation promoter, but also as an inhibitor of the insulin receptor substrate 1 (IRS1) which by phosphorylation at S636/639 [Dann *et al.*, 2007; Tremblay *et al.*, 2007] favours its degradation and blocks the insulin signal. This pathway is referred to as p70-S6K1-induced negative feedback towards IRS1. Recently, p70-S6K1 was also shown to phosphorylate Rictor at T1135, regulating the mTORC2 activity negatively [Julien *et al.*, 2010; Treins *et al.*, 2010]. Thus, p70-S6K1 interrupts Akt function by negative feedbacks to IRS1 and mTORC2. These negative feedbacks arrest the pathways which determine the Akt phosphorylation at T308 and S473, respectively [Foster and Fingar, 2010].

3.3.3 The downstream substrate 4E-BP1

The 4E-binding protein 1 (4E-BP1) is another well studied mTORC1 substrate. When unphosphorylated, 4E-BP1 forms a complex with eukaryotic Initiation Factor 4E (eIF4E) acting as a translation repressor. The phosphorylation of 4E-BP1 by mTORC1 disrupts the complex and frees it from eIF4E [Dann and Thomas, 2006]. Thus eIF4E associates with a specific complex represented by the initiation factors eIF4G and eIF4A, forming the new complex eIF4F. eIF4G is known to be the mediator for this binding [Gingras *et al.*, 1999]. Therefore, mTORC1 regulates cell growth and proliferation by disabling 4E-BP1 activity and enhancing cap-dependent mRNA translation mediated by eIF4F. By regulating 4E-BP1 phosphorylation by inhibiting mTOR, it is possible to extend lifespan [Zid *et al.*, 2009].

3.3.4 Roles of mTORC1 and AMPK in autophagy

mTORC1 and AMPK play an opposite role in autophagy[1], which is the process by which a cell is able to degrade and recycle useless or damaged organelles

[1] In this context, autophagy is meant as macroautophagy

under nutrients or energy stress conditions, through direct phosphorylation of ULK1 [Kim *et al.*, 2011; Lee *et al.*, 2010a] in response to glucose. Under high levels of glucose, AMPK is inactive and mTORC1 is active. Active mTORC1 phosphorylates ULK1 at S757, inhibiting autophagy. Conversely, active AMPK inhibits mTORC1 and phosphorylates ULK1 at S317 and S777, promoting autophagy [Kim *et al.*, 2011]. Once autophagy is activated, new amino acids are produced through the degradation of organelles by autophagy. This presence of amino acids in the cytoplasm is able to restore mTORC1 activity through the amino acids pathway after 6-8 h of autophagy activation in mice [Yu *et al.*, 2010]. A functional balance between AMPK and mTORC1 is fundamental to maintain cell homoeostasis and healthy cellular function. Therefore, controlling and optimising this interplay, potentially through pharmacological intervention, may have beneficial consequences in lifespan and healthspan.

3.3.5 A novel substrate: DAP1

mTOR regulates the activity of a large number of substrates in addition to p70-S6K and 4E-BP1. The function for many of them is still unknown and in need of further study, but of those known, Death-Associated Protein 1 (DAP1) may have particular relevance to ageing and cancer.

Contrary to ULK1 and Atg13 which are positive regulators of autophagy, DAP1 is the first mTORC1 substrate found to inhibit autophagic flux upon amino acid starvation [Koren *et al.*, 2010]. Under nutrient-rich conditions, active mTOR directly phosphorylates DAP1 at S3 and S51, silencing DAP1-dependent inhibition of autophagy. Conversely, during amino acids starvation, the mTOR pathway is reduced and DAP1 remains unphosphorylated, inhibiting autophagy. Furthermore, Koren *et al.* [2010] found that DAP1 did not feed back on mTORC1, since DAP1 knock down increased autophagy levels but did not affect mTORC1. The authors explained this result by speculating a mTOR-governed *buffering mechanism* which would prevent autophagy hyperactivation under nutrient deprivation [Koren *et al.*, 2010]. In conclusion, this new apparently contradictory signalling pathway suggests that much knowledge on mTOR regulation of autophagy is still missing and that new combinatorial drug-intervention are required to clarify

these potential discrepancies.

3.4 Downstream targets of mTORC2

In contrast to mTORC1 there is little knowledge about the substrates and downstream signalling of mTORC2. Although the complex was found to be an important regulator of AGC kinases, such as Akt, SGK1 and PKC, a comprehensive investigation of the roles and interactions as well as a delineation of an exhaustive signalling network of mTORC2 are still at an early stage of research. In this section, three important substrates of mTORC2 are presented. Particular emphasis is attributed to FoxO, a key target downstream of Akt, and its role in ageing.

3.4.1 Akt-S473

Akt is a central regulator in the TOR network and its double regulation as an AGC kinase makes its functional mechanism difficult to understand. As an AGC kinase, Akt can be further phosphorylated at S473 on its hydrophobic motif (HM), after being phosphorylated at T308 on its T-loop. Several kinases have been found to regulate the phosphorylation at the hydrophobic motif of Akt. Historically, these proteins have been called PDK2 candidates in order to highlight the necessity of PDK1 in the Akt switch mechanism. Among these PDK2 candidates, one of the most important is mTORC2 [Copp *et al.*, 2009; Sarbassov *et al.*, 2006, 2005]. Interestingly, the S473 phosphorylation is not required to phosphorylate TSC2 [Jacinto *et al.*, 2006]. Therefore, although Akt can act downstream of mTORC2, but upstream of mTORC1, mTORC2 cannot be considered an mTORC1 activation upstream through Akt. The double phosphorylation at T308 and S473 permits Akt to phosphorylate other proteins and to promote survival signals. Among these proteins are the subclass O of the Forkhead family of transcription factors (FoxO).

3.4.2 FoxO transcription factors

The Forkhead box (Fox) proteins are a family of transcription factors controlling a multitude of genes implicated in cellular differentiation, glucose metabolism, cell

growth, cell death, DNA repair, ROS detoxification and cell cycle. Among the several genes belonging to the Fox family, the subclass O has attracted particular interest in ageing research since it was found that Daf-16, the homologue gene of mammal FoxO3, extended lifespan in *C. elegans* [Lehtinen *et al.*, 2006; Libina *et al.*, 2003; Lin *et al.*, 2001]. The FoxO subgroup of the Forkhead family consists of four members: FoxO1, FoxO3, FoxO4 and FoxO6 [Greer and Brunet, 2005]. In the absence of insulin or growth factors, FoxO localises in the nucleus and targets genes regulating cell cycle arrest (e.g. GADD45, p27), stress resistance (e.g. MnSOD) and cell death (e.g. Bim). In the presence of insulin or growth factors, fully activated Akt phosphorylates FoxO3, predominately at S253, which results in the translocation of the transcription factor from the nucleus to the cytoplasm where it is sequestered by the protein 14-3-3. Notably, elevated Akt activity is often found in malignant tumour cells [Hara *et al.*, 2005], whereas FoxO up-regulation was shown to increase lifespan [Kenyon, 2011; Willcox *et al.*, 2008]. Under oxidative stress conditions, c-Jun N-terminal kinase (JNK) is activated and phosphorylates FoxO. This phosphorylation forces the localisation of FoxO to the nucleus, over-riding previous phosphorylation by Akt [Chaanine *et al.*, 2012; Greer and Brunet, 2005]. Whether FoxO play different roles in the nucleus in absence of insulin or growth factors, or under oxidative stress conditions has not yet been clarified. Besides phosphorylation, FoxO can also be regulated by acetylation by NAD-dependent deacetylase sirtuin-1 (Sirt1, Sirtuin 1) in the nucleus. Sirt1 is responsible for deacetylating FoxO at several sites, promoting oxidative stress resistance instead of genes regulating apoptosis [Brunet *et al.*, 2004]. FoxO also represents an important interconnecting point in the cellular signalling network. Under stress stimuli or nutrient starvation, FoxO was also found to associate with p53 in the nucleus, trascribing several genes with p53 [Brunet *et al.*, 2004]. Another important interaction is between FoxO and SMAD transcription factors, which up-regulates p21 expression. This binding also represents a link between IIS and Transforming Growth Factor β (TGF-β) signalling pathways [Seoane *et al.*, 2004].

3.4.3 SGK1

Another important member of the AGC family is the protein Serum- and Glucocorticoid-induced protein Kinase 1 (SGK1). SGK1 is activated by growth factors, such as insulin, and is responsible for the regulation of sodium channel, transport and cellular processes such as cell growth, proliferation, survival and apoptosis. mTORC2 was found to phosphorylate the SGK1 hydrophobic motif at S422 [Garcia-Martinez and Alessi, 2008], which undergoes a conformational change permitting PDK1 to further phosphorylate the kinase on its catalytic domain at T256 [Kobayashi and Cohen, 1999; Mora *et al.*, 2004]. As with other AGC kinases, the double phosphorylation enables a full activation of SGK1 [Pearce *et al.*, 2010]. Some substrates are shared between SGK1 and Akt. Particularly, SGK1 activates MDM2, leading to a MDM2-dependent ubiquitination of p53 [Amato *et al.*, 2009]. SGK1 was also found to phosphorylate FoxO3a predominately at S315, driving its translocation from the nucleus to the cytoplasm, interrupting its transcription activity [Brunet *et al.*, 2001].

3.4.4 PKC family

The family of Protein Kinase C (PKCs) contains oncogene AGC kinases involved in cell proliferation and differentiation [Griner and Kazanietz, 2007]. As Akt, PKC is phosphorylated at the activation loop by PDK1 and at the hydrophobic loop by mTORC2 [Ikenoue *et al.*, 2008]. mTORC2 is also responsible for the phosphorylation of PKC at its turn motif, which preserves the phosphorylation of PKC hydrophobic motif [Hauge *et al.*, 2007; Ikenoue *et al.*, 2008]. PKC can also phosphorylate the TSC2 subunit, leading to the disruption of the TSC1/TSC2 complex and following activation of mTORC1. Whereas some phosphorylation sites overlap with those targeted by Akt, others are PKC-dependent only [Tee *et al.*, 2003]. The authors also showed that these PKC-dependent phosphorylation sites are also PI3K-independent, supporting the idea of multiple independent signalling toward TSC1/TSC2 complex [Inoki *et al.*, 2006]. Interestingly, PKC was also shown to be involved in the transcription of IRS1 in MCF-7 breast cancer cells [deVente *et al.*, 1996], suggesting a positive feedback loop driven by IRS1 through mTORC2 and PKC2.

3.5 Figures

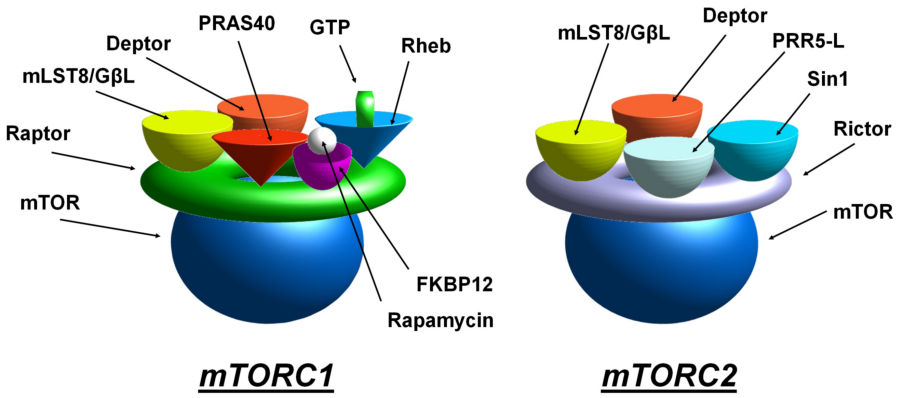

Figure 3.1: mTOR complexes 1 and 2. In mammals, the complexes mTORC1 and mTORC2 share mTOR, the mammalian LST8/G-protein β-subunit like protein (mLST8/GβL) and Deptor [Peterson *et al.*, 2009]. mLST8/GβL likely binds to the kinase domain of mTOR regulating its kinase activity. Deptor is known to have an inhibiting role in both complexes. A peculiar characteristic of mTORC1 is the binding with Raptor (Regulatory associated protein of mTOR). Raptor is known to be essential for the phosphorylation of mTORC1 downstream targets p70-S6K1 and 4E-BP1. It is supposed that it binds to the HEAT repeats of mTOR and it is sensitive to Rapamycin because it reduces its binding strength with mTOR in the presence of the drug. mTORC2 differs by containing Rictor (Rapamycin-insensitive companion of mTOR), the mammalian stress-activated protein kinase interacting protein 1 (mSIN1) [Frias *et al.*, 2006] and PRR5-L [Woo *et al.*, 2007]. mSIN1 is necessary for the binding between mTOR and Rictor, whereas PRR5 has not been found relevant. The detailed function of PRR5-L is still unknown.

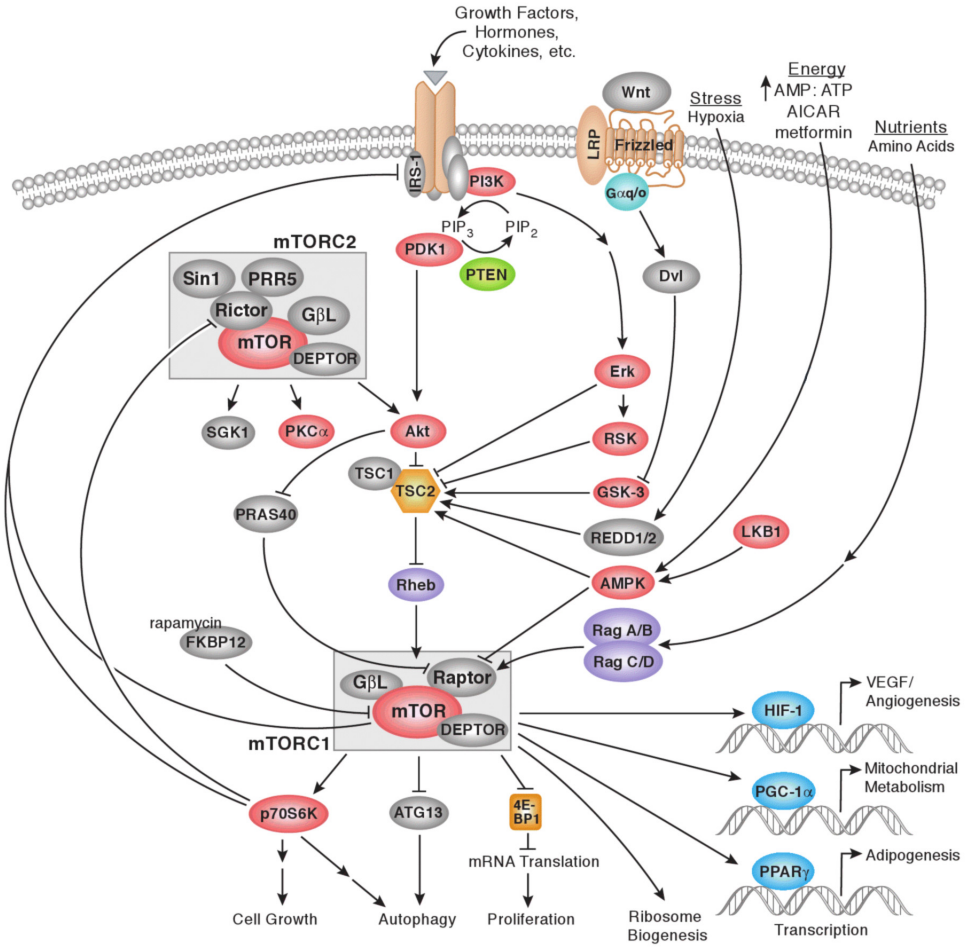

Figure 3.2: The mTOR signalling network is complicated by the numerous inputs and interaction between signals. In addition, the network presents several negative and positive feedback loops and most of them are not completely understood. Understanding the relationships among the proteins and the mechanisms by which mTOR-dependent processes are regulated is of fundamental importance to enable intervention on numerous age-related diseases. New systems biology approaches, such as modelling, using phosphoproteomics data, are able to deal with the complexity of the network and predict both qualitative and quantitative regulations. (Source: Cell Signaling Technology® (CST), Inc., website: `http://www.cellsignal.com/`; proteins are linked to PhosphoSitePlus® (PSP), website: `http://www.phosphosite.org/` (CC BY-NC-SA 3.0) [Hornbeck *et al.*, 2012]).

Chapter 4

Systems biology for investigating mTOR network in ageing

This chapter begins by presenting the main concepts of systems biology, from parameter estimation to advanced techniques of dynamical system theory. Finally, published work on systems modelling of the mammalian TOR network are described.

4.1 Introduction to systems biology

Understanding the connections between proteins to form networks and determining the emergent properties of dynamical interactions has been a major focus of research in recent years. Due to the complexity of biological systems, the need for an appropriate level of abstraction in order to characterise the key signalling network governing cell behaviour is essential. An approach to address the problem is provided in the mathematical modelling of signalling pathways [Hughey *et al.*, 2010; Kolch *et al.*, 2005]. So far, several key pathways have been modelled and simulated such as the epidermal growth factor (EGF) pathway [Borisov *et al.*, 2009; Schilling *et al.*, 2009; Wang *et al.*, 2009], the insulin insulin-like pathway [Brännmark *et al.*, 2010; Nyman *et al.*, 2012; Smith and Shanley, 2010] or p53/MDM2 oscillation signalling [Geva-Zatorsky *et al.*, 2006; Proctor and Gray, 2008]. This chapter presents a concise introduction to systems biology and other more advanced techniques imported from dynamical systems theory with the aim of introducing the current mathematical models of the TOR network.

4.1.1 Why systems biology?

Before introducing the main concepts important for dynamic modelling in systems biology, I think it is reasonable to discuss what systems biology is and how it can improve our understanding in biological studies. Systems biology is not simply a means to replace expensive wet-experiments with dry alternatives. It would not be very useful to consider systems biology just as an additional tool to provide more evidence to support scientific findings. From this point of view, a systems biology approach does not reveal much more than using wet-experimental techniques.

The advantages of systems biology are multiple. Firstly, the system representation is an abstraction of the biological context, and therefore it is simpler to investigate. Systems biology offers an extraordinary possibility to represent our biological knowledge as an interconnected system using an appropriate formalism. Secondly, this system can be formally analysed from multiple perspectives using theories coming from other sciences such as mathematics and computer science (e.g. dynamical systems, optimisation, formal methods), and statistics (e.g. stochastic simulation of models). Thirdly, from these analyses, specific properties of the system can be extracted and formulated as modelling predictions which can be tested in the laboratory. Systems biology permits the biologist to selectively search those predictions (e.g. systematic sensitivity analysis of system components) as well as provides the user with new non-trivial results (e.g. system bifurcations at specific protein amounts). Moreover, the feasibility of obtaining these predictions is mainly due to fast numerical computing tools, which allows the user to perform high-throughput tasks which would be impossible for wet-experimentalists.

4.1.2 Model definition

Over the last 20 years, the necessity of creating a standard language for systems biology models has emerged. Systems Biology Markup Language (SBML) [Hucka *et al.*, 2003] was developed as an XML standard aimed at porting systems biology models amongst different platforms and therefore increasing systems biology interoperability. In the field of molecular systems biology, a model is described as:

(1) a set S of species (e.g. unphosphorylated or phosphorylated proteins, complexes), (2) a set R of reactions between species (e.g. phosphorylation, binding), (3) a set I of inputs (e.g. insulin stimuli), and (4) a set C of compartments (e.g. cytoplasm, nucleus). These biological models can be graphically represented using CellDesigner[1] [Funahashi *et al.*, 2008, 2003]. Although this representation can be user-friendly, it hides the real representation of a model from a mathematical point of view. Instead, a mathematical representation explicitly offers the details for dealing with tasks such as parameter estimation and model quality analysis. A biological model can be described as follows:

$$\dot{\vec{x}}_{t,\theta} = \vec{f}(\vec{x}_{t,\theta}, \vec{u}_{t,\theta}, \theta), \quad \vec{x}_{t_0,\theta} = \vec{x}_{0,\theta} \tag{4.1}$$

$$\vec{y}_{t,\theta} = \vec{g}(\vec{x}_{t,\theta}, \theta) + \vec{\epsilon} \tag{4.2}$$

where 4.1 is a system of Ordinary Differential Equations (ODEs) and 4.2 describes the model observable variables. The ODE-based model is characterised by n species $\vec{x}$ (e.g. protein concentrations), whose dynamics are dependent on l input functions $\vec{u}$ (e.g. constant or impulse stimulation) and j model parameters $\theta = \{\theta_1, \ldots, \theta_j\}$ (e.g. protein initial concentrations, kinetic rates constants, scaling factors) over time $t = \{0, \ldots, T\}$. The species in $\vec{x}$ which can be experimentally measured (e.g. by immunoblotting, mass spectrometry), are mapped into m observable variables $\vec{y}$ by an observable function $\vec{g}$ and a measurement error $\epsilon \approx N(0, \sigma^2(d_{i,k}))$, where $\sigma^2(d_{i,k})$ is the variance of the i-th measurement at the time point k.

4.1.3 Parameter estimation

The choice of the observable variables depends on the measurements that can be feasibly measured in the laboratory. Once these are collected, the model can be optimised in order to represent the experimental data within a certain error. Parameter estimation is the task in which the model parameters are established in order to reduce this error. Let $d_{i,k}$ and $y_{i,k,\theta}$ be the i-th data measurement and observable at the time point k respectively, and $\sigma(d_{i,k})$ be the standard deviation

[1] http://www.celldesigner.org/

for $d_{i,k}$, parameter estimation aims at measuring the distance between the model observables and the experimental data:

$$\chi^2(\theta) = \sum_{i=1}^{m} \sum_{k=0}^{T} \left(\frac{d_{i,k} - y_{i,k,\theta}}{\sigma(d_{i,k})} \right)^2 \tag{4.3}$$

and computing a solution, or assignment of values to the parameters θ, which minimises such a distance:

$$\hat{\theta} = \underset{\theta}{\operatorname{argmin}} \left(\chi^2(\theta) \right) \tag{4.4}$$

Parameter estimation is therefore a problem of minimum optimisation. Optimisation algorithms can be classified into two classes: global and local algorithms. Global optimisation algorithms aim at finding the solution of minimum cost[1] in the differential χ^2 manifold[2] $\mathcal{M}$ of the search space. Although these algorithms can be very accurate since the performed research is more extended, they usually have exponential time complexity. An additional problem is that they can stall on local minima, which may not be suitable as solutions. Examples of these algorithms are simulating annealing (SA) [Corana *et al.*, 1987; Kirkpatrick *et al.*, 1983], genetic algorithms (GA) [Bäck *et al.*, 1997; Bäck and Schwefel, 1993; Michalewicz, 1994; Mitchell, 1998] and evolutionary programming (EP) [Bäck *et al.*, 1997; Bäck and Schwefel, 1993; Fogel *et al.*, 1991]. Local optimisation algorithms focus on retrieving the minimum solution closest to the current assignation of parameter values. These algorithms usually permit to calculate a solution quickly, although this may not be optimal. Instances of this class are Trust Region (TR) [Byrd *et al.*, 1987; Celis *et al.*, 1984; Yuan, 2000], Levenberg-Marquardt (LM) [Levenberg, 1944; Marquardt, 1963], Steepest Descent (SD) [Fogel *et al.*, 1991] and Truncated-Newton (TN) [Gill *et al.*, 1981; Nash, 1984]. A common approach is to perform a global optimisation and then improve the solution quality by a local optimisation. These methods are implemented in several software tools for

[1] Maximum cost in the case of maximum optimisation.

[2] An n-dimensional manifold is a topological space having the property that the neighbourhood of each point approximates (formally, it is *homeomorphic* to), the Euclidean space of dimension n, whereas this may not hold true globally.

calibrating and analysing systems biology models. The models presented in this thesis were developed using Copasi[1] [Hoops *et al.*, 2006] and the Matlab toolboxes Potterswheel[2] [Hengl *et al.*, 2007; Maiwald and Timmer, 2008; Raue *et al.*, 2009] and SBToolbox2[3] [Schmidt and Jirstrand, 2006]. In the case of testing different biological hypotheses, each corresponding to a specific network structure, parameter estimation can be used for establishing a rank within these different networks, based on fitting quality. The χ^2 measure is sufficient to define this hypothesis rank if the number of parameters is the same for each model, otherwise other measures taking into account the number of parameters, such as Akaike information criterion (AIC) [Akaike, 1973] or Bayesian information criterion (BIC) [Schwarz, 1978], should be adopted. This hypothesis ranking can be useful as a means to predict likely network structure and to guide further experimental test that could discriminate between alternatives. An example of this approach can be found in [Sonntag *et al.*, 2012].

4.1.4 Identifiability analysis

In parameter estimation, two problems arise depending on model structure and data availability. The former concerns model structural non-identifiability [Balsa-Canto *et al.*, 2010; Bellu *et al.*, 2007; Chiş *et al.*, 2011; Raue *et al.*, 2010, 2009]. This type of non-identifiability happens when the model structure is not sufficiently mapped by the available data. For instance, if a sub-graph of the network is over-parameterised or there are not sufficient observables characterising those dynamics, that sub-component may result structurally non-identifiable. From a graphical point of view, structural non-identifiability is represented in the $|\theta|$-dimensional χ^2 space as an unlimited plateau along the dimensions of the structurally non-identifiable parameters. Formally, assuming absence of measurement noise $\vec{\epsilon} = 0$, a subset of parameters $\eta \subset \theta$ is structurally non-identifiable if the overall χ^2 remains constant for each assignment $a \in A$ to the parameters in η:

$$\{\forall\, \eta := a \mid \eta \subset \theta, a \in A\} \Rightarrow \chi^2(\theta) = const \tag{4.5}$$

[1] http://www.copasi.org/
[2] http://www.potterswheel.de/
[3] http://www.sbtoolbox2.org/

In other words, the parameters in θ cannot be uniquely determined due to a lack of observable information:

$$\vec{y}_{t,\eta} = \vec{g}(\vec{x}_{t,\eta}, \eta) = \vec{0} \Rightarrow \chi^2(\theta) = const \tag{4.6}$$

In practical terms, if a model is structurally non-identifiable, parameter estimation results are inconclusive, as infinite different solutions report the same χ^2. Structural identifiability can be solved by altering the model structure or increasing the numbers of observable variables for the structurally non-identifiable sub-graph. Among the software for testing structural identifiability, the software GenSSI[1] [Balsa-Canto *et al.*, 2010; Chiş *et al.*, 2011] was used in this thesis. GenSSI computes the successive k orders of Lie derivatives of $\vec{g}$ with respect to the vector field $\vec{f}$, evaluated at the initial time $t = t_0$. In this generating series approach, GenSSI searches for a *exhaustive summary*, which is a vector of the series coefficients, evaluated at the initial conditions, that only depends on the model parameters to estimate and identify. Then, GenSSI uses the exhaustive summary for computing solutions for the parameters θ. If a unique solution is found, then the parameters are structurally globally identifiable; in the case of multiple solutions, the parameters are structurally locally identifiable. Finally, in the case of no solution, the parameters are structurally non-identifiable.
Although a parameter is structural identifiable, it may still be practically non-identifiable [Raue *et al.*, 2010, 2009]. Practical non-identifiability depends on the amount or quality of data sets used to estimate model parameters and can therefore be solved by increasing or improving the measured data. In case of time-course-based experiments, this means that the collected time points are not enough in number or that their standard deviations are too big to allow the optimisation algorithm to infer clear time-dependent signalling trajectories. Therefore, practical identifiability concerns the problem of assessing finite confidence intervals for each parameter. A parameter p is practically non-identifiable when its confidence interval is infinite, although there may exist a unique minimum for it. Graphically, the χ^2 measured as a function of p, $\chi^2(p)$, is always lower than a desired confidence threshold Δ_α, in the neighbourhood of the parameter

[1] http://www.iim.csic.es/~genssi/

minimum p_m:

$$\forall\, \delta \in \mathbb{R}^+ : \{\chi^2(p := p_m) \leq \chi^2(p := p_m \pm \delta)\}, \quad \{\chi^2(p := p_m - \delta) < \Delta_\alpha \vee \chi^2(p := p_m + \delta) < \Delta_\alpha\} \tag{4.7}$$

This results in a deficiency in estimating a valid confidence interval for p [Kreutz *et al.*, 2012; Raue *et al.*, 2010, 2009; Raue and Timmer, 2011]. A problem with this approach regards the choice of Δ_α. This threshold is defined as $\Delta_\alpha = \chi^2(\alpha, df)$, where $\chi^2(\alpha, df)$ is the χ^2-distribution with confidence level α and degrees of freedom df which corresponds to the number of parameter estimations. Therefore, an accurate Δ_α depends on a sufficiently large number of precise parameter estimations which requires a considerable time to compute.
In this thesis, the Potterswheel plugin Mean Optimal Transformations Analysis (MOTA) [Hengl *et al.*, 2007] was employed for detecting functionally related parameters and therefore solving structural non-identifiability issues in relation with data sets adopted for parameter estimation, in conjunction with a structural identifiability analysis theoretically performed using GenSSI. From a fit sequence of parameters, the MOTA algorithm returns the tuples of highly related parameters, permitting the user to fix independent parameters and estimate the remaining related parameters in the *reduced* parameter space. These iterations of parameter estimation and fixing may eventually terminate leading to model identifiability, decreasing the variability of estimated parameters. In order to provide the user a graphical intuition of identifiability issue, Figure 4.1 illustrates parameter non-identifiability through graphical χ^2 landscape surface.

4.1.5 Model simulation

Before introducing a definition for simulation and describing the operations which can be done over a simulation, it is worth formalising the concept of algorithm. An algorithm $\mathcal{A}$ is a step-by-step procedure with an internal state $\mathcal{S}$ which receives an input $\mathcal{I}$, performs a list of instructions evolving $\mathcal{S}$ and returns an output $\mathcal{O}$ [Cormen *et al.*, 2009]:

$$\mathcal{A} : (\mathcal{I}, \mathcal{S}) \longrightarrow \mathcal{O} \tag{4.8}$$

Therefore, a simulation can be defined as the task of reproducing a real problem, using an algorithm [Malesani, 2004]. In this context, the interest is in simulating aspects of cellular behaviour, formally represented by mathematical models, and collecting information related to their temporal evolution. A mathematical model can be simulated deterministically or stochastically, depending on the type of algorithm used for reproducing its dynamical behaviour. For a certain input, a deterministic algorithm always returns the same output, reproducing the same internal state sequence. In other words, a deterministic algorithm does not contain any form of randomisation. An example of these algorithm is LSODA [Hindmarsh, 1983; Petzold, 1983]. Stochastic algorithms differ as they include some form of randomisation, defined by a specific probability distribution, in their procedure [Wilkinson, 2006]. This randomisation can be limited to the internal state sequence only or be propagated to the output. In the former case, a stochastic algorithm is called *Las Vegas*[1] (LV), whereas in the latter case the algorithm is named *Monte Carlo* (MC) [Cormen *et al.*, 2009; Motwani and Raghavan, 1995]. In the context of systems biology, the stochasticity of a biological context can be reproduced by MC stochastic algorithms, such as Gillespie [Gillespie, 1976], Gibson-Bruck [Gibson and Bruck, 2000], Tau-Leap [Rathinam *et al.*, 2003] or Runge-Kutta [Kloeden and Platen, 1999]. This is of particular importance in the case of modelling gene transcription or low levels of protein amounts, since these systems are highly stochastic. The major drawback of stochastic simulations is their long computation-time as compared to deterministic simulations. For this reason, if the system stochasticity is low, a deterministic simulation may be more convenient for representing the dynamical behaviour of the model.

4.1.6 Sensitivity analysis

In mathematical modelling, establishing the influence of the parameters on overall behaviour is of fundamental importance to understand which of them play a more significant role then others [Aldridge *et al.*, 2006]. The analysis addressing this question is called sensitivity analysis. Sensitivity analysis is particularly useful in several areas. For instance, the detection of irrelevant parameters on the global

[1] An instance of this class of algorithm is Randomised-Quicksort.

dynamics may suggest model reduction [Jia and Yue, 2008], whereas assessing important ones may lead to new experimental design [Cho *et al.*, 2003]. Sensitivity analysis offers a means to explore the robustness of a system, as it shows how the dynamics change depending on parameter perturbation. There exist two types of sensitivity analysis: global and local. Global sensitivity analysis aims at retrieving multidimensional sensitivity operating multiple parameter changes. Local sensitivity analysis aims at exploring the domain of one parameter only and analysing the effect on the others [Marino *et al.*, 2008].
The main concepts of sensitivity analysis are presented limiting the objective to linear models [Saltelli *et al.*, 2005]. A linear model can be represented as

$$Y = \sum_{i=1}^{n} \Omega_i Z_i \tag{4.9}$$

where Y is the model output, Z_i are uncertain input factors chosen from a normal distribution $Z_i \approx N(0, \sigma_{Z_i})$ and Ω_i are the coefficients for Z_i. Y is also normally distributed $Y \approx N(0, \sigma_Y)$, where $\sigma_Y = \sqrt{\sum_{i=1}^{n} \Omega_i^2 \sigma_{Z_i}^2}$. Therefore, measuring a normalised sensitivity of Z_i over Y can be defined as:

$$S_{Z_i}^{\sigma} = \frac{\sigma_{Z_i}}{\sigma_Y} \frac{\partial Y}{\partial Z_i} \tag{4.10}$$

In case of a non-linear model, an extension of the previous calculation of sensitivity analysis based on MC methods can be found in [Cho *et al.*, 2003; Saltelli *et al.*, 2008, 2005].
Sensitivity analysis can be used in combination with model simulation. In fact, model simulations become particularly interesting when the initial conditions, such as the initial protein amounts or input stimuli, are changed. This type of simulation can reveal specific predictions, which can then be tested experimentally. For instance, reducing the amount of a protein species corresponds to a simulated knock-down, whereas increasing it represents a simulated over-expression. In the field of systems biology, cases of study involving this type of approach are [Dalle Pezze *et al.*, 2012a; Ihekwaba *et al.*, 2004; Mahdavi *et al.*, 2007; Suresh-Babu *et al.*, 2004]. In this work, the term *model perturbation* will be used to refer to a generic alteration of protein amount. Model perturbations can

be interpreted as local sensitivity analyses performed on target species by varying their expression level. Of course, the number of protein species perturbed is not necessarily limited to one at a time. In fact, an advantage of systems modelling is the possibility to compute these dry-experiments relatively easily compared to wet-experiments in a laboratory. These predictions may reveal non-trivial dynamical changes at certain time points as well as at specific protein levels. Therefore, a biologist may use this information for reducing the number of experiments, as models can return optimal conditions for detecting differences or similarities, and extending biological knowledge, as models can predict completely new system behaviours.

4.2 Advanced analyses from dynamical systems theory

Dynamical systems theory constitutes a powerful body of knowledge which can be used to investigate dynamical properties of the model. This section presents some of these analyses and their importance in the study of biological models.

4.2.1 Steady-state analysis

After a certain amount of time, a system may reach a state characterised by invariability. This state is called steady state. A definition of steady state based on [Ay *et al.*, 2009; Garg *et al.*, 2007] can be proposed as follows. Let S be a set of states. $\forall s_i \in S$, s_i is steady if and only if the following two conditions are verified:

$$\begin{aligned} &1.\ Succ(S) = S \\ &2.\ \forall\ s_i, s_j \in S,\ \ \forall\ t \in T \mid t : s_i \rightarrow s_j, \\ &\quad \exists\ n \in \mathbb{N}^+ finite \mid Prob(t^{(n)}(s_i) = s_i) = 1 \end{aligned} \tag{4.11}$$

which means that (1) the set of the successors of S is equal to S, and (2) for each visited $s_i \in S$ the probability of re-visiting s_i is 1 in a finite number of state transitions.

In other words, a steady state corresponds to a point at which the system reaches a condition of equilibrium or a fixed point from a mathematical point of view. This analysis is of particular interest for biological systems in order to elucidate the temporal length of specific dynamics and investigate the conditions leading to these steady states. Steady-state conditions also provide scientists with a starting point for analysing system behaviour at such states as illustrated in the following analyses.

4.2.2 Stability analysis

An interesting question arising from the discovery of steady states in a dynamical model regards the system response upon a small perturbation of a steady state. Does this perturbed state move away from or towards its previous steady state? The analysis pertaining to this question is called stability analysis. These sort of questions are of particular interest in biological systems [Thomson and Gunawardena, 2009] and highly relevant in ageing. For example, a senescent cell can be seen as a cell staying in a specific steady state. As stochasticity increases with ageing [Bahar *et al.*, 2006; Finch and Kirkwood, 2000; Kirkwood, 2008], the study of stability of a senescent steady state upon stochastic perturbations may reveal important information about the evolution of senescent cells. To provide an intuition of this analysis in the linear case[1], let us consider an n-dimensional linear system of ODEs[2] [Hirsch *et al.*, 2004; Parks, 1992]:

$$\frac{dx_i}{dt} = f_i(x_1, \ldots, x_n), \quad (i = 1, \ldots, n) \tag{4.12}$$

and assume $\vec{s} = (s_1, \ldots, s_n)$ be a steady state. Therefore:

$$f_i(s_1, \ldots, s_n) = \frac{ds_i}{dt} = 0, \quad \forall\, i \ \in \ [1, n] \tag{4.13}$$

This system is now perturbed by a small perturbation $\vec{\rho} = (\rho_1, \ldots, \rho_n)$, such that the new perturbed state is $\vec{s^*} = (s_1^*, \ldots, s_n^*) = (s_1 + \rho_1, \ldots, s_n + \rho_n)$.

[1] In case of non-linear systems, this linearisation technique can still be used although not generally.

[2] For simplicity, the Leibniz notation of derivative is used here.

In order to determine whether the perturbed state $\vec{s}^*$ moves away from or towards $\vec{s}$, it is necessary to derive the System 4.12 at the perturbed state $\vec{s}^*$.

$$\begin{aligned}\frac{d(s_i+\rho_i)}{dt} = \frac{d\rho_i}{dt} &= \frac{ds_i^*}{dt}, \quad (i=1,\ldots,n) \quad \text{(by Formula 4.13)} \\ &= f_i(s_1^*,\ldots,s_n^*) \quad \text{(by definition)} \\ &= f_i(s_1+\rho_1,\ldots,s_n+\rho_n) \quad \text{(by substitution)} \\ &= f_i(s_1,\ldots,s_n) + \frac{\partial f_i}{\partial x_1}(s_1,\ldots,s_n)\rho_1 + \cdots + \frac{\partial f_i}{\partial x_n}(s_1,\ldots,s_n)\rho_n + \mathcal{T} \\ &\text{(Taylor series expansion)} \\ &= \frac{\partial f_i}{\partial x_1}(s_1,\ldots,s_n)\rho_1 + \cdots + \frac{\partial f_i}{\partial x_n}(s_1,\ldots,s_n)\rho_n \quad \text{(by Formula 4.13)}\end{aligned} \tag{4.14}$$

where $\mathcal{T} = \mathcal{O}(\rho_1^n, \rho_2^n, \ldots, \rho_1 \ldots \rho_n)$ are the Taylor series higher-order terms which can be neglected as $\vec{H}$ is assumed a small perturbation. Therefore, the evolution of the perturbation is determined by the following n-dimensional linear system:

$$\begin{aligned}\left(\tfrac{d\rho_i}{dt}\right) &= \left(\tfrac{\partial f_i}{\partial x_j}(s_1,\ldots,s_n)\right)\left(\rho_i\right), \quad (i,j=1,\ldots,n) \\ &= J\vec{\rho}\end{aligned} \tag{4.15}$$

where J is the Jacobian matrix of the System 4.12 at the fixed point $\vec{s}$. At this stage, it is necessary to calculate the complex *eigenvalues* $\lambda = (\lambda_1, \ldots, \lambda_n)$, such that $J\vec{\rho} = \lambda\vec{\rho}$. Let $T = trace(J)$[1] and $D = det(J)$, the classification for the fixed point $\vec{s}$ by linear stability analysis is summarised as follows:

- Unstable fixed point (repellers or sources):
  $T > 0$, $D > 0$, $\forall\lambda_i \in \lambda : Re(\lambda_i) > 0$
- Stable fixed point (attractors or sinks):
  $T < 0$, $D > 0$, $\forall\lambda_i \in \lambda : Re(\lambda_i) < 0$
- Unstable fixed point (saddle points):
  $D < 0$, $\exists\lambda_i \in \lambda : Re(\lambda) > 0$

[1]The trace of a square matrix is the sum of the elements located on the main diagonal.

Additional study is required for the case in which there exist at least one eigenvalue with a null real part [Hirsch *et al.*, 2004].

4.2.3 Bifurcation analysis

Bifurcation analysis offers a way to detect and characterise qualitative behaviour variations around a selected steady state of a model. This leads to the investigation of signal trajectory changes by systematically exploring the domain of one or more model parameters. In conjunction with stability analysis, bifurcation analysis enables one to map the possible states of a system and how this system can switch between them [Aldridge *et al.*, 2006]. Biological systems are typically characterised by multiple steady states. Therefore, understanding the conditions by which a system transits from one steady state to another one is important, especially when investigating biological states which are apparently irreversible. Many age-related diseases discussed in Section 2.3 are defined by a cellular dysregulation which denies the system to restore its normal functionality. More generally, since ageing itself has been considered an irreversible process, it would be interesting to investigate under which conditions, a senescent phenotype may *resume* a pre-ageing phenotype or at least remain locked at the current state. Bifurcation analysis provides an exceptional tool for treating and possibly answering these biological questions. Due to the large body of bifurcation theory, this section only provides an overview of it in order to give a graphical interpretation insight of the analysis without dealing with the mathematical details. More formal introductions of this theory can be found in [Borisuk, 1997; Hirsch *et al.*, 2004].

The study of bifurcations concerns the individualisation of *bifurcation points* which are the points corresponding to specific parameter values at which a system undergoes a qualitative state change. A bifurcation is said to be *local* if the bifurcation point is located in the neighbourhood of a fixed point, also called steady-state, or periodic solution, otherwise it is called *global*. The number of parameters which must be specified in order to detect a bifurcation is called *codimension*. To clarify these concepts, two instances of bifurcation are graphically represented in Figure 4.2.

A system containing a bifurcation b can always be reduced to its *normal form*, which is the simplest system preserving b. Local bifurcations requires that the perturbation of a parameter alters the stability of a fixed point, that is that the real part of an eigenvalue in J passes through 0[1]. Because of this, a common approach when working on higher dimensional models consists of calculating the normal form of such a model and then focusing on the *eigenvectors* in the *centre* subspace[2], ignoring the *stable* and *unstable* subspaces [Borisuk, 1997; Borisuk and Tyson, 1998]. Conversely, a pragmatic way of mapping the states of a system is by systematically sampling the parameter space and then looking for qualitative differences in the phase space [Araujo *et al.*, 2007; Wang and Krueger, 2010]. Of course this approach is only suitable for lower-dimensional models.

4.2.4 Lyapunov exponents

When studying a dynamical system, it may be of interest to investigate qualitative behaviour changes over time [Aldridge *et al.*, 2006]. A measure used for characterising this quantity is the vector of *Lyapunov exponents*. This type of analysis allows one to determine specific attractors in the system evolution as well as the rate of these dynamical changes. Interestingly, the determination of this rate also provides an estimation of the rate of entropy production of the system. In a biological context, Lyapunov exponents can be used to prove whether a biological system is stable, asymptotically stable or presents some form of chaotic behaviour. To provide an intuition of this analysis, let us consider a reduced system composed of two points $x_1(t)$ and $x_2(t)$ in the state space of a dynamical system, assuming that they are very close together at initial time $t = 0$. Therefore, the objective is to study how these two points evolve over time. The trajectories individualised by these points diverge at a rate estimated by:

$$|x_1(t) - x_2(t)| \approx e^{\lambda t}|x_1(0) - x_2(0)| \tag{4.16}$$

[1] This typology of fixed points are called non-hyperbolic.

[2] *Centres* are fixed points for which the eigenvalue of J are purely imaginary. For these fixed points, the solution within their subspace do not converge to nor diverge from them.

where λ is a Lyapunov exponent. Since this exponent, which resembles a separation rate of trajectories, depends on the considered dimensions of the phase space, a general dynamical system evolving in an n-dimensional space $\mathbb{R}^n$ will be characterised by a *spectrum of Lyapunov exponents* $\{\lambda_1, \ldots, \lambda_n\}$. Moreover, as a spectrum depends on the positions of the trajectories at time $t = 0$, different spectra of Lyapunov exponents can be found by changing the initial time. Therefore, for each reached attractor, a particular spectrum can be calculated.
Among the Lyapunov exponents of a selected spectrum, the largest one, defined using the previous example as

$$\lim_{t \to +\infty} \frac{1}{t} \ln \frac{|x_1(t) - x_2(t)|}{|x_1(0) - x_2(0)|} \tag{4.17}$$

permits to obtain an overview of the global behaviour of the system, whereas the signs of all the exponents in the spectrum provides information about the type attractor [Parks, 1992]. In more detail, assuming that a system of the first approximation is regular[1], such as systems characterised by constant or periodic coefficients [Kuznetsov, 2008; Leonov and Kuznetsov, 2007], if all its Lyapunov exponents are negative, then the system is asymptotically Lyapunov stable, otherwise some form of chaotic behaviour occurs [Kuznetsov, 2008; Lyapunov, 1992; Parks, 1992]. This knowledge can be important in characterising the system in long-term dynamics. Furthermore, it may be significant to characterise the topologies of attractors to which a system may evolve and study how these states mutate in presence of stochasticity.

4.3 mTOR dynamical models

Interest in the mTOR network has increased in the recent years but only few, often incomplete, models have been developed. In this section, an overview of these existing mTOR models are presented.

[1]This condition is substantial [Leonov and Kuznetsov, 2007] as shown in [Perron, 1930] by counter-example.

4.3.1 Model of Jain and Bhalla

In [Jain and Bhalla, 2009], the authors proposed a signalling network model involving growth factors such as brain-derived neurotrophic factor (BDNF) and neurotransmitters such as glutamate to predict mTOR activity and downstream effects. The focus was the analysis of protein synthesis in dendrites which is fundamental for memory formation. Their model predicted levels of protein synthesis from the complex formed by eiF4F and S6, which are downstream targets of mTORC1. Three inputs were considered: a BDNF pathway which propagates the signal to mTORC1, metabotropic glutamate which binds to its receptor and stimulates Akt, and ionotropic glutamate and its relative calcium (Ca^{2+}) production. Once calcium levels are increased, the signal activates the ERK pathway by stimulating p21/Ras protein and MAPK, and the calcium-calmodulin type III kinase (CaMKIII) by inhibiting eukaryotic elongation factor-2 (eEF2). The model was parameterised using previously published experimental data, combined with published models of Ca^{2+} and MAPK signalling.
The authors found that the protein synthesis is primarily due to the BDNF signal and that MAPK serves to increase responses further. Three positive feedbacks related to BDNF, 40S and eEF2 were implemented. From the introduction of positive feedback, the authors identified bistability which is however not sufficient to declare that the system exhibits an inner switch-like behaviour because the model could not show bistability when fixed fractions of the total synthesised proteins were considered for each kind of feedback molecule.
The implemented model was based on about 130 molecular species. However, it does not consider mTORC2 nor any negative feedbacks. Also, the mTORC1 inhibiting-substrate protein PRAS40 is not included. The model lacks negative signals which are common in biological systems and it appears rather unlikely that there is no negative feedback in biological neuronal systems, since neuronal transmission is tightly controlled.

4.3.2 Model of Vinod and Venkatesh

In [Vinod and Venkatesh, 2009], a model of mTOR activated by amino acids and insulin growth factors (IGF) was proposed. Amino acids are necessary for the

mTOR activity and nutrient starvation is recognised to inhibit mTOR even when stimulated by growth factors such as insulin. In the developed model, amino acids regulate the activity of Class III PI3K or hVps34, regulating mTORC1 and p70-S6K. The insulin pathway involves the classic IRS1/PI3K/Akt/TSCs pathway. The model also introduces PRAS40 and FKBP38 as mTORC1 inhibitors. The authors mentioned mTORC2 in their model, although it is not associated with any other protein. The insulin pathway is parameterised by using data from an earlier more specific insulin model [Giri *et al.*, 2004]. Other parameters are taken from literature or assumed.
The authors found that amino acids are necessary to regulate Rheb, mTORC1 and PRAS40. In the absence of amino acids, their model predicted that an overexpression of the GTP form of Rheb is able to achieve the same effects of a stimulation based on amino acids.
In this ODE-based model, many parameters are assumed without any connection with experimental data and robust experimental validation and testing of the model predictions is missing.

4.3.3 Model of Borisov et al.

The model proposed by [Borisov *et al.*, 2009] studies the interactions between the insulin and epidermal growth factor (IGF and EGF), comprising positive and negative feedbacks. The PI3K/Akt pathway is activated by either IGFR directly or by EGFR indirectly involving the phosphorylation of Grb2-associated binder 1 (GAB1). The Ras/ERK pathway is activated directly by EGFR which can either bind with the complex Grb2-SOS or with Shc. The same pathway can also be activated indirectly by IRS1 binding with Grb2-SOS. There are numerous positive and negative feedbacks from IGFR and EGFR downstreams, such as mTORC1, GSK3 and ERK. These phosphorylate and inhibit proteins such as IRS1, Akt and GAB1 which then interrupt or increase the signal propagation. By using an experimental parameterisation, this model shows how insulin enhances the activation of the MAPK/ERK pathway whenever applied in combination with EGF. This cooperation between the two pathways is demonstrated to occur both upstream and at the level of p21/c-Raf (Ras/Raf) level.

The model predicts that the stimulation of insulin is only a weak indirect activator of EGF pathway. However, a synergistic effect was found in the presence of a co-stimulation of both EGF and IGF due to crosstalk interactions. This synergy becomes insignificant at saturating EGF levels.
The model is made of nearly 80 species and 110 reactions. In order to fit and customise the model, data from *in vitro* and *in vivo* experiments are used in combination with previously published models by the same authors. All performed simulations of the model were deterministic. Although an explicit identifiability analysis of the estimated parameters is missing, the authors reported numerous model predictions opportunely validated with experimental data. This continuous link between *in silico* and *in vitro* experiments is of crucial importance in systems biology in order to increase the confidence of the model predictions. This study therefore offers a clear example of how modelling-experimental-based approaches should work.

4.3.4 Model of Araujo et al.

In [Araujo *et al.*, 2007], dynamical systems properties were investigated in a reduced model of the TOR network. In this study, a minimal model comprising of just IRS1, Akt and mTORC1 was generated in order to determine and map dynamical states of the system to healthy or cancer phenotypes. A cancer phenotype was modelled by an hyper-activated positive feedback loop driven by Akt to the IRS1 [Gual *et al.*, 2005]. The authors analysed the case of no-treatment versus the cases of single inhibitory treatments of mTOR, Akt or IRS1 by gradually perturbing the input signal, represented by insulin. Therefore, their approach illustrates network behaviours under different conditions upon parameter perturbation, using techniques based on dynamical systems theory. In case of no-treatment or inhibition of mTOR, or IRS1, the hyper-activated positive feedback loop showed a one-way switch represented by bi-stability at low levels of input stimulus and by a monostable high response above a critical threshold of input level. In the case of inhibition of Akt, the one-way switch was converted to a two-way toggle switch (for a graphical representation of these two bifurcations, see Figure 4.2), permitting to control the positive feedback intensity by reducing the input stim-

ulus. Finally, the authors showed that these dynamical switches can be removed by a treatment inhibiting the positive interaction between Akt and IRS1[1]. This treatment would act to restore the functionality of the negative feedback loop, and a response control to different stimulus levels, changing the disease phenotype. Recently, Wang and Krueger [2010] showed that it is highly likely that only two dynamical states are possible for the model defined by [Araujo *et al.*, 2007]. This result was achieved by systematically exploring the model 6-dimensional parameter space and mapping types of signalling responses, without using any other experimental data sets. Although such reduced model may seem too simplistic to approximate the corresponding biological TOR network, it includes the two most important components of the network and the negative feedback loop. Therefore, the applied abstraction is correct because it contains all the necessary information for determining TOR regulatory mechanism, conserving the network behaviour. This study also represents a clear example of how dynamical systems theory can provide systems biologist with new interesting insights of a case of study, herein a simplified TOR network.

4.3.5 Model of Caron et al.

The knowledge about the mammalian TOR network has been steadily increasing in the last few years. Caron *et al.* [2010] reviewed this information in Systems Biology Graphical Notation (SBGN) [Le Novère *et al.*, 2009] and SBML [Hucka *et al.*, 2003] using the software CellDesigner [Funahashi *et al.*, 2008, 2003]. In contrast to the previous models, this work does not involve any time-course experimental data, parameter estimation or model simulation. Instead, the objective was to link all the pathways interacting with the complexes mTORC1 or mTORC2 into a single network. This integrative model comprises a total number of 777 reactions and 964 species, incorporating the upstream and downstream signalling of mTOR. In more detail, the included upstream signalling modules are growth factors, nutrients, energy, hypoxia, WNT, TNF, whereas the downstream modules comprise autophagy, protein folding, rRNA and ribosome

[1]IRS1 can also activate a positive feedback loop through its downstream target PKC as shown in 3.4.4.

biogenesis, cap-dependent translation, mitochondrial metabolism, cytoskeleton dynamic, transcription and cell cycle. The authors also generated a simplified network extracting the most relevant information from their extended model and highlighting the activation and inhibition reactions. In addition, a version is available as a web-service[1] and continuously updated. This review represents the first attempt to reproduce the TOR network on a large scale and therefore it undoubtedly constitutes an important achievement in systems biology.

4.4 Figures

[1]Web-service: http://sblab.celldesigner.org/Payao10/bin/

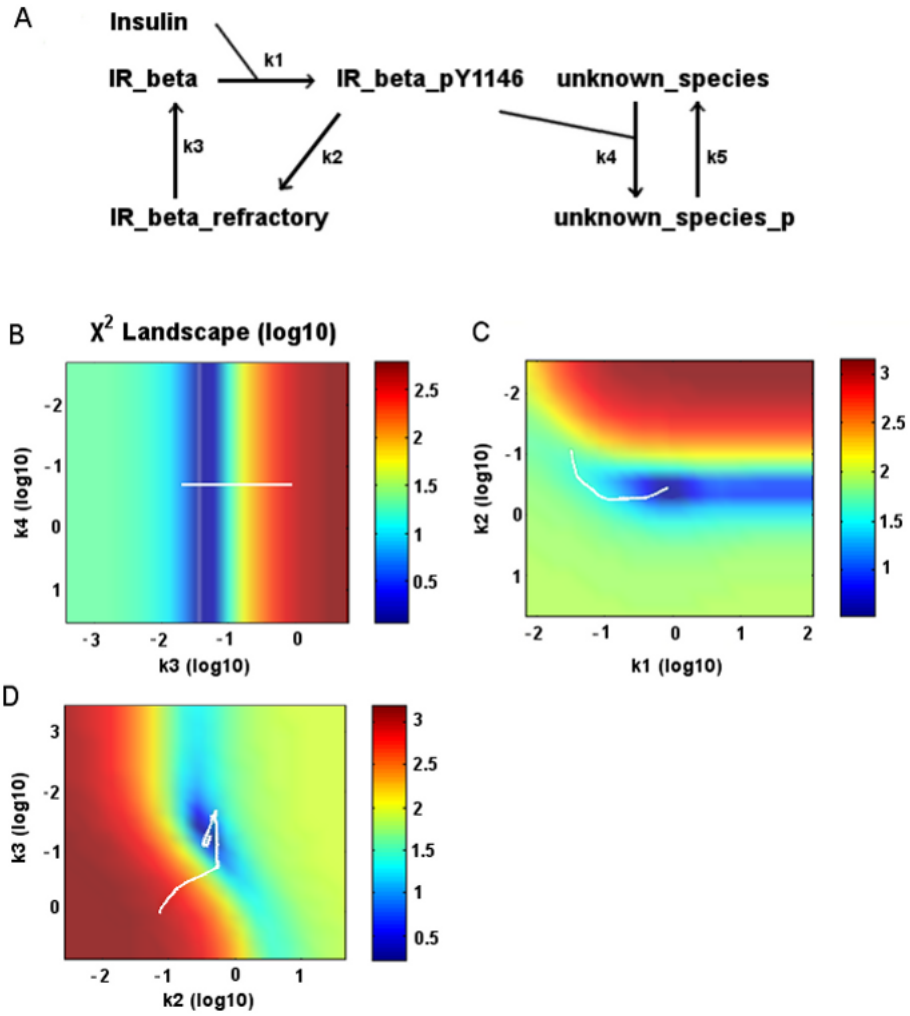

Figure 4.1: Graphical visualisation of parameter non-identifiability by $\log_{10}(\chi^2)$ landscape (darker colour correspond to parameter minimum). (A) Graphical mini-model of the insulin receptor with an additional unknown species. In this example, the only observable species is IR_beta_pY1146 which is phosphorylated by Insulin. IR_beta_pY1146 is responsible for the phosphorylation of unknown_species, a species for which no information is available. (B) Structural non-identifiability for the parameter regulating the phosphorylation of unknown_species. This parameter is clearly structurally non-identifiable as its dynamics are not mapped by any data. This parameter does not affect the search of solutions in the $\log_{10}(\chi^2)$ landscape. (C) Practical non-identifiability shown as an infinite upper bound confidence interval slightly above the parameter minimum (see blue χ^2 region on the right). (D) Parameter identifiability. The parameter is clearly identifiable showing a well defined minimum and a confidence region. White line indicates the convergence path to a solution in the $\log_{10}(\chi^2)$ landscape.

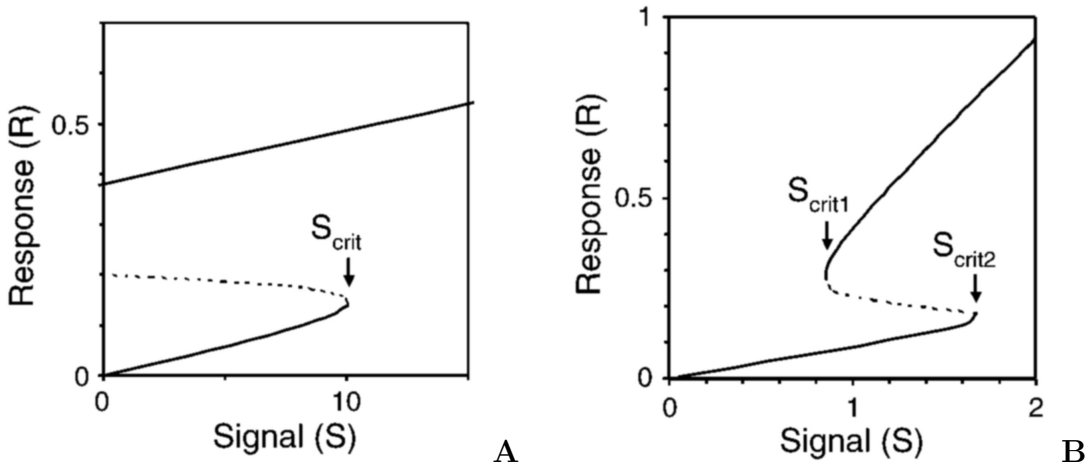

Figure 4.2: Graphical examples of bifurcations. (A) One-way switch bifurcation. At low levels of input stimulus, the system shows a bistable signalling response. After reaching a critical point, or bifurcation point, S_{crit}, the previous response dramatically changes into a monostable elevated response. This signalling response is characterised by two steady states (a low one and a high one) separated by an unstable state. However, the high steady state is the only one which persist above a certain threshold S_{crit} of input stimulus, since the system is not able to restore its signalling response to the low steady-state. (B) Two-way toggle switch bifurcation. This type of bifurcation presents two bifurcation points, called S_{crit1} and S_{crit2}, depending on both the strength and history of the input stimulus. This dependency of the response on the previous and current levels of the input stimulus represents the reason why these switches are also called *hysteresis*. In contrast to the previous case, this bifurcation permits to free the system from a constitutively activated response, since this one can be reduced by altering the signal strength. Adapted from [Tyson *et al.*, 2003, Fig. 1].

Chapter 5

A dynamical network model of mTOR signalling reveals TSC-independent mTORC2 regulation

This chapter describes a systems biology-based investigation of mTORC2 regulation as described in [Dalle Pezze *et al.*, 2012a]. The results here focus on the modelling point of view and only include *in vitro* experimental work necessary for model validation and test. All the *in vitro* data included in this project were collected by Annika Sonntag, PhD student supervised by Dr Kathrin Thedieck, Department of Bioinformatics and Molecular Genetics, Freiburg University, Germany. A copy of the published work, which includes the *in vitro* experimental data used for parameterising and testing the model, is attached in Appendix A.

5.1 Introduction

In this project an insulin-mTOR network model integrating both mTORC1 and mTORC2 was built and used to investigate alternative mTORC2 activation mechanisms. In contrast to mTORC1, little is known about mTORC2 upstream regulation (see Section 3.2). mTORC2 is mainly regulated by growth factors (see Section 3.2.1), but the molecular mechanism has not yet determined.
Many substrates of mTORC2 are proteins belonging to the family of AGC kinases (see Sections 3.1.3, 3.4). Using these AGC kinases as indicators of mTORC2 activity, the TSC1/TSC2 complex has been implicated in mTORC2 activation by insulin. It was found that TSC1/TSC2 inhibition reduces phosphorylation

of Akt at S473 [Huang *et al.*, 2008; Huang and Manning, 2009; Huang *et al.*, 2009; Inoki *et al.*, 2005], which contrasted with TSC1/TSC2 inhibition increasing mTORC1 activity [van Veelen *et al.*, 2011]. Two models have been proposed to explain mTORC2 regulation by TSC1/TSC2, one involving direct mTORC2 activation by TSC1/TSC2 [Huang *et al.*, 2008; Huang and Manning, 2009; Huang *et al.*, 2009], the other by an indirect mechanism through inhibition of PI3K in response to TSC1/TSC2 ablation via mTORC1-p70-S6K-dependent negative feedback loop (NFL) activation [Yang *et al.*, 2006]. However, data showing that mTORC2 contributes to proliferation in TSC2-null cells suggests that mTORC2 can be active in the absence of TSC1/TSC2 [Goncharova *et al.*, 2011]. A third hypothesis for mTORC2 activation is through a PI3K-independent mechanism, which has been identified in Dictyostelium [Cai *et al.*, 2010; Charest *et al.*, 2010; Kamimura *et al.*, 2008; Lee *et al.*, 2010b]. Interestingly, in mammals, several cellular processes that are regulated by mTORC2 have been described as PI3K independent [Jacinto *et al.*, 2004; Kamada *et al.*, 2005; Sarbassov *et al.*, 2004; Worthen *et al.*, 1994; Zheng *et al.*, 1997].

To distinguish among the possible mTORC2 activation mechanisms and to determine whether they acted independently or in combination, a dynamical model was developed, assuming that different modes of mTORC2 regulation would result in distinguishable, dynamical network responses. The model was parameterised with dynamic quantitative time course data and its predictions experimentally validated. Then, perturbations were used to simulate and experimentally test alternative network structures connecting upstream insulin signalling to mTORC2. This approach also provided the benefit of both a structural and dynamical network analysis [Papin *et al.*, 2005].

In contrast to the previous hypotheses, TSC1/TSC2 complex was found not to be a direct activator of mTORC2 and that mTORC2 activity was insensitive to the mTORC1-induced NFL. Although PI3K was inhibited by the NFL, activation of the NFL-insensitive mTORC2 also required active PI3K. Therefore, none of the three literature-based hypotheses was confirmed and we proposed a new hypothesis that insulin signalling activated mTORC2 through a PI3K that was insensitive to the NFL. This new model fitted all our collected experimental data.

5.2 Results

5.2.1 Development of a dynamical insulin-TOR network model

Initially, a static network model in SBGN format [Le Novère *et al.*, 2009] of insulin-mTOR signalling was established as a means to integrate current knowledge [Cybulski and Hall, 2009; Feldman and Shokat, 2010; Garcia-Echeverria, 2011; Howell and Manning, 2011; Polak and Hall, 2009; Sengupta *et al.*, 2010; Zoncu *et al.*, 2011] and as a platform to chose appropriate targets for measurement (Figure 5.1). It is impractical to work with such a large network, due to the high number of parameters and the difficulty in obtaining sufficient experimental data under reasonable time and cost. The extended model presented in Figure 5.1 was therefore abstracted by selecting (1) regulation mechanisms with an important role in dynamical behaviour (e.g. the activation of mTOR complexes by the presence of both amino acids and insulin, the pathways connecting these stimuli to the mTOR complexes, and the NFL from p70-S6K to IRS), and (2) measurable molecules and interactions distributed across the network (Y1146-phosphorylated IR, the S636- phosphorylated IRS1, S473- and T308-phosphorylated Akt, S2448- and S2481-phosphorylated mTOR, T246- and S183-phosphorylated PRAS40, and T389-phosphorylated p70-S6K). These readouts are marked with an asterisk in Figure 5.1. This simplified network shows insulin signalling propagating from the IR through the TSC1/TSC2 complex to the mTORC1 complex and includes p70-S6K, PRAS40, and Akt. In addition, mTORC1 induction by amino acids was included. At this stage, no upstream pathway regulating mTORC2 was assumed (see Figure 5.2).

Studies suggesting that TSC1/TSC2 regulates mTORC2 commonly used Akt phosphorylated at S473 (Akt-pS473) as an mTORC2 readout. However, Akt activity depends on PI3K-dependent relocalisation to the plasma membrane and subsequent phosphorylation at T308 by PDK1 and at S473 by mTORC2 [Pearce *et al.*, 2010]. PI3K and Akt are inhibited in the absence of the inhibitory TSC1/TSC2 complex, due to mTORC1 and NFL hyperactivation. Consequently, under conditions of TSC1/TSC2 deficiency and NFL activation, monitoring Akt-

pS473 does not distinguish between PI3K, PDK1, and mTORC2 activity, and therefore may not be a suitable readout to investigate the mode of mTORC2 regulation by TSC1/TSC2 [Huang and Manning, 2009]. Other AGC kinases that are targeted by mTORC2 (SGK and PKC) have similar issues [Bruhn *et al.*, 2010; Jacinto and Lorberg, 2008]. In this study mTOR-S2481 was used as a direct marker of mTORC2 activity in addition to using Akt-S473. Details about the specificity of mTOR-S2481 as an mTORC2 readout for HeLa cells can be found in [Copp *et al.*, 2009] and in [Dalle Pezze *et al.*, 2012a,b].

5.2.2 Parameterisation of the network model

Immunoblot-based phosphorylation time-courses for network components along the signalling cascade were generated to parameterise the model depicted in Figure 5.2. Data were collected from HeLa cells under amino acids/insulin starvation and restimulation conditions and quantified from 1 min up to 2 hours post induction with amino acids/insulin. The model parameters were estimated using the mean time course, computed from four time-course repetitions (Figure 5.3). The initial concentrations of the species in their non-phosphorylated state were determined directly from these semi-quantitative data (see Section 5.4.1). For all other species, the initial concentrations were set to 0.

Due to the known difficulty in calibrating a large number of parameters from the data [Chen *et al.*, 2010; Moles *et al.*, 2003; Zhan and Yeung, 2011], in this case kinetic rate constants, parameter estimation was divided into calibration phases (see Figure 5.4). In Phase 1 of the parameter estimation, isolated modules that could be calibrated independently within the network, were identified. Because the IR regulation was not affected by the rest of the network, the 3 parameters governing the kinetics of IR activation by insulin, dephosphorylation to a refractory state and transition to a receptive state could be isolated and independently calibrated. In Phase 2, due to the lack of knowledge about mTORC2 upstream, a model that was independent of the pathway by which mTORC2 was activated, was generated. The regulation of the mTORC2 substrate Akt-S473 and mTORC2 component mTOR-S2481 were temporarily modelled with two auto-activation mechanisms, which were then calibrated using Akt-pS473 and

mTOR-pS2481 experimental datasets. This guaranteed to reproduce Akt-pS473 activation while maintaining mTORC2 isolated from the network. During Phase 2, a total of 24 reaction rate constants were estimated using eight experimental readouts. Finally, in Phase 3, the autoactivation mechanism of Akt-pS473 was replaced with a phosphorylation mediated by mTORC2-pS2481. Because the initial induction of Akt-pS473 occurred before mTOR-pS2481 was induced (see Figure 5.3), mTORC2-pS2481 alone could not completely reproduce the dynamics of the experimental data for Akt-pS473. mTORC2 is not the only PDK2 candidate that may phosphorylate Akt-S473; therefore, an additional PDK2 species was introduced and parameters governing the phosphorylation of Akt-S473 under the influence of the two kinases, were re-estimated. In this phase, three kinetic rate constants were estimated using the Akt-pS473 experimental data.
Each of these phases was resolved using an iterative procedure (see Figure 5.5). This procedure is summarised by the following steps:

1. The initial values of the parameters that needed optimisation were assigned by random generation;

2. the calibration was repeated until a set of parameters with consistent values was identified;

3. this set of parameters was fixed and the remaining free parameters were calibrated again by repeating the process.

Once this process of parameterisation was complete, the simulated time courses matched the experimental data for all the analysed mTOR network readouts (Figure 5.3). The ordinary differential equations (ODEs) and estimated parameters for the general model are provided in Tables 5.1-5.2. Identifiability analysis, which indicates whether the parameters can be estimated with confidence from the available data, and sensitivity analyses, which indicates how sensitive model behaviour is to variation in each parameter, for the general model are shown in Figures 5.6-5.7. Importantly, the identifiability analysis did not show high correlation between estimated parameters indicating that they could indeed be identified.

5.2.3 Validation of the mTORC1 branch

If a parameterised model correctly represents the biological mTOR network dynamics in response to amino acids/insulin, model simulations must accurately reflect the dynamics of known network responses to a gradual perturbation. To validate the mTORC1 branch of the model, the network was perturbed by gradually inhibiting mTORC1 first *in silico*, and then experimentally by Raptor knock down (shRaptor). The model was used to simulate the effect of gradual mTORC1 inhibition on the activation dynamics of the direct mTORC1 substrate p70-S6K-pT389, at several time points after induction with amino acids/insulin.
The model predicted a constant increase in p70-S6K-pT389 signal from 10 min to 2 hours after induction. Furthermore, the model also predicted that p70-S6K-pT389 would decrease starting 10 minutes after induction in a near linear manner in response to gradual Raptor (mTORC1) inhibition, whereas there should be no detectable increase or Raptor-dependent change in p70-S6K-pT389 below 5 min after induction (see Figure 5.8A). This simulated quantitative p70-S6K-pT389 response upon gradual mTORC1 inhibition (see Figure 5.8B) was experimentally validated (see Figure 5.8, C and D) at 3, 20 and 45 min, also indicated in the simulation in Figure 5.8A by the green lines. The simulations (Figure 5.8B) and the experimental results (Figure 5.8D) monitoring p70-S6K-pT389 activity in response to gradual Raptor inhibition at 20 and 45 min after induction with amino acids/insulin consistently showed an overall increase in signal at 45 min and no signal at 3 min after induction.
Therefore, the model accurately reproduced the dynamic behaviour of the mTORC1 substrate p70-S6K-T389 upon gradual mTORC1 inhibition.

5.2.4 Alternative models of mTORC2 regulation by TSC1/-TSC2

Two alternative mechanisms of TSC1/TSC2-dependent regulation of mTORC2 have been suggested: either direct activation or indirectly through mTORC1 and NFL [Huang *et al.*, 2008, 2009; Yang *et al.*, 2006]. Since the different suggested molecular mechanisms by which TSC1/TSC2 regulates mTORC2 should result in mechanism-specific changes in the dynamics of the mTORC2 readouts, the

response of the readouts to network perturbations should be predictable and distinguishable through dynamical modelling.
On the basis of the existing literature, we postulated three different hypotheses for the molecular connection, or lack thereof, between TSC1/TSC2 and mTORC2 (see Figure 5.9):

Hypothesis 1 (TSC-dependent): TSC1/TSC2 directly activates mTORC2 in response to insulin, and has opposite effects on mTORC1 and mTORC2

Hypothesis 2 (NFL-dependent): mTORC2 is activated by insulin through PI3K, but independently of Akt and TSC1/TSC2, however mTORC2 activity can be inhibited indirectly by TSC1/TSC2 ablation through NFL-mediated inhibition of PI3K;

Hypothesis 3 (PI3K-independent): mTORC2 is activated by insulin in a manner that is independent of both TSC1/TSC2 and PI3K.

These hypotheses were directly implemented into the established model, re-using the same kinetic parameters. To keep the hypotheses as comparable as possible, each hypothesis shared the network topology of this general model but assumed a specific mTORC2 upstream regulator according to each hypothesis (see Figure 5.9). These kinetic parameters regulating mTORC2 were re-estimated according to each hypothesis (see Tables 5.1, 5.3). The total goodness-of-fit for the general model and each hypothesis showed that no model could be statistically rejected (see Table 5.4), in accordance with the following:

Lemma 1. *Let $\mathcal{M}$ be a model correctly parameterised with some data*[1] *and s a species in $\mathcal{M}$. If a modifier f directly upstream of s is selected and re-calibration solely of the dynamics of s maintains a close fit between the simulated time course for s and the experimental data for s, then all the time course curves downstream of s will continue to fit their corresponding data.*

Proof. Let U be the set of the upstream species of f ($U = \{upstream\_species(f)\}$) and D be the set of the downstream species of d ($D = \{downstream\_species(s)\}$)

[1]This assumes that the model parameters are structurally and practically identifiable (see Section 4.1.4).

by applying a cut of the feedback loops. Depending on the existence of a feedback loop connecting an arbitrary species $d \in D$ to an arbitrary species $u \in U$, there exist two cases.
Case 1: $\nexists\ d \to u \mid d \in D, u \in U$. After model re-calibration, the time-course of f remains unchanged and the time-course of s is not affected by the dynamics of the network. Since the simulated time course of s still fits the experimental data for s by hypothesis, the signalling cascade from s does not significantly differ, maintaining the fitting of the species in D with their corresponding experimental data.
Case 2: $\exists\ d \to u \mid d \in D, u \in U$. In this case, the time-course of f is also modulated by some $d \in D$ and s dynamics are therefore affected by the network. However, f can be interpreted as downstream target of s beyond the application of the cut. Thus, for the previous case, the simulated time course of f maintains the fit with its corresponding experimental data. □

For each hypothesis, time course simulations and experimental validation for the mTORC2 readouts mTOR-pS2481 and Akt-pS473, the PI3K readout Akt-pT308, and the mTORC1 substrate p70-S6K-pT389 (see Figure 5.10) were performed. The curves for all other analysed network components are provided in Figure 5.11. The simulations matched the experimental time courses, indicating that the hypotheses were compatible with the observed dynamics for mTORC2 activation and more generally for the mTOR signalling network. Further experimental validation of these models for the mTORC1 branch, monitoring p70-S6K-pT389 can be found in [Dalle Pezze *et al.*, 2012a, Fig. 7A]. Identifiability and sensitivity analyses for the three models representing each hypothesis are shown in Figures 5.12-5.17.

5.2.5 Perturbations of alternative models of mTORC2 regulation

As independent parameter estimation for the three models could not clearly reject any of the previous hypotheses, gradual network perturbations of TSC1/TSC2, the NFL (through perturbation of mTORC1), or PI3K were computationally applied and then experimentally tested. The idea was that the hypotheses might

have been rejected by first perturbing the respective upstream modulators of mTORC2 as determined for each hypotheses for each model and then finding experimental inconsistencies with the predicted perturbations. In formal terms:

Definition 1. *Let* $t : f \rightarrow s \mid f, s \in Species$ *be a connection. Then,* t *is said* correct *if it can be experimentally proved.* t *is said* incorrect *if it can be experimentally negated.*

Lemma 2. *Let us assume the conditions established in Lemma 1 and that all the connections besides the connection* $t : f \rightarrow s$ *for a model* $\mathcal{M}$ *correctly parameterised with some data, are* experimentally correct*. If the introduced upstream connection* t *is* correct *then the model output following perturbation of* f *will* necessarily *maintain a fit with the corresponding data. Instead, if* t *is* incorrect*, then the model output following perturbation of* f *will not* necessarily *maintain a fit with the corresponding data.*

Proof. This lemma shows a semi-decidability property for model rejection.
Case 1: t is *correct*. Then, a simulated perturbation of f is consistent with the corresponding data upon experimental perturbation of f, since the model was correctly parameterised.
Case 2: t is *incorrect*. Then, a simulated perturbation of f may or may not be consistent with the corresponding data upon experimental perturbation of f. In fact, if this is not consistent, then the network can be clearly rejected. Instead, if the prediction is still consistent, then nothing can be asserted with such a simulated perturbation and further testing is required. Instances of this case can arise due to model abstraction or multiple input besides f to s. □

From Lemma 2, a tool for rejecting a model was formalised in case of detection of model inconsistency with some data upon perturbation.

In this study, the connection t referred to as the link from a kinase regulating mTORC2 and mTORC2 itself. For each of the three perturbations and each of the three hypotheses, the dynamical network response of the readouts of mTORC2-pS2481 activity (see Figure 5.18), Akt-pS473 activity (see Figure 5.19), Akt-pT308 activity (see Figure 5.20), and p70-S6K-pT389 activity (see

Figure 5.21) were detected. These simulated perturbations unambiguously distinguished network behaviour, indicating specific experimental testing treatments, and highlighted time points in which these differences occurred (see green lines in Figures 5.18-5.19).

5.2.6 Predictions and experimental testing of mTORC2 regulation

Prediction and testing for Hypothesis 1

The models predicted that for gradual TSC1/TSC2 inhibition, if Hypothesis 1 was correct, then the abundance of mTOR-pS2481 would be affected by TSC1/TSC2 inhibition in a linear manner down to minimum levels (Figure 5.18). In contrast, for Hypothesis 2, simulated mTOR-pS2481 dynamics were only slightly affected by TSC1/TSC2 inhibition, and for Hypothesis 3, mTOR-pS2481 was not affected (Figure 5.18). For Akt-pS473 dynamics, the phosphorylation should only be affected after 5-10 minutes since the PDK2 candidates are modelled as independent of TSC1/TSC2. If Hypotheses 2 or 3 are correct, then Akt-pS473 should exhibit a gradual decrease starting 10 min after induction for the rest of the time course (Figure 5.19). For Hypothesis 1, the model predicted a stronger reduction of Akt-pS473 in response to TSC1/TSC2 inhibition, compared to the reduction predicted for Hypothesis 2 or 3. Thus, these simulation results indicated that observation of mTOR-pS2481 in response to gradual TSC1/TSC2 inhibition should effectively distinguish Hypothesis 1 from the two other hypotheses.
Quantifications for Akt-pS473 and mTOR-pS2481 at 60 min after amino acids/ insulin induction are shown for the simulations of the three hypotheses, and for the experimental data in Figure 5.22A. The time course analysis on Akt-pS473 suggested that Hypothesis 2 or 3 may be correct. Hypothesis 1 (direct TSC1/TSC2 activation of mTORC2) was clearly excluded because the reduction in mTOR-pS2481 activity upon TSC2 inhibition was not statistically significant. For experimental details, see [Dalle Pezze *et al.*, 2012a, Fig. 6].

Prediction and testing for Hypothesis 2

For gradual mTORC1 inhibition and consequent NFL inhibition, the models predicted an increase of Akt-pS473 with decreasing mTORC1 activity (Figure 5.19). The simulations also predicted that mTOR-pS2481 would remain unaffected in Hypotheses 1 and 3, and would gradually increase in response to mTORC1 inhibition in Hypothesis 2 starting 40 min after induction with amino acids/insulin (Figure 5.18). This effect should be clearly experimentally visible at 100 min after induction with amino acids/insulin and this paradigm could be used to distinguish Hypothesis 2 from the other hypotheses.
Quantifications for Akt-pS473 and mTOR-pS2481 in response to gradual Raptor inhibition are shown in Figure 5.22B. The time course analysis on Akt-pS473 suggested that all three hypotheses may be correct. Hypothesis 2 (indirect TSC1/TSC2 activation of mTORC2 by NFL) was clearly excluded because no increase in mTOR-pS2481 activity upon Raptor inhibition was detected as statistically significant. For experimental details, see [Dalle Pezze *et al.*, 2012a, Fig. 7].

Prediction and testing for Hypothesis 3

For gradual PI3K inhibition, all the three models predicted strong reduction in Akt-pS473 levels (Figure 5.19). In contrast, the models predicted that mTOR-pS2481 (Figure 5.18) would remain either unaffected by PI3K inhibition (Hypothesis 1, 3), or to decline with decreasing PI3K starting 20 min after induction (Hypothesis 2).
Quantification for Akt-pS473 and mTOR-pS2481 at 30 min after induction with amino acids/insulin are shown in Figure 5.22C). The time course analysis on Akt-pS473 suggested that all the three hypotheses may be corrected. Hypothesis 3 (PI3K-TSC1/TSC2-independent activation of mTORC2) was excluded since mTORC2 was inhibited by the PI3K inhibitor Wortmannin. For experimental details, see [Dalle Pezze *et al.*, 2012a, Fig. 8].

5.2.7 A novel hypothesis of mTORC2 activation

The results reported in Section 5.2.6 showed that mTORC2 was not regulated by TSC1/TSC2 or the NFL, whereas it was activated by insulin in a PI3K-dependent manner. Since mTORC2 regulation was independent of NFL, the PI3K involved in mTORC2 activation had to be IRS1 independent. It is well known from literature that several isoforms of PI3Ks exist and only some of them bind with IRS1. Therefore, it is reasonable that a PI3K isoform independent of IRS may be responsible of mTORC2 regulation. This new hypothesis, referred to as Hypothesis 4, was implemented into a model (see Figure 5.23). This model did not require recalibration, because the new branch for mTORC2 activation by insulin was similar to the PI3K-independent Hypothesis 3, but contained the new proposed PI3K, which is sensitive to Wortmannin and independent of the NFL.
The simulated time courses of this new model matched all the available experimental data presented in this study (see Figure 5.24A for mTOR-pS2481 and Akt-pS473 and Figure 5.25A for all other readouts). For each of the three network perturbations (gradual TSC1/TSC2, mTORC1, or PI3K inhibition), the predictions for all readout dynamics (see Figures 5.24A-D, 5.25B) matched the experimental data (Figures 5.22). Additional model validation for mTORC2 activity was performed by mTORC2 and mTORC1 knock down, experimentally obtained by Rictor and Raptor knock down respectively, at 20 minutes after amino acids/insulin induction, showing a close match with the experimental data (see Figure 5.26). This last result was published in [Dalle Pezze *et al.*, 2012b].
Identifiability and sensitivity analyses for Hypothesis 4 are shown in Figures 5.27-5.28. The identifiability analysis reports low correlation between the estimated parameters, indicating that the parameters can be identified. Thus, the new model representing mTORC2 induced by a PI3K-variant species independent of NFL and IRS1 accurately predicted the responsiveness of mTORC2 to PI3K inhibition, and mTORC2 insensitivity to gradual TSC1/TSC2 or mTORC1 inhibition.

5.3 Discussion

This work presents the development of a computational model of the TOR network, whose parameters were estimated by immunoblot-based semi-quantitative time-course data. From this model, three hypotheses of mTORC2 activation based on literature were investigated: (1) mTORC2 was directly activated by complex TSC1/TSC2; (2) mTORC2 was indirectly activated by complex TSC1/TSC2 through the NFL; (3) mTORC2 activation was independent of complex TSC1/TSC2 and NFL. This current confusion in the literature concerning the modalities of mTORC2 activation was mainly due to the use of mTORC2 substrate Akt-S473 as readout of mTORC2 activity [Huang *et al.*, 2008, 2009; Yang *et al.*, 2006]. However, Akt is involved in the NFL induced by p70-S6K to IRS1 and therefore it is not a reliable candidate for monitoring mTORC2 activity. In this study we used mTOR-S2481 in addition to Akt-S473, as readouts of mTORC2 activity. mTOR-S2481 was previously shown to be a specific marker for mTORC2 activity [Copp *et al.*, 2009] and we also validated it in this study [Dalle Pezze *et al.*, 2012a,b]. For each hypothesis, a dynamical model was derived from the generic one (see Figures 5.2, 5.9). Since the parameter estimation for each derived-model does not allow rejection of any hypothesis, model perturbation analysis was conducted by varying the levels of mTORC2 input candidates. Perturbations of TSC1/TSC2, mTORC1 and PI3K were selected for predicting differential network behaviours and the specific time points at which these differences were maximised. These predictions clearly indicated experimental modes of intervention for testing the three hypotheses. By experimental testing of the model predictions, all three hypotheses were rejected. Surprisingly, the PI3K inhibitor Wortmannin was found to inhibit mTORC2. Since mTORC2 was proved independent of the NFL in testing Hypothesis 2, and mTORC2 levels were reduced less than Akt levels upon Wortmannin treatment, it appeared that mTORC2 could be activated in an NFL-independent and PI3K-dependent manner. This new pathway (Hypothesis 4) was implemented in a new model which was shown to be consistent with all the generated experimental data.

Dynamical modelling has been used extensively in the study of cell signalling networks, yielding many important insights related to cellular behaviour [Kholo-

denko, 2006]. Here we use dynamical modelling to discriminate among alternative network structures, in particular alternative modes of mTORC2 regulation. Others have used similar approaches to study the possible network structures for the segment polarity gene network [von Dassow *et al.*, 2000] and the extracellular signal-regulated kinase pathway [Xu *et al.*, 2010]. Although network testing can be performed using a Bayesian statistical approach [Xu *et al.*, 2010], we chose to perform experimental testing to distinguish among the proposed network topologies, because our simulated conditions and outputs were experimentally tractable. This work differs from earlier studies [Huang *et al.*, 2008; Huang and Manning, 2009; Huang *et al.*, 2009] due to the inclusion of a direct readout for mTORC2 activity (mTOR-S2481) and in using a combined modelling-experimental approach. The modelling enabled us to predict network hypothesis dynamics and define a precise experimental plan to test these predictions. Through this methodology of hypothesis-modelling and experimental testing, a new PI3K-mTORC2 pathway, which was not previously discovered, was hypothesised and confirmed by several experimental tests.

In the tasks of data collection and parameter estimation, Akt regulation showed a high degree of complexity which is largely overlooked in other insulin signalling modelling studies. Model parameterisation revealed more complex dynamics for mTORC2's target site S473 in the AGC kinase Akt than for S2481 in mTOR, and this could not be explained exclusively by mTORC2 activation. To integrate Akt-pS473 dynamics into the dynamic network model, a second PDK2 that accounted for the early peak of Akt-pS473 at 3 min after induction with amino acids/insulin (Figure 5.3) was considered. This need arose since, in addition to mTORC2, various other PDK2 candidates for Akt have been reported, including DNA-PK [Bozulic *et al.*, 2008; Feng *et al.*, 2004], ILK [Troussard *et al.*, 2003], ATM [Viniegra *et al.*, 2004], MAPKAPK-2 [Rane *et al.*, 2000], PKC [Kawakami *et al.*, 2004; Partovian and Simons, 2004], Pak1 [Mao *et al.*, 2008b], and even Akt autophosphorylation [Toker and Newton, 2000], any of which may contribute to Akt-pS473 dynamics under different metabolic conditions.

This model implements the NFL as induced by p70-S6K which phosphorylates and degrades IRS. However, this is not the only negative feedback in the insulin-TOR signalling. For example, mTORC1 activation leads to GRB10-dependent

IR inhibition [Hsu *et al.*, 2011; Yu *et al.*, 2011]. Although the identification of GRB10 as a contributor to the NFL is mechanistically relevant, the effect is the same, namely the inhibition of IRS in response to mTORC1 activity, and is readily detected by the reduction of Akt-pT308 upon high mTORC1 activity. Given the need to reduce the complexity of our model to enable parameterisation, we did not introduce such mechanisms separately into our model, but combined them into one step.

In this work, a new PI3K, independent of IRS and NFL, was found to mediate the insulin signalling from the insulin receptor to mTORC2. Interestingly, previous studies detected PI3K activity in cells lacking IRS [Myers, Jr *et al.*, 1994; Peruzzi *et al.*, 1999], or PI3K activation in part by direct binding with the insulin receptor [Horn *et al.*, 1994]. Therefore, it could be that an IRS-independent PI3K may be responsible for propagating alternative insulin signalling in order to activate mTORC2. In this study, a maximum Wortmannin concentration of 100nM was used to inhibit PI3K and this level was reported to inhibit class I PI3Ks only [Brunn *et al.*, 1996]. Particularly, we showed that a Wortmannin concentration of 20nM was sufficient to inhibit mTOR-pS2481 and this furthermore confirmed mTORC2 dependency on class I PI3K, in agreement with other studies [Peterson *et al.*, 2000; Soliman *et al.*, 2010]. Despite the identification of class I PI3Ks, for this class, there are at least seven alternative regulatory subunits and four alternative catalytic subunits, and specific combinations of these subunits may mediate different physiologic outputs. Therefore, the existence of an NFL-independent class I PI3K is conceivable and requires further investigation.

In conclusion, the discovery of mTORC2 activation by an IRS-independent PI3K means that a new perspective of the insulin signalling network is required. This study is also of importance for developing new drugs in cancer and ageing research. Due to the complexity of the TOR network, this work showed the high impact that mathematical modelling can have on biology by formalising hypotheses, predicting outcomes and offering modalities of interventions to test these predictions. Importantly, despite being an abstraction of the insulin-TOR network, model simulations mathematically showed that the simplified system was sufficient to explain the experimental observations. Finally, the model provides a resource for future work and other modelling efforts can extend and build upon

it, as well as provide a framework on which pharmacological interventions can be tested.

5.4 Materials and methods

5.4.1 Modelling

CellDesigner 4.2 [Funahashi *et al.*, 2008, 2003] was used to construct the model network topology in SBGN [Le Novère *et al.*, 2009]. COPASI 4.7.34 [Hoops *et al.*, 2006] was used for all deterministic simulations, parameter estimations, parameter scanning and sensitivity analysis. The deterministic simulation algorithm (LSODA) was configured with parameters: Duration (1440), Interval Size (1), Intervals (1440), Integrate Reduced Model (0), Relative Tolerance (1e-06), Absolute Tolerance (1e-12), Max Internal Steps (10000). The algorithm used for parameter estimation was Simulated Annealing [Corana *et al.*, 1987; Kirkpatrick *et al.*, 1983], configured with parameters: Start Temperature (1), Cooling Factor (0.85), Tolerance (1e-06), Random Number Generator (1), Seed (0). The parameter estimation weight method was Mean Square and the experiment type was Time Course. The initial concentration of the species in non-phosphorylated state was fixed to the maximum intensity of the third quantile time course, computed from the four experimental datasets, of the corresponding experimental phosphorylated protein. This ensured that the modelled kinases did not saturate their substrates and that the level of concentration of the substrates remained small. The initial concentration of the species in any other state was fixed to 0. The initial concentration of PDK2 was assumed equal to the concentration of the beta subunit of the IR because the two species are directly connected in the model. In the absence of experimental data for the TSC complex, the initial concentration was assumed to be 10. The models were formalised using only mass action reactions. For each phase, the kinetic rate constants were estimated by running 350 independent calibrations, each initialised with a random initial configuration of the parameters. The parameter values were constrained within the interval [1e-04, 1], except for the Akt parameters, which were constrained within the interval [1e-04, 10]. For each calibration phase (F), the solutions of the estimations con-

sistent with the data and achieving the lowest root mean square error (RMSE) were selected as the best solutions set (BS). Among these, the solution closest to the centroid of the BS cluster in the parameter space was selected using the following formula:

$$\underset{S \in BS_F}{\operatorname{argmin}} \sum_{i=1}^{N} (S(p_i) - \mu_i)^2 \tag{5.1}$$

with:

$$BS_F = \left\{ \begin{array}{c} x \mid \forall y \in AllSolutions, \\ RMSE(Model(x), Data) \leq RMSE(Model(y), Data) \end{array} \right\}$$

where p_i, is the i^{th} estimated parameter in S, μ_i is the i^{th} parameter mean computed from BS_F and N is the number of estimated parameters.
Model identifiability based on correlation analysis of sensitivity trajectories was calculated using SBToolbox2 and SBPDToolbox [Schmidt and Jirstrand, 2006] for MATLAB. SBMLToolbox 4.0.1 [Keating *et al.*, 2006] was used to import our SBML [Hucka *et al.*, 2003] models into SBToolbox2. Identifiability analysis tables for the general model and the four hypotheses models are depicted in Figures 5.6, 5.12, 5.14, 5.16 and 5.27.
All parameter values for the final models are given in Tables 5.2-5.3. The sensitivity analysis algorithm was configured for time series with parameters: Delta Factor (0.001) and Delta Minimum (1e-12) (Figures 5.7, 5.13, 5.15, 5.17, 5.28). Models were exported in SBML Level 2 Version 4 using Copasi and CellDesigner. The latter was used to generate the extended mTOR network model in SBGN graphical notation.

5.4.2 Statistics

The statistical and programming language R v.2.12.1 [R Development Core Team, 2010] was used to calculate the statistics and generate the plots of this study. The Standard Error of the Mean (SEM) was chosen to estimate the statistical variability of the measured samples of experimental time course. Model goodness-of-fit was defined by computing Akaike information criterion [Akaike, 1973] and

χ^2 calculated as in Formulae 4.3 and 4.4. For the general model and the four hypotheses, χ^2 and Akaike information criterion measures are provided in Table 5.4. Tukey's Honest Significant Differences (HSD) test, in conjunction with one-way analysis of variance (ANOVA), was used as statistical test for multiple comparisons among groups of experimental data.

5.5 Figures and tables

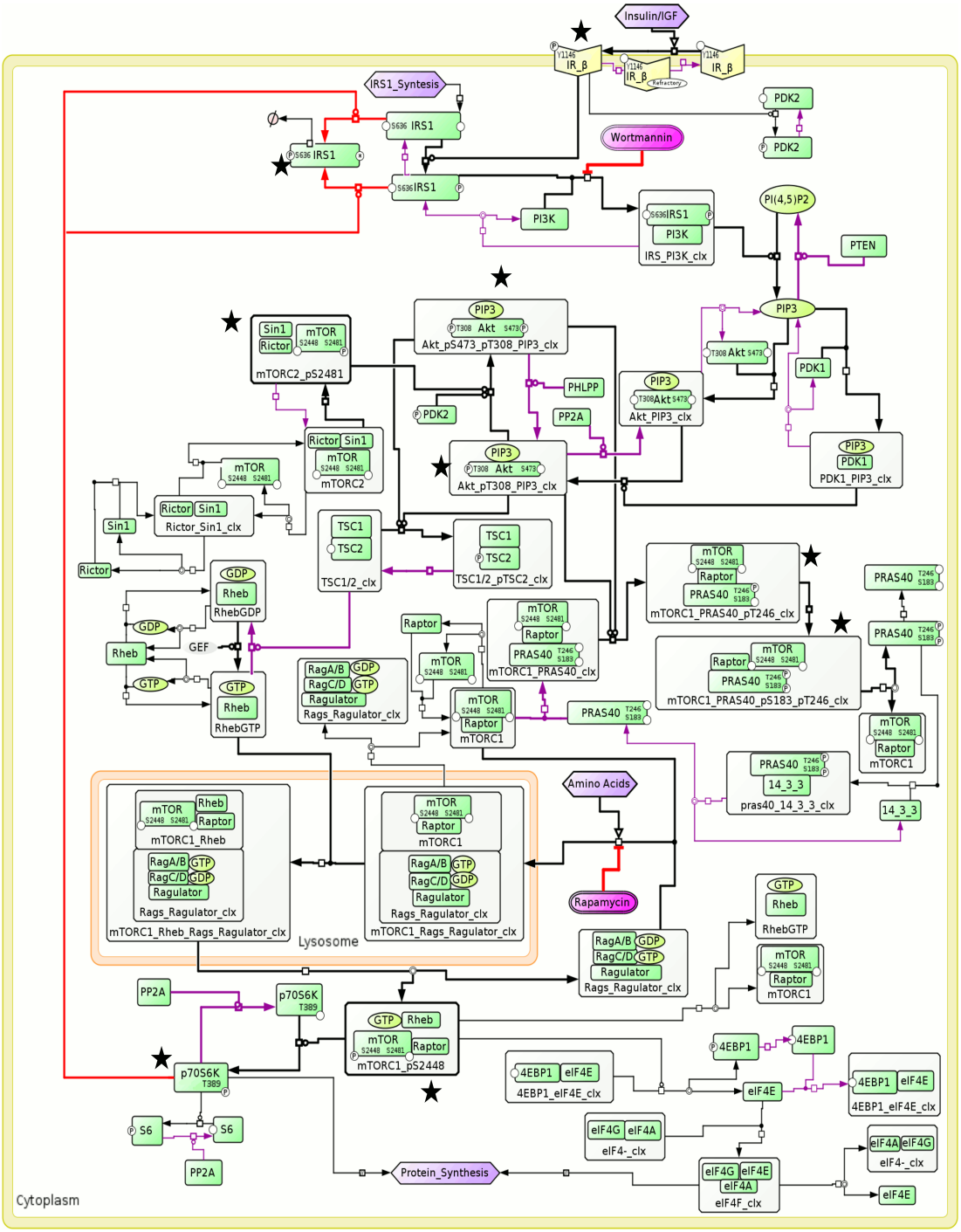

Figure 5.1: A static network model of TOR signalling stimulated by amino acids plus insulin is shown in SBGN notation. This model integrates the current knowledge and guided our decision on appropriate targets for measurement. The selected targets are marked with an asterisk.

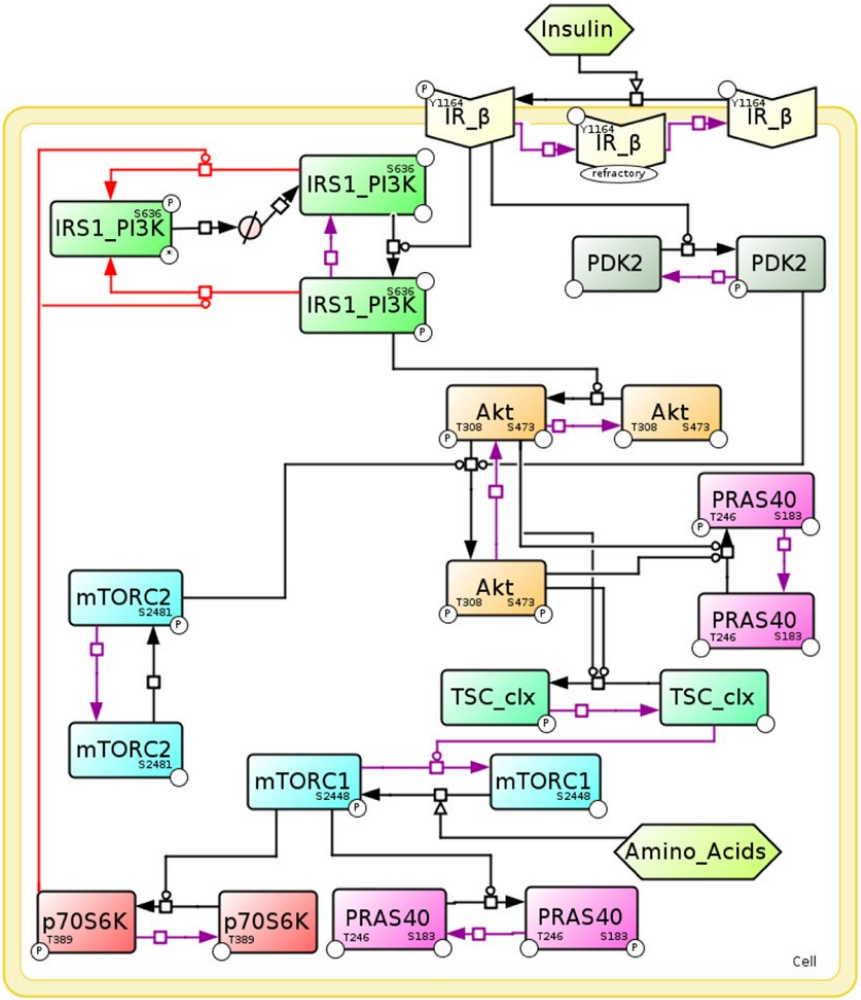

Figure 5.2: An insulin/mTOR network graphical model. Reduced graphical model of the mTOR network activated by amino acids/insulin (see Figure 5.1 for the extended graphical model).

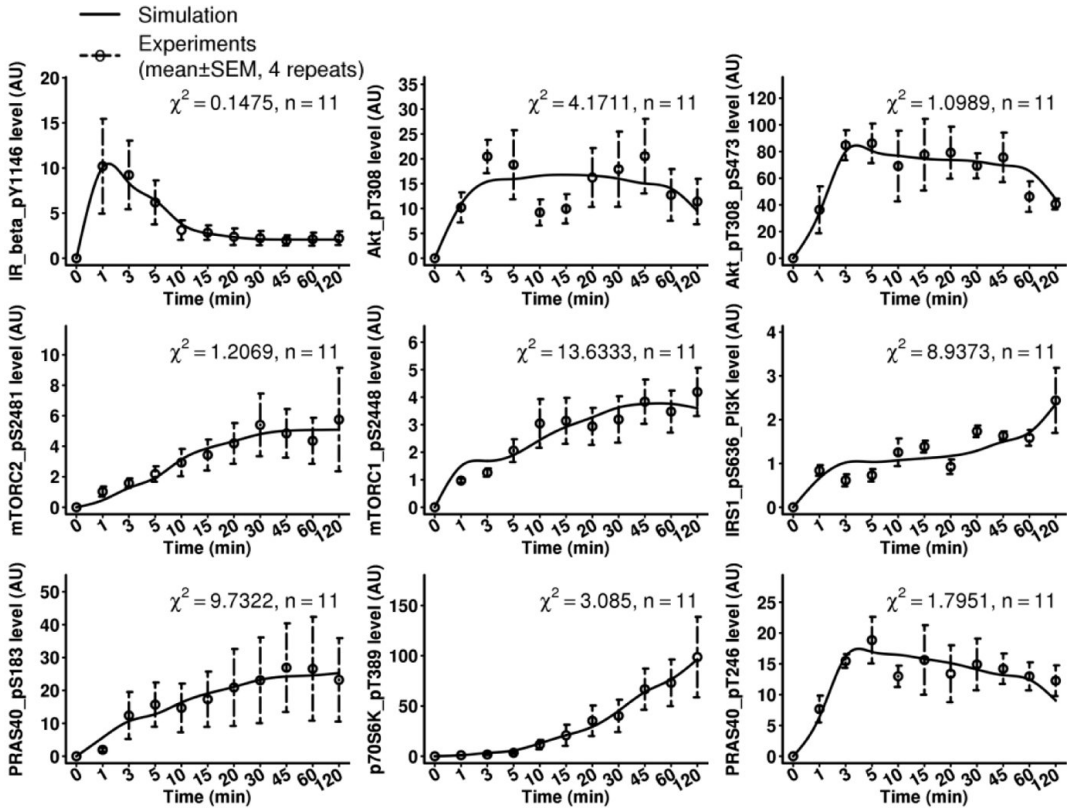

Figure 5.3: Development of a dynamic insulin/mTOR network model. Comparison between the simulated time courses of the general model (solid lines) and the experimental time courses (points, dotted error bars) within [0, 120] min. For each curve, the χ^2 computed over n time points, is reported as goodness-of-fit measure. Experimental data based on quantitative immunoblotting time course by measuring phosphorylation dynamics of central network components (four replicates). *In vitro* experiments were performed by Annika Sonntag, Freiburg University, Germany.

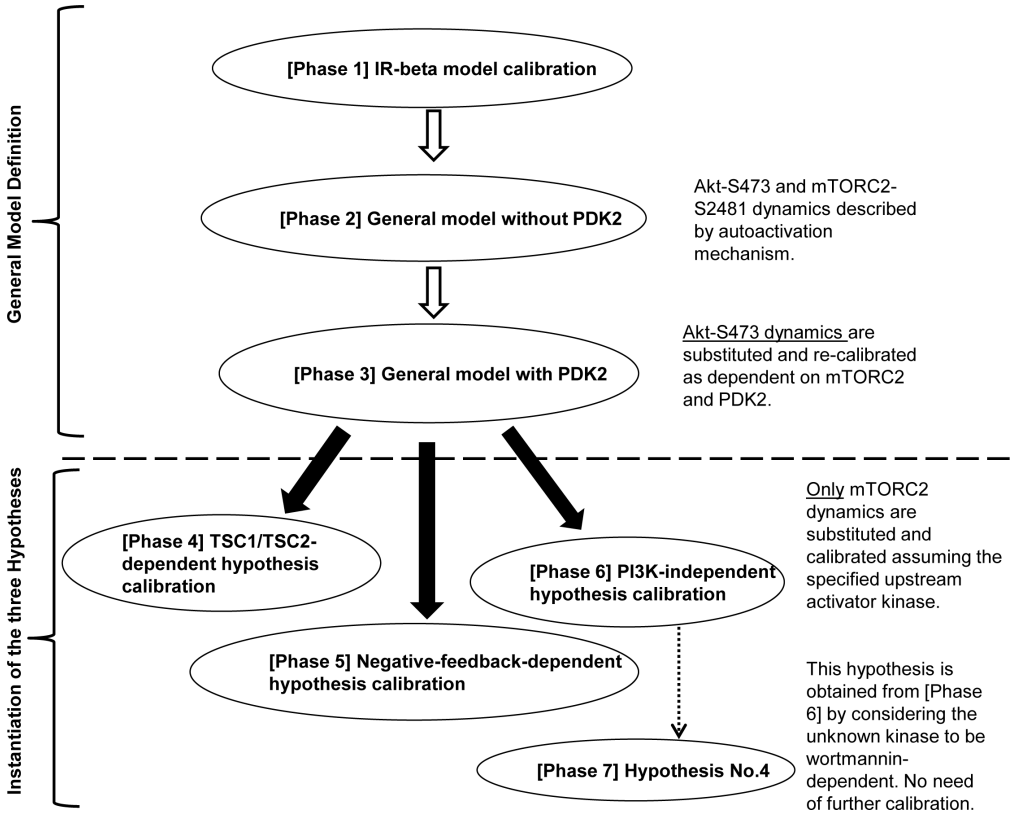

Figure 5.4: Phases of the calibration process. The approach for defining our model was hierarchical and structured in two main parts. Part 1 (Phases 1-3) was the development of a general model without regulation of mTORC2 and Part 2 (Phases 4-7) was the introduction of specific hypotheses for regulation of mTORC2. In Phase 1, the kinetic rate constants of the insulin receptor were calibrated independently because the insulin receptor module was not regulated by the rest of the network. In Phase 2, the kinetic rate constants for the model representing the entire network without PDK2 were calibrated, assuming that the phosphorylation dynamics of mTOR-S2481 and Akt-S473 dynamics were regulated by autoactivation. In Phase 3, PDK2 was added to the network and the autoregulation mechanism controlling phosphorylation of Akt-S473 was replaced with the regulation by both mTORC2 and PDK2. Part 2 (Phases 4-7) of the calibration process concerned the introduction of the three hypotheses (Hypothesis 1,2, and 3) for mTORC2 activation from the general model defined in Part 1 (Phase 3). The development and calibration of these hypotheses only required substitution of the mTORC2 dynamics of the general model with the specific regulation of the corresponding hypothesis and then recalibration of these new kinetic parameters. In Phase 7, Hypothesis 4 was obtained from the PI3K-independent model by transforming the unknown kinase into one dependent on Wortmannin, which did not involve further calibration.

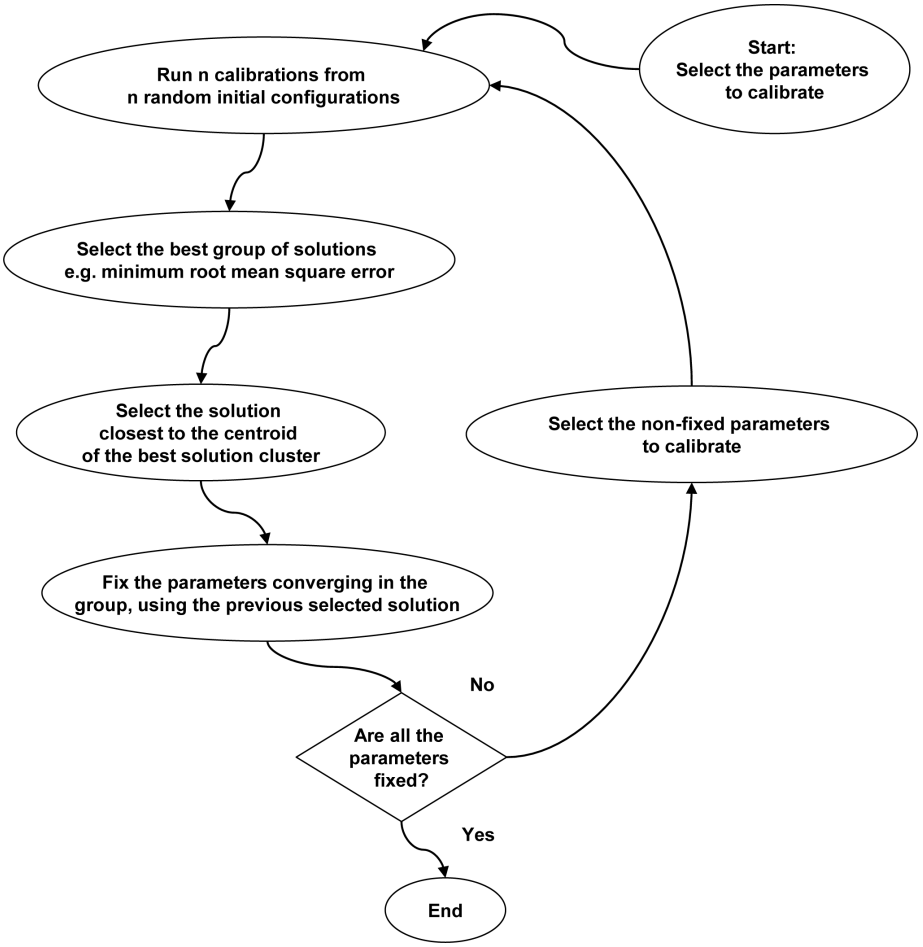

Figure 5.5: Detail of a calibration phase. The flow chart shows the details of the parameter calibration procedure. The procedure began with the selection of the set of parameters to estimate. After completing the calibrations, the procedure selected the subset of the solutions that obtained the minimum root mean square error (best solutions). The closest solution to the centroid of the best solution cluster was selected and the values common to all the solutions were fixed. All the parameters that were not fixed were selected for the next step of calibration. The procedure terminated when there were no further parameters to calibrate. In the model calibration, all the parameters were identified in only one iteration step.

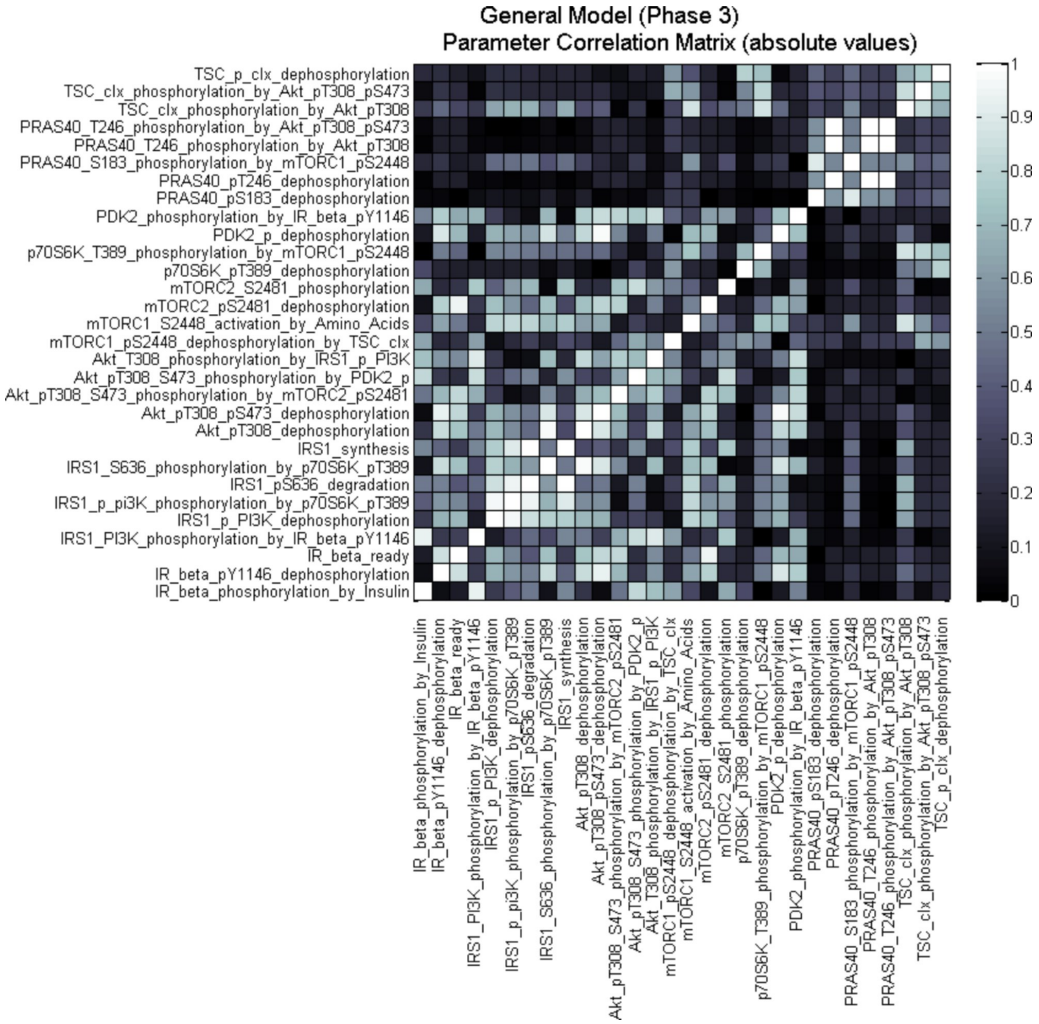

Figure 5.6: Identifiability analysis for the general model. Parameter identifiability is based on sensitivity analysis and parameter correlation as computed by SBPD Matlab Toolbox. The symmetric matrix shows the parameter correlation in absolute values. High parameter correlations suggest potential issues in identifying the corresponding parameters independently (the elements on the diagonal obviously have correlation equal to 1). Conversely, low parameter correlations indicate that the corresponding parameters can be identified independently. Our experimental data were used in computing the reported identifiability analysis.

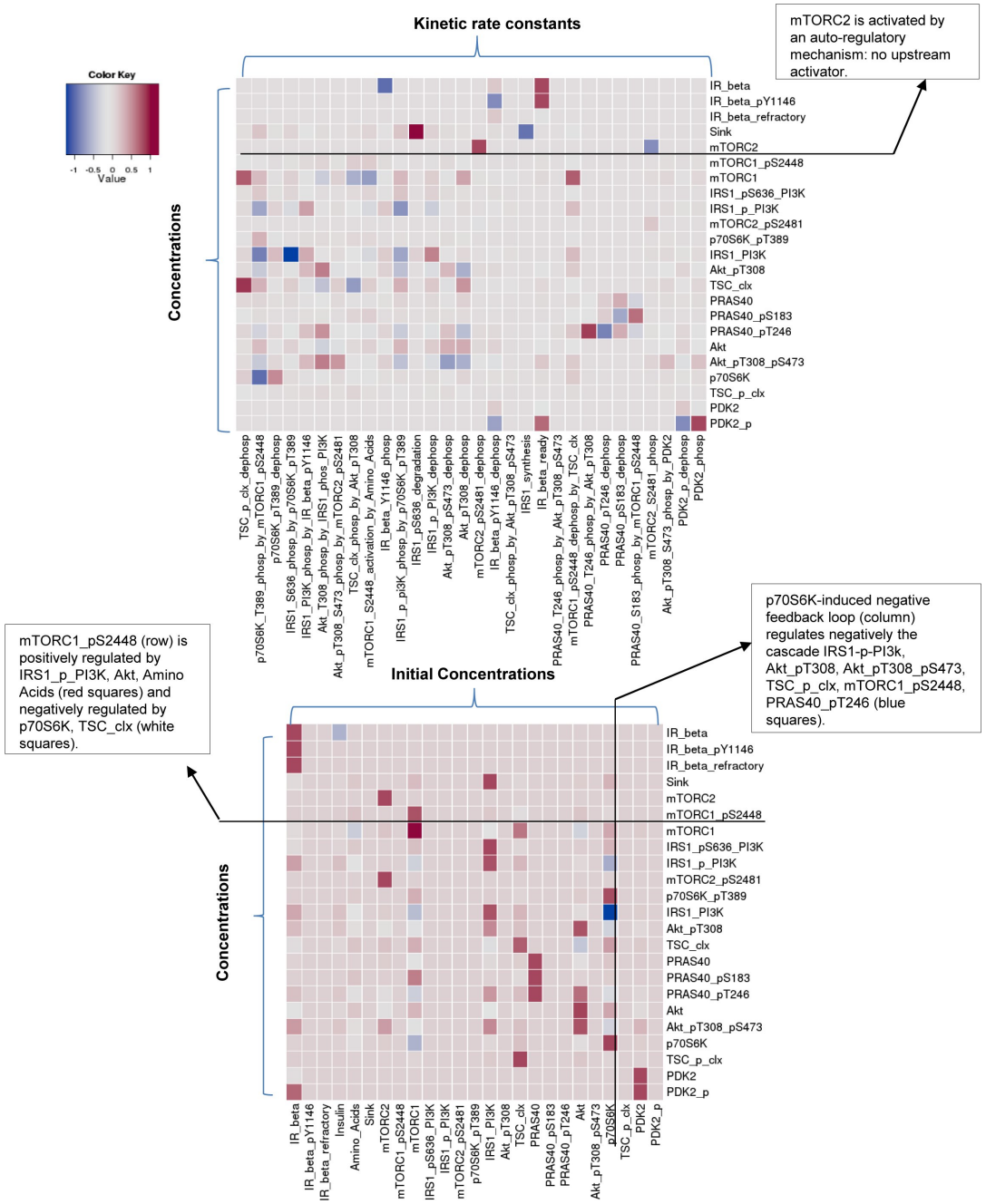

Figure 5.7: Sensitivity analysis for the general model. The top plot illustrates the sensitivity analysis of the model by row, in response to the perturbations of the kinetic rates constants shown in columns. The bottom plot shows the model sensitivity analysis of the initial concentrations of the modelled species by row with perturbations shown in columns. Values were normalised in the range [-1, 1]. Positive values (red squares) represent positive regulation; negative ones (white-blue squares) represent inhibition.

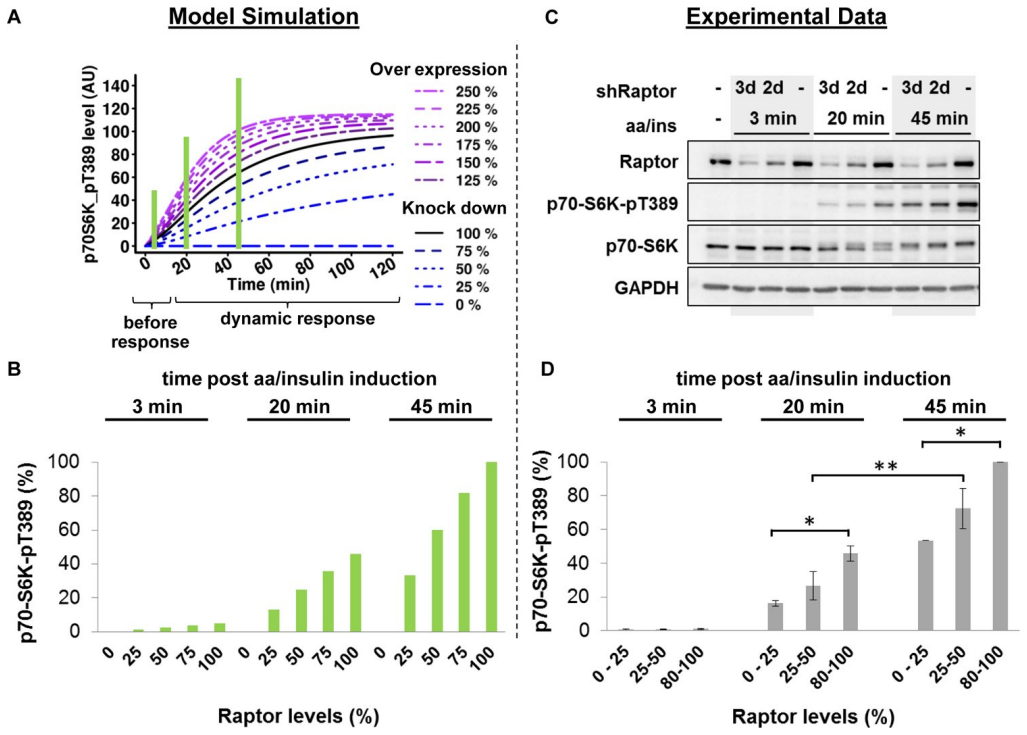

Figure 5.8: Validation: dynamic response of p70-S6K-pT389 to gradual Raptor inhibition. (A) Model predictions for p70-S6K-pT389 dynamics in response to a perturbation of mTORC1. The curves show the simulated response to gradual mTORC1 inhibition starting at 5-10 minutes after induction with amino acids/insulin. The model was simulated with both mTORC1 overexpression and knockdown conditions. Time points for experimental validation are indicated by green lines. (B) Simulated and quantified relative amounts of p70-S6K-pT389 under conditions of mTORC1 reduction (0, 25, 50, 75, 100 %) at selected time points after induction with amino acids/insulin. (C) Experimental validation of the effect of gradual Raptor knockdown (shRaptor) on p70-S6K phosphorylation in starved cells induced with amino acids/ins for the indicated times. Data are representative of 3 experiments. d = days. (D) Experimentally determined and quantified p70-S6K-pT389 amounts at the indicated times after induction with amino acids/insulin in cells in which Raptor was knocked down. Data are the average and SEM of 3 experiments. * $P < 0.05$, ** $P < 0.01$; low Raptor levels compared to high Raptor levels after 20 min and 45 min induction, 20 min compared to 45 min induction. Differences in p70-S6K-pT389 were significant. *In vitro* experiments were performed by Annika Sonntag, Freiburg University, Germany.

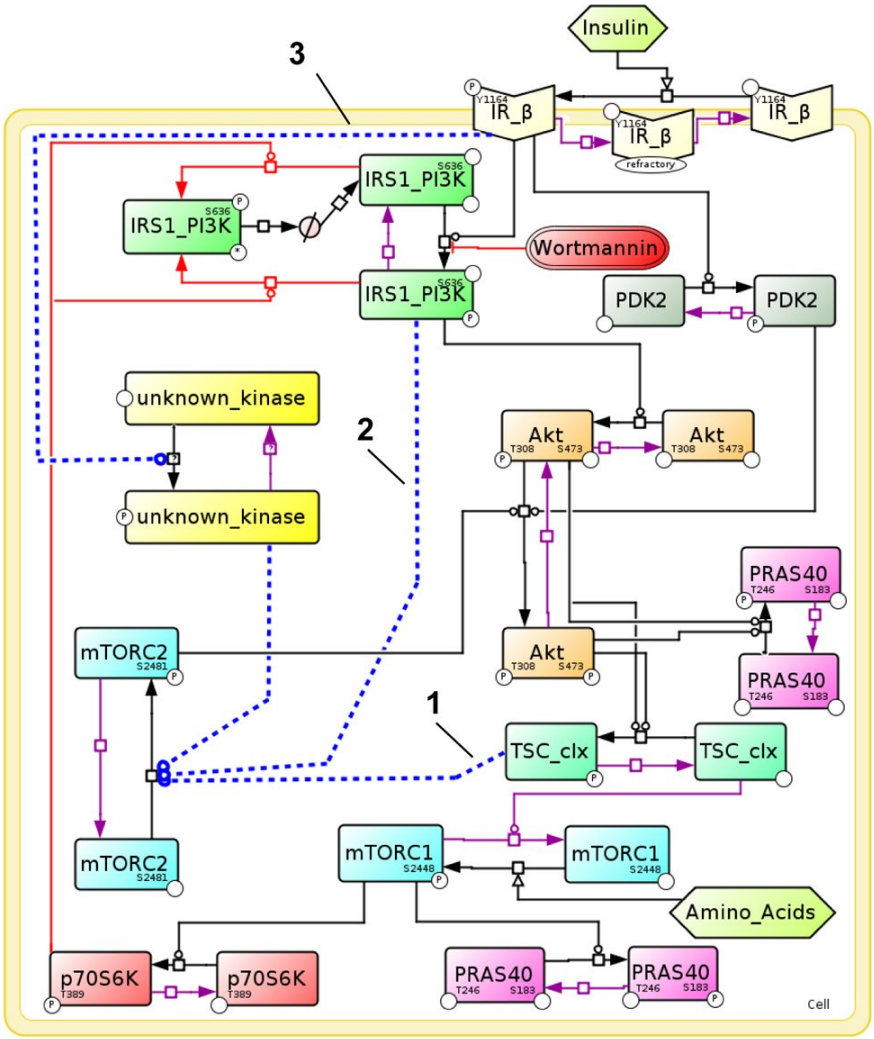

Figure 5.9: Three different hypotheses on mTORC2 regulation by insulin (graphical model). Reduced graphical network model including the three hypotheses (1, 2, 3, indicated by the dotted lines), translated into different network structures.

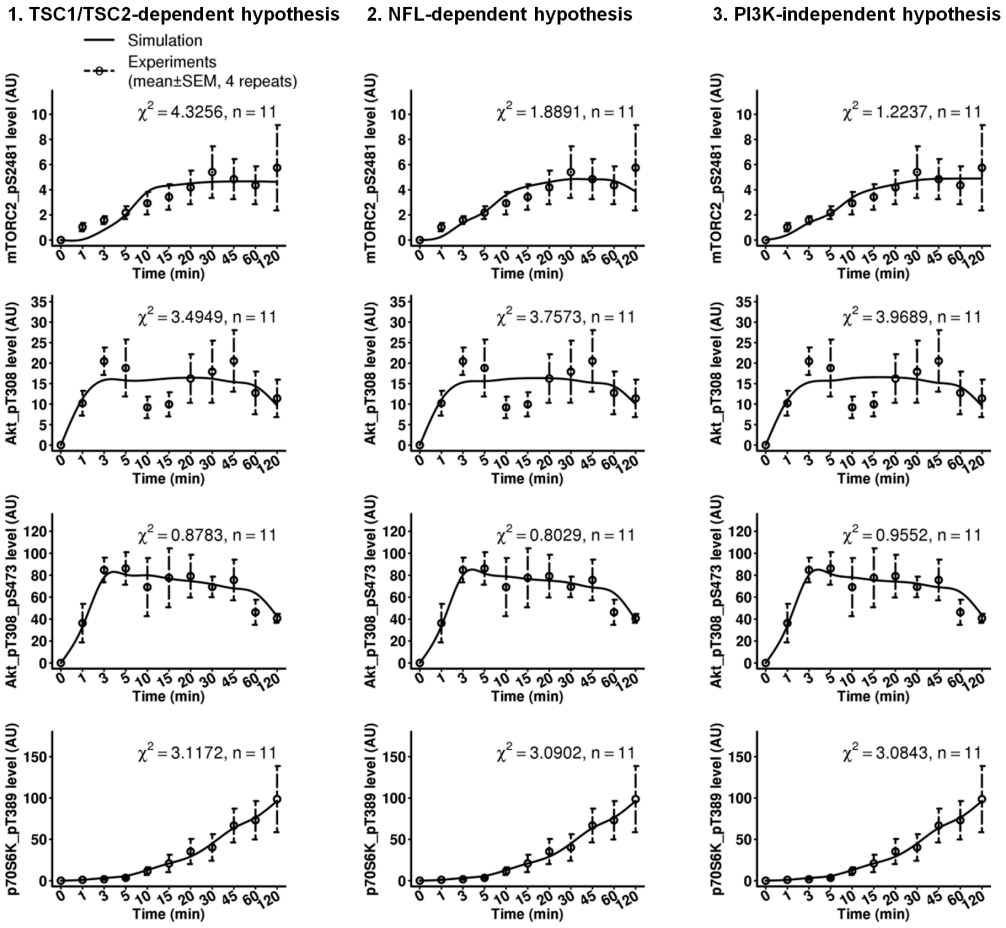

Figure 5.10: Three different hypotheses on mTORC2 regulation by insulin (dynamical models). Comparisons of simulated time courses, calibrated for each hypothesis, with experimental data. Data shown are for mTORC2 readouts (mTOR-pS2481, Akt-pS473), the PI3K readout Akt-pT308, and the mTORC1 readout p70-S6K-pT389 (see Figure 5.11 for curves of all other readouts). *In vitro* experiments were performed by Annika Sonntag, Freiburg University, Germany.

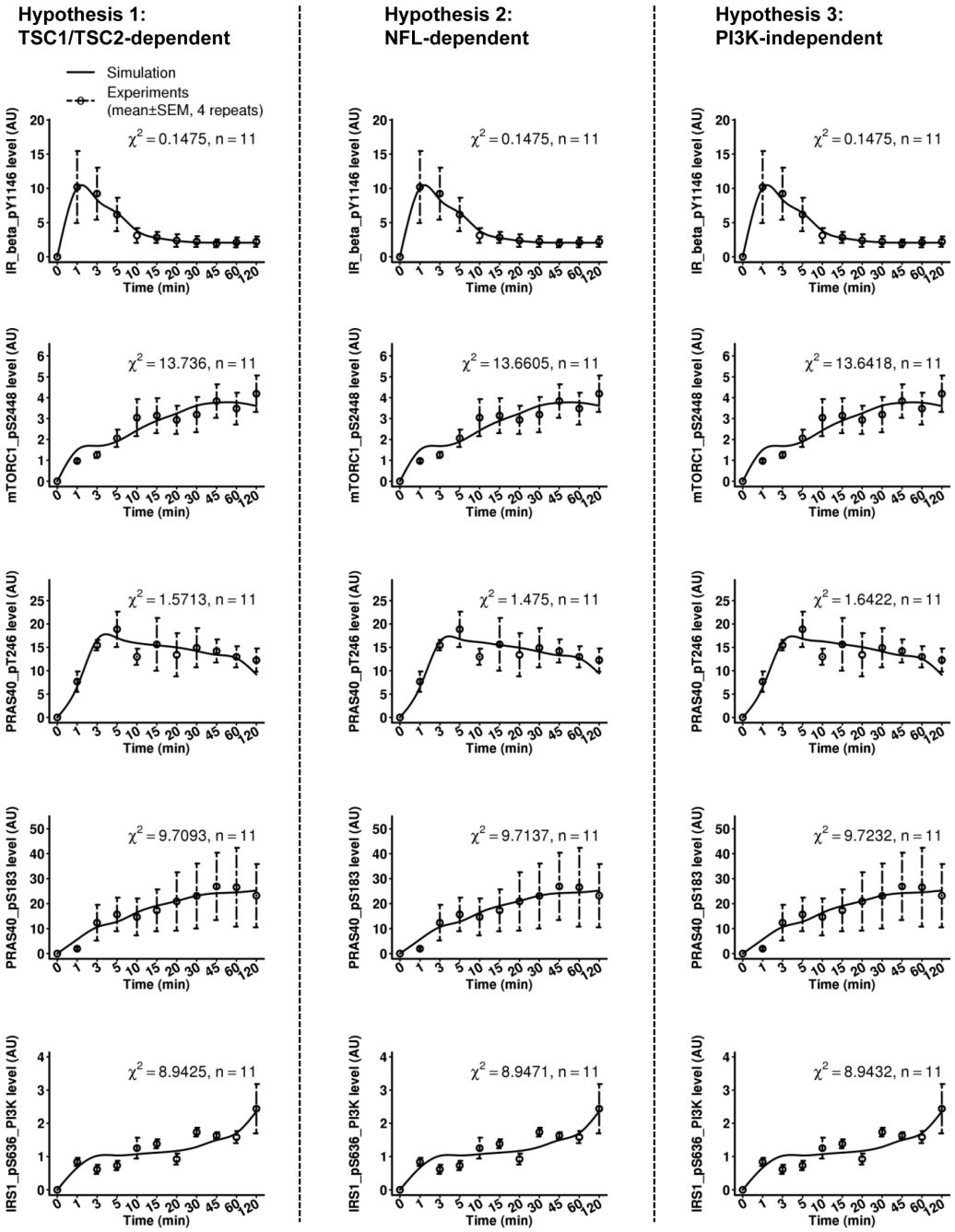

Figure 5.11: Comparison between the simulated and experimental time-courses for Hypothesis 1, 2, and 3 for readouts of the mTOR network. The three hypotheses were consistent with each other for all the readouts indicating that introducing each hypothesis into the general model did not perturb the network. NFL = Negative Feedback Loop. *In vitro* experiments were performed by Annika Sonntag, Freiburg University, Germany.

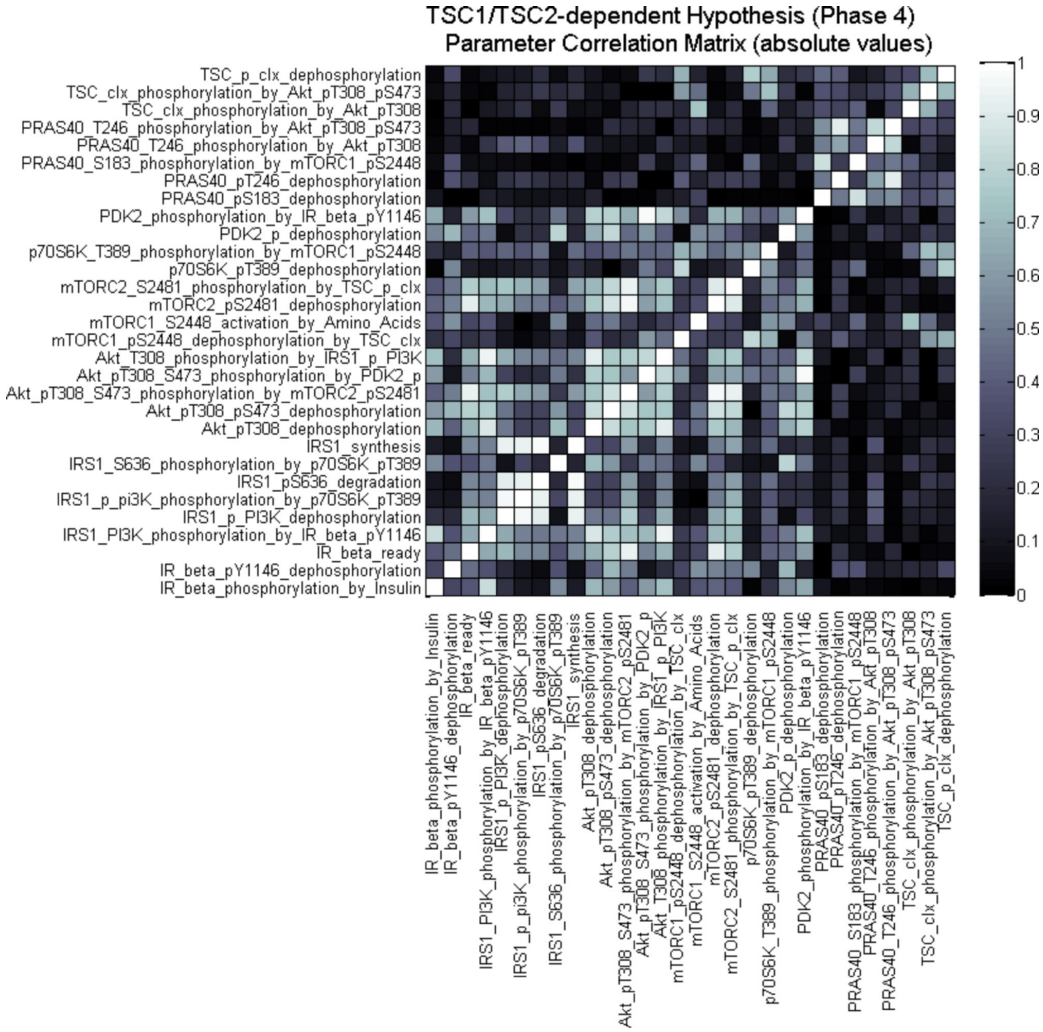

Figure 5.12: Identifiability analysis for Hypothesis 1: TSC1/TSC2-dependent mTORC2 regulation. Parameter correlation matrix for TSC1/TSC2-dependent hypothesis is shown. See Figure 5.6 for details.

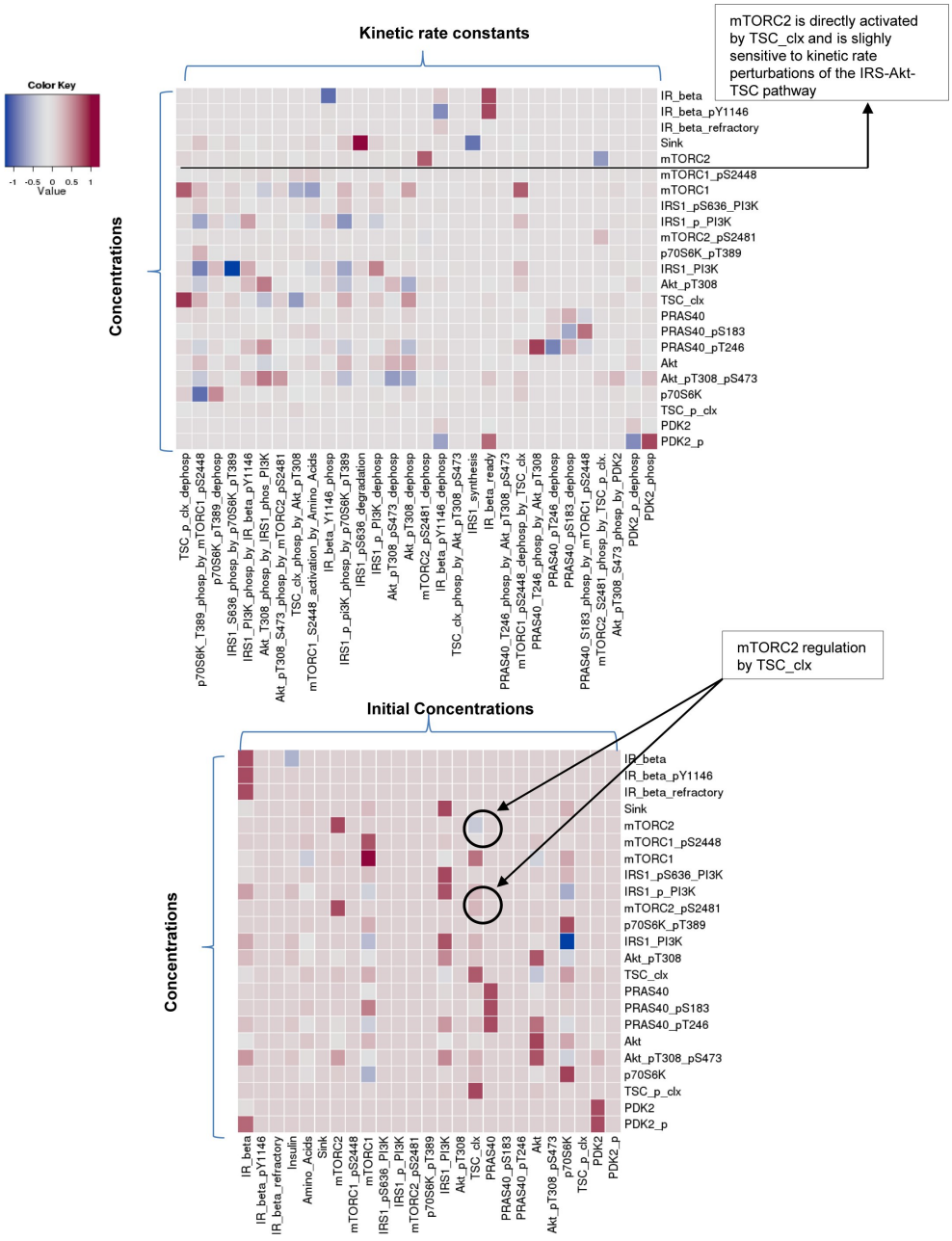

Figure 5.13: Sensitivity analysis for Hypothesis 1: TSC1/TSC2-dependent mTORC2 regulation. The sensitivity analyses of the three hypotheses (see Figures 5.15 and 5.17) showed a similar sensitivity analysis excluding the sensitivity for the parameters characterizing each specific hypothesis. This provided evidence that the proposed general model (common to the three hypotheses) behaved in a consistent manner following introduction of the three hypothetical models and, therefore, the three models were comparable. See Figure 5.7 for details of the top and bottom plots.

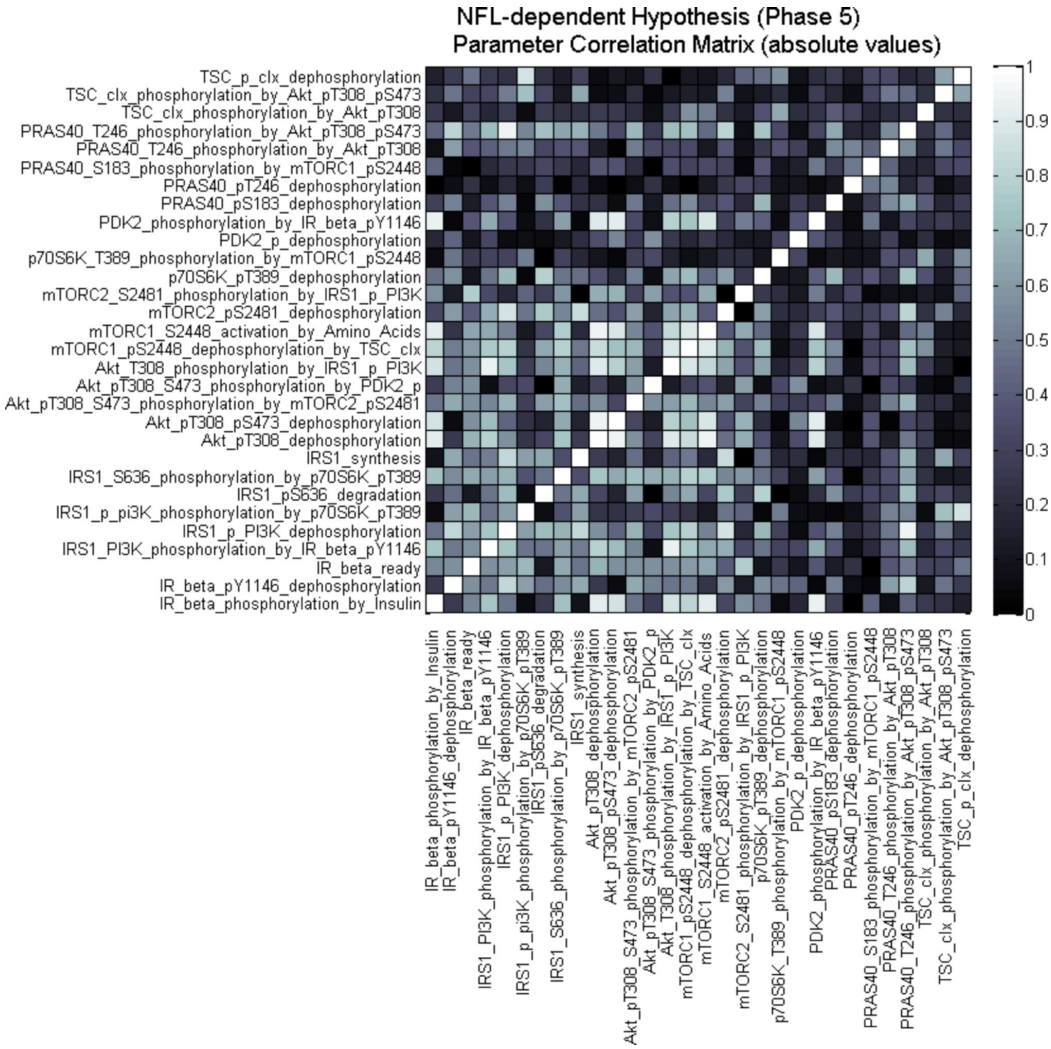

Figure 5.14: Identifiability analysis for Hypothesis 2: NFL-dependent mTORC2 regulation. Parameter correlation matrix for NFL-dependent hypothesis is shown. See Figure 5.6 for details.

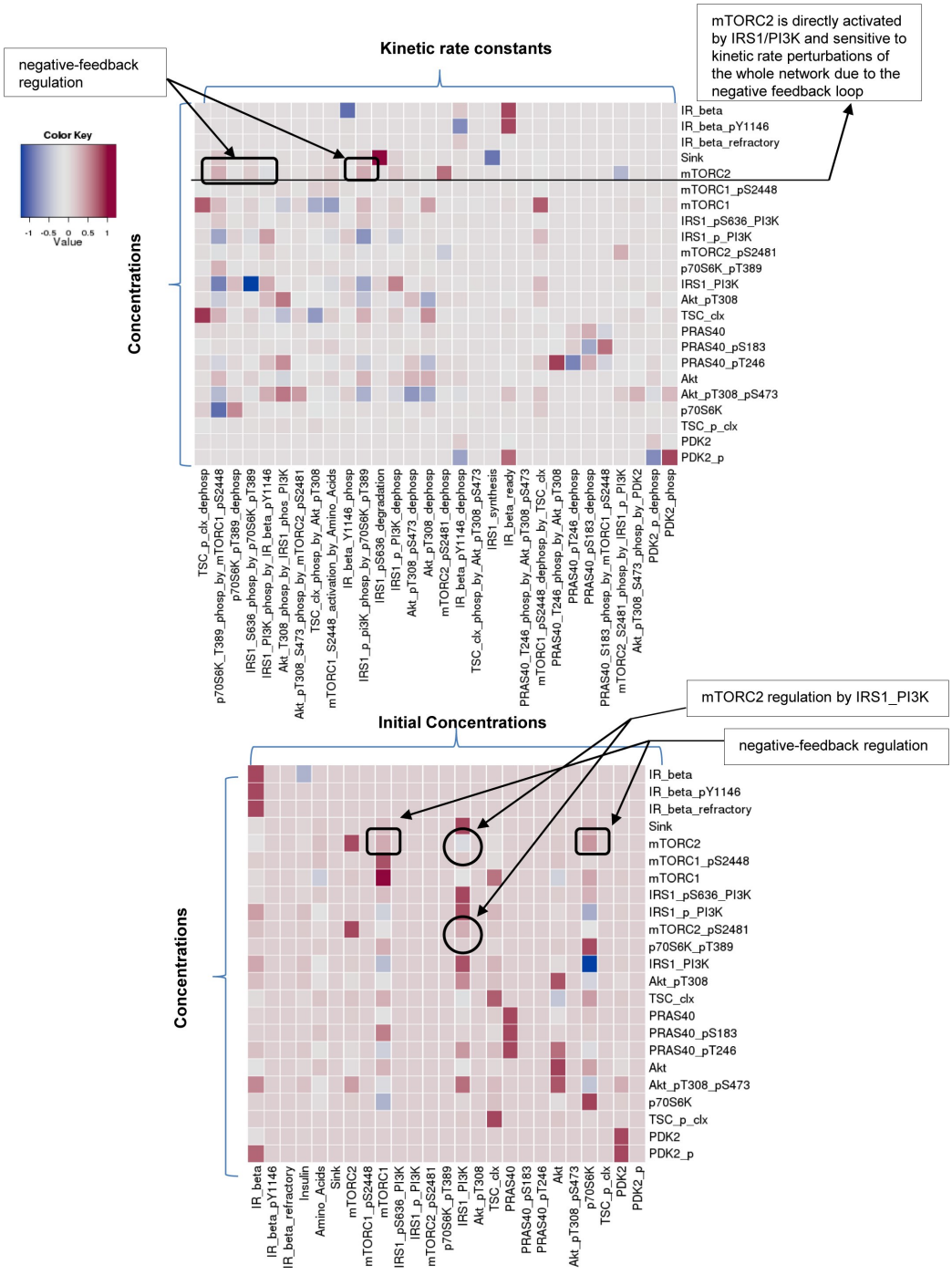

Figure 5.15: Sensitivity analysis for Hypothesis 2: NFL-dependent mTORC2 regulation. Sensitivity analysis for the initial concentrations and the kinetic rates parameters for the NFL-dependent hypothesis is shown. See Figure 5.7 for details of the top and bottom plots.

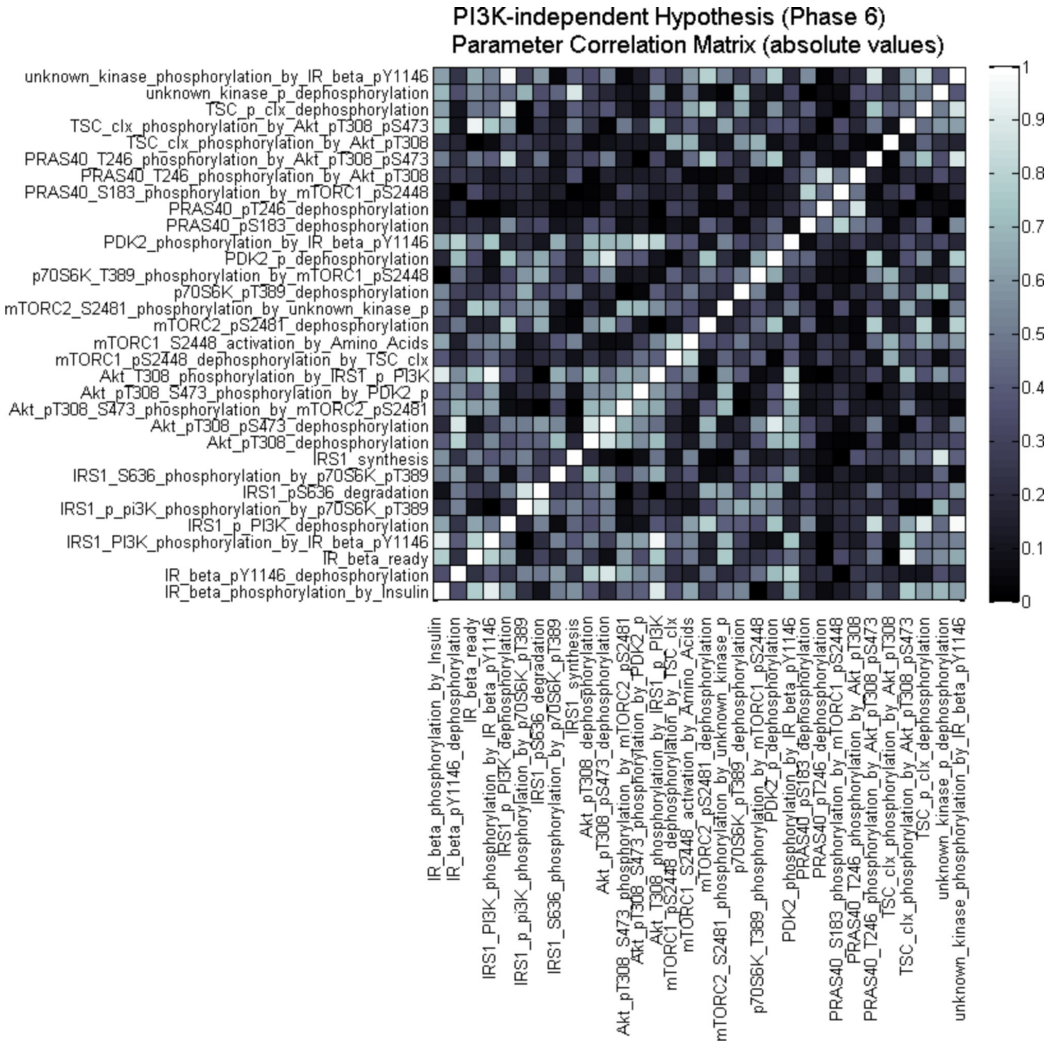

Figure 5.16: Identifiability analysis for Hypothesis 3: PI3K-independent mTORC2 regulation. Parameter correlation matrix for PI3K-independent hypothesis is shown. See Figure 5.6 for details.

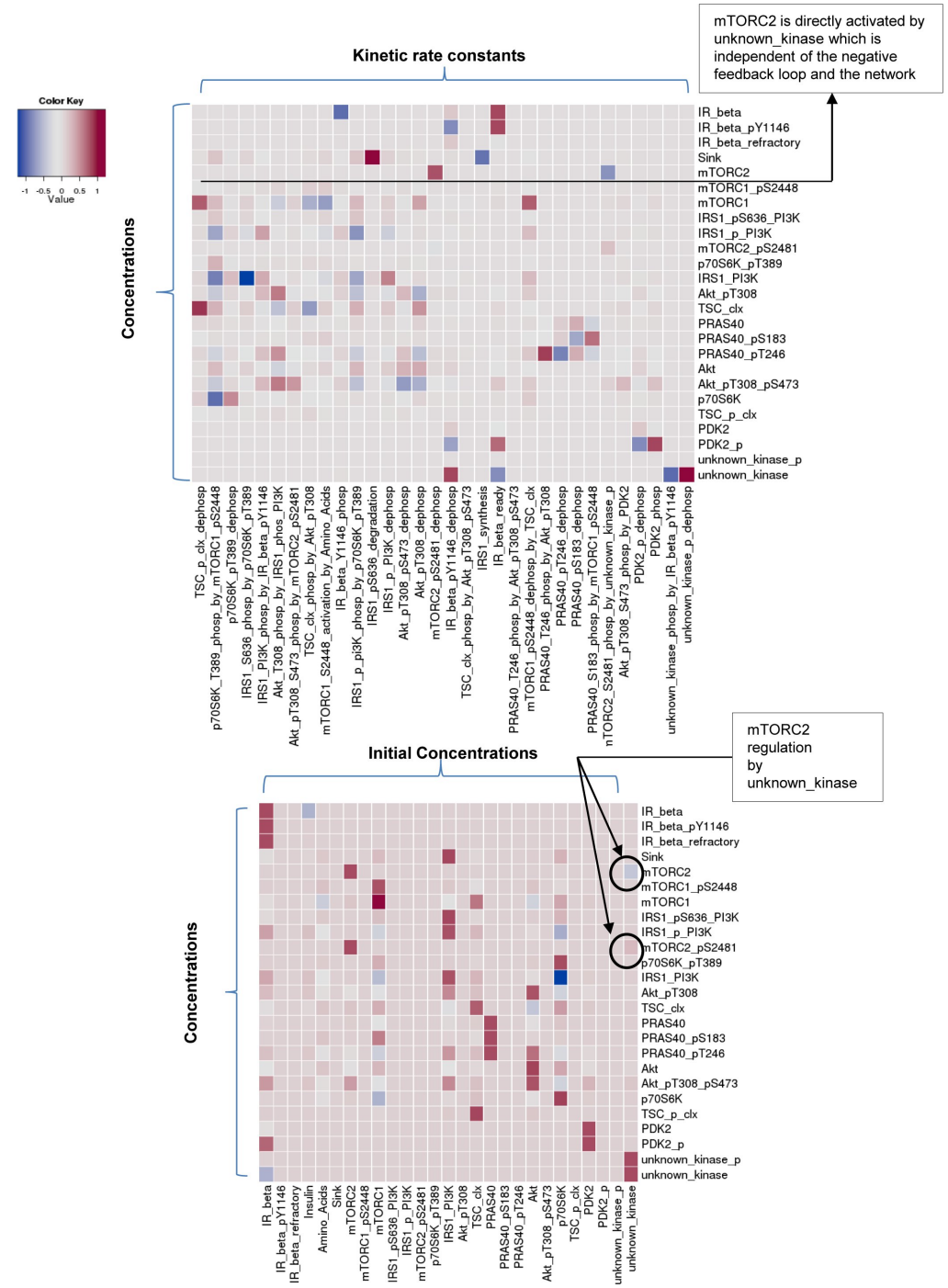

Figure 5.17: Sensitivity analysis for Hypothesis 3: PI3K-independent mTORC2 regulation. Sensitivity analysis for the initial concentrations and the kinetic rates parameters for the PI3K-independent hypothesis is shown. See Figure 5.7 for details of the top and bottom plots.

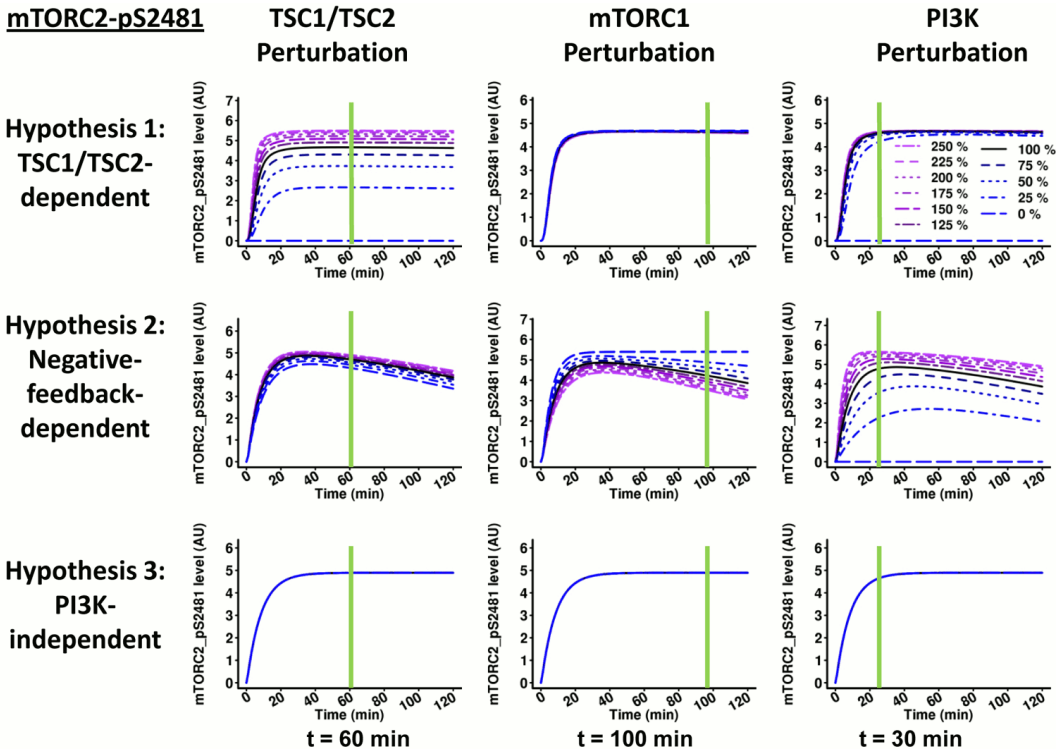

Figure 5.18: Simulations of network perturbations at several levels and differential dynamical network responses for the three different hypotheses (mTOR-pS2481 readout). Simulated mTOR-pS2481 response upon amino acids/insulin induction in systems with the indicated perturbations: TSC1/TSC2 (experimental equivalent: gradual TSC2 knockdown), mTORC1 (experimental equivalent: gradual Raptor knockdown), and PI3K (experimental equivalent: gradual PI3K inhibition with Wortmannin) for Hypothesis 1, 2, and 3. The time points that were experimentally tested are indicated with green lines.

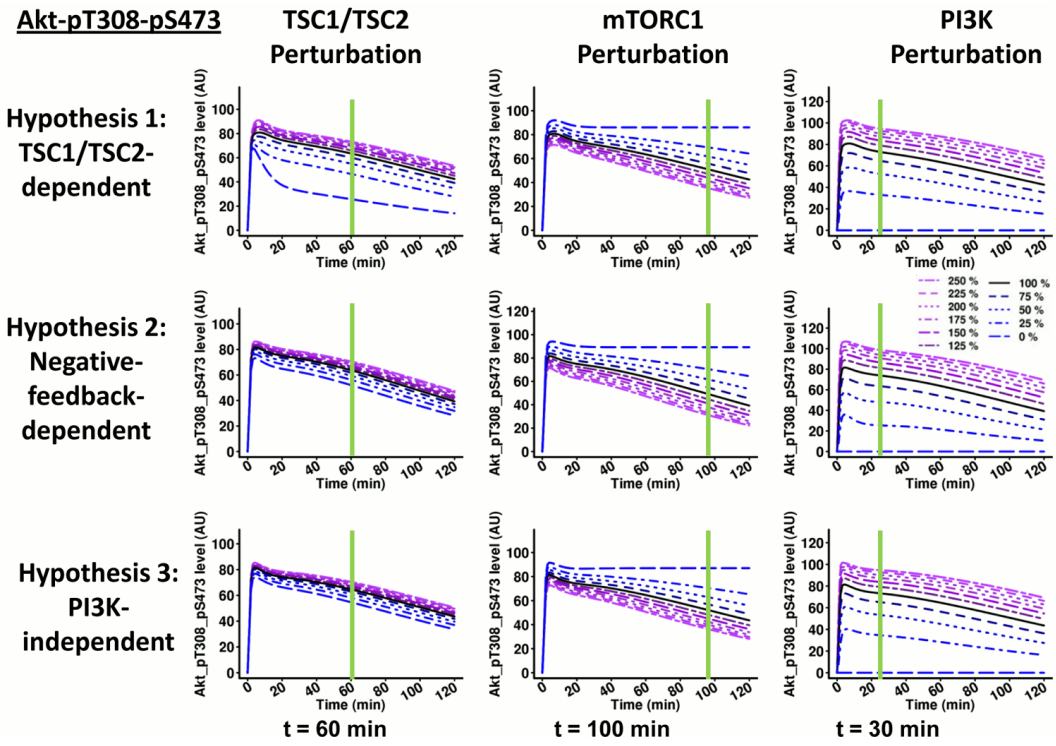

Figure 5.19: Simulations of network perturbations at several levels and differential dynamical network responses for the three different hypotheses (Akt-pS473 readout). Simulated Akt-pT308-pS473 response for each of the three hypotheses upon amino acids/insulin induction in systems with perturbations of TSC1/TSC2, mTORC1, and PI3K. The time points that were experimentally tested are indicated with green lines.

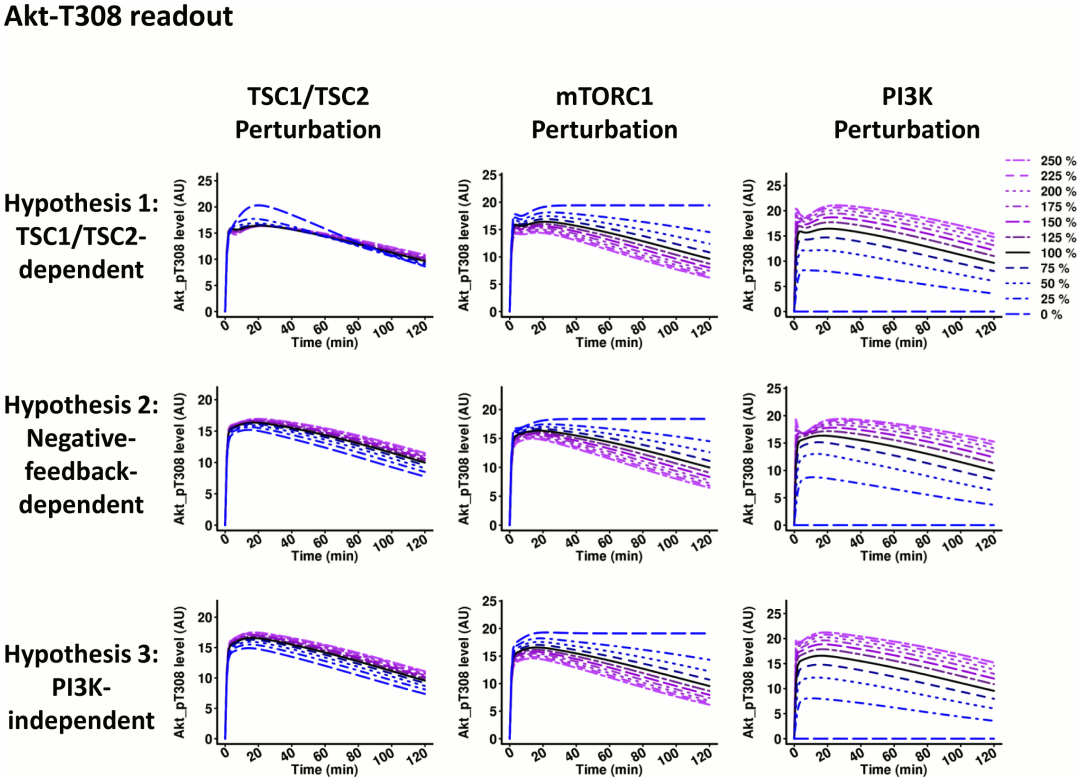

Figure 5.20: The influence of perturbations of TSC1/TSC2, mTORC1, or PI3K on the phosphorylation of Akt-T308 for the three hypotheses. The three hypotheses did not show any difference in the dynamics of Akt-T308 phosphorylation when varying the amounts of PI3K and mTORC1. A small difference was observed for TSC1/TSC2 perturbation where the TSC1/TSC2-dependent hypothesis showed a slight increase in Akt-T308 phosphorylation when TSC1/TSC2 activity was reduced. In the TSC1/TSC2-dependent hypothesis, the mTORC2 activity is reduced when the amount of TSC1/TSC2 is reduced.

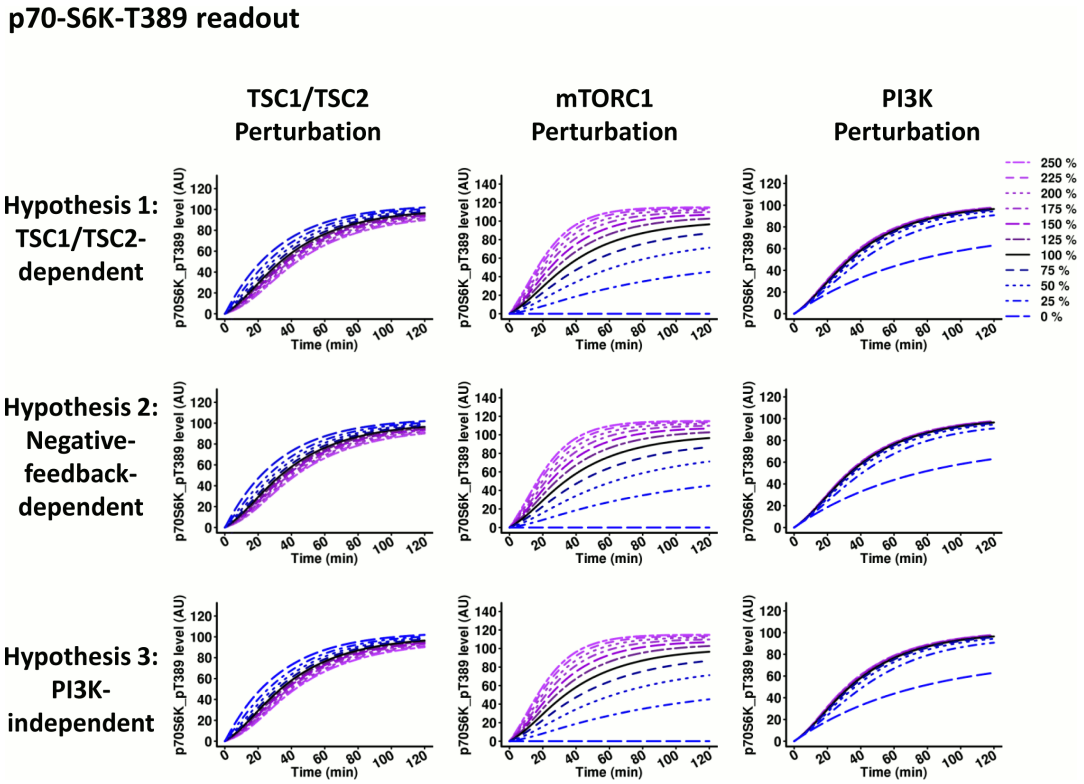

Figure 5.21: The influence of perturbations of TSC1/TSC2, mTORC1, or PI3K on the phosphorylation of p70-S6K-T389 for the three hypotheses. The effect of each perturbation on the networks representing each hypothesis for the phosphorylation of p70-S6K-T389, which is a readout for mTORC1 activity, is shown.

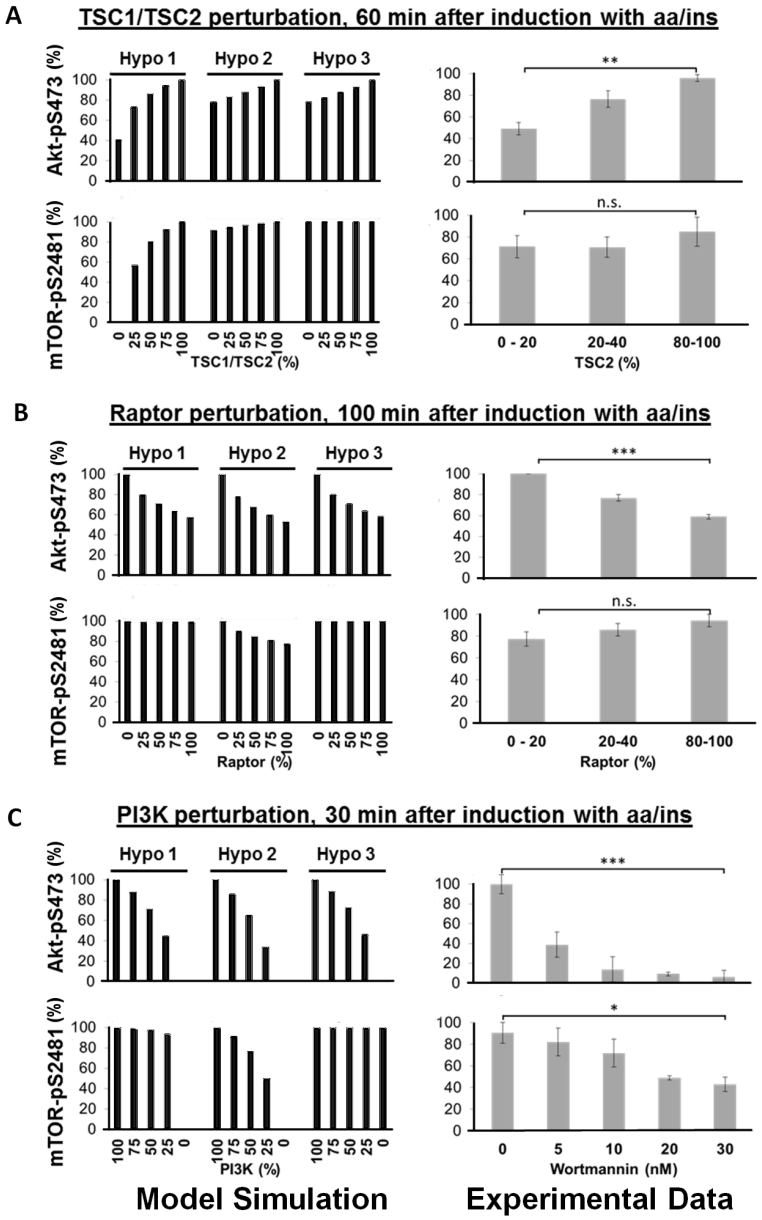

Figure 5.22: Quantitative representations of simulated and experimentally determined Akt-pS473 and mTOR-pS2481. (A) mTOR-pS2481 is not affected in response to a gradual TSC2 knock down for 60 min after induction with amino acids/insulin. (B) mTOR-pS2481 is not affected by the NFL in response to Raptor knock down for 100 min after induction with amino acids/insulin. (C) mTOR-pS2481 is sensitive to the PI3K inhibitor Wortmannin (Wmn) for 30 min after induction with amino acids/insulin. Data are the average and SEM computed from 3 repeats. * $P < 0.05$, ** $P < 0.01$, *** $P < 0.001$, n.s. not significant. d = days, Hypo = hypothesis. *In vitro* experiments were performed by Annika Sonntag, Freiburg University, Germany.

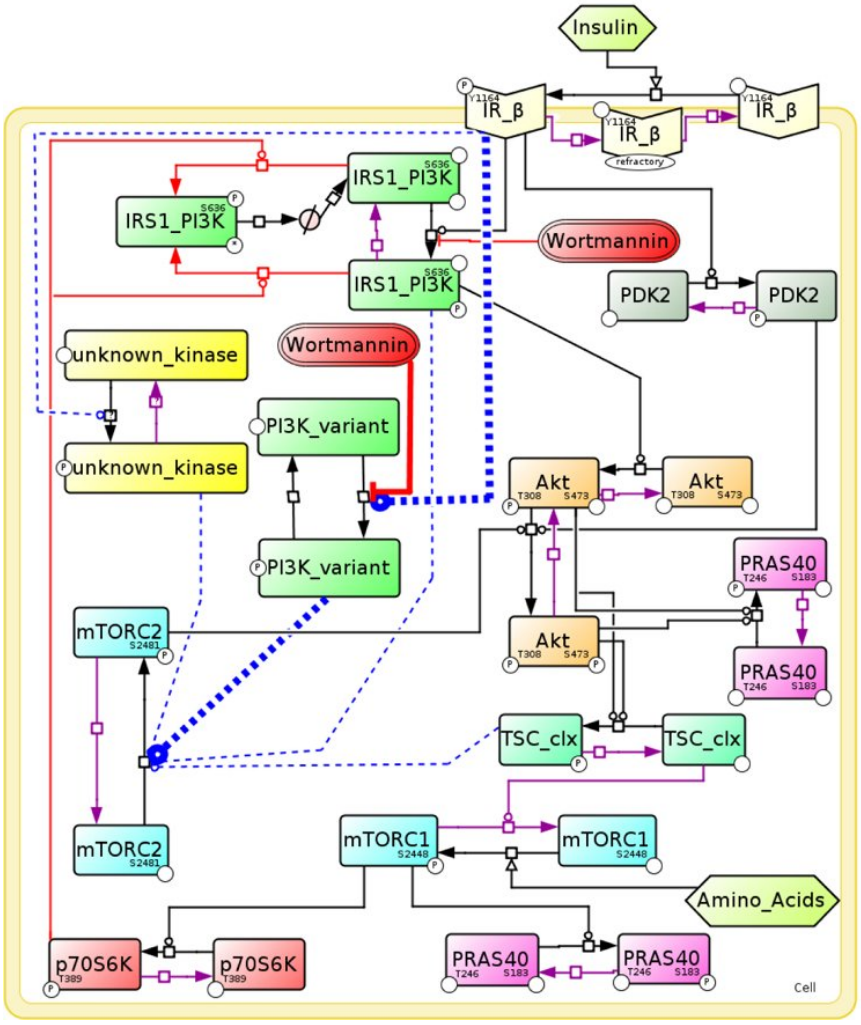

Figure 5.23: A new hypothesis and network structure for mTORC2 regulation by insulin. Schematic representation of the pathway for Hypothesis 4: Insulin induction of mTORC2 by a PI3K (red) that is insensitive to TSC1/TSC2 and to the S6K to IRS-mediated NFL. This hypothesis was equivalent to Hypothesis 3 (PI3K and TSC1/TSC2-independent activation), assuming that the mTORC2 activator was sensitive to Wortmannin.

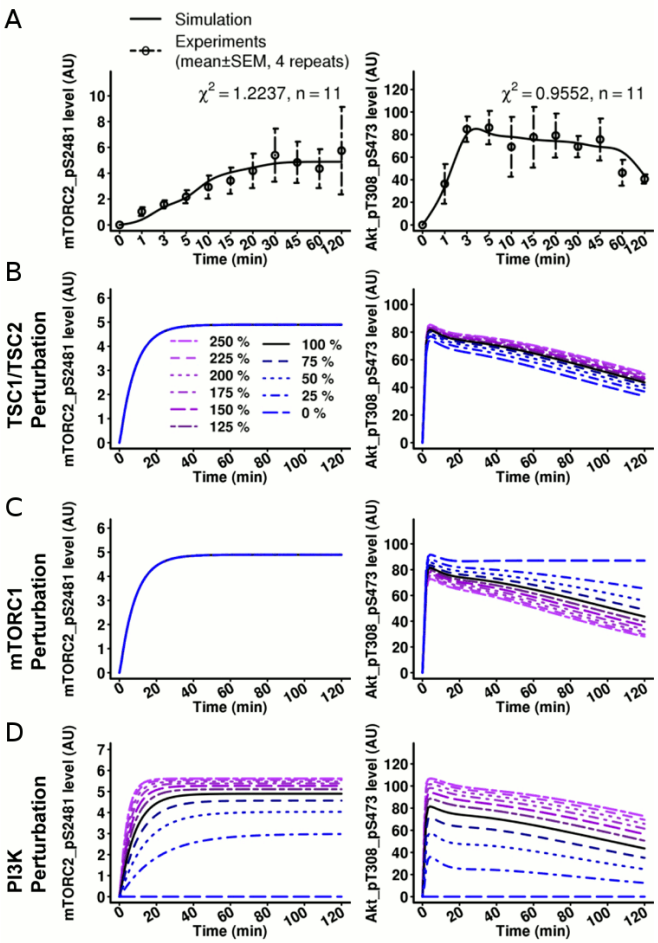

Figure 5.24: A new hypothesis and network structure for mTORC2 regulation by insulin. (A) The model simulation data for Hypothesis match the experimental dynamical phosphorylation data. The simulated and experimentally measured dynamics are shown for the mTORC2 readouts mTOR-pS2481 and Akt-pS473 (see Figure 5.25 for all other readouts). (B) Predictions for mTOR-pS2481 and Akt-pS473 upon gradual TSC1/TSC2 knock down match the experimental data, which is presented in Figure 5.22A. Whereas at 60 min after induction Akt-pS473 is gradually reduced by TSC2 inhibition, mTOR-pS2481 is TSC2-insensitive. See Figure 5.25 for Akt-pT308 and p70-S6K-pT389. (C) Predictions for mTOR-pS2481 and Akt-pS473 readouts upon gradual Raptor knock down match the experimental data, which is presented in Figure 5.22B. Whereas at 100 min after induction Akt-pS473 is gradually induced by Raptor inhibition, mTOR-pS2481 is Raptor-insensitive. See Figure 5.25 for Akt-pT308 and p70-S6K-pT389. (D) Predictions for mTOR-pS2481 and Akt-pS473 readouts upon gradual PI3K inhibition match the experimental data, which is presented in Figure 5.22C. Both Akt-pS473 and mTOR-pS2481 are gradually reduced by Wortmannin at 30 min after induction. See Figure 5.25 for Akt-pT308 and p70-S6K-pT389. *In vitro* experiments were performed by Annika Sonntag, Freiburg University, Germany.

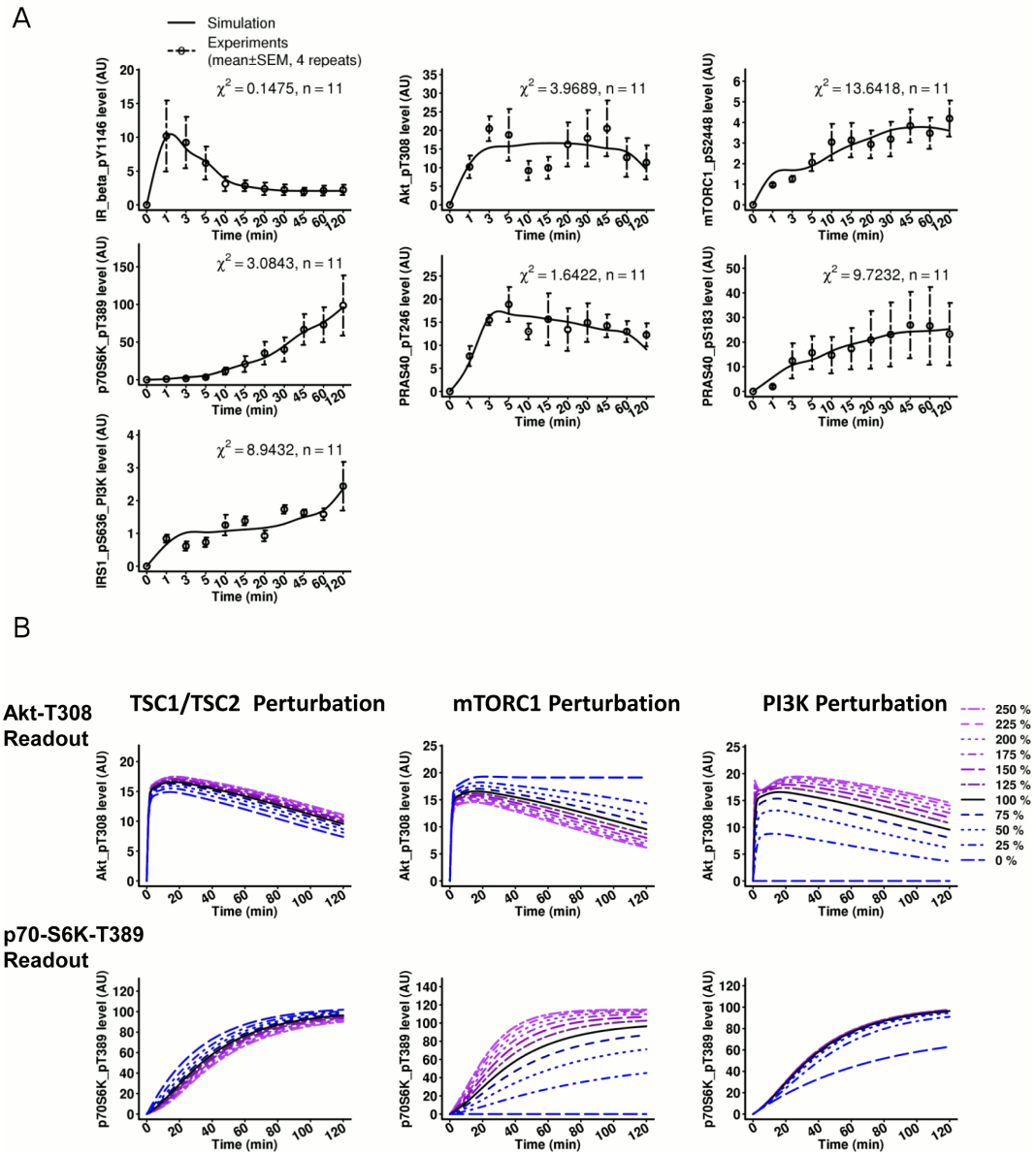

Figure 5.25: Simulation and perturbations for the new network structure based on Hypothesis 4: PI3K-dependent, NFL-independent regulation of mTORC2. (A) Comparison between the simulated and experimental time courses for Hypothesis 4 shows that the simulated time courses match the experimental readouts. (B) The influence of perturbations of TSC1/TSC2, mTORC1, or PI3K on the dynamics of phosphorylation of Akt-T308 and p70-S6K-T389 for Hypothesis 4. *In vitro* experiments were performed by Annika Sonntag, Freiburg University, Germany.

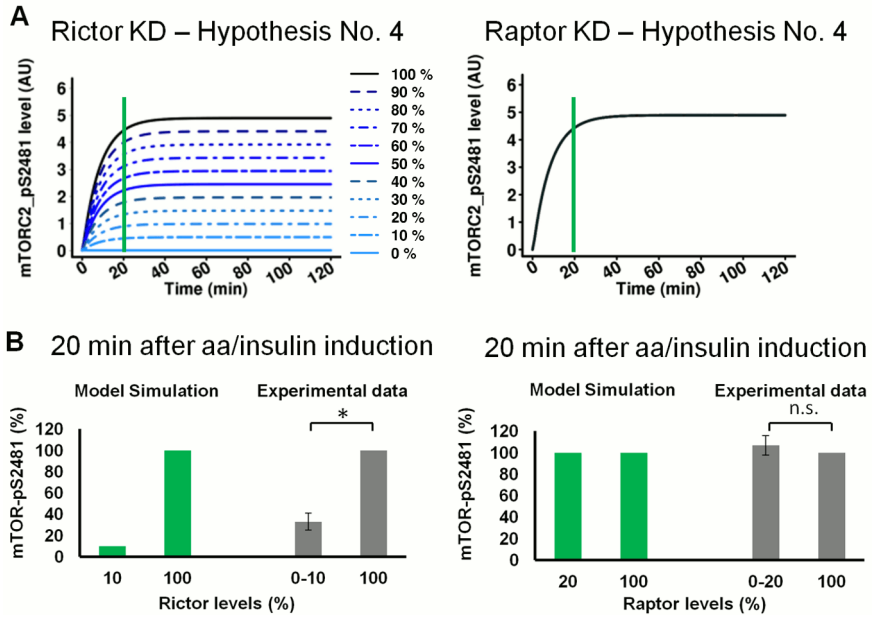

Figure 5.26: Validation Hypothesis 4 by Rictor and Raptor knock down. (A) Simulation of mTOR-pS2481 dynamic in response to addition of amino acids and insulin when Rictor or Raptor is knocked down (KD). (B) Quantifications of the simulations and experimental data for mTOR-pS2481 upon Rictor or Raptor knock down 20 min after amino acids/insulin induction. * $P < 0.01$; n.s., not significant; Student's t-test. *In vitro* experiments were performed by Annika Sonntag, Freiburg University, Germany. (See [Dalle Pezze *et al.*, 2012b, Fig. 1]).

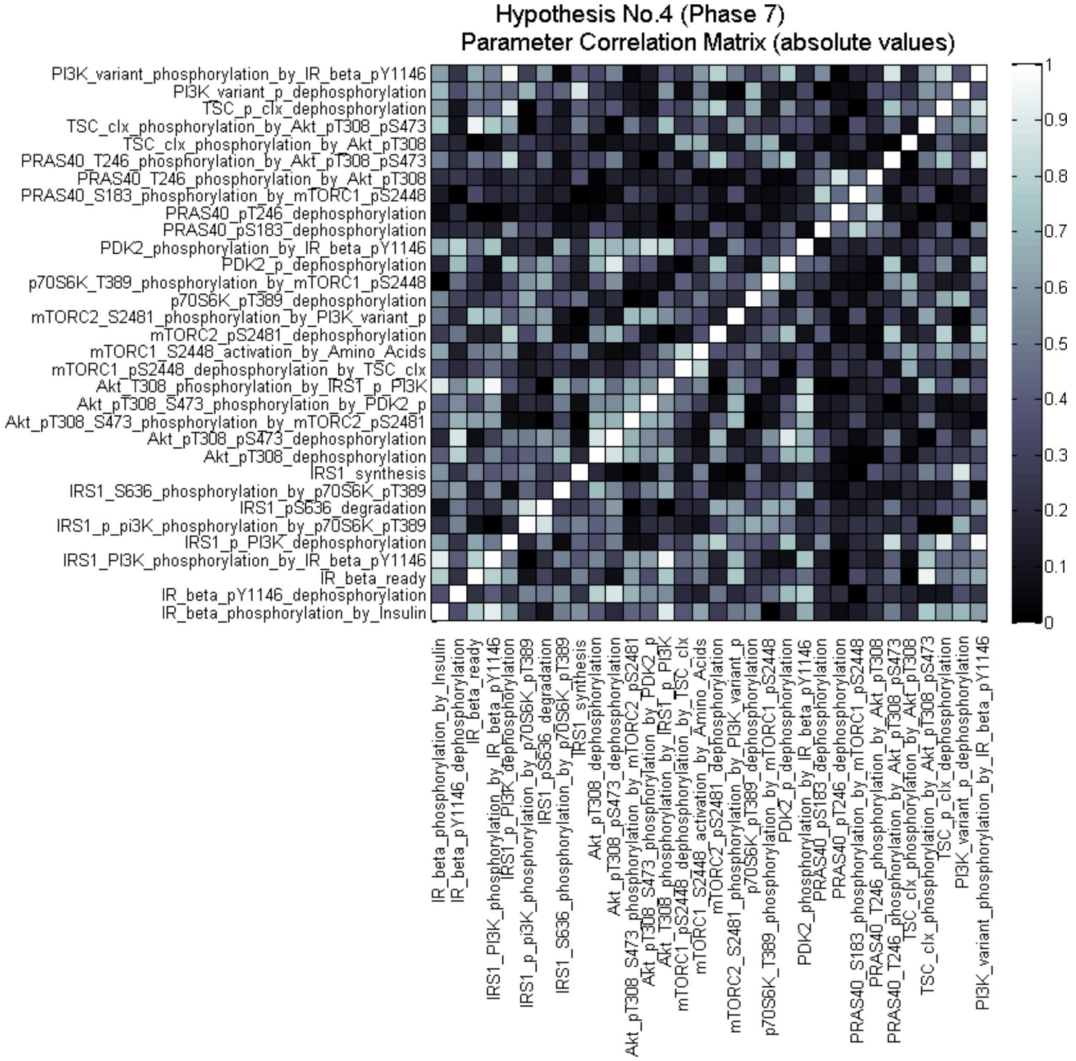

Figure 5.27: Identifiability analysis for Hypothesis 4: PI3K-dependent, NFL-independent regulation of mTORC2. Parameter correlation matrix for Hypothesis 4 is shown. See Figure 5.6 for details.

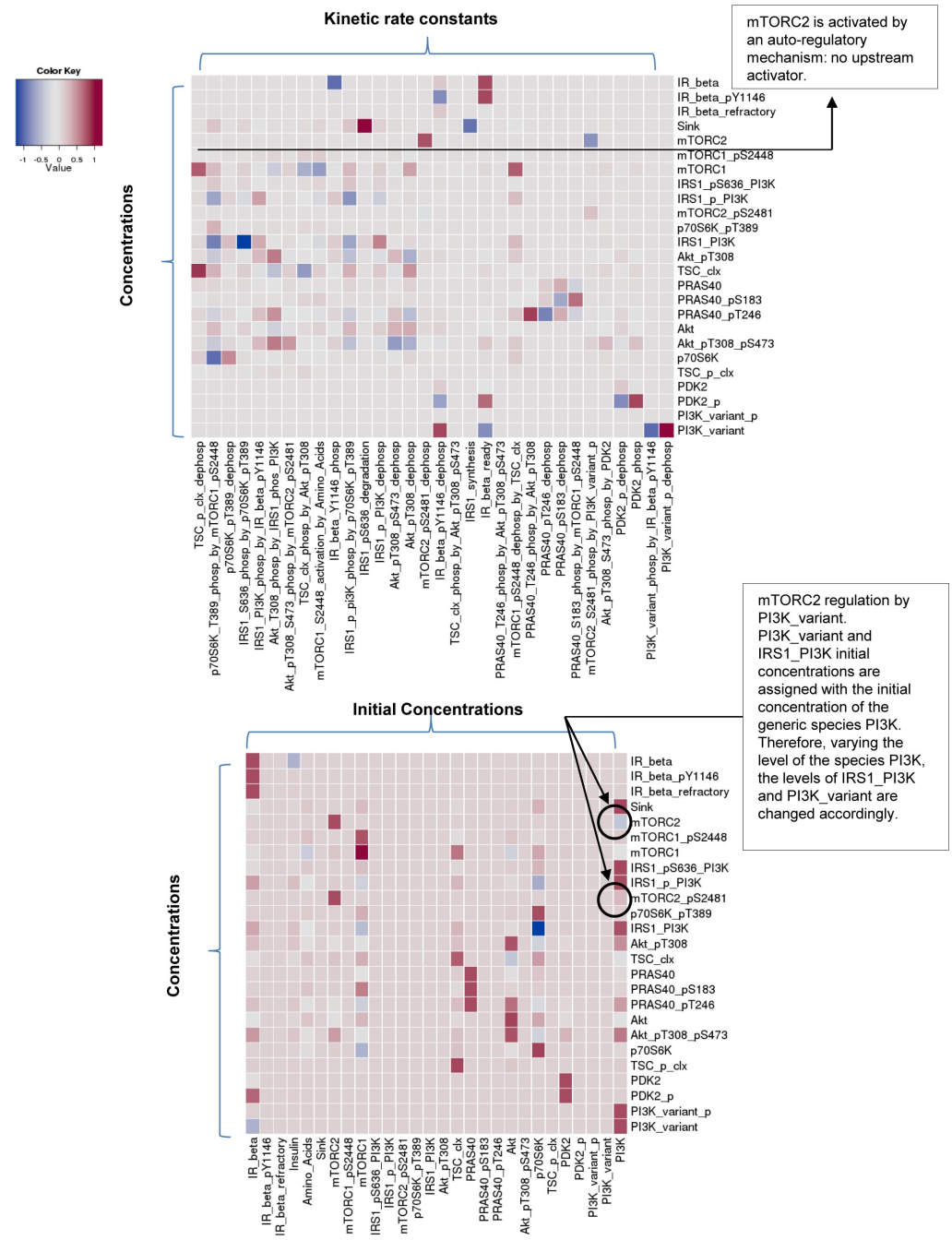

Figure 5.28: Sensitivity analysis for Hypothesis 4: PI3K-dependent, NFL-independent regulation of mTORC2. Sensitivity analysis for the initial concentrations and the kinetic rates parameters for Hypothesis 4 is shown. See Figure 5.7 for details of the top and bottom plots.

A) ODEs of the General Model

Parameters	
Akt_pT308_dephosphorylation:	K_1
Akt_pT308_pS473_dephosphorylation:	K_2
Akt_pT308_S473_phosphorylation_by_mTORC2_pS2481:	K_3
Akt_pT308_S473_phosphorylation_by_PDK2:	K_4
Akt_T308_phosphorylation_by_IRS1_phos_PI3K:	K_5
IR_beta_pY1146_dephosphorylation:	K_6
IR_beta_ready:	K_7
IR_beta_Y1146_phosphorylation:	K_8
IRS1_PI3K_phosphorylation_by_IR_beta_pY1146:	K_9
IRS1_p_PI3K_dephosphorylation:	K_{10}
IRS1_p_pi3K_phosphorylation_by_p70S6K_pT389:	K_{11}
IRS1_pS636_degradation:	K_{12}
IRS1_S636_phosphorylation_by_p70S6K_pT389:	K_{13}
IRS1_synthesis:	K_{14}
mTORC1_pS2448_dephosphorylation_by_TSC_clx:	K_{15}
mTORC1_S2448_activation_by_Amino_Acids:	K_{16}
mTORC2_pS2481_dephosphorylation:	K_{17}
mTORC2_S2481_phosphorylation:	K_{18}
p70S6K_pT389_dephosphorylation:	K_{19}
p70S6K_T389_phosphorylation_by_mTORC1_pS2448:	K_{20}
PDK2_p_dephosphorylation:	K_{21}
PDK2_phosphorylation:	K_{22}
PRAS40_pS183_dephosphorylation:	K_{23}
PRAS40_pT246_dephosphorylation:	K_{24}
PRAS40_S183_phosphorylation_by_mTORC1_pS2448:	K_{25}
PRAS40_T246_phosphorylation_by_Akt_pT308:	K_{26}
PRAS40_T246_phosphorylation_by_Akt_pT308_pS473:	K_{27}
TSC_clx_phosphorylation_by_Akt_pT308:	K_{28}
TSC_clx_phosphorylation_by_Akt_pT308_pS473:	K_{29}
TSC_p_clx_dephosphorylation:	K_{30}

Ordinary Differential Equations	
Akt:	$\dot{X}_1 = + K_1 \cdot X_2 - K_5 \cdot X_1 \cdot X_{10}$
Akt_pT308:	$\dot{X}_2 = + K_2 \cdot X_3 - K_1 \cdot X_2 - K_4 \cdot X_2 \cdot X_{19} + K_5 \cdot X_1 \cdot X_{10} - K_3 \cdot X_2 \cdot X_{15}$
Akt_pT308_pS473:	$\dot{X}_3 = - K_2 \cdot X_3 + K_4 \cdot X_2 \cdot X_{19} + K_3 \cdot X_2 \cdot X_{15}$
Amino_Acids	$\dot{X}_4 = \text{const}_{Ins}$
Insulin	$\dot{X}_5 = \text{const}_{AA}$
IR_beta:	$\dot{X}_6 = + K_7 \cdot X_8 - K_8 \cdot X_6 \cdot X_5$
IR_beta_pY1146:	$\dot{X}_7 = - K_6 \cdot X_7 + K_8 \cdot X_6 \cdot X_5$
IR_beta_refractory:	$\dot{X}_8 = + K_6 \cdot X_7 - K_7 \cdot X_8$
IRS1_PI3K:	$\dot{X}_9 = + K_{10} \cdot X_{10} + K_{14} \cdot X_{24} - K_{13} \cdot X_9 \cdot X_{17} - K_9 \cdot X_9 \cdot X_7$
IRS1_p_PI3K:	$\dot{X}_{10} = - K_{11} \cdot X_{10} \cdot X_{17} - K_{10} \cdot X_{10} + K_{19} \cdot X_9 \cdot X_7$
IRS1_pS636_PI3K:	$\dot{X}_{11} = + K_{11} \cdot X_{10} \cdot X_{17} - K_{12} \cdot X_{11} + K_{13} \cdot X_9 \cdot X_{17}$
mTORC1:	$\dot{X}_{12} = + K_{15} \cdot X_{13} \cdot X_{24} - K_{16} \cdot X_{12} \cdot X_4$
mTORC1_pS2448:	$\dot{X}_{13} = - K_{15} \cdot X_{13} \cdot X_{24} + K_{16} \cdot X_{12} \cdot X_4$
mTORC2:	$\dot{X}_{14} = + K_{17} \cdot X_{15} - K_{18} \cdot X_{14}$
mTORC2_pS2481:	$\dot{X}_{15} = - K_{17} \cdot X_{15} + K_{18} \cdot X_{14}$
p70S6K:	$\dot{X}_{16} = - K_{20} \cdot X_{16} \cdot X_{13} + K_{19} \cdot X_{17}$
p70S6K_pT389:	$\dot{X}_{17} = + K_{20} \cdot X_{16} \cdot X_{13} - K_{19} \cdot X_{17}$
PDK2:	$\dot{X}_{18} = - K_{22} \cdot X_{18} \cdot X_7 + K_{21} \cdot X_{19}$
PDK2_p:	$\dot{X}_{19} = + K_{22} \cdot X_{18} \cdot X_7 - K_{21} \cdot X_{19}$
PRAS40:	$\dot{X}_{20} = - K_{27} \cdot X_{20} \cdot X_3 - K_{26} \cdot X_{20} \cdot X_2 + K_{24} \cdot X_{22} + K_{23} \cdot X_{21} - K_{25} \cdot X_{20} \cdot X_{13}$
PRAS40_pS183:	$\dot{X}_{21} = - K_{23} \cdot X_{21} + K_{25} \cdot X_{20} \cdot X_{13}$
PRAS40_pT246:	$\dot{X}_{22} = + K_{27} \cdot X_{20} \cdot X_3 + K_{26} \cdot X_{20} \cdot X_2 - K_{24} \cdot X_{22}$
Sink:	$\dot{X}_{23} = + K_{12} \cdot X_{11} - K_{14} \cdot X_{23}$
TSC_clx:	$\dot{X}_{24} = + K_{30} \cdot X_{25} - K_{29} \cdot X_{24} \cdot X_3 - K_{28} \cdot X_{24} \cdot X_2$
TSC_p_clx:	$\dot{X}_{25} = - K_{30} \cdot X_{25} + K_{29} \cdot X_{24} \cdot X_3 + K_{28} \cdot X_{24} \cdot X_2$

B) ODEs of the there Hypotheses

Parameters		
1st Hypothesis	mTORC2_pS2481_dephosphorylation:	K_{31}
	mTORC2_S2481_phosphorylation_by_TSC_p_clx:	K_{32}
2nd Hypothesis	mTORC2_pS2481_dephosphorylation:	K_{33}
	mTORC2_S2481_phosphorylation_by_IRS1_phos_PI3K:	K_{34}
3rd Hypothesis	mTORC2_S2481_phosphorylation_by_unknown_kinase_p:	K_{35}
	mTORC2_pS2481_dephosphorylation:	K_{36}
	unknown_kinase_p_dephosphorylation:	K_{37}
	unknown_kinase_phosphorylation_by_IR_beta_pY1146:	K_{38}

Ordinary Differential Equations		
1st Hypothesis	mTORC2:	$\dot{X}_{26} = - K_{32} \cdot X_{26} \cdot X_{25} + K_{31} \cdot X_{27}$
	mTORC2_pS2481:	$\dot{X}_{27} = + K_{32} \cdot X_{26} \cdot X_{25} - K_{31} \cdot X_{27}$
2nd Hypothesis	mTORC2:	$\dot{X}_{28} = - K_{34} \cdot X_{28} \cdot X_{10} + K_{33} \cdot X_{29}$
	mTORC2_pS2481:	$\dot{X}_{29} = + K_{34} \cdot X_{28} \cdot X_{10} - K_{33} \cdot X_{29}$
3rd Hypothesis	mTORC2:	$\dot{X}_{30} = - K_{35} \cdot X_{30} \cdot X_{33} + K_{36} \cdot X_{31}$
	mTORC2_pS2481:	$\dot{X}_{31} = + K_{35} \cdot X_{30} \cdot X_{33} - K_{36} \cdot X_{31}$
	unknown_kinase:	$\dot{X}_{32} = - K_{38} \cdot X_{32} \cdot X_7 + K_{37} \cdot X_{33}$
	unknown_kinase_p:	$\dot{X}_{33} = + K_{38} \cdot X_{32} \cdot X_7 - K_{37} \cdot X_{33}$

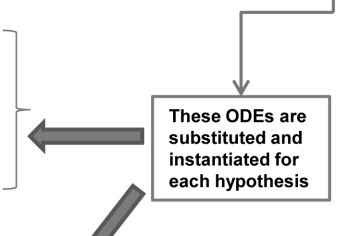

Table 5.1: Ordinary differential equations of the general model and the models representing Hypothesis 1, 2, and 3 for mTORC2 activation. List of kinetic rate constants and ordinary differential equations (ODEs) for the general model (A) and the Hypotheses 1, 2, and 3 (B). Each hypothesis is derived from the general model by replacing the mTORC2 ODEs, shown in the box, with those corresponding to the hypothesis.

Parameter Names	IR_beta model calibration [Phase 1 ; 3 parameters]	General model (no PDK2) [Phase 2 ; 24 parameters]	General model (+ PDK2) [Phase 3 ; 3 parameters]	Parameter Values
Kinetic Rate Constants (min^{-1})				
Akt_pT308_dephosphorylation		4.0737591667 ± 0.0009002079	fixed	**4.0739**
Akt_pT308_pS473_dephosphorylation		2.113835 ± 0.0001043631	(replaced with the next reaction)	**2.11397**
Akt_pT308_pS473_dephosphorylation			7.5280777714 ± 0.0225877871	**7.52842**
Akt_pT308_S473_phosphorylation (autoregulation)		9.9999975 ± 4.330127018e-06	(replaced with the next 2 reactions)	**9.99999**
Akt_pT308_S473_phosphorylation_by_mTORC2_pS2481			4.5073187429 ± 0.0142519251	**4.50769**
Akt_pT308_S473_phosphorylation_by_PDK2			5.9038608857 ± 0.0168590452	**5.90372**
Akt_T308_phosphorylation_by_IRS1_phos_PI3K		0.6994409167 ± 0.0001739753	fixed	**0.699505**
IR_beta_pY1146_dephosphorylation	0.1493278 ± 2.92916370e-06	fixed		**0.149328**
IR_beta_ready	0.030973095 ± 1.45639108e-06	fixed		**0.0309731**
IR_beta_Y1146_phosphorylation	0.025376377 ± 5.51335650e-07	fixed		**0.0253763**
IRS1_PI3K_phosphorylation_by_IR_beta_pY1146		0.1346880833 ± 1.9302237924e-05	fixed	**0.134664**
IRS1_p_PI3K_dephosphorylation		0.0032827042 ± 1.1067027479e-06	fixed	**0.00328283**
IRS1_p_pi3K_phosphorylation_by_p70S6K_pT389		0.0001 ± 2.7105054312e-20	fixed	**0.0001**
IRS1_pS636_degradation		0.0001000023 ± 2.1650635094e-09	fixed	**0.000100001**
IRS1_S636_phosphorylation_by_p70S6K_pT389		0.9999995 ± 5.0000000001e-07	fixed	**1**
IRS1_synthesis		0.0999933667 ± 5.4945933021e-06	fixed	**0.0999968**
mTORC1_pS2448_dephosphorylation_by_TSC_clx		0.9999950833 ± 4.0095372412e-06	fixed	**0.999989**
mTORC1_S2448_activation_by_Amino_Acids		0.05138455 ± 6.6251415079e-06	fixed	**0.0513784**
mTORC2_pS2481_dephosphorylation		0.0174131917 ± 1.795577127e-06	fixed	**0.0174149**
mTORC2_S2481_phosphorylation		0.0781611 ± 4.6502688094e-06	fixed	**0.0781585**
p70S6K_pT389_dephosphorylation		0.0052853975 ± 2.2100683435e-06	fixed	**0.00528455**
p70S6K_T389_phosphorylation_by_mTORC1_pS2448		0.0057393217 ± 5.0554975576e-07	fixed	**0.00573896**
PDK2_p_dephosphorylation			assumed	**1**
PDK2_phosphorylation			assumed	**0.1**
PRAS40_pS183_dephosphorylation		0.4034775833 ± 0.000106986	fixed	**0.403706**
PRAS40_pT246_dephosphorylation		0.9999980833 ± 2.841898817e-06	fixed	**0.999991**
PRAS40_S183_phosphorylation_by_mTORC1_pS2448		0.073052733 ± 1.8625892968e-05	fixed	**0.073093**
PRAS40_T246_phosphorylation_by_Akt_pT308		0.0239171 ± 8.6986589004e-07	fixed	**0.0239178**
PRAS40_T246_phosphorylation_by_Akt_pT308_pS473		0.000100002083 ± 2.09993386e-09	fixed	**0.000100001**
TSC_clx_phosphorylation_by_Akt_pT308		0.0062716025 ± 1.4869326649e-06	fixed	**0.00627315**
TSC_clx_phosphorylation_by_Akt_pT308_pS473		0.000100009083 ± 9.79335091e-09	fixed	**0.000100039**
TSC_p_clx_dephosphorylation		0.0081260025 ± 3.274604619e-06	fixed	**0.00812537**
Protein Amounts (Arbitrary Unit – AU)				
Akt		determined		**144.13**
Amino_Acids (input)		determined		**100**
Insulin (input)	determined			**100**
IR_beta	determined			**12.1175**
IRS1_PI3K		determined		**2.965**
mTORC1		determined		**4.3225**
mTORC2		determined		**6.2175**
p70S6K		determined		**127.0725**
PDK2			assumed = IR_beta	**12.1175**
PRAS40		determined		**73.2175**
TSC_clx		assumed		**10**
Number of Estimated Solutions Sets:	**1**	**2 (1 rejected as inconsistent with data)**	**1**	

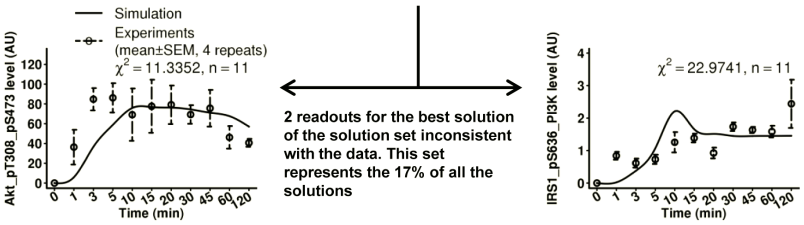

Table 5.2: Parameter values of the general model. The general model was fully parameterised by three steps. Phase 1, 3 kinetic rate constants of the insulin receptor (IR-beta) were determined. Phase 2, the general model without PDK2 was obtained by parameterising 24 kinetic rate constants. In this phase, Akt-S473 activation is modelled as autoregulation, independent of mTORC2 and PDK2. Phase 3, PDK2 dynamics were added to the system and the 3 parameters regulating Akt-S473 phosphorylation were calibrated by substituting the previously introduced autoregulatory mechanism (parameters values shown in red) of Akt. For each phase, 350 independent calibrations, starting from random initial configurations of the parameters, were executed and the best solution set fitting the data was selected. Phase 1 and 3 converged to a single solution set. Phase 2 converged to two solutions sets of which one was discarded as inconsistent with the experimental data (shown for phosphorylated Akt-S473 and IRS1-S636 readouts). For each phase, the mean and standard deviation of the estimated parameters were computed from the selected solution set. The solution closest to the centroid of the selected solution cluster was chosen for fixing the parameter values. *In vitro* experiments were performed by Annika Sonntag, Freiburg University, Germany.

Hypotheses	No. Estimated Solutions Sets:	Parameter Names	Hypotheses calibration	Parameter Values
Hypothesis No.1		Kinetic Rate Constants (min^{-1})		
(TSC1/TSC2-dependent)	1	mTORC2_pS2481_dephosphorylation	0.2060607514 ± 0.0001069	**0.206059**
[Phase 4 ; 2 parameters]		mTORC2_S2481_phosphorylation_by_TSC_p_clx	0.0668916283 ± 3.03470106e-05	**0.0668912**
Hypothesis No.2 (NFL-dependent)	1	mTORC2_pS2481_dephosphorylation	0.0250001279 ± 1.5959455e-05	**0.025**
[Phase 5 ; 2 parameters]		mTORC2_S2481_phosphorylation_by_IRS1_phos_PI3K	0.0561080757 ± 3.78781639e-06	**0.0561081**
Hypothesis No.3 (PI3K-independent)	1	mTORC2_S2481_phosphorylation_by_unknown_kinase	0.0318873566 ± 1.02655930e-05	**0.0318902**
[Phase 6 ; 4 parameters]		mTORC2_pS2481_dephosphorylation	0.0255700314 ± 1.63113942e-05	**0.0255714**
		unknown_kinase_p_dephosphorylation	0.0002336665 ± 5.21539673e-05	**0.000232165**
		unknown_kinase_phosphorylation_by_IR_beta_pY1146	0.9999865686 ± 2.02074847e-05	**0.999985**
		Protein Amounts (Arbitrary Unit – AU)		
		unknown_kinase	assumed = IRS1_PI3K	**2.965**

Table 5.3: Parameter values of Hypotheses 1, 2, and 3. For each hypothesis, the estimated parameters were calibrated using the same protocol provided in Table 5.2. For each hypothesis, all the corresponding calibrations converged to a single solution set.

Model	General Model	TSC1/TSC2-dependent Hypothesis	NFL-dependent Hypothesis	PI3K-independent Hypothesis	4th Hypothesis
Total χ^2	43.8073	45.9226	43.4833	43.33	43.33
Total Time Points (N)	99	99	99	99	99
Total Estimated Parameters (k)	30	30	30	32	32
AIC	434.2002	438.8688	433.4653	437.1157	437.1157

Table 5.4: Summary of model goodness-of-fit. The total χ^2 and Akaike Information Criterion (AIC) measures are reported for the general model and the four hypotheses. Both the measures slightly penalise the TSC1/TSC2-dependent hypothesis. AIC also penalises the PI3K-independent and the fourth hypotheses due to the higher number of parameters in these two models. However, these differences are not statistically significant for rejection of any model.

Chapter 6

A modelling-experimental approach reveals IRS dependent regulation of AMPK by insulin

This chapter describes a systems biology-based investigation of AMPK regulation as described in [Sonntag *et al.*, 2012]. The results here focus on the modelling point of view and only include *in vitro* experimental work necessary for model validation and test. All the *in vitro* experimental data included in this project were collected by Annika Sonntag, PhD student supervised by Dr Kathrin Thedieck, Department of Bioinformatics and Molecular Genetics, Freiburg University, Germany. A copy of the published work, which includes the *in vitro* experimental data used for parameterising and testing the model, is attached in Appendix B.

6.1 Introduction

After generating an insulin-mTOR dynamical model and determining mTORC2 induction by a distinct PI3K which is insensitive to the NFL [Dalle Pezze *et al.*, 2012a], the upstream regulation of both mTOR Complex 1 and 2 was elucidated and implemented. The next step was to add the energy signalling pathway, as represented by the AMPK module, into the model.

The choice of AMPK reflected the fact that this trimeric complex not only represents one of the most well known energy-dependent regulators within the cell [Thedieck and Hall, 2009], but also promotes, whereas mTORC1 inhibits, autophagy through ULK1 phosphorylation [Kim *et al.*, 2011; Lee *et al.*, 2010a] (see Section 3.3.4). Under low energy conditions, AMPK directly phosphorylates and increases TSC2 GAPase activity [Inoki *et al.*, 2003], thereby inhibiting mTORC1.

In addition, AMPK phosphorylates the mTORC1 scaffold protein Raptor on two serine residues [Gwinn *et al.*, 2008]. This phosphorylation induces 14-3-3 binding to Raptor and is required for mTORC1 inhibition by energy deprivation. Therefore, the inclusion of AMPK into the model is essential for achieving a computational framework for both studying molecular mechanisms and achieving simulated drug interventions with the ultimate aim of extending lifespan. Further details concerning the biology of the energy signalling pathway can be found in Section 3.2.3.
In the process of data collection, we found that AMPK not only responds to energy deprivation but is also strongly activated by insulin within 3 minutes post induction, and is further induced in Raptor deficient cells. Although it was already shown that AMPK can be regulated by insulin [Aguilar *et al.*, 2007; Polak *et al.*, 2008; Suzuki *et al.*, 2004], the mechanism involved in this regulation has not yet been clarified. The immunoblot-based AMPK-mTOR dynamical model was employed for generating a quality-of-fit based ranking of hypotheses of AMPK activation. This prediction using this procedure indicated that the most probable point in the network at which the insulin and AMPK signalling forked was at the level of IRS and that AMPK was dependent on the negative feedback loop (NFL). This was experimentally tested and confirmed in LKB1-deficient and -functional cells lines. In summary, this study shows that AMPK is positively regulated initially by IRS and inhibited by the NFL.

6.2 Results

6.2.1 An insulin-TOR-AMPK model

AMPK is another important mTOR regulator that suppresses mTORC1 activity in response to energy deprivation [Mihaylova and Shaw, 2011]. A new dynamical mTOR-AMPK model was generated including AMPK signalling to the earlier mTOR model as developed in [Dalle Pezze *et al.*, 2012a] which only assumed insulin and amino acids as mTORC1 regulators. This new model implemented AMPK inhibition of mTORC1 through promotion of TSC1/TSC2 complex activity only. We chose not to include direct phosphorylation of Raptor by AMPK for

two reasons: first, the AMPK functional regulation on mTORC1 was still maintained, since these two pathways both contributed to mTORC1 inhibition; second, the inclusion of a regulatory mechanism of Raptor and 14-3-3 was out of the scope of this project. The following new connection was added into the model presented in [Dalle Pezze *et al.*, 2012a]: AMPK phosphorylation at T172 allows active AMPK to phosphorylate TSC2 at S1387 (species TSC1/TSC2) which leads to TSC1/TSC2 activity enhancement and subsequent inhibition of mTORC1 [Inoki *et al.*, 2005, 2003; Mihaylova and Shaw, 2011]. Conversely, the phosphorylation of TSC2 at T1462 (species TSC1/TSC2) by Akt-pT308 inhibits the TSC1/TSC2 complex, activating mTORC1 [Inoki *et al.*, 2002]. Finally, the species Akt-pS473, PRAS40-pT246 and PRAS40-pS183 were defined as supplementary readouts for mTORC2, Akt, and mTORC1, respectively.

Although AMPK is known to be induced by energy depletion [Mihaylova and Shaw, 2011], AMPK was described to be induced in Raptor deficient cells [Aguilar *et al.*, 2007; Polak *et al.*, 2008] and also gradually induced in gradual Raptor knock down HeLa cell line upon amino acids/insulin after only 20 min post induction (p.i.) (see [Sonntag *et al.*, 2012, Fig. 1A]). Surprisingly, we found that insulin alone was able to strongly induce AMPK-pT172 and its readout TSC2-pS1387 already at 3 min p.i. and that these phosphorylations decreased over time. Although it has been described previously that AMPK is induced by IGF-1 [Suzuki *et al.*, 2004], this signalling connection has to date only been poorly explored. Therefore, in the present study, the possible AMPK-activators in the insulin-mTORC1 signalling were systematically investigated. The AMPK activator candidates were selected among the upstream species of mTORC1 because: (1) mTORC1 is maximally induced at 30 - 45 min p.i. [Dalle Pezze *et al.*, 2012a], (2) AMPK induction by insulin peaked already as early as 3 min p.i., and (3) AMPK was induced by Raptor knockdown (e.g. mTORC1 inhibition). Therefore, we focused on the following AMPK activator candidates:

Hypothesis 1 (Insulin) where insulin is considered as a constant and direct input to AMPK;

Hypothesis 2 (IR_beta_pY1146) reflecting IR activation;

Hypothesis 3 (IRS1_p) reflecting IRS1 activation by insulin receptor;

Hypothesis 4 (mTORC2_pS2481) reflecting mTORC2 activation by amino acids/insulin;

Hypothesis 5 (Akt_pT308) reflecting Akt activation downstream of PI3K;

Hypothesis 6 (TSC1_TSC2_pT1462) reflecting TSC1/TSC2 deactivation by Akt.

A graphical representation of this insulin-mTOR-AMPK model depicting our six alternative hypotheses of AMPK activation is provided in Figure 6.1. In order to add and calibrate the AMPK module, time course data for AMPK-pT172 and TSC1/TSC2-pS1387, monitoring the activity of AMPK and its readout TSC2, were acquired under serum and amino acids starvation followed by induction by insulin and amino acids, the same conditions used for calibration of the dynamic mTOR network model [Dalle Pezze *et al.*, 2012a]. All signal intensities were quantified, and descriptive statistics were computed over three replicates. The experimental mean time courses were used to calibrate the model parameters.

6.2.2 Parameter estimation and identifiability

A specific model was instantiated for each hypothesis and calibrated using the same data sets and using the Matlab Toolbox PottersWheel [Maiwald and Timmer, 2008]. Before calibrating the models, structural identifiability analysis was performed using the software GenSSI [Chiş *et al.*, 2011]. This software calculated the symbolic solution of the problem computing Lie derivatives for each hypothesis confirming structural global identifiability for all six models. For the IRS1-induced AMPK model, structural identifiability analysis is reported in Figure 6.2A, showing that all the parameters were structurally identified in the first (blue circles) or second (magenta circles) order identifiability tableau.
To calibrate the models, experimental time course data upon amino acids/insulin induction for nine readouts (IR-beta-pY1146, IRS1-pS636, Akt-pT308, Akt-pS473, mTORC1-pS2448, mTORC2-pS2481, p70S6K-pT389, PRAS40-pT246, PRAS40-pS183; data set 1) in wild type cells along the insulin-mTOR signalling axis were used in combination with time course data under gradual mTORC1 inhibition (Raptor knock down; data set 2) in wild type cells, as measured previously [Dalle

Pezze *et al.*, 2012a]. Furthermore, in order to calibrate the species AMPK-pT172 and TSC1/TSC2-pS1387, the five time points (0, 3, 20, 45, and 100 min. p.i.; [Sonntag *et al.*, 2012, Fig. 1A]) without knock down induction, i.e. corresponding to wild type, were added as an additional data set (data set 3).
Parameter estimation was executed for each model independently over multiple data sets in order to reduce the bias of the solution and therefore overfitting. However, the addition of data sets used to calibrate a model can lead to a serious increment of variance, particularly due to the increase in intrinsic noise in experimental data, which does not permit to estimate the model correctly. Our second data set was characterised by three different levels of Raptor knock down, obtained by doxycycline treatment for 1, 2 or 3 days respectively (subsets 1-3). A satisfactory bias-variance trade off was found by combinatorially and singularly testing these three subsets and eventually selecting only the subset of Raptor knock down induced by doxycycline treatment for 3 days (subset 3). Subset 3 was selected as it represented the strongest signal reduction and consequently novel information with respect to wild type time courses (data set 1) for calibrating the model. Moreover, the readouts in our data sets (data set 1, data set 2-subset 3, data set 3) were scaled in order to have species time course profiles of comparable intensity. This evenly distributes the cost of the solution over the simulated time course profiles approximating the data, avoiding an implicit preference ranking of calibration.
For calibrating the models, only the kinetic rate constant parameters were estimated, whereas the species protein concentrations were determined from immunoblot time course data sets by selecting the corresponding readout maximum intensity plus two standard deviations measured at that time point. The addition of two standard deviations to the maximum signal peak guaranteed to avoid species protein saturation conditions. The kinetic rate constants regulating PI3K-variant dynamics were fixed a priori assuming a time course similar to the insulin receptor. In fact, no experimental data is available for this PI3K insensitive to the negative feedback loop and it is more likely that it follows the IR-beta receptor than other curves. Furthermore, fixing these parameters led us to a full structural identifiability of the model.
A posterior identifiability analysis was performed using Mean Optimal Transfor-

mation Approach (MOTA) plugin [Hengl *et al.*, 2007; Maiwald and Timmer, 2008] after selecting 50% of the best fits (shown in Figure 6.2B for the IRS1-induced AMPK model). This analysis revealed that high parameter correlations had coefficient of variation (CV) lower than 0.05 for all our models except for the IR -beta-induced AMPK model (Hypothesis 2; Figure 6.3). For this model, MOTA analysis highlighted high correlation and CV for the pair of parameters regulating AMPK dynamics. Model identifiability was obtained after fixing one of the two parameters and recalibrating the remaining one in a second round of calibration. In combination with the previous analysis, parameter non-identifiability was also checked by directly analysing the estimated percentage of standard deviations of the parameters, computed over the 50% best fits, and considering non-identifiable the parameters with standard deviations higher than a threshold of 5%. Table 6.1 presents the estimated parameters values with mean, standard deviations and CV for the IRS1-induced AMPK model showing parameter identifiability. Sensitivity analysis for the same model is provided in Figure 6.4, showing a balanced sensitivity among the parameters and that all of them were required.
In summary, six models sharing the main network structure and differing in AMPK activation were independently calibrated. The next step was therefore to find at which level in the network AMPK is induced by insulin.

6.2.3 Hypotheses ranking and testing of AMPK activation by insulin

Once parameter estimation was achieved, the simulated time courses for the readouts AMPK-pT172 and TSC1/TSC2-pS1387 of each model were compared with the corresponding experimental time courses (see Figure 6.5). Surprisingly, the readouts AMPK-pT172 and TSC1/TSC2-pS1387 for the IRS1-induced AMPK model (Hypothesis 3) were found to fit the data with high accuracy, whereas the goodness-of-fit decreased for species downstream of IRS1 (Akt and TSC1/TSC2; Hypotheses 5 and 6) and upstream of IRS1 (Insulin, IR-beta; Hypotheses 1 and 2), as indicated by the measure χ^2. Furthermore, the two readouts fitted worse for the mTORC2-induced AMPK model (Hypothesis 4).
At this point, the question was whether these local differences could lead to a

possible ranking of the overall models. In order to achieve this, several additional likelihood-based statistical criteria, such as Akaike Information Criterion (AIC, AICc) [Akaike, 1973] and Bayesian Information Criterion (BIC) [Schwarz, 1978], were used besides the total χ^2, to estimate the goodness-of-fit calculated over the entire models. Through these estimations a ranking of the hypotheses in according to the goodness-of-fit was established (see Table 6.2). All these measures were consistent between them in selecting the IRS1-induced AMPK model (Hypothesis 3) as the most probable model. The remaining simulated versus experimental time courses for IRS1-induced AMPK model are reported in Figure 6.6. An SBML model is provided for the IRS1-induced AMPK hypothesis.
In order to test hypotheses ranking and specifically Hypothesis 3 validity, four experimental tests were conducted: IRS over-expression, PI3K inhibition by Wortmannin, PTEN over-expression and myristoylated Akt. Schematic diagrams illustrating these tests are provided in Figure 6.7. These tests consistently confirmed the predicted validity of Hypothesis 3, rejecting all the other hypotheses and are in line with the observed AMPK induction in mTORC1 deficient cells (see [Aguilar *et al.*, 2007; Polak *et al.*, 2008]). Moreover, since HeLa cells do not express AMPK upstream kinase LKB1 [Sun *et al.*, 2007; Suzuki *et al.*, 2004], this mechanism of AMPK induction by insulin was also tested and confirmed in C2C12 cell line, which is LKB1 functional. Experimental testing details can be found in [Sonntag *et al.*, 2012, Fig. 4]. A graphical representation of the IRS1-induced AMPK model (Hypothesis 3) in SBGN notation is given in Figure 6.8.

6.3 Discussion

In the present study, amino acids/insulin was observed to induce AMPK, confirming a previous report [Suzuki *et al.*, 2004]. Here, we showed that this induction happened already at 3 minutes post treatment with amino acids/insulin and increased under Raptor inhibition. The dynamical model developed in [Dalle Pezze *et al.*, 2012a] was employed and extended with an AMPK module. This work systematically explored which component in the IIS-TOR signalling pathway was the most likely candidate activator of AMPK. Applying a hypothesis ranking based

on quality-of-fit between the model and experimental data sets, a signalling fork was predicted at the level of IRS (Hypothesis 3), one fork leading to the canonical insulin signalling pathway, another one to AMPK. This prediction was experimentally confirmed in LKB1-deficient (HeLa) and -functional (C2C12) cells lines. Besides confirming this hypothesis, experimental tests also rejected all the other hypotheses, which were already considered less probable by our predictions due to poor fitting with the data. These results showed that AMPK induction was dependent on IRS and was therefore sensitive to the NFL, in agreement with our previous finding that Raptor inhibition increased AMPK activation.

From a modelling point of view, a comprehensive mTOR network has been studied statically [Caron *et al.*, 2010] and parts of the mTOR network have been modelled dynamically [Borisov *et al.*, 2009; Dalle Pezze *et al.*, 2012a; Faratian *et al.*, 2009; Jain and Bhalla, 2009; Kiselyov *et al.*, 2009; Kuepfer *et al.*, 2007; Sedaghat *et al.*, 2002; Vinod and Venkatesh, 2009]. The network presented in this study is the most extensive mTOR-AMPK model, incorporating AMPK as directly regulated by amino acids/insulin. Six models were defined and calibrated using our experimental data. The models shared the main network structure, but differed for the AMPK activation mechanism. After repeating cycles of parameter calibration and identifiability for each model, likelihood-based statistical measures were used to estimate a model ranking, based on the goodness-of-fit between each model and the experimental data.

Interestingly, other studies reported that AMPK inhibits IRS by phosphorylation of IRS1 at S794 [Jakobsen *et al.*, 2001; Ning and Clemmons, 2010; Tzatsos and Tsichlis, 2007]. What is the meaning of this inhibition along with the activation mechanism reported in this study? May this be an additional mechanism to switch off the insulin signalling analogous with the canonical IIS-TOR signalling and the p70-S6K-induced negative feedback loop? A possible explanation of this redundancy may be to increase the robustness of the cellular system upon insulin stimulation. Certainly, further investigation on the dual regulation of AMPK and IRS is required in order to better characterise the role of IRS and the meaning of its downstream effect on AMPK.

In this study, we found that AMPK activation was dependent on IRS in HeLa cells, which are known to be LKB1-deficient, and confirmed this results in C2C12

cells line, which are LKB1-functional cells. Another study reported that IGF1 could induce AMPK in LKB1-functional PANC1 cells, besides HeLa cells [Suzuki *et al.*, 2004]. Therefore, the activation of AMPK at the level of IRS, presented in this work, could be conserved in other cells in addition to HeLa, C2C12 and PANC1.
Finally, linking AMPK with IRS1 and the NFL is a crucial aspect in drug intervention, since the positive effects of AMPK activity can be maximised by mTOR-inhibitors [Garcia-Echeverria, 2011]. In this context, model simulations of drug treatments can offer a parsimonious and rapid methodology for predicting best protein-dependent drug intervention and administration in preventing or treating metabolic and tumour diseases.

6.4 Materials and methods

6.4.1 Modelling

The illustrated graphical model in SBGN graphical notation [Le Novère *et al.*, 2009] were designed using CellDesigner 4.2 [Funahashi *et al.*, 2008, 2003]. The Matlab Toolbox PottersWheel [Maiwald and Timmer, 2008] was used for designing and calibrating the models. The parameters for each of the models were estimated by 1000 fits with parameter disturbance noise of 0.4 using the best fit as starting value. For each fit a maximum of 250 iterations with χ^2 and parameters tolerances of 1e-07 were run using the optimisation algorithm TrustRegion. To reduce the computation time, CVODES integrator was selected and configured with the following parameters: maximum number of steps = 1500, relative tolerance = 1e-06, absolute tolerance = 1e-08. The reactions representing the dynamics of the models were described by mass action laws. Only the kinetic rate constants were estimated and the interval [1e-06, 1e+04] was selected as a constraint for each parameter. The initial protein concentrations were directly determined from our experimental data and scaled to distribute the fitting quality over the model. Experimental error bars indicate standard error of the mean (SEM). The dynamics for the species PI3K-variant were assumed by reproducing the dynamics of the insulin receptor, whereas its initial concentration was the

same as IRS1 species.
Structural identifiability was calculated a priori with GenSSI [Chiş *et al.*, 2011]. The model in Potterswheel format was exported in SBML and converted to Octave format using The System Biology Format Converter (SBFC)[1]. Then the model in Octave format was adapted for the software GenSSI. Symbolic solutions for each model were computed setting 10 as maximum number of iterations. After executing each sequence fits, parameters were considered non-identifiable when their coefficients of variance (CV), measured in the best 50% fits of the calibration sequence, were higher than 5%. In combination to this preliminary analysis, the PottersWheel plugin MOTA was used to confirm the parameter non-identifiability and to assess the relations between the target parameter and the others.
3D Sensitivity analysis was performed using PottersWheel and provided in Figure 6.4. Models were exported in SBML [Hucka *et al.*, 2003] Level 2 Version 4 using PottersWheel.

6.4.2 Statistics

The Standard Error of the Mean (SEM) was chosen to estimate the statistical variability of the measured samples of experimental time course. The goodness-of-fit statistical measures χ^2 [Maiwald and Timmer, 2008], AIC, AICc [Akaike, 1973] and BIC [Schwarz, 1978] were used in order to rank the hypotheses. All these measures were directly computed using PottersWheel Toolbox. The statistical and programming language R v. 2.13.1 [R Development Core Team, 2010] was selected for the graphic representation of the identifiability matrix computed with MOTA and for all the computed statistics.

6.5 Figures and tables

[1]Software available from http://sourceforge.net/

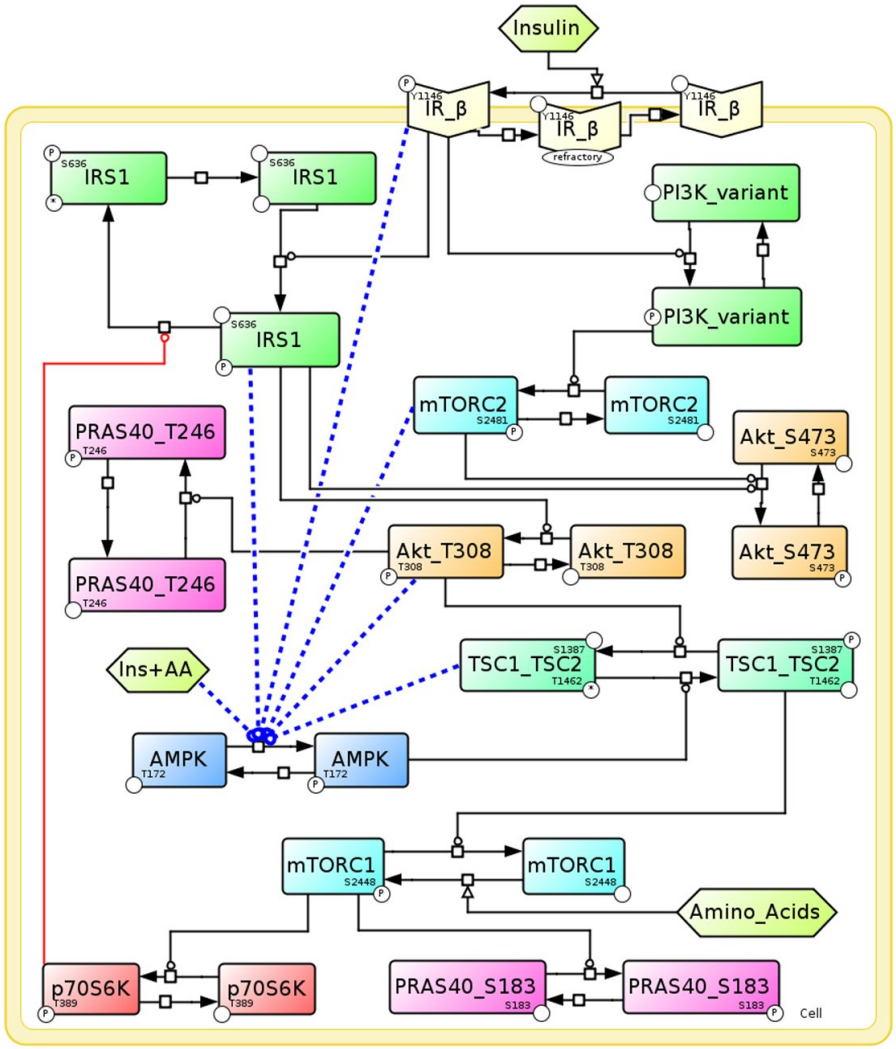

Figure 6.1: Graphical insulin-mTOR-AMPK model. This model integrates the insulin-mTOR model presented in [Dalle Pezze *et al.*, 2012a] with AMPK regulation. Six hypotheses of AMPK activation are investigated (blue dotted lines). Except for the Insulin- and IR-beta-induced AMPK hypotheses, all the others implicitly assume AMPK being dependent on the p70-S6K-negative feedback loop.

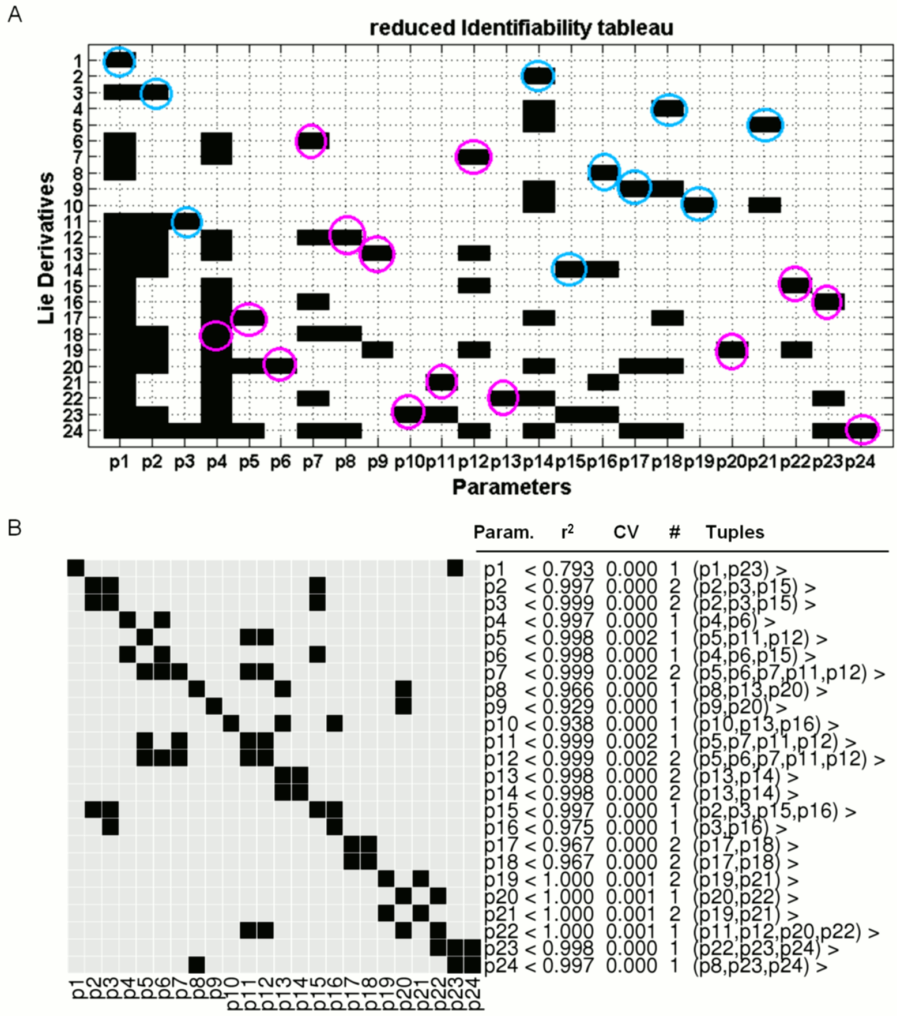

Figure 6.2: Identifiability analysis for IRS1-induced AMPK model (Hypothesis 3). (A) Structural identifiability analysis was performed with the software GenSSI a priori. In the reduced identifiability tableau, blue circles indicate the parameters detected directly as structurally globally identifiable at the first order tableau, whereas magenta circles highlight the parameters detected as structurally globally identifiable at the second order tableau after computing the symbolic solution. (B) MOTA identifiability analysis was executed using the 50% of the best fits of the calibration fits sequence. A correlation among a set of parameters is indicated by the tuple of correlated parameters, their correlation coefficient (r^2), coefficient of variation (CV) and the number of times this correlation is identified by varying the parameters of the tuple (#). Even though there are high correlations among some parameters, the corresponding coefficient of variation was lower than 0.002, which can be explained as numeric approximation error in the fit sequence calibration process. (*) $r^2 > 0.9$ & $CV > 0.1$ (**) $r^2 > 0.9$ & $CV > 0.1$ & #> 1.

A

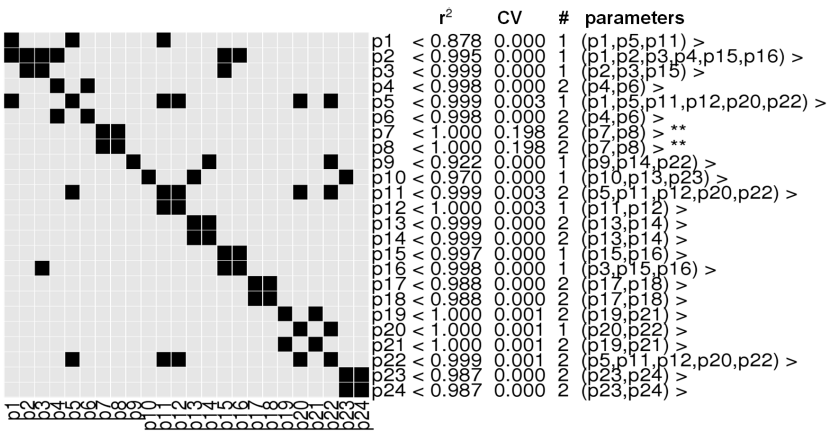

B

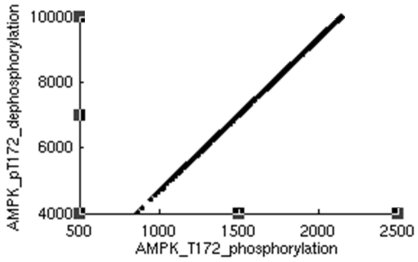

C

Parameter Name (AMPK induced by IR-Beta Model) (Kinetic rate constants [min⁻¹])	*Calibration Rounds (mean, sd, %) Round 1*	*Round 2*	*Value*
p1=IR_beta_phosphorylation_by_Insulin	0.127895 ± 1.87856e-05 (0%)	fixed	0.127892
p2=IR_beta_pY1146_dephosphorylation	0.421933 ± 6.72417e-05 (0%)	fixed	0.421835
p3=IR_beta_ready	0.0613301 ± 1.39536e-05 (0%)	fixed	0.0613094
p4=IRS1_phosphorylation_by_IR_beta_pY1146	0.00506354 ± 9.74753e-07 (0%)	fixed	0.00506217
p5=IRS1_p_phosphorylation_by_p70S6K_pT389	2166.01 ± 7.00991 (0%)	fixed	2164.5
p6=IRS1_pS636_dephosphorylation	0.0150341 ± 7.28345e-06 (0%)	fixed	0.0150241
p7=AMPK_T172_phosphorylation	1726.2 ± 342.304 (20%)	fixed	2145.27
p8=AMPK_pT172_dephosphorylation	8034.56 ± 1593.25 (20%)	9985.01 ± 1.63853 (0%)	9983.42
p9=Akt_pT308_dephosphorylation	0.00255589 ± 4.5546e-07 (0%)	fixed	0.00255584
p10=Akt_pS473_dephosphorylation	0.00624137 ± 2.30368e-07 (0%)	fixed	0.00624136
p11=Akt_S473_phosphorylation_by_mTORC2_pS2481_n_IRS1_p	14.2914 ± 0.0471528 (0%)	fixed	14.2858
p12=Akt_T308_phosphorylation_by_IRS1_p	7.16228 ± 0.018444 (0%)	fixed	7.16055
p13=mTORC1_pS2448_dephosphorylation_by_TSC1_TSC2_pS1387	0.010212 ± 2.66286e-06 (0%)	fixed	0.0102132
p14=mTORC1_S2448_activation_by_Amino_Acids	0.00414963 ± 8.15228e-07 (0%)	fixed	0.00414999
p15=mTORC2_pS2481_dephosphorylation	0.0204082 ± 2.94073e-06 (0%)	fixed	0.0204037
p16=mTORC2_S2481_phosphorylation_by_PI3K_variant_p	0.385463 ± 3.02274e-05 (0%)	fixed	0.385417
p17=p70S6K_pT389_dephosphorylation	0.0099792 ± 1.57728e-06 (0%)	fixed	0.00997852
p18=p70S6K_T389_phosphorylation_by_mTORC1_pS2448	0.00171206 ± 7.63572e-08 (0%)	fixed	0.00171203
p19=PRAS40_pS183_dephosphorylation	2.79774 ± 0.00410708 (0%)	fixed	2.80277
p20=PRAS40_pT246_dephosphorylation	1.61657 ± 0.00185418 (0%)	fixed	1.61721
p21=PRAS40_S183_phosphorylation_by_mTORC1_pS2448	0.224023 ± 0.00032552 (0%)	fixed	0.224421
p22=PRAS40_T246_phosphorylation_by_Akt_pT308	0.136366 ± 0.000154248 (0%)	fixed	0.136417
p23=TSC1_TSC2_S1387_phosphorylation_by_AMPK_pT172	0.0232386 ± 2.30029e-06 (0%)	fixed	0.0232365
p24=TSC1_TSC2_T1462_phosphorylation_by_Akt_pT308	0.00994593 ± 1.45625e-06 (0%)	fixed	0.00994482
p25=PI3K_variant_p_dephosphorylation	assumed		10
p26=PI3K_variant_phosphorylation_by_IR_beta_pY1146	assumed		0.01

Figure 6.3: Identifiability and parameter estimation for IR-beta-induced AMPK model (Hypothesis 2). (A) Identifiability analysis for the IR-beta-induced AMPK model indicated non identifiability issues for the parameters regulating AMPK dynamics (p7, p8). (B) Correlation plot between the two parameters (p7, p8) confirms non-identifiability of the parameters. (C) Finally, the first round of the parameter estimation reported a standard deviation percentage higher than 5% for the two parameters. p8 was further recalibrated in a second round in which it was correctly identified. (*) $r^2 > 0.9$ & $CV > 0.1$ (**) $r^2 > 0.9$ & $CV > 0.1$ & $\# > 1$.

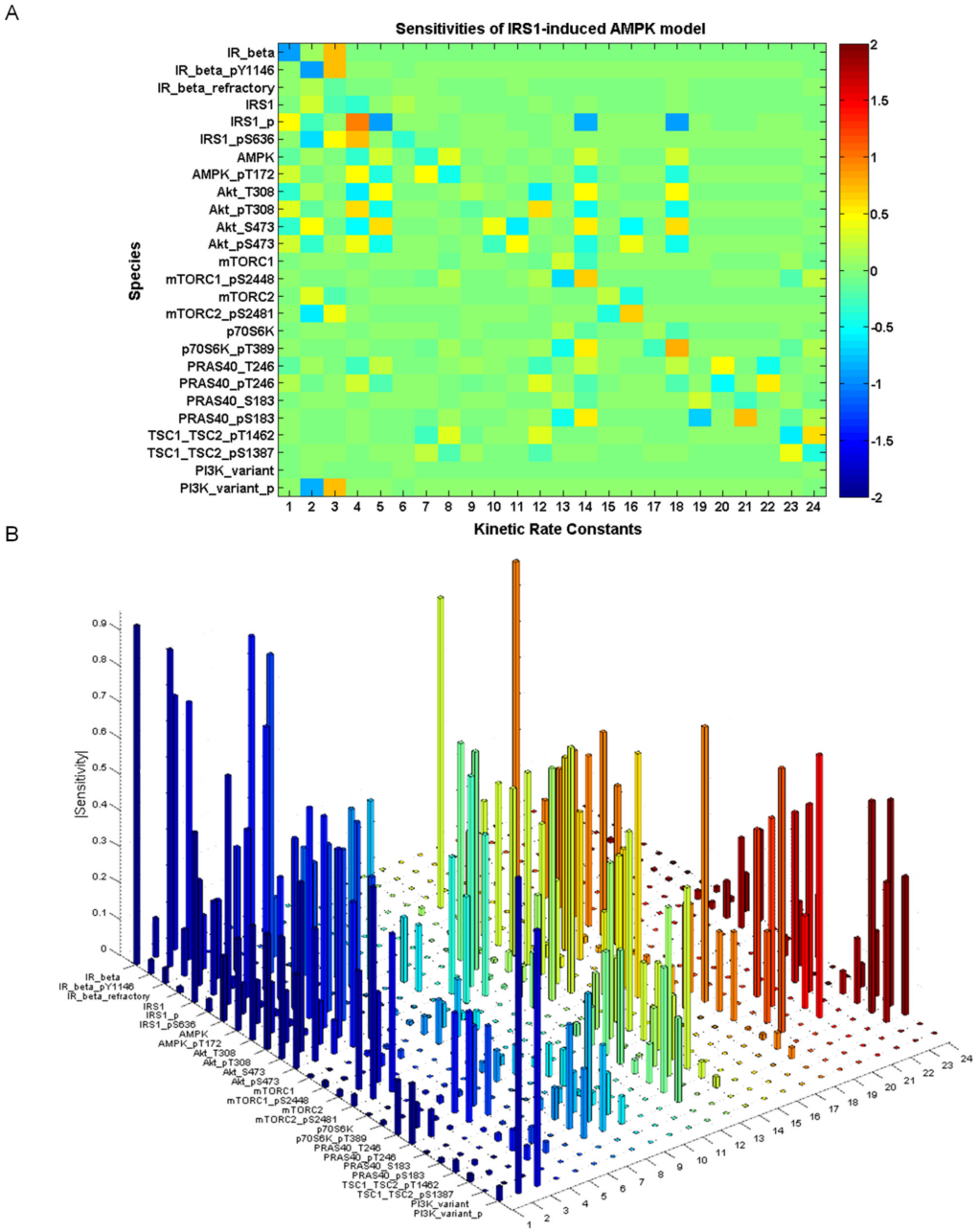

Figure 6.4: Sensitivity analysis for IRS1-induced AMPK model (Hypothesis 3). (A) 2-dimensional sensitivity analysis between the estimated kinetic rate constants versus the protein concentrations. The table shows that all the parameters are essential for describing the model and the IRS1-p regulation is the most important as it mediates the insulin signalling as well as the p70-S6K-negative feedback loop. Colours indicate sensitivity levels. (B) 3-dimensional sensitivity analysis as normalised in [0,1]. Colours distinguish different estimated kinetic rate constant parameters.

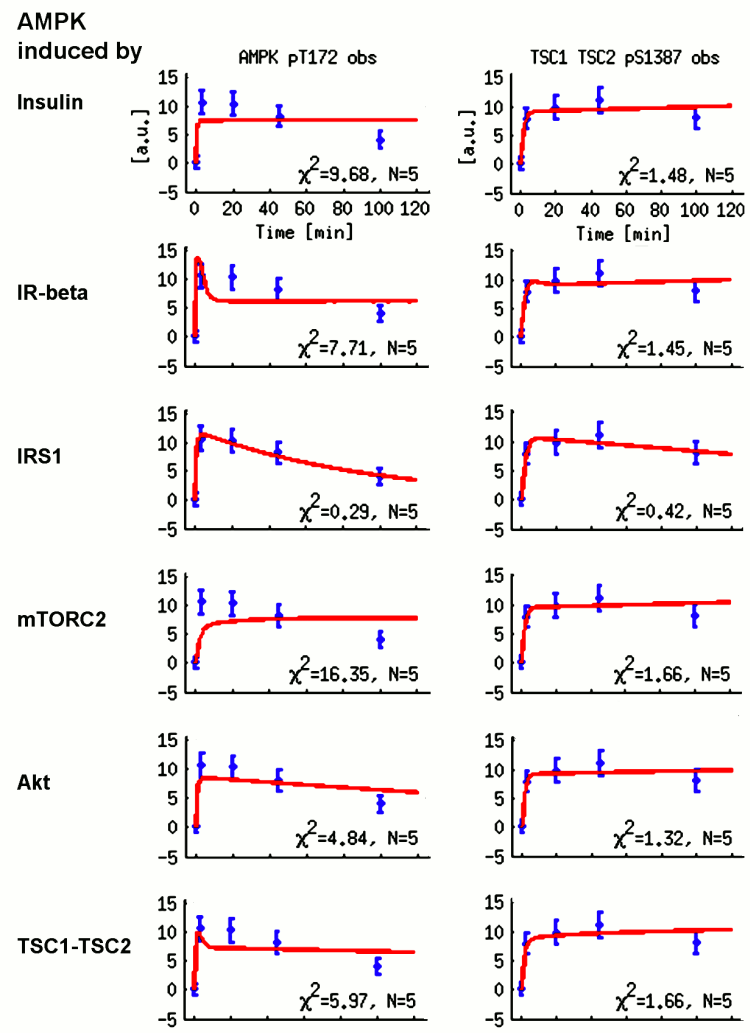

Figure 6.5: Prediction of the intersection between insulin and AMPK signalling. Simulated time courses (red lines) versus experimental data (blue points) for AMPK-pT172 and its downstream readout TSC1/TSC2-pS1387 (columns) shown for the six hypotheses: Insulin-, IR-beta-, IRS-, mTORC2-, Akt-, TSC1/TSC2-induced AMPK (rows). These predictions suggest that AMPK could be regulated by kinases downstream of the insulin receptor. The IRS-induced AMPK model (Hypothesis 3) fitted experimental data best. Experimental data error bars indicate standard error of the mean (SEM) calculated from three repetitions. Goodness-of-fit χ^2 is reported for each plot along with the number of measured time points. *In vitro* experiments were performed by Annika Sonntag, Freiburg University, Germany.

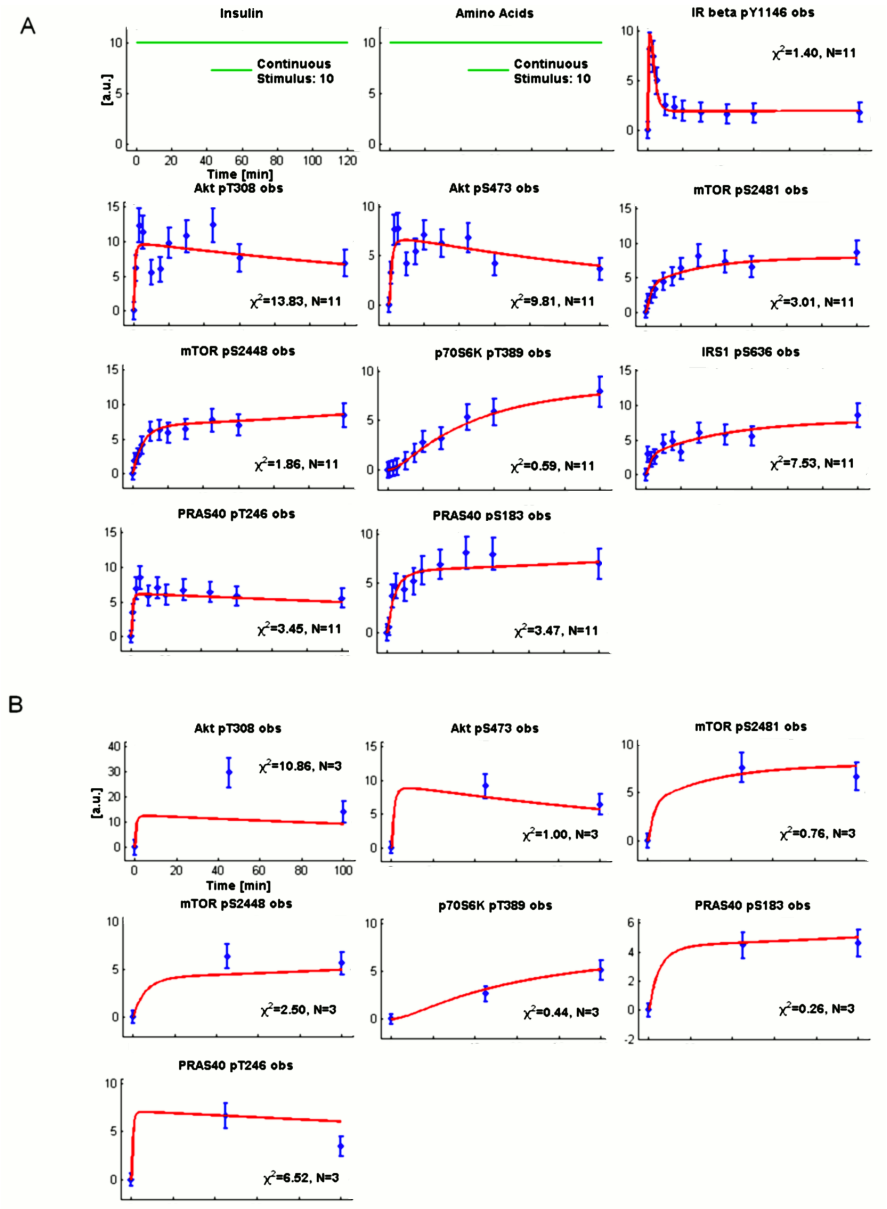

Figure 6.6: Additional simulated versus experimental additional time courses for IRS1-induced AMPK model (Hypothesis 3). (A) Main data set used for parameter estimation. Simulated (red lines) versus experimental data (blue points) are plotted for nine wild type (WT) readouts along the insulin-TOR network upon amino acids/insulin induction. (B) Additional data set used for parameter estimation. Experimental data for seven readouts for a Raptor knock down (KD) upon amino acids/insulin induction. Experimental data error bars indicate standard error of the mean (SEM) calculated from four repetitions. Goodness-of-fit χ^2 is reported for each plot along with the number of measured time points. *In vitro* experiments were performed by Annika Sonntag, Freiburg University, Germany.

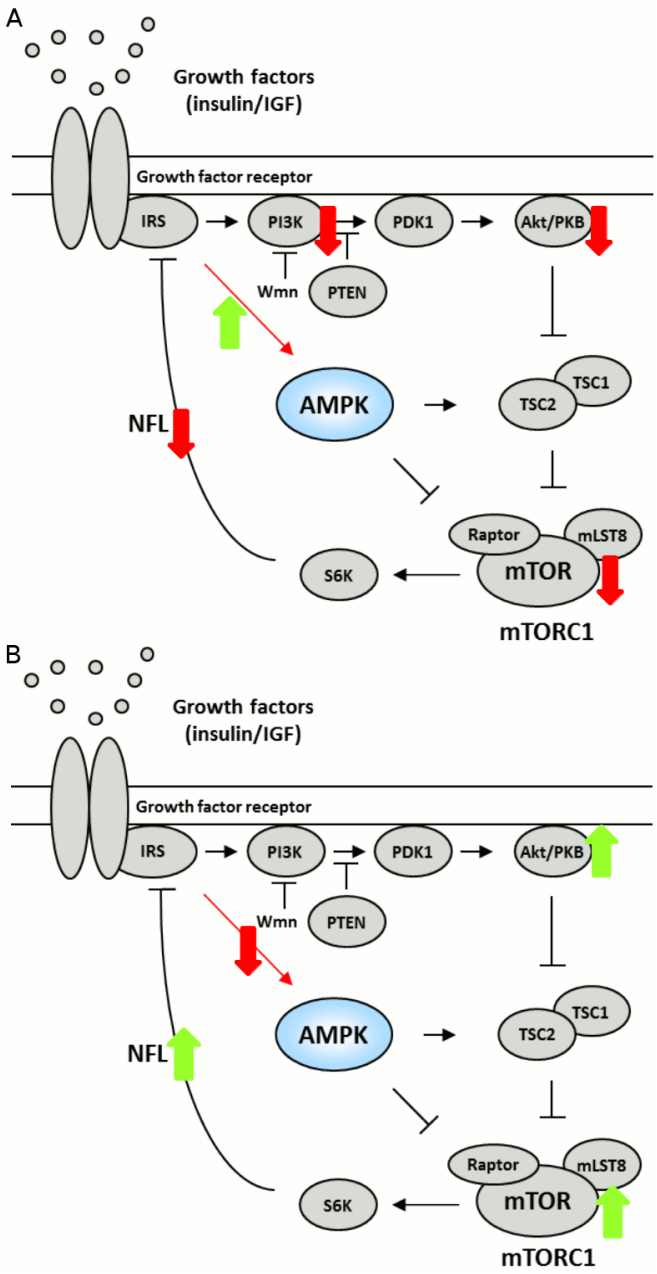

Figure 6.7: Schematic diagrams for testing hypotheses ranking. (A) IRS overexpression induced AMPK and TSC1/TSC2 activity directly and indirectly by inhibiting the negative feedback loop (NFL). In addition, AMPK was also positively regulated by either inhibiting PI3K with Wortmannin or overexpressing PTEN. (B) Constitutively active Akt inhibited AMPK by hyperactivating the NFL. Wmn: Wortmannin. Figures adapted from [Sonntag *et al.*, 2012, Fig. 5A].

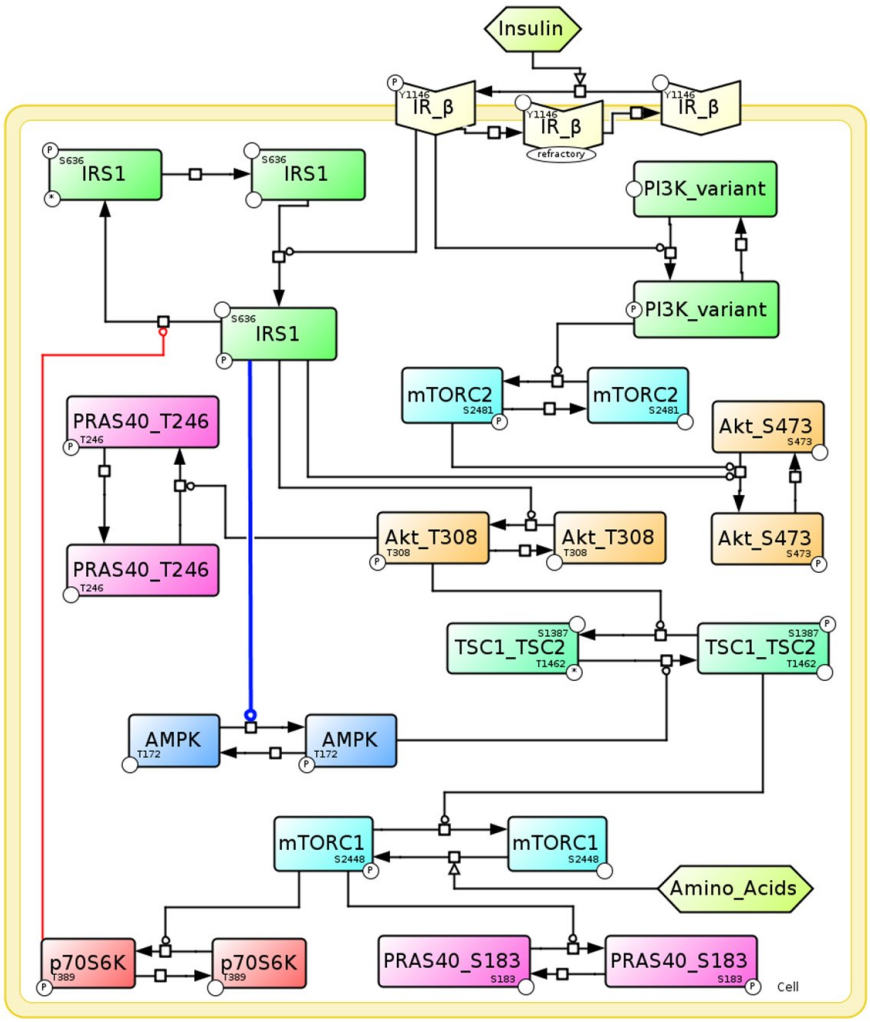

Figure 6.8: IRS is required for AMPK induction by insulin (Hypothesis 3). Graphical model of the insulin induced mTORC1 pathway in SBGN notation, including IRS dependent AMPK induction. Importantly, the negative feedback loop (NFL) via IRS targets not only PI3K but also AMPK.

Parameter Name (AMPK induced by IRS1 Model)	*Calibration*	*Value*
(Kinetic rate constants [min^{-1}])	*(mean, sd, %)*	
p1=IR_beta_phosphorylation_by_Insulin	0.124278 ± 1.21324e-05 (0%)	0.124273
p2=IR_beta_pY1146_dephosphorylation	0.396251 ± 3.02338e-05 (0%)	0.396235
p3=IR_beta_ready	0.0532808 ± 6.9999e-06 (0%)	0.053277
p4=IRS1_phosphorylation_by_IR_beta_pY1146	0.00491628 ± 5.46924e-07 (0%)	0.00491599
p5=IRS1_p_phosphorylation_by_p70S6K_pT389	1681.94 ± 3.80623 (0%)	1682.75
p6=IRS1_pS636_dephosphorylation	0.0130526 ± 4.45303e-06 (0%)	0.01305
p7=AMPK_T172_phosphorylation	9.79357 ± 0.0177607 (0%)	9.79766
p8=AMPK_pT172_dephosphorylation	0.0107217 ± 4.13895e-07 (0%)	0.0107215
p9=Akt_pT308_dephosphorylation	0.00335553 ± 3.70977e-07 (0%)	0.00335545
p10=Akt_pS473_dephosphorylation	0.00640225 ± 1.80374e-07 (0%)	0.00640216
p11=Akt_S473_phosphorylation_by_mTORC2_pS2481_n_IRS1_p	13.1374 ± 0.0302136 (0%)	13.1442
p12=Akt_T308_phosphorylation_by_IRS1_p	6.9152 ± 0.0123683 (0%)	6.91811
p13=mTORC1_pS2448_dephosphorylation_by_TSC1_TSC2_pS1387	0.0106657 ± 9.77042e-07 (0%)	0.0106652
p14=mTORC1_S2448_activation_by_Amino_Acids	0.00438932 ± 3.03977e-07 (0%)	0.00438916
p15=mTORC2_pS2481_dephosphorylation	0.0183743 ± 1.62188e-06 (0%)	0.0183735
p16=mTORC2_S2481_phosphorylation_by_PI3K_variant_p	0.375358 ± 1.34923e-05 (0%)	0.375353
p17=p70S6K_pT389_dephosphorylation	0.0113508 ± 6.03276e-07 (0%)	0.0113512
p18=p70S6K_T389_phosphorylation_by_mTORC1_pS2448	0.0018404 ± 3.38908e-08 (0%)	0.00184043
p19=PRAS40_pS183_dephosphorylation	2.33046 ± 0.00198802 (0%)	2.33014
p20=PRAS40_pT246_dephosphorylation	1.60545 ± 0.00132301 (0%)	1.60513
p21=PRAS40_S183_phosphorylation_by_mTORC1_pS2448	0.187646 ± 0.000157968 (0%)	0.187621
p22=PRAS40_T246_phosphorylation_by_Akt_pT308	0.137756 ± 0.000112104 (0%)	0.137729
p23=TSC1_TSC2_S1387_phosphorylation_by_AMPK_pT172	0.0365597 ± 4.61345e-06 (0%)	0.0365589
p24=TSC1_TSC2_T1462_phosphorylation_by_Akt_pT308	0.0177568 ± 1.993e-06 (0%)	0.0177562
p25=PI3K_variant_p_dephosphorylation	assumed	10
p26=PI3K_variant_phosphorylation_by_IR_beta_pY1146	assumed	0.01
(Concentrations [a.u.])		
u1=Insulin (INPUT)	fixed	10
u2=Amino_Acids (INPUT)	fixed	10
x1=IR_beta	determined	16.56070782
x4=IRS1	determined	18.93446968
x7=AMPK	determined	20.50644836
x9=Akt_T308	determined	21.41085271
x11=Akt_S473	determined	12.25170805
x13=mTORC1	determined	25.14
x15=mTORC2	determined	18.79587754
x17=p70S6K	determined	14.30096315
x19=PRAS40_S183	determined	13.56128255
x21=PRAS40_T246	determined	17.55000883
x23=TSC1_TSC2_pT1462	determined	14.9175
x25=PI3K_variant	determined	18.93446968
x2=IR_beta_pY1146 ; x3=IR_beta_refractory ; x5=IRS1_p ; x6=IRS1_pS636 ; x8=AMPK_pT172 ; x10=Akt_pT308 ; x12=Akt_pS473 ; x14=mTORC1_pS2448 ; x16=mTORC2_pS2481 ; x18=p70S6K_pT389 ; x20=PRAS40_pS183 ; x22=PRAS40_pT246 ; x24=TSC1_TSC2_pS1387 ; x26=PI3K_variant_p	fixed	0
(Scaling Factors)		
s1=scale_IR_beta_pY1146_obs ; s2=scale_IRS1_pS636_obs ; s3=scale_AMPK_pT172_obs ; s4=scale_Akt_pT308_obs ; s5=scale_Akt_pS473_obs ; s6=scale_TSC1_TSC2_pS1387_obs ; s7=scale_mTOR_pS2448_obs ; s8=scale_mTOR_pS2481_obs ; s9=scale_p70S6K_pT389_obs ; s10=scale_PRAS40_pT246_obs ; s11=scale_PRAS40_pS183_obs	fixed	1
(Observables [a.u.])		
y1=IR_beta_pY1146_obs	assigned	s1 * x2
y2=IRS1_pS636_obs	assigned	s2 * x6
y3=AMPK_pT172_obs	assigned	s3 * x8
y4=Akt_pT308_obs	assigned	s4 * x10
y5=Akt_pS473_obs	assigned	s5 * x12
y6=TSC1_TSC2_pS1387_obs	assigned	s6 * x14
y7=mTOR_pS2448_obs	assigned	s7 * x16
y8=mTOR_pS2481_obs	assigned	s8 * x18
y9=p70S6K_pT389_obs	assigned	s9 * x20
y10=PRAS40_pT246_obs	assigned	s10 * x22
y11=PRAS40_pS183_obs	assigned	s11 * x24
(Compartments [a.u.])		
c1=Cell	fixed	1

Table 6.1: Parameter table for the IRS1-induced AMPK model (Hypothesis 3). The estimated kinetic rate constants together with the species concentrations are provided. The mean, standard deviations and percent of standard deviation over the mean, computed over the 50% of the best fits, are also indicated. These statistics shows that all the 24 estimated parameter could be fixed at the first round of calibration. Scaling factor parameters and observable variables are also indicated.

Hypothesis No.	AMPK induction by	Chi-Square	AIC	AICc	BIC	Rank
1	Insulin	80.3086	367.233	378.66	436.053	5
2	IR-beta	78.1345	365.058	376.487	433.879	4
3	**IRS1**	**68.0217**	**354.946**	**366.374**	**423.767**	**1**
4	mTORC2	90.1238	377.048	388.476	445.869	6
5	Akt	75.5272	362.451	373.88	431.272	2
6	TSC1-TSC2	76.4666	363.391	374.819	432.211	3

N.Points=130
K.Parameters=24

Table 6.2: Statistical ranking of the models. Quality of fitting measures were used to determine a ranking of the investigated models. IRS1-induced AMPK model (Hypothesis 3) showed the lowest χ^2 value, indicating that this model was the most probable. AIC, AICc and BIC values are reported as additional measures.

Chapter 7

A dynamical mTOR-ROS model for irradiation-induced cellular senescence

This chapter describes a systems biology-based investigation on cellular senescence. The presentation focuses on the modelling point of view and only include *in vitro* experimental work necessary for model validation and test. All the *in vitro* experimental data included in this project were collected by Dr Glyn Nelson, supervised by Professor Thomas von Zglinicki, Institute for Ageing and Health, Newcastle University, United Kingdom.

7.1 Introduction

Cellular senescence is a phenomenon characterised by loss of mitosis and the dysregulation of multiple cellular processes. Ageing is associated with a progressive accumulation of DNA damage and reactive oxygen species (ROS) are a major cause of this damage [Finkel and Holbrook, 2000]. ROS are mostly generated as a by-product of mitochondrial activity in supplying cells with energy [Turrens, 2003]. ROS are highly reactive and can cause severe damage to macromolecules and organelles, leading to loss of function. As most ROS are generated from the mitochondria, it is not surprising that mitochondrial DNA (mtDNA) is particularly vulnerable and damage leads to impaired mitochondrial function [Passos *et al.*, 2007; Shokolenko *et al.*, 2009]. Recent studies also showed that telomere dysfunction can compromise mitochondrial function through activation of p53 and consequently repression of PGC-1α/β [Sahin *et al.*, 2011]. The result is a viscous cycle whereby ROS cause mitochondrial dysfunction which leads to fur-

ther increases in the level of ROS.

DNA damage and oxidative stress initiate a multitude of signalling pathways which may, in the case that damage is unrepaired, be reinforced through signalling feedback loops. Under such chronic conditions the downstream consequences may ultimately impair cellular function as is the case with the inflammatory response [Passos *et al.*, 2010]. Oxidative stress also activates c-Jun N-terminal kinases (JNK), which is responsible for FoxO3 translocation to the nucleus through phosphorylation [Greer and Brunet, 2005, 2008]. Oxidative stress promotes SIRT1-dependent deacetylation of FoxO3 favouring the transcription of genes controlling cell cycle arrest [Brunet *et al.*, 2004; Greer and Brunet, 2005]. Moreover, nuclear FoxO3 induces autophagy by expressing autophagic genes LC3, Gabarapl1 and Atg12 [Sengupta *et al.*, 2009; van der Vos *et al.*, 2012].

In recent years, interest has increased on the roles of the insulin/TOR signalling pathway in the mechanisms regulating ageing processes. Its importance was first recognised in worms where inhibition of insulin signalling, particularly Akt activity, leading to enhanced transcriptional activity of Daf-16, the homologue of FoxO3a in humans, was shown to extend lifespan [Lee *et al.*, 2003; Murphy *et al.*, 2003]. In agreement with this, TOR inhibition by caloric restriction or Rapamycin treatment, or AMPK activation by resveratrol or metformin treatment, increases autophagy [Kim *et al.*, 2011; Lee *et al.*, 2010a] and SIRT1 activity [Cantó *et al.*, 2009; Lagouge *et al.*, 2006; Rodgers *et al.*, 2005]. In turn, SIRT1-dependent deacetylation activity was shown to suppress p53 [Vaziri *et al.*, 2001] and increase transcriptional activity of FoxO3a and activity of PGC-1α/β [Cantó *et al.*, 2009; Lagouge *et al.*, 2006; Rodgers *et al.*, 2005]. As a consequence, autophagy and mitochondrial biogenesis are promoted, whereas ROS levels are reduced.

The network arising from these signalling pathways is clearly complex, especially due to the numerous signalling pathways and regulatory feedbacks. Moreover, it appears that the cellular transition from normal to senescence involves internal dynamical changes which need to be carefully investigated. In this study, we used a systems biology approach to develop the first dynamical model for irradiation-induced cellular senescence as a means to unravel the main processes governing the transition from a healthy to a senescent cell. We used this model to study FoxO3a-dependent mechanisms of regulating mitochondrial fusion and

membrane potential. We provide evidence for the importance of two nuclear states of FoxO3a: unphosphorylated and JNK-dependent phosphorylated. The former predominantly triggered Mfn2 and improved mitochondrial membrane potential. The latter mostly acted in response to DNA-damage and oxidative-stress, and promoted cell cycle arrest through p21 signalling which contributes to ROS production. This dual role of FoxO3a was critical for determining cellular senescence progression and consolidation. Also, this work showed that new drug-interventions aimed at preventing cellular senescence, should include combinatorial inhibition of the insulin/TOR pathway and JNK/ROS oxidative-stress response.

7.2 Results

7.2.1 A dynamical model for cellular senescence

The model presented in Figure 7.1 aimed to integrate five key regulators of ageing: insulin-TOR, FoxO3a, DNA damage, reactive oxidative species (ROS), mitochondrial function. The insulin-TOR network was abstracted in order to reproduce Akt, mammalian TOR Complex I (mTORC1) and the mTORC1-p70-S6K-induced negative feedback loop. Akt was responsible for FoxO3a translocation from the nucleus to the cytoplasm and this migration was overridden by JNK activity [Brunet *et al.*, 2004; Greer and Brunet, 2005, 2008]. This resulted in two nuclear FoxO3a states for which no specific assumption was made on their respective downstream activity. Since PGC-1α/β is linked to FoxO3a and activated by AMPK, PGC-1α/β-dependent mitochondrial biogenesis signalling was embedded within FoxO3a-AMPK-Mfn2 signalling, where Mfn2 is indicative of mitochondrial fusion (mitofusin2) [Koshiba *et al.*, 2004], mitochondrial metabolism [Bach *et al.*, 2003] and herein mitochondrial biogenesis through PGC-1β [Liesa *et al.*, 2008; Soriano *et al.*, 2006]. Therefore, global mitochondrial function was improved by Mfn2, abstracting PGC-1α/β activity. Three states of mitochondrial membrane potential (high, low, null) were assumed. Each state contributed to ROS production and total ROS was responsible for mitochondrial membrane potential decrement. ROS also increased DNA damage levels and induced the oxidative

stress response through JNK, which promoted FoxO3a translocation from the cytoplasm to the nucleus. Both nuclear FoxO3a states and DNA damage triggered p21 signalling, which led to an increase in ROS production [Passos *et al.*, 2010]. p53 was not directly included into the model because its time-course was similar to DNA damage H2A.X foci marker. Finally, p27 and GSK3α activities were monitored as additional readouts.

7.2.2 Time-course analysis upon irradiation-induced senescence

In vitro experimental time course data were collected in MRC5 fibroblast cells for 13 experimental readouts in the network up to 21 days post 20 Gy X-ray irradiation. The *in vitro* data and model simulation upon X-ray irradiation are shown in Figure 7.2. Following irradiation, *in vitro* and *in silico* data showed a dramatic increase in DNA damage and oxidative stress responses, and a consequent decrease in mitochondrial membrane potential. Immediately following cellular damage, an Mfn2 response was observed indicative of unphosphorylated nuclear FoxO3a activity combined with AMPK. The increasing levels of AMPK should result in an increase in the levels of PGC-1α/β, which in turn should promote mitochondrial biogenesis. However, the mitochondrial membrane potential was not restored, despite AMPK activity. The model parameter estimation explained this conflict by attributing differential roles to the two nuclear FoxO3a pools (see graphical model in Figure 7.1 and predicted nuclear FoxO3a time courses in Figure 7.3A). The JNK-phosphorylated nuclear FoxO3a played a more minor role in activating the processes of mitochondrial fusion and biogenesis than the unphosphorylated-state nuclear FoxO3a. In fact, high JNK levels indicated that FoxO3a mainly resided in the nucleus and was phosphorylated on its JNK-dependent sites. However, JNK-phosphorylated FoxO3a interaction with AMPK was reduced in promoting Mfn2, and consequently mitochondrial membrane potential levels were maintained low and unaffected by JNK activity. Interestingly, although ROS levels were maximised and were maintained stable, JNK was only at half of its maximal observed activity and was gradually increasing, highlighting that other factors, such as chronic inflammation as regulated by other pathways,

may be responsible for further JNK activation.
This consideration provided a preliminary understanding about how a senescent state was driven and consolidated. Firstly, DNA damage and ROS production would be responsible for loss of mitochondria function. Secondly, the system would enter a *point of no return*, due to mitochondrial fusion and biogenesis failure, which in this framework was explained by a shift of FoxO3a activity due to JNK high levels. Therefore, JNK-phosphorylated FoxO3a would not respond to AMPK and potentially would not mediate signals with PGC-1α/β to correctly activate the processes of mitochondrial fusion and biogenesis.

7.2.3 JNK inhibition promotes cytoplasmic FoxO3a migration and Mfn2

To better formalise and test this hypothesis, we perturbed JNK levels in the model at day 0 and then analysed the effects on FoxO3a and FoxO-downstream proteins. These predictions were tested experimentally *in vitro*.
As a first step, the model predicted that a JNK inhibition of 25-50% applied at day 0 would correspond to a reduction in JNK-pT183 levels to 48-73% at 10 days post irradiation. To experimentally test this prediction, cells were treated with 1μM of the JNK inhibitor SP600125 at day 0. Consistent with this prediction, *in vitro* JNK inhibition measured at 10 days post irradiation showed a reduction in JNK-pT183 levels to 68%. Thus, this preliminary result indicated that our *in vitro* JNK inhibition at day 0 was between 25 and 50% of total JNK level (see Figure 7.3B and C). Since JNK constrains FoxO3a to reside inside the nucleus, inhibition of JNK would have allowed FoxO3a translocation to the cytoplasm. The model predicted an increment in cytosolic/nuclear FoxO3a ratio between 117% and 152% at 10 days post irradiation upon 25-50% *in silico* JNK inhibition applied at day 0. This result was experimentally confirmed *in vitro* showing an increase in cytosolic/nuclear FoxO3a ratio of 140% (see Figure 7.3B and C). Cytosolic FoxO3a levels were increased as Akt-pS473 induced FoxO3a translocation from the nucleus to the cytoplasm and this translocation was opposed by JNK-pT183. A reduction in JNK-levels thereby released the JNK counter-effect of Akt.

We then investigated downstream of FoxO3a detecting the levels of mTOR-pS2448, which reflects the activation of mTORC1 through Akt, and Mfn2 upon the same JNK inhibition treatment. The model predicted an increase in both mTOR-pS2448 and Mfn2 levels with respect to the control after 3-5 days post irradiation (see Figure 7.3D). In addition, the simulation showed that these levels could stabilise if JNK was inhibited by more than 50%. This prediction was experimentally verified *in vitro* (see Figure 7.3E). Under JNK-inhibition treatment, mTOR-pS2448 and Mfn2 levels were significantly higher than the corresponding control levels. Moreover, these curves gradually decreased after 9-11 days, which was predicted by the model when JNK was inhibited at approximately 50%.
These predictions and *in vitro* confirmations indicated that nuclear FoxO3a acted differently depending on whether it was phosphorylated by JNK in response to oxidative stress. Mfn2 levels remained sensitive even after 9-11 days post irradiation upon JNK inhibition treatment. See Figure 7.4 for model predictions of AMPK-pT172, FoxO3a-pS253, JNK-pT183 and mitochondrial membrane potential upon JNK gradual perturbation. Interestingly, the mitochondrial membrane potential increased upon gradual inhibition of JNK, although the original levels at day 0 were not restored.

7.2.4 ROS inhibition improves mitochondrial membrane potential

As ROS is a central driver for mitochondria dysfunction we gradually perturbed the variable ROS in the model at day 0 and analysed the effects on mitochondrial membrane potential along the time course.
At 15 days post irradiation, model simulation predicted an increase in mitochondrial membrane potential up to 154% upon ROS scavenging from day 0 (see Figure 7.5A). This prediction was experimentally tested *in vitro* by measuring the TMRM/MTG ratio. The mitochondrial membrane potential increased to 149% with respect to the control. As the model predicted that an increase to 154% was obtained by reducing the total ROS amount to 50% at day 0, we could infer that the *in vitro* experimental test scavenged approximatively 50% of ROS (see Figure 7.5B and C).

In addition to these prediction-test results, we also theoretically predicted the effects on Akt-pS473, mTOR-pS2448, Mfn2 and AMPK-pT172 upon ROS gradual perturbation (see Figure 7.6). ROS inhibition was responsible for increasing mTOR-pS2448 and consequently decreasing AMPK-pT172, Akt-pS473 and Mfn2. Intriguingly, Mfn2 was again confirmed to lose sensitivity after 9-11 days post irradiation upon ROS scavenging treatment. This result highlighted the fact that, despite ROS inhibition, the levels of Mfn2 were not restored after 9-11 days, suggesting that a ROS inhibition treatment alone was not sufficient.

7.2.5 Combinatorial intervention for improving both Mfn2 and mitochondrial membrane potential

By applying a JNK gradual inhibition, we predicted and tested an increase in Mfn2 and cytoplasmic FoxO3a levels. Since FoxO3a translocation to the cytoplasm depends on Akt-pS473, the model predicted that an intervention for increasing Mfn2 levels and mitochondrial membrane potential could be a combined JNK-Akt perturbation. In fact, this intervention allowed us full control over the nuclear states of FoxO3a and therefore its downstream signals (see Figure 7.7A). Figure 7.7B shows the levels of cytoplasmic FoxO3a-pS253, Mfn2 and mitochondrial membrane potential at day 10 upon combined JNK-Akt perturbation applied at day 0. Cytoplasmic FoxO3a-pS253 levels notably increased upon gradual inhibition of JNK and gradual overexpression of Akt. As our focus was to maintain FoxO3a predominantly in the nucleus and we have showed a beneficial effect upon JNK gradual inhibition, we considered the area of JNK-Akt inhibition (see white square marked by *) as a region of study. Interestingly, the model predicted that Mfn2 levels significantly increased up to 166% by reducing the levels of JNK and Akt in combination to 60% (see arrow inside square). The mitochondrial membrane potential was also predicted to increase to 133% by applying the same combined inhibition, although it showed dependency on Akt only when the activity of this protein was reduced.
The next step was therefore to use this new information together with the previous prediction-test that ROS inhibition improved mitochondrial membrane potential (see Section 7.2.4). The idea was to use the benefits of the predicted output for

FoxO3a and Mfn2 upon combined JNK-Akt perturbation (see Figure 7.7B) as an input for a combined Mfn2-ROS perturbation (see Figure 7.7C). From Figure 7.7B, we found a way to increase Mfn2 levels by decreasing both JNK and Akt. Therefore, in a combined Mfn2-ROS perturbation we could simply consider the area of Mfn2 hyperactivation (Mfn2 >100%) (see Figure 7.7D). This area could be further reduced by two reasons:

R1. Cytoplasmic FoxO3a-pS253 levels should be at the basal level of 1 (see Figure 7.7B and D, magenta/dark blue colour for FoxO3a-pS253);

R2. ROS levels should be maintained as low as possible, since ROS inhibition increases mitochondrial membrane potential (as shown in Figure 7.5).

From Figure 7.7B, reduced levels of FoxO3a-pS253 (bottom-right) determined low levels of Mfn2 (bottom-right), since FoxO3a acted upstream of Mfn2. Therefore, the region could be safely limited along the threshold 1 of FoxO3a (see magenta/dark blue colour for FoxO3a-pS253) which interestingly corresponded to 50% of ROS levels in agreement with Figure 7.5 (see regions indicated by ** in Figure 7.7D). Accordingly with Figure 7.5 and R1, a decrease in ROS levels also determined a significative increase in mitochondrial membrane potential upon a combined Mfn2-ROS perturbation. At this point, we investigated the effect on mitochondrial membrane potential at day 10, upon combined ROS-Mfn2 perturbation applied at day 0, on the correspondent region (marked by **). In agreement, we again found a significant increase to 133% in mitochondrial membrane potential. This predictive result indicated that Mfn2 levels and mitochondrial membrane potential could significantly increase by applying a targeted triple inhibition of Akt, JNK and ROS. In contrast to the application of a combined JNK-Akt inhibition, this intervention had the additional benefit that the network was not unbalanced by oxidative stress signals, as ROS levels were maintained low. Moreover, mitochondrial activity promotes ROS production, which can in turn re-activate JNK and decrease membrane potential. Therefore, it was crucial to limit the levels of ROS in order to avoid losing the achieved benefit.
Furthermore, the simulated single perturbation of Mfn2 at day 0 along the time course was also investigated (see Figure 7.8). Interestingly, by reducing Mfn2, the mitochondrial membrane potential decreased accordingly. Therefore, since

the AMP/ATP ratio increased, activated AMPK negatively regulated mTOR-pS2448. In addition, Mfn2 inhibition produced a moderate ROS reduction, caused by a decrease in mitochondrial membrane potential.

7.2.6 Time course analysis of combined TOR-ROS perturbation

In the previous section, we outlined an intervention for increasing both Mfn2 levels and mitochondrial membrane potential by applying a triple inhibition of Akt, JNK and ROS. However, it is well known that TOR plays a crucial role in the regulation of autophagy [Kim *et al.*, 2011; Lee *et al.*, 2010a] and Akt-pS473 [Sarbassov *et al.*, 2006, 2005]. Therefore it was of interest to study the effect of a combined TOR-ROS perturbation, applied at day 0, on Mfn2 and mitochondrial membrane potential. Moreover, it may be that this new double intervention would be able to restore the mitochondrial membrane potential to its original level and avoid potentially toxic high Mfn2 levels.

Perturbation of mTORC1 alone produces serious undesired effects in the insulin/TOR signalling pathway. In fact, mTORC1 inhibition reduces mTORC1-p70-S6K-dependent negative feedback to the insulin receptor substrate (IRS) and therefore hyper-activates Akt [Harrington *et al.*, 2004; Shah *et al.*, 2004]. A cleaner approach was to perturb both the complexes simultaneously by interacting with TOR kinase directly. In the model mTORC2 was abstracted since Akt-pS473 was dependent on both insulin and mTORC1-p70-S6K-negative feedback loop, whereas mTORC2 was sensitive to insulin but not to the negative feedback loop [Dalle Pezze *et al.*, 2012a]. Nevertheless, we could still approximate a TOR kinase perturbation by adjusting a global percentage of the initial protein levels for mTORC1 and Akt at the same time. Therefore, the initial levels of the two protein variables, Akt and mTORC1, were increased or decreased together, simulating a TOR kinase inhibition or over-expression, equivalent to affecting both mTORC1 and mTORC2 in the cell (using a TOR inhibitor, such as Torin [Liu *et al.*, 2011], treatment).

In simulating a double perturbation of the main TOR kinase and ROS, we detected a non-linear qualitative change along the time course of Mfn2 (see Figure

7.9A, column 1). Two days after irradiation, Mfn2 was predominantly regulated by ROS levels, with little sensitivity to TOR inhibition. At the same time, mitochondrial membrane potential was affected almost equally by both ROS and TOR at lower levels (<100% TOR, ROS), whereas slightly more by ROS at higher levels (>100% TOR, ROS) (see Figure 7.9A, column 2). As time progressed, Mfn2 levels decreased and became more affected by TOR perturbation rather then ROS. Meanwhile, mitochondrial membrane potential maintained a combined sensitivity to TOR and ROS, although gradually reduced to low levels along the time course. At days 15-21, TOR and ROS perturbation split the Mfn2 response into two activation states. One state (S_1) was characterised by low levels of ROS (<75% at day 15), the other (S_2) by high levels of ROS (>100% at day 15). Whereas ROS divided the space of Mfn2 response, TOR shaped the boundaries of these two states. In S_2, the Mfn2 response maintained an equilibrium by increasing ROS and TOR in combination. This state space was thus concave with respect to the two parameters within the explored boundaries. In S_1, the Mfn2 response vanished by increasing TOR levels. Therefore, TOR was responsible for the S_1 convex space. Interestingly, the S_1 state gradually diminished along the time course. Hence, we simulated the Mfn2 response to TOR and ROS perturbations up to 40 days post irradiation, in order to study the evolution of S_1. As shown, at day 40 this second state is almost lost due to the extremely low levels of Mfn2. Moreover, in the extreme regions outside of these two states, Mfn2 levels were either very high (<10% of TOR) or very low (<10% of ROS) (see left or bottom of the plot). This could be explained because ROS-JNK-dependent oxidative stress response antagonises Akt-dependent translocation of FoxO3a to the cytoplasm, and therefore promotes fusion.

The prediction of these two time-dependent states indicated two modalities of intervention to increase Mfn2 levels: one by increasing ROS levels, the other one by reducing them. Since mitochondrial membrane potential was maximised at low levels of ROS, we experimentally tested the model prediction of Mfn2 and mitochondrial membrane potential upon inhibition of TOR, ROS or TOR-ROS. At day 15, the model predicted a similar Mfn2 response upon inhibition of TOR (to 10-25%) or TOR-ROS (to 10-25% and to 45-55%, respectively). This similarity was also found at day 21 (see Figure 7.9B). These predictions were experimen-

tally tested *in vitro* by inhibiting TOR (to 10-25%) or TOR-ROS (to 10-25% and to 45-55%, respectively) (see Figure 7.9C). We were not able to test the non linear response of Mfn2 upon combined perturbation of TOR and ROS at day 21, as the predicted signal differences along the sigmoid curves were too small (<20%). At day 12 the model predicted no significant response of mitochondrial membrane potential upon TOR inhibition (to 10-25%) or ROS inhibition (to 45-55%), although both these inhibitions showed a statistically significant increase in membrane potential with respect to the control. In the case of a TOR-ROS combined inhibition (to 10-25% and 45-55%, respectively), the model predicted a significant increase in membrane potential with respect to the control or to the single inhibition treatments (see Figure 7.9D). These predictions were experimentally tested *in vitro* (see Figure 7.9E), and confirmed the beneficial effect of a double inhibition and the prevailing role of ROS over TOR at low medium doses of treatment.
These results show that TOR inhibition is sufficient for increasing Mfn2 and mitochondrial membrane potential levels, but a combined TOR-ROS treatment is more effective for restoring mitochondrial membrane potential.

7.3 Discussion

In the present work, a dynamical model was employed for investigating the dynamical process of irradiation-induced cellular senescence and studying modalities of combined drug interventions in order to reduce progression of ageing in the middle and long term. We hypothesised that FoxO3a existed in the nucleus in at least two states, unphosphorylated FoxO3a and JNK-phosphorylated FoxO3a, and that these two states mediated distinct cellular processes. Nuclear unphosphorylated FoxO3a was mainly responsible for Mfn2 activation and partially for cell cycle arrest, whereas JNK-phosphorylated FoxO3a was mostly responsible for cell cycle arrest. DNA damage and oxidative stress response activated the inflammatory system through JNK and gradually shifted the FoxO3a nuclear system from the unphosphorylated state to the JNK-phosphorylated state. In addition to the initial establishment of positive feedback loops which systematically increased ROS production, DNA damage and dysfunctional mitochondria,

this state transition of FoxO3a also had the adverse effect of arresting Mfn2 and strengthening cell cycle arrest. As a consequence, this state transition had the effect of switching off these positive feedbacks maintaining the system in an unproliferative and low energy state.

Why would FoxO3a disregard Mfn2 when phosphorylated by JNK? A possible explanation is that progressive mitochondrial dysfunction would cause a drastic loss of energy in the cell. In conditions of low energy availability and high levels of damage, the cell would promote cheaper austerity forms for limiting the seriousness of the problem (DNA damage, ROS, mitochondrial dysfunction) and resources deployment (energy). It would broadly limit all expensive processes, such as cellular proliferation, cell growth (through TOR) and finally mitochondrial biogenesis. In fact, these processes are expensive and it is reasonable to think that in the presence of high levels of damage and low levels of energy, the benefit of promoting anabolic programs is little compared to its cost. In this context, JNK would be responsible for shifting FoxO3a activity towards more severe processes, such as cell cycle arrest and apoptosis, rather than investing energy in mitochondrial fusion and biogenesis. The choice of limiting mitochondrial fusion and biogenesis would have opposing effects. On one side, it would increase the total number of dysfunctional mitochondria and this would reduce energy levels further. On the other side, this energy reduction would gradually weaken the existing positive feedback loops. As consequence, the cell would enter a *pseudo* steady state, which would slowly lose intensity due to progressive lack of energy.

Despite its power, the presented model misses important components. The most important is the inflammatory system as controlled by NF-κB, TNF-α and TGF-β signalling pathways. This inflammatory response is heavily abstracted in this model by JNK through ROS regulation. The inflammatory system has important positive feedback loops that may develop independently and may therefore be responsible for permanent activation of JNK, despite ROS signalling stabilisation. Although the abstraction applied in this study is sufficient for the conclusions provided, the inclusion of an inflammatory system would give important insights about other persistent mechanisms of positive feedback loop initiation and consolidation as well as potential drug interventions.

An explicit signalling pathway governing mitochondrial biogenesis through FoxO3a,

AMPK, mitophagy was discarded since the mechanism through mitochondria fusion and biogenesis (Mfn2) had the same beneficial effect on mitochondria: the increase in total membrane potential. However, a precise analysis of the roles of these two distinguished pathways and their effect on mitochondrial mass may unravel important questions concerning the role of TOR in middle and late senescence.
In conclusion, aside from caloric restriction, multiple interventions for limiting the progression of senescence are theoretically possible and include down regulation of ROS and mTOR. Due to the high number of regulatory feedback loops, these interventions should focus on the reduction of these senescence-positive feedback loops. Conversely, it is important that these combinatorial interventions applied to reverse senescence, do not negatively affect the senescent beneficial effect of preventing cancer diseases, by inducing dysregulated cell proliferation.

7.4 Materials and methods

7.4.1 Mathematical model

The ODE-based mathematical model consisted of 30 dynamical variables covering 5 cellular modules: DNA-damage, oxidative stress, FoxO, IIS-mTOR and mitochondria. These model variables were regulated by 3 inputs: insulin, amino acids and irradiation. 13 observables were used to link the model to experimental data. The initial amount of each dynamical variable in inactive state was fixed to the maximum measured intensity of the associated experimental signal plus two times the standard deviation at that time point. For dynamical variables in active state related to DNA-damage or oxidative stress responses, the initial amounts were fixed to 0. For all the other variables in active state, the initial amount was fixed to 1, approximating the basal level of the proteins upon insulin and amino acid stimuli. The dynamical variables were connected by 39 reactions expressed as mass action kinetics. 37 kinetic rate constant parameters were estimated using Potterswheel Matlab Toolbox [Maiwald and Timmer, 2008] by executing 4 rounds of parameter estimation and identifiability as shown in Table 7.1. Parameters were calibrated using trust region algorithm (MaxIter: 250;

TolFun: 1e-07; TolX: 1e-07) and cvodes integration algorithm (AbsTol: 1e-08; RelTol: 1e-06; MaxNumSteps: 1500). For each round, a sequence of 1000 fits was computed by setting the highest possible strength of disturbance (Value: 1) over the parameters initial value in order to extensively explore the parameter space. Parameters were fitted among the interval [1e-08, 1e+05]. Nonlinear MOTA identifiability analysis, as implemented in PottersWheel [Hengl *et al.*, 2007; Maiwald and Timmer, 2008], identified tuples of related parameters as well as the sets of parameters which could be identified at each calibration round. A threshold of 35% was applied for selecting the best fits before computing linear and nonlinear MOTA analysis. Model simulation and perturbation were performed using Copasi [Hoops *et al.*, 2006]. The complete tables of model parameters comprising the details of parameter estimation rounds, model ODEs and sequence fit selection are reported in Tables 7.1-7.4 and Figure 7.10. Identifiability analysis, as performed for each parameter estimation round, is provided in Figures 7.11-7.15. Deterministic simulations used LSODA algorithm (RelTol: 1e-06; AbsTol: 1e-12; MaxIntSteps: 1e+04). Stochastic simulations used Direct method (MaxIntSteps: 1e+06; UseRandomSeed: 0; RandomSeed: 1). Simulated stochastic simulation performed up to 50 days post irradiation indicated model steady state after 20-25 days for all the measured readouts (see Figure 7.16). Model 2D sensitivity analysis for model observables was computed at days 1, 10 and 20 by perturbing the kinetic rate constant values (see Figure 7.17). Double perturbations data were computed using Copasi by varying each of the two parameters from 0% to 300% by step 0.25%. Double perturbation plots were achieved using Matlab. Plots related to parameter estimation and identifiability analysis were generated by Potterswheel. Model structure was graphically represented using CellDesigner [Funahashi *et al.*, 2008, 2003] and exported to SBML [Hucka *et al.*, 2003] Level 2 Version 4 using Potterswheel. The statistical and programming language R v. 2.14.1 [R Development Core Team, 2010] was selected for the graphic representation of the identifiability matrix computed with MOTA and single perturbation plots.

7.4.2 Statistics

The programming language R was used for computing time course mean and standard deviation of 5 independent *in vitro* time-course measurements. Mean and standard deviation values were then used for calibrating the model observables. The goodness-of-fit statistical measures χ^2 [Maiwald and Timmer, 2008], AIC, AICc [Akaike, 1973] and BIC [Schwarz, 1978] were used to assess the quality of fit of the model at each calibration round. All these measures were directly computed using PottersWheel Toolbox.

7.5 Figures and tables

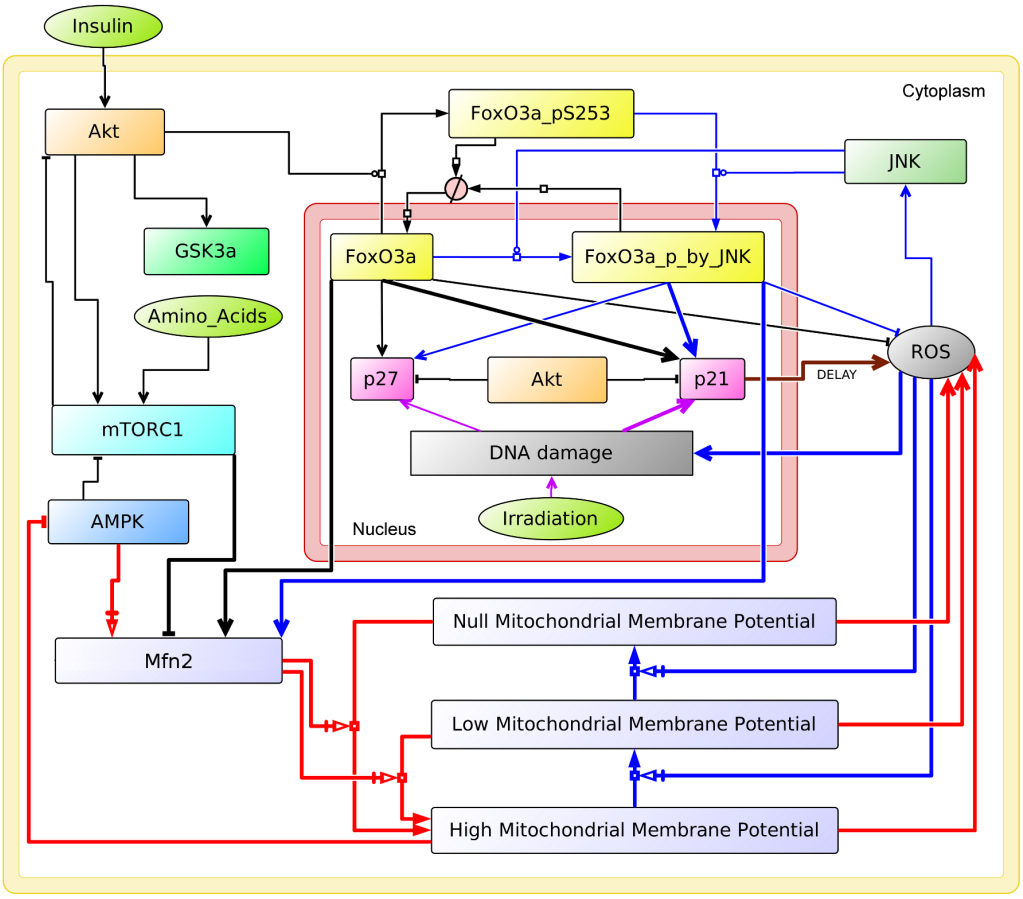

Figure 7.1: A dynamical model for irradiation-induced cellular senescence. Graphical model integrating the insulin-TOR (IIS-TOR) signalling pathway (left, black reactions), the oxidative stress response (right, blue reactions), FoxO3a regulation (top), nuclear DNA damage (centre, magenta reaction) and mitochondrial phenotype (bottom, red reactions).

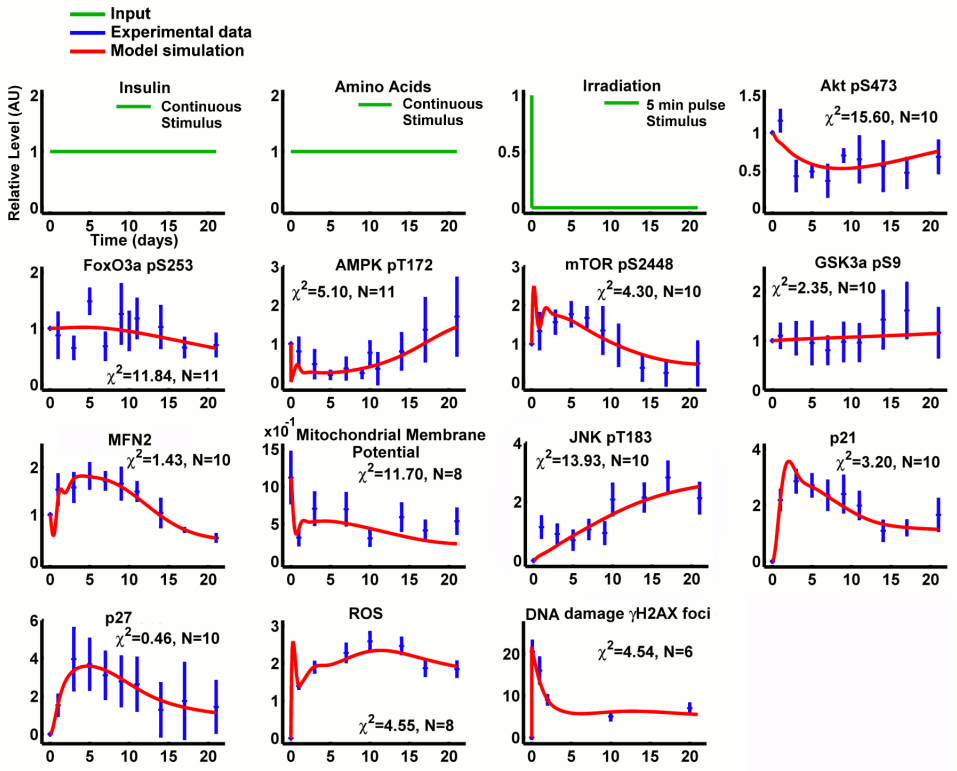

Figure 7.2: *In silico* versus *in vitro* time courses. The model (red lines) was calibrated over experimental time course data (see blue points) collected for 13 readouts in the network up to 21 days. The inputs are amino acids/insulin (constant inputs) and irradiation (pulse input of 5 min which simulates 20 Gy X ray irradiation over 5 min). Experimental time points (blue points) are mean +/- 1 standard deviation collected from 5 repetitions. *In vitro* experiments were performed by Dr Glyn Nelson, Newcastle University, UK.

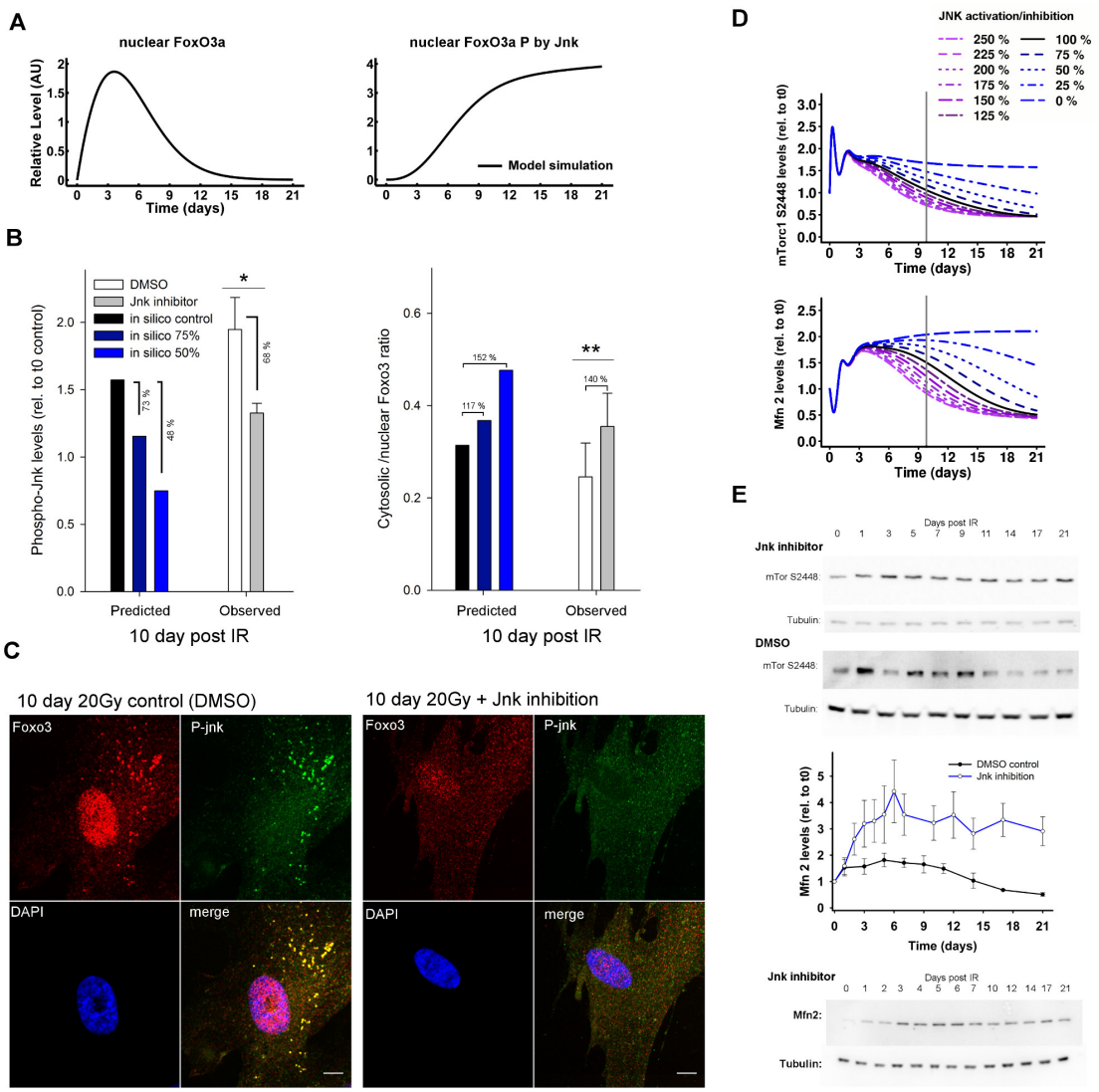

Figure 7.3: JNK inhibition promotes cytoplasmic FoxO3a migration and Mfn2. (A) *In silico* time-courses for nuclear unphosphorylated FoxO3a and JNK-phosphorylated FoxO3a showing a shift towards active FoxO3a being predominantly phosphorylated by JNK over time after stress induced premature senescence. (B) At 10 days post irradiation, the model quantitatively predicted a decrease in total phosphorylated JNK and an increase in cytosolic fraction of FoxO3a upon JNK inhibition (black and blue histograms). These predictions were confirmed *in vitro*. MRC5 cells were irradiated to cause stress-induced senescence then incubated with a JNK inhibitor (1μM SP600125). 10 days post irradiation, cells were stained for phosphorylated JNK (T183/Y185) and total FoxO3a. Quantification of fluorescence intensities indicated a significant decrease in total phosphorylated JNK (Mann-Whitney test, * P = 0.014) and a significant increase in cytosolic fraction of FoxO3a (t-test, ** P = 0.010) (white and grey histograms). (C) Example fluorescence images for the previous quantification. (D) Downstream of FoxO3a, the model predicted increases in mTORC1-pS2448 phosphorylation and mitofusin2 upregulation in a JNK-dependent manner. (E) Western blotting data confirmed the changes in mTORC1-pS2448 and mitofusin2 levels following MRC5 cells up to 21 days post irradiation in the presence of JNK inhibitor. See Figure 7.4 for other readouts upon *in silico* JNK perturbation. *In vitro* experiments (Panels B:Observed, C and E) were performed by Dr Glyn Nelson, Newcastle University, UK.

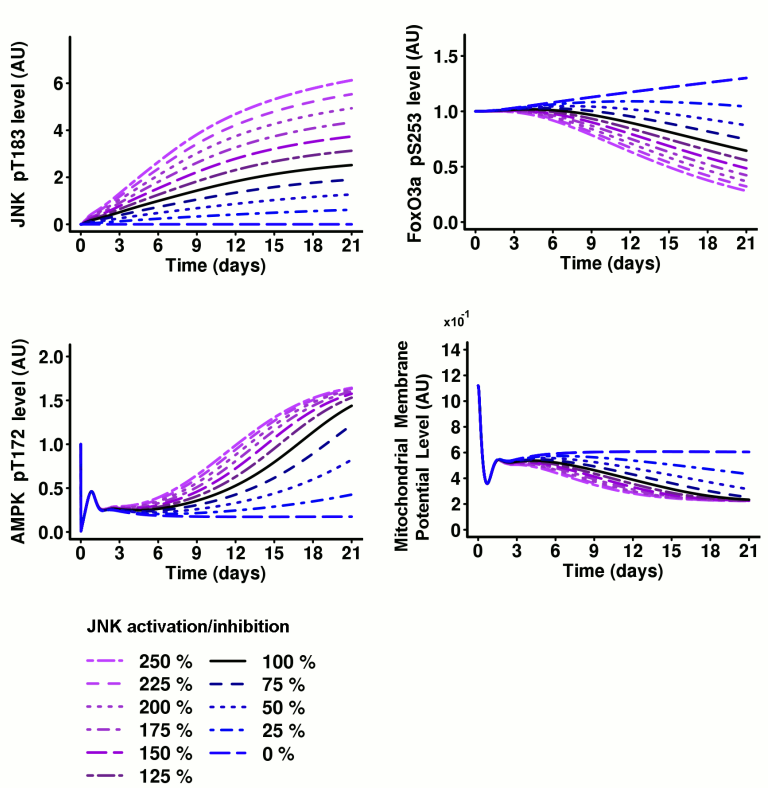

Figure 7.4: Other simulated readouts for JNK single perturbation. After 6-9 days post irradiation, the levels of AMPK dramatically decreased in a JNK inhibition treatment. Conversely, the mitochondrial membrane potential increased although its level did not recover to levels achieved before day 3.

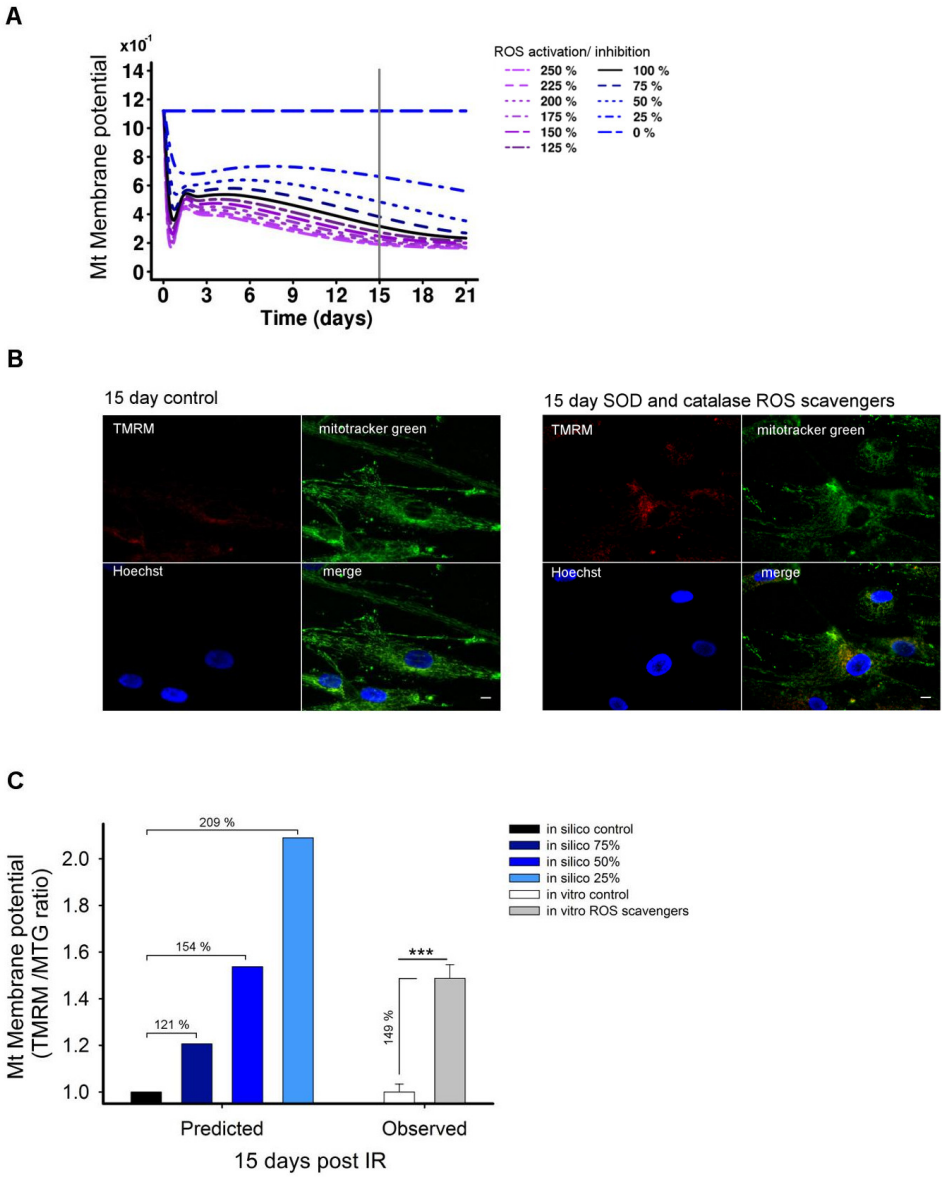

Figure 7.5: ROS inhibition improves mitochondrial membrane potential. (A) At 15 days post irradiation, the model quantitatively predicted an increase in mitochondrial (mt) membrane potential upon ROS inhibition (black and blue histograms). (B) Example images of control cells (upper panel) and cells treated with SOD and catalase (100U each) in the medium (lower panel) for 15 days post IR are shown. (C) The model prediction was confirmed by quantification of the fluorescence intensities. Exogenous addition of SOD and catalase significantly increased the average membrane potential (Mann-Whitney test, *** $P < 0.001$) *in vitro*. *In silico* inhibition of ROS levels also partially reactivated mt membrane potential in a dose dependent manner, with between 75 and 50% levels giving equivalent restoration of membrane potential to the *in vitro* data. *In vitro* mt membrane potential was determined in MRC5 cells 15 days post IR using live cell imaging of cells loaded with the mt membrane potential dependent dye TMRM, non-potential dependent mitotracker green and nuclear counterstain Hoechst 33342. Scale bar is 10 μm. See Figure 7.6 for other readouts upon *in silico* ROS perturbation. *In vitro* experiments (Panels B, C:Observed) were performed by Dr Glyn Nelson, Newcastle University, UK.

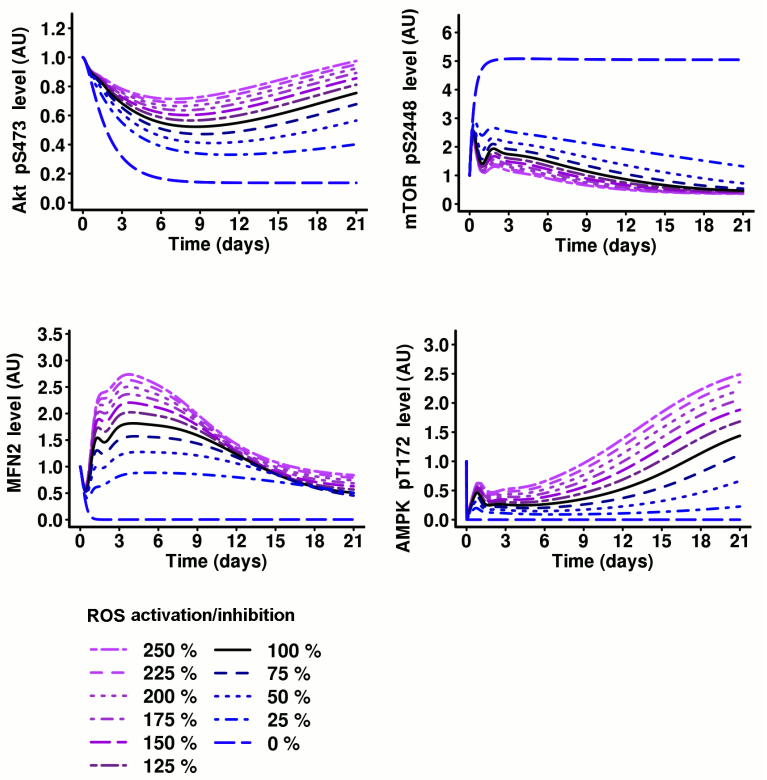

Figure 7.6: Other simulated readouts for ROS single perturbation. Upon ROS perturbation, the insulin/TOR pathway was severely affected. In details, mTOR-pS2448 levels were increased, whereas AMPK-pT172 were decreased. The reduction in mTOR-pS2448 led to an intensified mTORC1-p70-S6K-dependent negative feedback loop, reducing Akt-pS473 levels. Contrary to mTOR and AMPK dynamics, the levels of Mfn2 decreased. In addition, the system strongly lost sensitivity after day 9-11 post irradiation. This prediction meant that a ROS inhibition treatment alone is not expected to reverse senescence, especially after 9-11 days post irradiation.

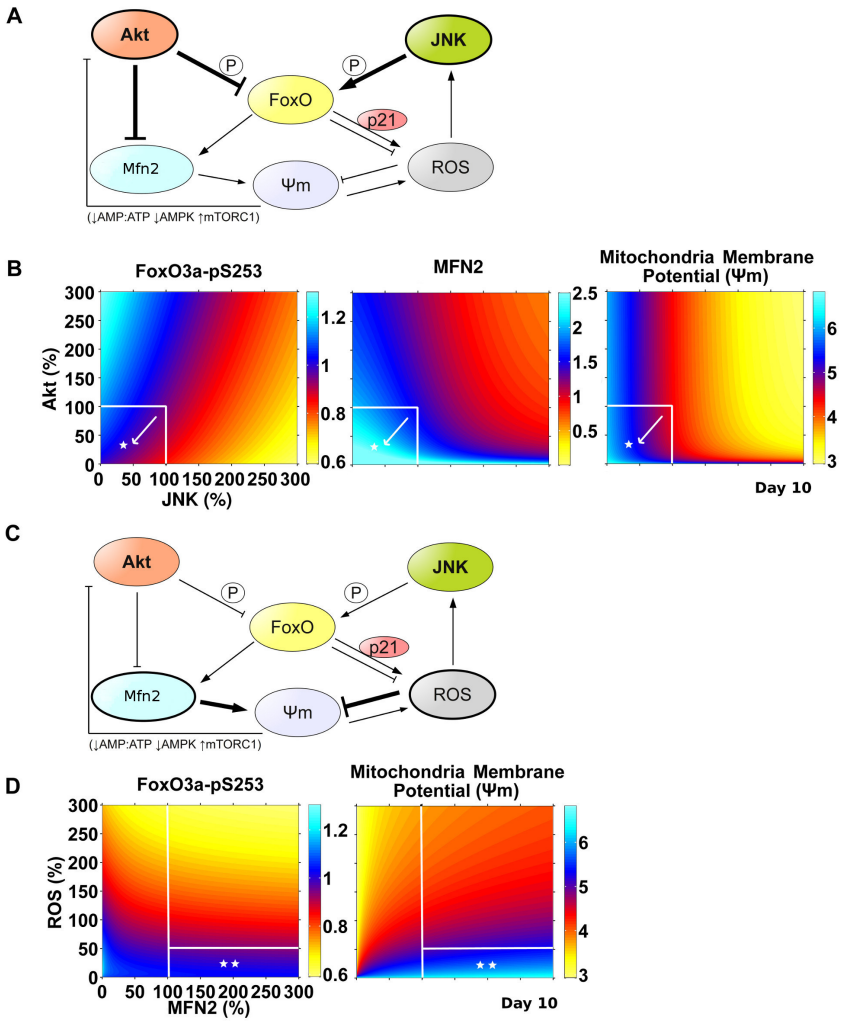

Figure 7.7: Predicted outcomes for double perturbations of JNK-Akt and Mfn2-ROS. (A) Schematic model illustrating the application of a combined JNK-Akt perturbation. (B) Simulation of combined JNK-Akt perturbation applied at day 0. To limit cytoplasmic FoxO3a-pS253 and to maintain JNK inhibition positive effects, intervention on cytoplasmic FoxO3a-pS253 was applied only on the *inhibition region* (white square, *). Accordingly with this, Mfn2 levels and mitochondrial (mt) membrane potential increased at day 10 post irradiation. (C) Schematic model illustrating the application of a combined Mfn2-ROS perturbation. (D) Simulation of combined Mfn2-ROS perturbation applied at day 0. Using the prediction obtained in B, the double perturbation region could be largely limited to the area in the bottom (white square, **), characterised by high Mfn2 and low ROS levels. Consistently, in this area the mt membrane potential was maximised at day 10 post irradiation. From a mathematical point of view, a double perturbation represents a function in two variables and in this case the generated surface is seen from the top.

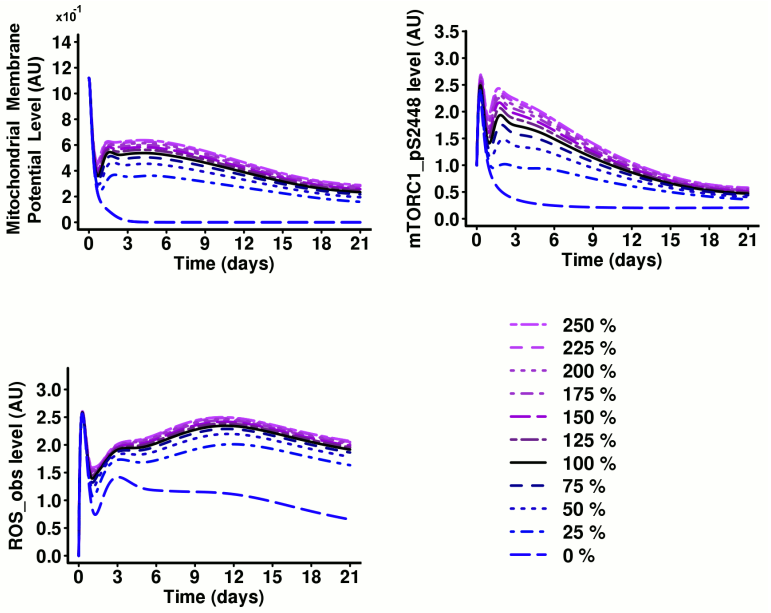

Figure 7.8: Exploration of Mfn2 simulated single perturbation. Upon a gradual inhibition of Mfn2 (blue lines), the model predicted a decrease in mitochondrial membrane potential and ROS levels. Black line indicates no perturbation of Mfn2, blue lines indicate inhibition, magenta lines indicate over-expression.

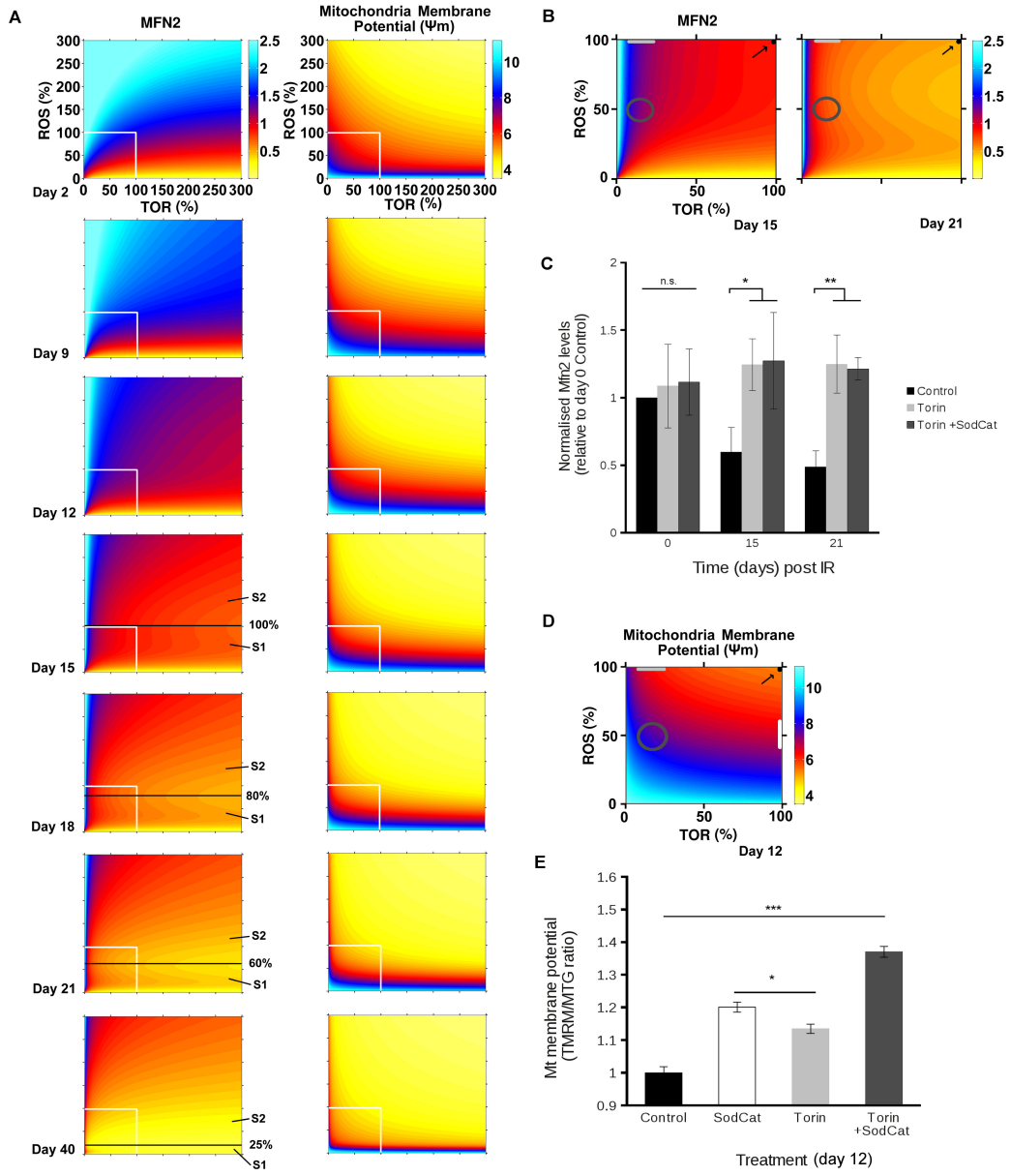

Figure 7.9: Time course analysis of combined TOR-ROS perturbation. (A) *In silico* Mfn2 and mitochondrial (mt) membrane potential time course responses upon combined TOR-ROS perturbation (0-300% TOR or ROS level). At days 15-21, TOR and ROS perturbation split the Mfn2 response into two activation states (see S_1, S_2 divided by black line). Later, S_1 almost disappeared. (B) *In silico* Mfn2 response upon combined TOR-ROS inhibition (0-100% TOR or ROS level) at days 15 or 21. The black point (100% TOR, 100% ROS) is the control, light grey line is TOR inhibition, and dark grey circle is combined TOR-ROS inhibition. (C) *In vitro* Mfn2 response upon inhibition of TOR or combined TOR-ROS at days 0, 15 or 21. Cells were treated with 20 nM Torin1 (TOR inhibitor), or Torin1 with SOD and catalase (100U each) (ANOVA with Tukey's post-hoc test, * P = 0.04, ** = 0.002, n.s. = non significant). (D) *In silico* mt membrane potential response upon combined TOR-ROS inhibition (from 0 to 100% TOR or ROS level) at day 12. The white line is ROS inhibition. (E) *In vitro* mt membrane potential response upon inhibition of TOR, ROS or combined TOR-ROS at day 12 (ANOVA with Tukey's post-hoc test, * P = 0.028, *** P < 0.001). *In vitro* experiments (Panels C, E) were performed by Dr Glyn Nelson, Newcastle University, UK.

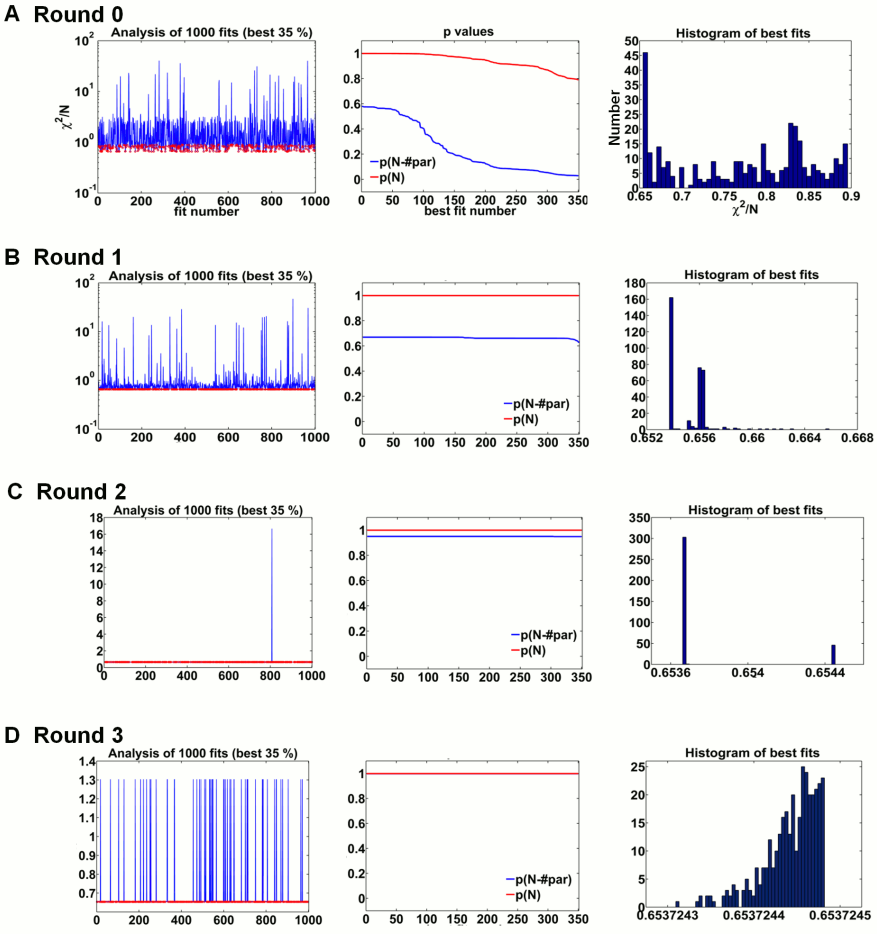

Figure 7.10: Sequence fits selection for parameter estimation round. For each calibration round, a sequence of 1000 fits was computed (see Table 7.1). The best 350 fits of the sequence were selected and statistics regarding their p-values and normalised χ^2 distribution were reported. Despite the high noise applied to the initial value of the parameters before estimation, the selected best fits clustered in each round in terms ofχ^2, particularly after Round 0. This suggested that the reported final χ^2 of the model (see Table 7.3) represented a point of convergence for many solutions. N=number of experimentally measured data point, $\#par$=number of estimated parameters, $p()$ = p-value function.

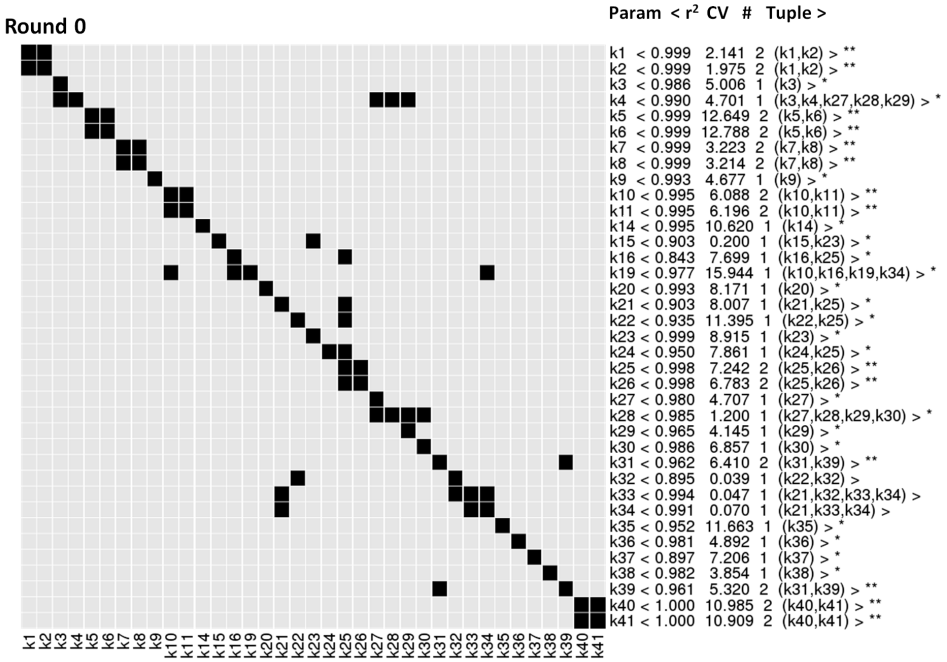

Figure 7.11: MOTA non-identifiability analysis for Round 0 of parameter estimation. MOTA non-identifiability analysis reported multiple tuples of statistically significant parameter correlations. However, the parameters k32, k33, k34 governing the DNA-damage module could be fixed since no statistically significant correlation was found and their confidence intervals could be measured. The analysis was performed on the best 35% fits of the calibration sequence without excluding any outlier. r^2=correlation, CV=coefficient of variance, #=number of times this correlation was found. (*) $r^2 > 0.8$ & $CV > 0.1$ (**) $r^2 > 0.8$ & $CV > 0.1$ & #> 1.

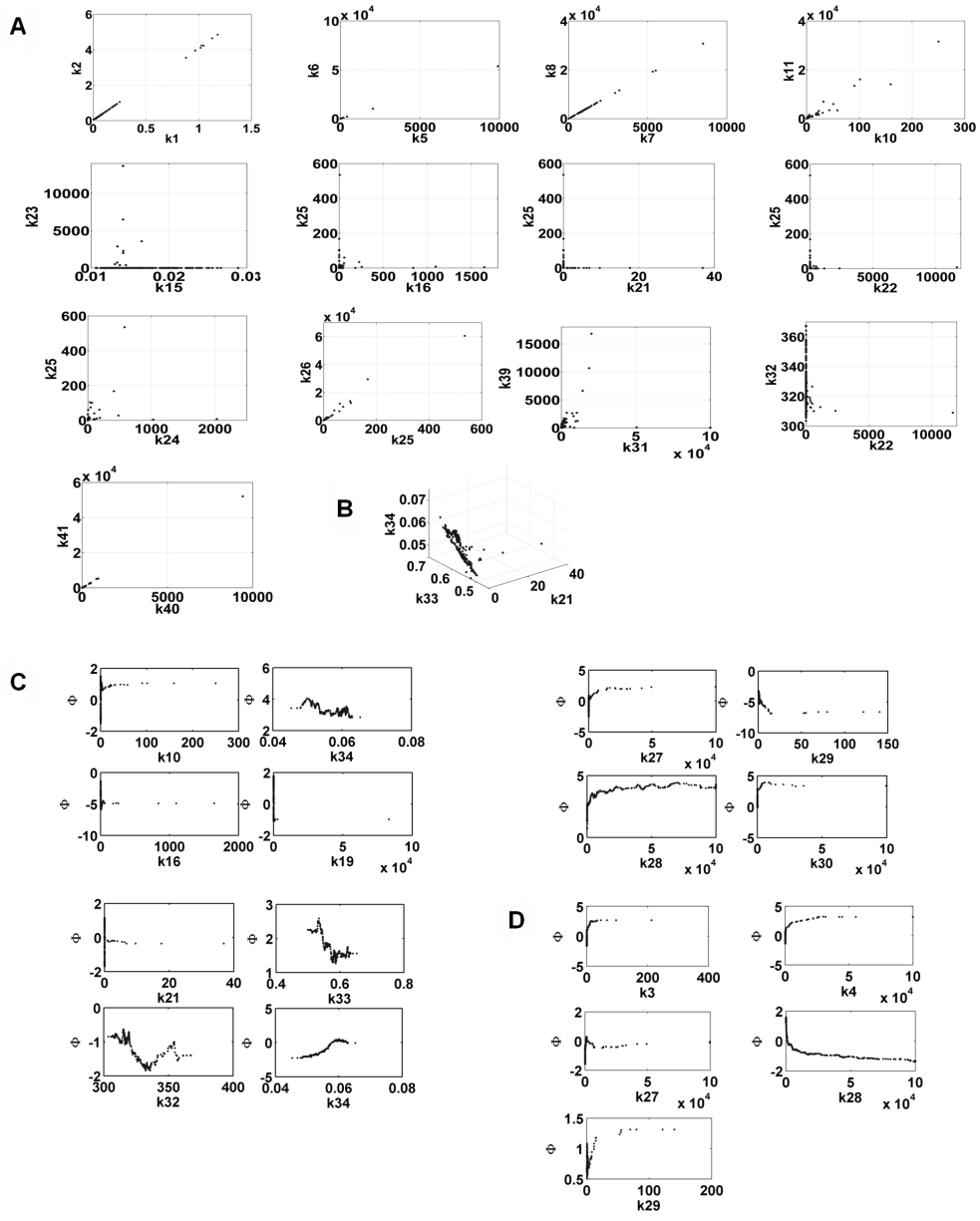

Figure 7.12: Plots of tuples of related parameters for Round 0. Doublets (A), triplets (B), quadruplets (C) and quintuplets (D) of related parameters as computed by MOTA non-identifiability analysis (see Figure 7.11) are shown. The analysis was performed over the best 35% of the fit sequence.

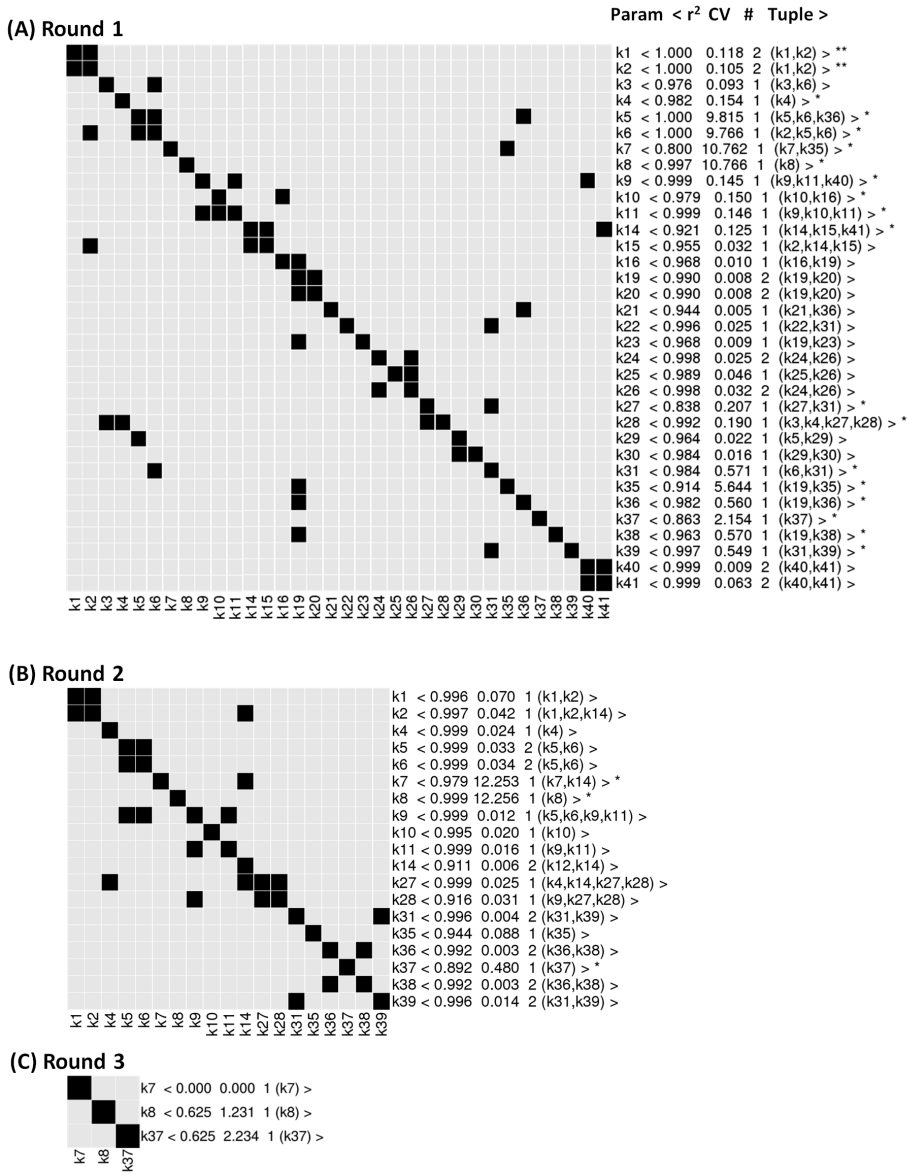

Figure 7.13: MOTA non-identifiability analysis for Round 1,2 and 3 of parameter estimation. (A) In Round 1, most of the parameters did not show statistically significant correlations and could therefore be fixed. (B) Round 2 only reported 3 parameters as non-identifiable which were finally determined in Round 3 (C). For each round, the analysis was performed on the best 35% fits of the calibration sequence without excluding any outlier. r^2=correlation, CV=coefficient of variance, #=number of times this correlation was found. (*) $r^2 > 0.8$ & $CV > 0.1$ (**) $r^2 > 0.8$ & $CV > 0.1$ & #> 1.

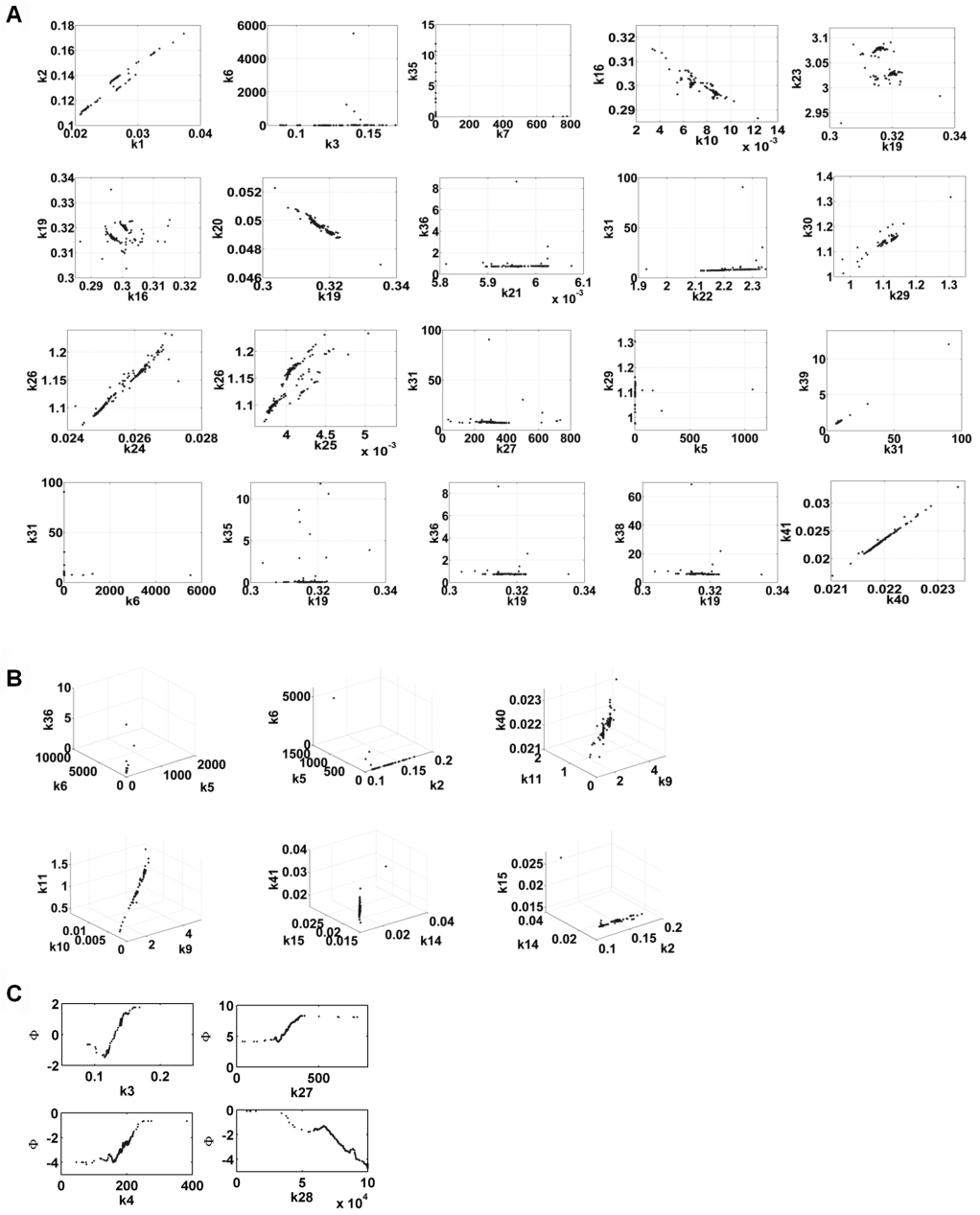

Figure 7.14: Plots of tuples of related parameters for Round 1. Doublets (A), triplets (B) and quadruplets (C) of related parameters as computed by MOTA non-identifiability analysis (see Figure 7.13) are shown. The analysis was performed over the best 35% of the fit sequence.

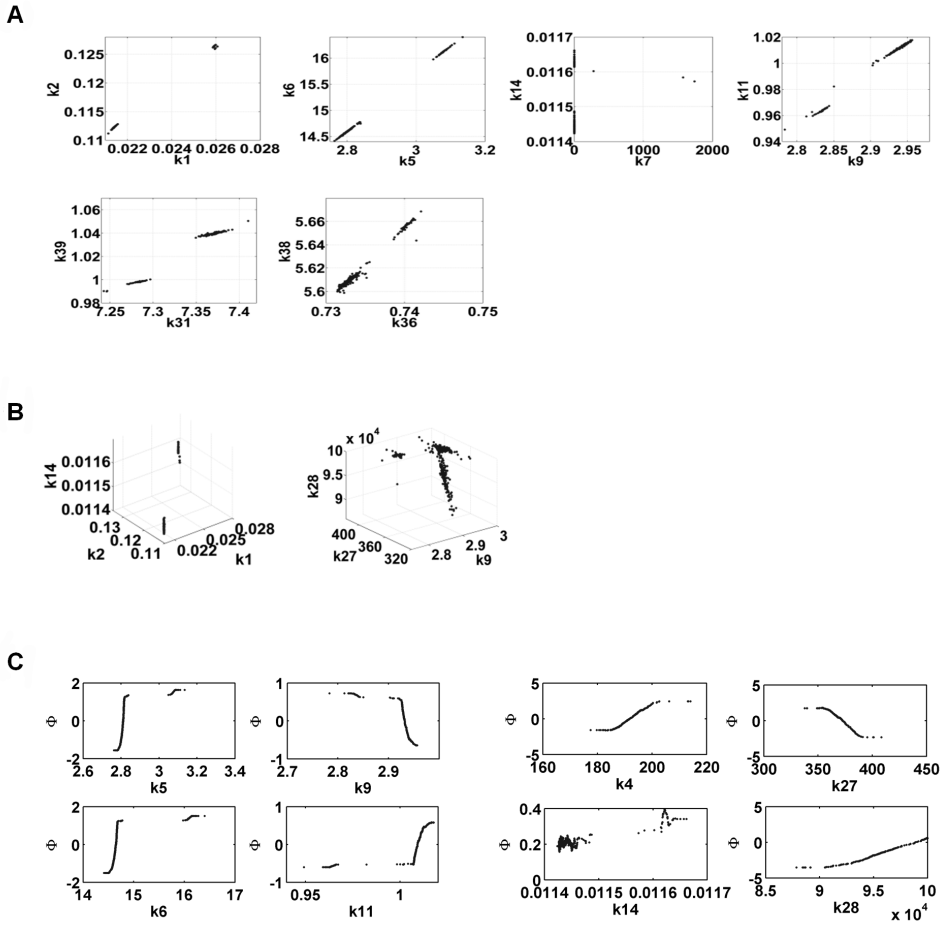

Figure 7.15: Plots of tuples of related parameters for Round 2. Doublets (A), triplets (B) and quadruplets (C) of related parameters as computed by MOTA non-identifiability analysis (see Figure 7.13) are shown. The analysis was performed over the best 35% of the fit sequence.

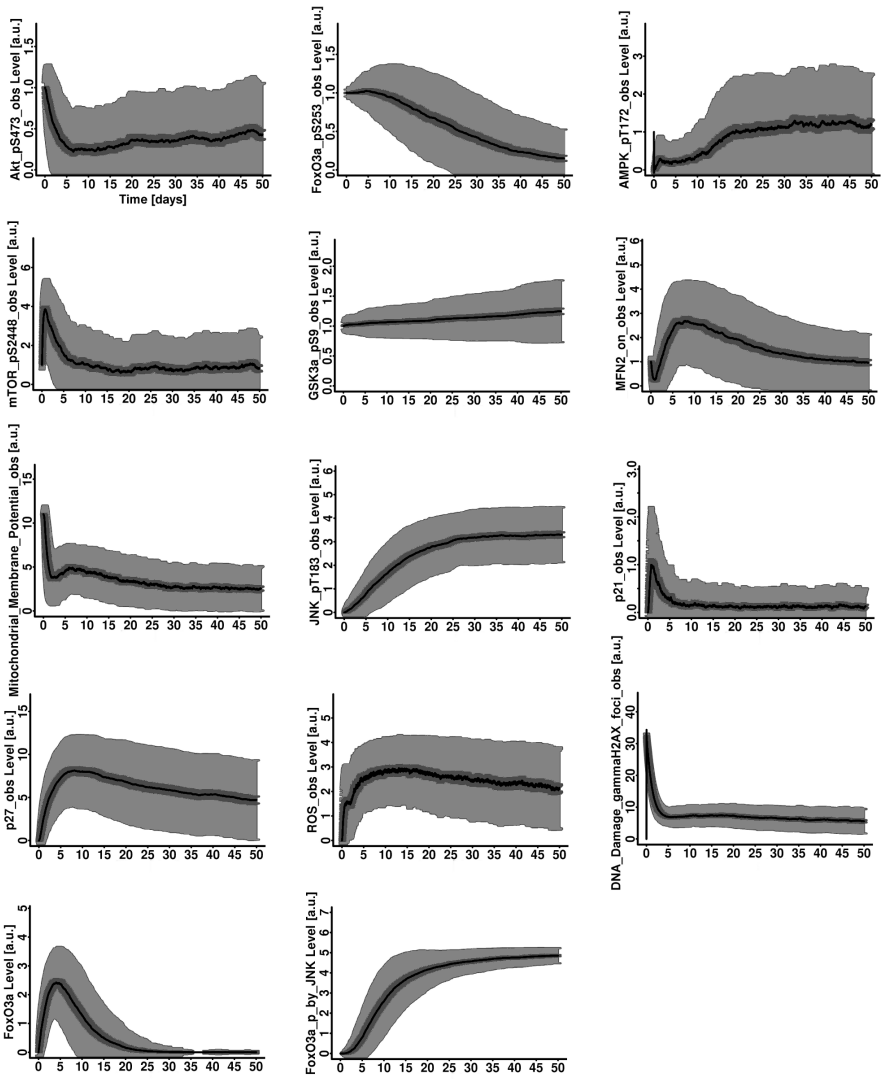

Figure 7.16: Stochastic simulation of the model. Model stochastic simulations up to 50 days graphically showed steady-state already after 20 days for all the species. Due to high ROS levels, the oxidative stress response forces almost all nuclear FoxO3a to be phosphorylated by JNK. For a formal analysis indicating that the system is asymptotically Lyapunov stable see Table 7.5. Number of stochastic runs: 500; black line indicates the means, dark grey area indicates 95% confidence interval of the mean and grey area indicates a standard deviation.

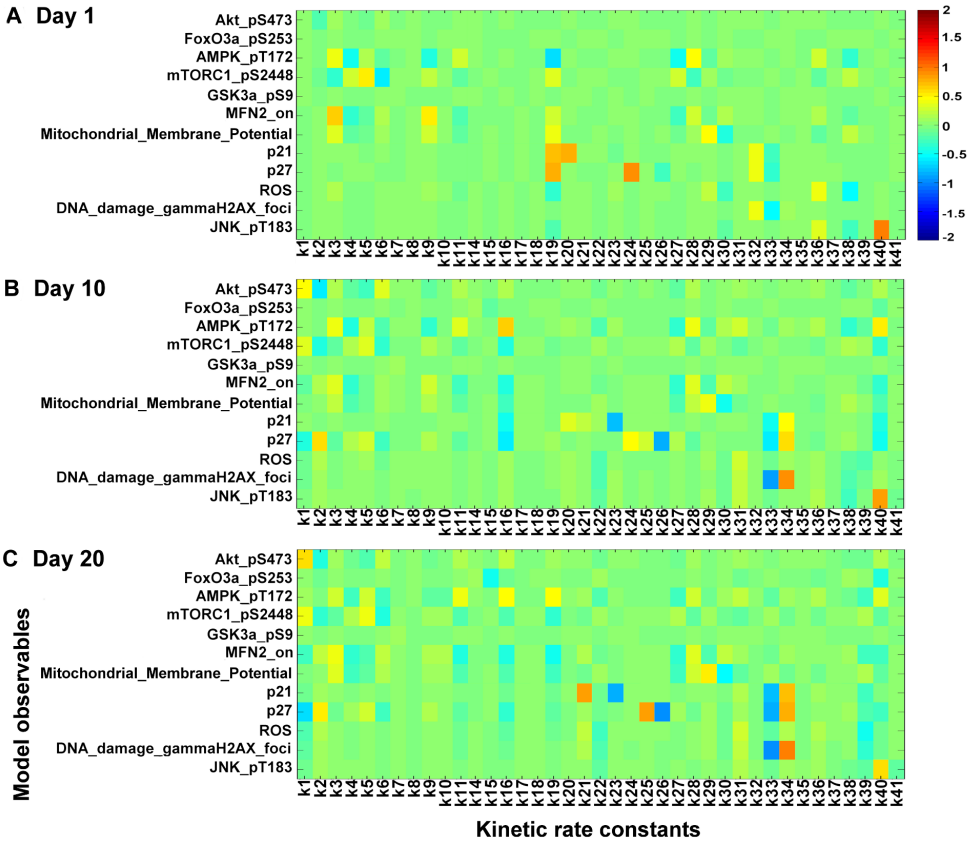

Figure 7.17: Model sensitivity analysis. Sensitivity analysis was calculated in order to measure the contribution of the kinetic rate constant parameters over the model observable variables. The analysis was performed at day 1 (representing normal cells population, panel A), day 10 (mixed cells population, panel B) and day 20 (senescent cells population, panel C) post irradiation. From day 1 to day 20, Mfn2 showed a decrease in sensitivity by AMPK (k3) and by nuclear FoxO3a when unphosphorylated by JNK (k9). Interestingly, the system presented an increase in the sensitivity of the parameters controlling DNA damage: DNA repair (k33) and DNA damage generated by ROS (k34).

Parameter Name	Parameter Estimation (mean, sd, %)				Value
(Kinetic rate constants [min-1])	Round 0	Round 1	Round 2	Round 3	
k1=Akt_S473_phosphorylation_by_Insulin	0.0706846 ± 0.151366 (214%)	0.0243519 ± 0.00287726 (012%)	0.0219927 ± 0.00153022 (007%)	Fixed	0.0214257568018194
k2=Akt_pS473_dephosphorylation	0.310935 ± 0.614252 (198%)	0.126151 ± 0.0132981 (011%)	0.114126 ± 0.00477327 (004%)	Fixed	0.112353926606627
k3=AMPK_T172_phosphorylation	2.7833 ± 13.9327 (501%)	0.131108 ± 0.0122031 (009%)	Fixed		0.139038960114649
k4=AMPK_pT172_dephosphorylation_by_energy	1719.1 ± 8081.49 (470%)	188.131 ± 28.9582 (015%)	191.777 ± 4.51107 (002%)	Fixed	194.932205773003
k5=mTORC1_S2448_phosphorylation_by_Amino_Acids_n_Akt_pS473	42.7583 ± 540.833 (1265%)	6.04164 ± 59.2985 (981%)	2.842 ± 0.0933013 (003%)	Fixed	2.80875839792972
k6=mTORC1_pS2448_dephosphorylation_by_AMPK_pT172	228.675 ± 2924.41 (1279%)	31.2221 ± 304.912 (977%)	14.8221 ± 0.51022 (003%)	Fixed	14.6379091660967
k7=GSK_S9_phosphorylation_by_Akt_pS473	228.283 ± 735.758 (322%)	6.38535 ± 68.7209 (1076%)	10.283 ± 125.998 (1225%)	0.00200684 ± 3.10797e-07 (000%)	0.00200693559649367
k8=GSK_pS9_dephosphorylation	827.9 ± 2661.06 (321%)	22.892 ± 246.454 (1077%)	36.8411 ± 451.51 (1226%)	4.34277e-07 ± 8.958e-09 (002%)	4.3357369e-07
k9=Mfn2_activation_by_FoxO3a_n_AMPK_pT172	2786.27 ± 13030.4 (468%)	3.22859 ± 0.46939 (015%)	2.92061 ± 0.0354739 (001%)	Fixed	2.93174973222514
k10=Mfn2_activation_by_FoxO3a_p_by_JNK_n_AMPK_pT172	3.00135 ± 18.2723 (609%)	0.0075885 ± 0.00113692 (015%)	0.00685054 ± 0.000139537 (002%)	Fixed	0.00680021025541758
k11=Mfn2_inactivation	361.195 ± 2237.84 (620%)	1.10891 ± 0.161425 (015%)	1.00367 ± 0.0159789 (002%)	Fixed	1.0088759629552
k14=FoxO3a_phosphorylation_by_Akt_pS473	0.266138 ± 2.82646 (1062%)	0.0115685 ± 0.00145043 (013%)	0.011464 ± 6.37531e-05 (001%)	Fixed	0.011148274977635
k15=FoxO3a_pS253_phosphorylation_by_JNK_pT183	0.0159929O.00319293 (020%)	0.0162993 ± 0.000527336 (003%)	Fixed		0.016286447022462 6
k16=FoxO3a_phosphorylation_by_JNK_pT183	15.0931 ± 116.206 (770%)	0.299398 ± 0.0028877 (001%)	Fixed		0.300624613882626
k17=FoxO3a_pS253_degradation	Assumed				0.001
k18=FoxO3a_p_by_JNK_degradation	Assumed				0.0001
k19=FoxO3a_production	279.049 ± 4449.11 (1594%)	0.3178 ± 0.00269075. (001%)	Fixed		0.320183348516727
k20=p21_transcription_by_FoxO3a_n_DNA_damage	84.2892 ± 688.732 (817%)	0.049492 ± 0.000415748 (001%)	Fixed		0.0490481816378451
k21=p21_transcription_by_FoxO3a_p_by_JNK_n_DNA_damage	0.291043 ± 2.33035 (801%)	0.0059783 ± 3.18243e-05 (001%)	Fixed		0.00595206006267852
k22=p21_inactivation_by_Akt_pS473	56.2809 ± 641.31 (1139%)	2.22555 ± 0.0566483 (003%)	Fixed		2.1965071473852 7
k23=p21_signalling	96.3023 ± 858.567 (892%)	3.04999 ± 0.0269036 (001%)	Fixed		3.0286182083837 33
k24=p27_transcription_by_FoxO3a_n_DNA_damage	16.5967 ± 130.468 (786%)	0.0256177 ± 0.000636943 (002%)	Fixed		0.0249679745527688
k25=p27_transcription_by_FoxO3a_p_by_JNK_n_DNA_damage	4.36722 ± 31.6274 (724%)	0.00397965 ± 0.000184811 (005%)	Fixed		0.00378713760555188
k26=p27_inactivation_by_Akt_pS473	568.033 ± 3852.91 (678%)	1.13377 ± 0.0361398 (003%)	Fixed		1.0952906691818 1
k27=mito_membr_pot_inc_1	2734.45 ± 12870.6 (471%)	325.989 ± 67.5019 (021%)	369.266 ± 9.33158 (003%)	Fixed	372.096047716
k28=mitochondrial_damage_by_ROS	31221.8 ± 37473.8 (120%)	89050.9 ± 16909.8 (019%)	97591.9 ± 3012.42 (003%)	Fixed	99983.7023611
k29=mito_membr_pot_inc_2	2.98161 ± 12.3597 (415%)	1.11584 ± 0.0250428 (002%)	Fixed		1.1357785426467 9
k30=mitochondrial_dysfunction_by_ROS	1419.5 ± 9733.06 (686%)	1.14411 ± 0.0183814 (002%)	Fixed		1.1524017456074 1
k31=ROS_production_through_p21	1282.31 ± 8219.34 (641%)	8.12313 ± 4.63993 (057%)	7.36144 ± 0.0320734 (000%)	Fixed	7.3732417989777 2
k32=DNA_damage_gammaH2AX_foci_by_irradiation	324.31 ± 12.7609 (004%)	Fixed			320.021834847805
k33=DNA_repair	0.575103 ± 0.0272533 (005%)	Fixed			0.584840135226026
k34=DNA_damage_gammaH2AX_foci_by_ROS	0.0571337 ± 0.00400375 (007%)	Fixed			0.0600583983831034
k35=ROS_production_by_functional_mitochondria	62.3283 ± 726.94 (1166%)	0.198835 ± 1.12228 (564%)	0.0348205 ± 0.00305172 (009%)	Fixed	0.0345601711770541
k36=ROS_production_by_damaged_mitochondria	3089.56 ± 15114.4 (489%)	0.777583 ± 0.435307 (056%)	0.73389 ± 0.00249538 (000%)	Fixed	0.7326226819882 2
k37=ROS_production_by_dysfunctional_mitochondria	0.898906 ± 6.47761 (721%)	1.31606e-08 ± 2.83435e-08 (215%)	1.10746e-08 ± 5.33135e-09 (048%)	1.01119e-08 ± 3.291426-10 (003%)	1.0048214e-08
k38=ROS_detoxification_by_FoxO3a	306.973 ± 1182.98 (385%)	6.12362 ± 3.49316 (057%)	5.6151 ± 0.0159174 (000%)	Fixed	5.6072589102902 2
k39=ROS_detoxification_by_FoxO3a_p_by_JNK	218.604 ± 1162.97 (532%)	1.10968 ± 0.60927 (055%)	1.03454 ± 0.0144041 (001%)	Fixed	1.0398332856003 26
k40=JNK_activation_by_ROS	46.4068 ± 509.761 (1098%)	0.0218862 ± 0.000203978 (001%)	Fixed		0.021733826467869 1
k41=JNK_pT183_dephosphorylation	258.738 ± 2822.46 (1091%)	0.0227313 ± 0.00142179 (006%)	Fixed		0.021645384800587 4

Table 7.1: Table of the kinetic rate constants. Kinetic rate constants values and confidence intervals were estimated in 4 calibration rounds. For each round a sequence of 1000 fits was generated by perturbing the parameters initial values with noise of 10^{d*eps}, where $d = 1$ and *eps* randomly chosen from a normal distribution $N(0, 1)$. The best 350 fits of the sequence were selected and MOTA non-identifiability analysis was employed for determining tuples of related parameters requiring further calibration. At each round, the identified parameters were fixed and their mean, standard deviation and confidence interval were reported.

Parameter Name	Approach	Value
(Concentrations [a.u.])		
u1=Insulin (Constant Input)	Fixed	1
u2=Amino_Acids (Constant Input)	Fixed	1
u3=Irradiation (5 min Input at time t=0)	Fixed	1
x1=Akt	Determined	2.746870097
x3=AMPK	Determined	5.700697393
x5=mTORC1	Determined	4.1296271683
x7=GSK3a	Determined	5.610420833
x9=MFN2_off	Determined	3.1116360576
x16=FoxO3a_source	Determined	3.564162683
x18=p21_source	Determined	6.8561152128
x21=p27_source	Determined	11.8581655987
x22=Functional_Mitochondria	Determined	11.2
x26=JNK	Determined	4.9131339599
x28=ROS_source	Determined	3.5132958599
x30=DNA_damage_gammaH2AX_foci_source	Determined	32.5
x2=Akt_pS473; x4=AMPK_pT172; x6=mTORC1_pS2448; x8=GSK3a_pS9; x10=MFN2_on; x13=FoxO3a_pS253	Determined	1
x14=FoxO3a; x15=FoxO3a_p_by_JNK; x17=p21; x19=p21_active; x20=p27; x23=Damaged_Mitochondria; x24=Dysfunctional_Mitochondria; x25=JNK_pT183; x27=ROS; x29=DNA_damage_gammaH2AX_foci; x31=Delay01_p21; x32=Delay02_p21; x33=Delay03_p21; x34=Delay04_p21	Fixed	0
(Scaling factors)		
s1=scale_Akt_pS473_obs; s2=scale_AMPK_pT172_obs; s3=scale_mTOR_pS2448_obs; s4=scale_GSK3a_pS9_obs; s5=scale_MFN2_on_obs; s7=scale_FoxO3a_pS253_obs; s8=scale_p21_obs; s9=scale_p27_obs; s10=scale_Mitochondria_Membrane_Potential_obs; s11=scale_JNK_pT183_obs; s12=scale_ROS_obs; s13=scale_DNA_damage_gammaH2AX_foci_obs	Fixed	1
(Observables [a.u.])		
y1=Akt_pS473_obs	Assigned	s1*x2
y2=AMPK_pT172_obs	Assigned	s2*x4
y3=mTOR_pS2448_obs	Assigned	s3*x6
y4=GSK3a_pS9_obs	Assigned	s4*x8
y5=MFN2_on_obs	Assigned	s5*x10
y7=FoxO3a_pS253_obs	Assigned	s7*x13
y8=p21_obs	Assigned	s8*x17
y9=p27_obs	Assigned	s9*x20
y10=Mitochondria_Membrane_Potential_obs	Assigned	s10*(x22+x23)
y11=JNK_pT183_obs	Assigned	s11*x25
y12=ROS_obs	Assigned	s12*x27
y13=DNA_damage_gammaH2AX_foci_obs	Assigned	s13*x29
(Compartments [a.u.])		
Cell	Fixed	1

Table 7.2: Table of the initial concentrations and auxiliary parameters. Protein initial concentrations were directly determined from experimental time course data. Initial concentrations of protein inactive states were calculated as the maximum peak of the relative activation level in the time course plus two times the standard deviation at that time point. Since at time t=0 cells were treated with X-rays irradiation, the initial concentrations of active states for proteins in the oxidative stress signalling were fixed to 0. The remaining initial concentrations were fixed to 1 in accordance with the normalised experimental basal level, since cells were not starved of amino acids and insulin. In Figure 7.1, the three states of mitochondrial membrane potential (high, low, null) are here mapped with the species identifiers x22, x23 and x24, respectively.

Calibration Step	Data Points (N)	Parameters (p)	χ2	P-value(N)	P-value(N-p)	AIC	AICc
Round 0	114	37	79.0263	0.994794	0.414686	362.544	399.544
Round 1	114	34	79.0002	0.994828	0.510605	356.518	386.645
Round 2	114	19	79.0001	0.994828	0.881809	326.518	334.603
Round 3	114	3	79.0001	0.994828	0.990658	294.518	294.736
Final Model	**114**	**37**	**79.0001**	**0.994828**	**0.415494**	**362.518**	**399.518**

Table 7.3: Model fit details for each calibration round. For each calibration round, the measures of χ^2, Akaike information criterion (AIC, AIC corrected) and Bayesian information criterion (BIC) are indicated. Since Round 0, the model was not statistically rejected (P-value(N-p) $>$ 0.05) and showed an accurate fitting with the data. Despite being required for parameter identification, the calibration rounds did not introduce significant improvements in the overall model fitting (see χ^2, P-value(N) between Round 0 and Final Model). Between rounds the measures P-value(N-p), AIC, AICc and BIC showed improvements due to the decrease in parameters number p. P-value(N), p-value(N-p): χ^2 tests with N or $N-p$ degrees of freedom, where N is the number of fitted data points and p corresponds to the number of fitted parameters.

Akt	: dx 1/dt = - k1 *x1 *u1 + k2 *x2 *x6;
Akt_pS473	: dx 2/dt = k1 *x1 *u1 - k2 *x2 *x6;
AMPK	: dx 3/dt = - k3 *x3 + k4 *x4 *x22;
AMPK_pT172	: dx 4/dt = k3 *x3 - k4 *x4 *x22;
mTORC1	: dx 5/dt = - k5 *x5 *u2*x2 + k6 *x6 *x4;
mTORC1_pS2448	: dx 6/dt = k5 *x5 *u2*x2 - k6 *x6 *x4;
GSK3a	: dx 7/dt = - k7 *x7 *x2 + k8 *x8 ;
GSK3a_pS9	: dx 8/dt = k7 *x7 *x2 - k8 *x8 ;
MFN2_off	: dx 9/dt = - k9 *x9 *x14*x4 - k10 *x9 *x15*x4 + k11 *x10 *x6;
MFN2_on	: dx10/dt = k9 *x9 *x14*x4 + k10 *x9 *x15*x4 - k11 *x10 *x6;
FoxO3a_pS253	: dx13/dt = k14 *x14 *x2 - k15 *x13 *x25 - k17 *x13 ;
FoxO3a	: dx14/dt = - k14 *x14 *x2 - k16 *x14 *x25 + k19 *x16 ;
FoxO3a_p_by_JNK	: dx15/dt = k15 *x13 *x25 + k16 *x14 *x25 - k18 *x15 ;
FoxO3a_source	: dx16/dt = k17 *x13 + k18 *x15 - k19 *x16 ;
p21	: dx17/dt = k20 *x18 *x29*x14 + k21 *x18 *x29*x15 - k23 *x17;
p21_source	: dx18/dt = - k20 *x18 *x29*x14 - k21 *x18 *x29*x15 + k22 *x19 *x2;
p21_active	: dx19/dt = k23 *x34 - k22 *x19 *x2;
p27	: dx20/dt = k24 *x21 *x29*x14 + k25 *x21 *x29*x15 - k26 *x20 *x2;
p27_source	: dx21/dt = - k24 *x21 *x29*x14 - k25 *x21 *x29*x15 + k26 *x20 *x2;
Functional_Mitochondria	: dx22/dt = k27 *x23 *x10 - k28 *x22 *x27 + k29 *x24 *x10;
Damaged_Mitochondria	: dx23/dt = - k27 *x23 *x10 + k28 *x22 *x27- k30 *x23 *x27;
Dysfunctional_Mitochondria	: dx24/dt = - k29 *x24 *x10 + k30 *x23 *x27;
JNK_pT183	: dx25/dt = k40 *x26 *x27 - k41 *x25 ;
JNK	: dx26/dt = - k40 *x26 *x27 + k41 *x25 ;
ROS	: dx27/dt = k31 *x28 *x19 + k35 *x28 *x22 + k36 *x28 *x23 + k37 *x28 *x24 - k38 *x27 *x14 - k39 *x27 *x15;
ROS_source	: dx28/dt = - k31 *x28 *x19 - k35 *x28 *x22 - k36 *x28 *x23 - k37 *x28 *x24 + k38 *x27 *x14 + k39 *x27 *x15;
DNA_damage_gammaH2AX_foci	: dx29/dt = k32 *x30 *u3 - k33 *x29 + k34 *x30 *x27;
DNA_damage_gammaH2AX_foci_source	: dx30/dt = - k32 *x30 *u3 + k33 *x29 - k34 *x30 *x27;
Delay01_p21	: dx31/dt = k23 *x17 - k23 *x31;
Delay02_p21	: dx32/dt = k23 *x31 - k23 *x32;
Delay03_p21	: dx33/dt = k23 *x32 - k23 *x33;
Delay04_p21	: dx34/dt = k23 *x33 - k23 *x34;
Insulin	: u1
Amino_Acids	: u2
Irradiation	: u3

Table 7.4: Ordinary differential equations of the model. List of the ordinary differential equations (ODEs) for the model. Kinetic rate constants were abbreviated using the notation shown in Table 7.1. Protein activation states (species) are reported from Table 7.2.

Lyapunov Exponents	
λ1	-0.0421666
λ2	-0.0453126
λ3	-0.0775854
λ4	-0.0777072
λ5	-0.326172
λ6	-0.47659
λ7	-0.48922
λ8	-0.756924
λ9	-0.728148
λ10	-0.831116
λ11	-1.22039
λ12	-1.20776
λ13	-2.76149
λ14	-3.12588
λ15	-3.14953
λ16	-4.75559
λ17	-4.89518
λ18	-7.82146
λ19	-27.4377
λ20	-168360
Sum	**-168420**
Avg divergence	**-168420**

Table 7.5: Lyapunov exponents of the model. The modelled system of first approximation is regular since all the coefficients are constant. The Lyapunov exponents computed for this model are all negative, indicating that the model is asymptotically Lyapunov stable and therefore the trajectories eventually converge to an equilibrium. The maximum Lyapunov exponent ($\lambda 20$) is significantly high because the value for the variable *Functional Mitochondria* ($x22$) dramatically dropped due to the initial irradiation and did not restore due to the high levels of ROS and DNA damage. The 20 Lyapunov exponents were computed for the reduced system (20 independent variables) using Copasi [Hoops *et al.*, 2006] and the inner Wolf method [Wolf *et al.*, 1985] was configured with parameters: orthonormalisation interval: 0.0001, overall time: 50, relative tolerance: 1e-06, absolute tolerance: 1e-10, maximum internal steps: 10000. The divergence computed using finite divergences (algorithm defined in [Hindmarsh, 1983] and implemented in Copasi) coincides with the sum of Lypunov exponents indicating high confidence in the computation of the exponents.

Chapter 8

Conclusions and outlook

This doctorate thesis presents the dynamical modelling study that I fulfilled for three systems biology-based projects. These works led to the following results:

1. mTORC2 can be activated by a PI3K isoform which is sensitive to Wortmannin and independent of p70-S6K-dependent negative feedback loop (NFL);

2. AMPK can be activated by insulin through insulin receptor substrate (IRS) and dependency on the NFL; and

3. formal mechanism underlying the initiation and consolidation of irradiation-induced senescence state with emphasis on the role of the forkhead box family subclass O (FoxO3).

Projects 1 and 2 focused on the mammalian target of Rapamycin (mTOR) network (using HeLa and C2C12 cells). Project 3 provided a comprehensive model of cellular ageing by integrating the mTOR pathway with the DNA-damage and oxidative-stress response, FoxO, and mitochondrial function (using human diploid fibroblast MRC5 cells).
Project 1 advanced our knowledge on the upstream activation of mTORC2 which is of particular importance because: (a) mTORC2 regulates numerous ageing- and cancer-related downstream targets, such as Akt, FoxO, SGK and PKC; (b) a link between mTORC2 and PI3K opens interesting directions on how to pharmacologically reduce PI3K and mTOR complexes activity in a combinatorial manner without unbalancing their downstream signalling function; and (c) the discovery of specific PI3K isoforms responsible for mTORC2 activation, all of which can result in a new major link between mTORC2 and other cellular functions.
Project 2 aimed to extend the previous model with an AMPK module, since mTOR is also regulated by energy, aside from growth factors and nutrients. The

finding that AMPK can be regulated by insulin through IRS and that this induction is reduced by the NFL highlights the following main aspects: (a) more study is required in order to understand the significance of AMPK regulation by insulin; (b) new drug interventions may take advantage of this interplay between AMPK and mTORC1, by improving their function and limiting undesired consequences; and (c) important regulatory feedback loops may still be missing and these will notably increase the complexity of the TOR network.

Finally, Project 3 theoretically formalised the mechanism by which normal cells become and stabilise as senescent cells upon irradiation. Importantly, this project shows that: (a) nuclear FoxO plays different roles depending on mode of activation and the characterisation of these must be carefully investigated in order to properly benefit from FoxO activity; (b) combinatorial intervention is necessary to avoid undesired effects in the network; (c) reactive oxygen species (ROS) are an important initiator and contributor for driving ageing, although other components, such as TOR and inflammatory system, also contribute; (d) long term time courses should also be considered for studying the progressive and irreversible state transition during senescence; (e) irradiation-induced senescent state consolidation may be the result of limiting cell damage accumulation in conditions of insufficient energy; (f) the senescent phenotype may be still reversed at later time points if mitochondrial function is restored (mitochondria re-modelling) and combinatorial intervention to limit internal and external cellular damage accumulation is applied; and (g) since ageing is a state transition, dynamical systems theory should be considered and applied for formalising dynamical models in ageing.

Appendix A

COMPUTATIONAL BIOLOGY

A Dynamic Network Model of mTOR Signaling Reveals TSC-Independent mTORC2 Regulation

Piero Dalle Pezze,[1,2]* Annika G. Sonntag,[3]* Antje Thien,[4] Mirja T. Prentzell,[3] Markus Gödel,[4] Sven Fischer,[3] Elke Neumann-Haefelin,[4] Tobias B. Huber,[4,5] Ralf Baumeister,[3,5,6,7] Daryl P. Shanley,[1,2]† Kathrin Thedieck[3,5,6]†

The kinase mammalian target of rapamycin (mTOR) exists in two multiprotein complexes (mTORC1 and mTORC2) and is a central regulator of growth and metabolism. Insulin activation of mTORC1, mediated by phosphoinositide 3-kinase (PI3K), Akt, and the inhibitory tuberous sclerosis complex 1/2 (TSC1-TSC2), initiates a negative feedback loop that ultimately inhibits PI3K. We present a data-driven dynamic insulin-mTOR network model that integrates the entire core network and used this model to investigate the less well understood mechanisms by which insulin regulates mTORC2. By analyzing the effects of perturbations targeting several levels within the network in silico and experimentally, we found that, in contrast to current hypotheses, the TSC1-TSC2 complex was not a direct or indirect (acting through the negative feedback loop) regulator of mTORC2. Although mTORC2 activation required active PI3K, this was not affected by the negative feedback loop. Therefore, we propose an mTORC2 activation pathway through a PI3K variant that is insensitive to the negative feedback loop that regulates mTORC1. This putative pathway predicts that mTORC2 would be refractory to Akt, which inhibits TSC1-TSC2, and, indeed, we found that mTORC2 was insensitive to constitutive Akt activation in several cell types. Our results suggest that a previously unknown network structure connects mTORC2 to its upstream cues and clarifies which molecular connectors contribute to mTORC2 activation.

INTRODUCTION

The kinase target of rapamycin (TOR) is conserved in all eukaryotes from yeast to humans and is a central regulator of cellular growth, aging, and metabolism (*1*, *2*). As a central metabolic regulator, TOR is involved in a multitude of human diseases, including metabolic syndromes, cancer, and neurodegenerative diseases (*1*). Rapamycin is a well-known immunosuppressant, and rapalogs and other TOR inhibitors are applied in cancer therapy (*3*). Because of its clinical importance, it is important to understand the exact dynamics and interconnections within the TOR network.

TOR occurs in two functionally and structurally distinct multiprotein complexes termed TOR complex 1 (TORC1) and TORC2. The mammalian TORC1 (mTORC1) contains the specific scaffold protein Raptor and the inhibitory binding partner PRAS40, whereas mTORC2 contains the proteins Rictor, mSin1, PRR5, and PRR5L (*1*). mTORC1 controls cellular growth, translation, transcription, and autophagy (*4*); mTORC2 controls spatial growth by regulating the actin cytoskeleton (*5*). mTORC1 is specifically inhibited by the small macrolide rapamycin, whereas mTORC2 is rapamycin-insensitive. Adenosine triphosphate (ATP) analog TOR kinase inhibitors (TORKinibs) that target both mTOR complexes have also been described (*6*). Although the upstream and downstream regulatory mechanisms controlling mTORC1 are well characterized, those regulating mTORC2 are less well understood.

mTORC1 is regulated by nutrients (amino acids), growth factors (insulin), and energy (*7*). Amino acids activate the Ragulator-Rag complex to translocate mTORC1 to lysosomes, where mTORC1 can be activated by the small guanosine triphosphatase (GTPase) Rheb (*8*–*10*). Insulin signaling induces a kinase cascade through the insulin receptor (IR), IR substrate (IRS), class I phosphoinositide 3-kinases (PI3Ks), phosphoinositide-dependent protein kinase 1 (PDK1), and the AGC kinase Akt (also known as PKB). Akt inhibits the tuberous sclerosis complex 1/2 (TSC1-TSC2) dimer, which is the inhibitory GTPase-activating protein (GAP) for Rheb (*4*). Through this cascade, Akt stimulates mTORC1 activity. The best-characterized mTORC1 substrates are the AGC kinase p70 ribosomal protein S6 kinase (p70S6K), the translation initiation regulator 4E binding protein (4E-BP), and the proline-rich Akt substrate PRAS40, which is an inhibitor of mTORC1 (*11*). By binding mTORC1, PRAS40 contributes to the inhibition of mTORC1 activity (*12*–*16*). In response to insulin, Ser^{183} of PRAS40 is phosphorylated by mTORC1 (*17*), which releases PRAS40 from the complex and relieves its inhibitory effect on mTORC1 (*18*), allowing mTORC1 to phosphorylate its downstream substrates p70S6K and 4E-BP and promote cellular growth. Furthermore, there is a negative feedback loop (NFL) that inhibits upstream insulin signaling upon mTORC1 activation: Active p70S6K phosphorylates and inhibits IRS, which prevents activation of PI3K in response to insulin (*4*).

mTORC2 is mainly regulated by growth factors (*1*), although induction by nutrients has also been described (*19*, *20*). Little is known about the molecular mechanism by which insulin induces mTORC2. The known substrates of mTORC2 are the AGC kinases Akt (*21*–*24*), serum- and glucocorticoid-induced protein kinase SGK (*25*), and protein kinase C α (PKCα) (*26*). AGC kinases must be phosphorylated twice to be fully active (*27*–*29*): They are phosphorylated by PDK1 in the T loop and in

[1]Institute for Ageing and Health, Newcastle University, Campus for Ageing and Vitality, Newcastle upon Tyne NE4 5PL, UK. [2]Centre for Integrated Systems Biology of Ageing and Nutrition, Institute for Ageing and Health, Newcastle University, Newcastle upon Tyne NE4 5PL, UK. [3]Bioinformatics and Molecular Genetics (Faculty of Biology), Albert-Ludwigs-Universität Freiburg, 79104 Freiburg, Germany. [4]Renal Division, University Hospital Freiburg, 79106 Freiburg, Germany. [5]BIOSS Centre for Biological Signalling Studies, Albert-Ludwigs-Universität Freiburg, 79104 Freiburg, Germany. [6]Center for Systems Biology (ZBSA), Albert-Ludwigs-Universität Freiburg, 79104 Freiburg, Germany. [7]ZBMZ (Faculty of Medicine) and Freiburg Institute for Advanced Studies (FRIAS), Albert-Ludwigs-Universität Freiburg, 79104 Freiburg, Germany.
*These authors contributed equally to this work.
†To whom correspondence should be addressed. E-mail: kathrin.thedieck@biologie.uni-freiburg.de (K.T.); daryl.shanley@newcastle.ac.uk (D.P.S.)

the hydrophobic motif by a PDK2. Only one PDK1 exists for all AGC kinases, but the identity of PDK2 differs among the AGC kinases. mTORC2 is a PDK2 for Akt, SGK, and PKCα (*27*–*29*), and phosphorylation of Ser^{473} of Akt is a commonly used readout for mTORC2 activity.

Using mTORC2 substrate AGC kinases as indicators of mTORC2 activity, the TSC1-TSC2 complex has been implicated in mTORC2 activation by insulin: TSC1-TSC2 inhibition reduces phosphorylation of the mTORC2 substrate Akt at Ser^{473} (*30*–*33*). This result was surprising because TSC1-TSC2 inhibits mTORC1 (*34*). Two models have been proposed to explain mTORC2 regulation by TSC1-TSC2, involving either direct mTORC2 activation by TSC1-TSC2 (*31*, *33*) or an indirect mechanism through an active NFL that inhibits PI3K when mTORC1 was hyperactive in response to TSC1-TSC2 ablation (*35*). However, data showing that mTORC2 contributes to proliferation in TSC2-null cells suggest that mTORC2 can be active in the absence of TSC1-TSC2 (*36*). A third hypothesis for mTORC2 activation is through a PI3K-independent mechanism, which has been identified in *Dictyostelium* (*37*–*40*). In mammals, several cellular processes that are regulated by mTORC2 have been described as PI3K-independent (*19*, *26*, *41*–*43*), making the hypothesis of PI3K-independent activation of mTORC2 conceivable.

To distinguish among the possible mTORC2 activation mechanisms and to determine whether they acted independently or in combination, we developed a mathematical dynamic network model. We hypothesized that different modes of mTORC2 regulation would result in distinguishable, dynamic network responses. With the mathematical model, we performed specific predictive dynamic simulations for alternative mechanisms of mTORC2 regulation, and then these were experimentally validated.

There are several computational studies related to mTOR signaling. These include static network models of known molecular interactions, for example, the map for the insulin-mTOR network (*44*). Dynamic models also exist. These require information about the molecular interactions and also detailed quantitative experimental time course data, which can be generated specifically for the model (*45*–*53*) or can use data from previous studies (*45*, *54*–*57*). Much of the currently available dynamic models focus on the upstream insulin signaling events, such as the binding of insulin to its receptor (*50*), and receptor autophosphorylation and receptor-mediated substrate phosphorylation, together with receptor cycling and endocytosis (*46*, *49*). More extensive models including activation of IRS, PI3K, Akt, and the NFL have been developed with specific functional emphasis on cycling of the glucose transporter GLUT4 (*54*), dendritic protein synthesis (*45*), or breast cancer therapy (*51*). Other models address complex issues, such as joint regulation of the NFL by insulin and amino acids (*56*), crosstalk with epidermal growth factor (EGF) signaling and the mitogen-activated protein kinase (MAPK) pathway (*48*), and TORC1 regulation by phosphatases in yeast (*52*). Because the combined experimental-computational approaches typically address specific questions, the generated data sets are often limited, representing one (*47*) or two time points (*53*), or representing limited parts of the network, such as binding of insulin and insulin-like growth factor (IGF) to their receptors (*50*). None of the existing models integrates mTORC2 regulation.

Here, we report an insulin-mTOR network model integrating both mTORC1 and mTORC2. The model was parameterized with dynamic quantitative time course data and experimentally validated. Subsequently, we introduced in silico and experimental network perturbations to simulate and experimentally test alternative network structures connecting mTORC2 to upstream insulin signaling. This approach provides the benefit of both a structural and a dynamic network analysis (*58*).

Our model and experimental testing indicated that in contrast to previous hypotheses, the TSC1-TSC2 complex was not a direct activator of mTORC2 and that mTORC2 activity was insensitive to the mTORC1-induced NFL. Furthermore, although PI3K is inhibited by the NFL, activation of the NFL-insensitive mTORC2 also required active PI3K. Hence, all three literature-based hypotheses were excluded by our combined simulation and experimental data. Instead, we postulate that insulin signaling activates mTORC2 through a PI3K that is insensitive to the NFL; thus, insulin triggers signaling networks that diverge upstream of Akt. We created a network structure that fits the available experimental data and provided experimental evidence supporting the network.

RESULTS

A dynamic insulin-regulated TOR network model

Initially, we established a static network model in SBGN (Systems Biology Graphical Notation) format (*59*) of insulin-mTOR signaling as a means to integrate current knowledge and as a platform to guide our decision on appropriate targets for measurement (fig. S1). The choice of boundaries for such a network and the level of molecular detail to include are subjective decisions. There is considerable existing knowledge concerning insulin signaling and the regulation of TOR (*1*, *7*). Although we used this information, we needed to minimize the amount of detail because precise dynamics for the extended graphical model could not be defined due to the high number of parameters and the difficulty in obtaining sufficient experimental data. Therefore, we abstracted the extended model on the basis of two main considerations. First, we selected regulation mechanisms with an important role in dynamic behavior, such as the activation of mTOR complexes by the presence of both amino acids and insulin, the pathways connecting these stimuli to the mTOR complexes, and the NFL from p70S6K to IRS. Second, we selected molecules and interactions that we could reliably measure. To capture the network dynamics upon starvation and in response to amino acids plus insulin (aa/insulin), we distributed our measurements widely across the network. We monitored the abundance of Tyr^{1146}-phosphorylated IR, Ser^{636}-phosphorylated IRS1, Ser^{473}- and Thr^{308}-phosphorylated Akt, Ser^{2448}- and Ser^{2481}-phosphorylated mTOR, Thr^{246}- and Ser^{183}-phosphorylated PRAS40, and Thr^{389}-phosphorylated p70S6K (see the selected targets marked with an asterisk in fig. S1).

On the basis of the molecules we could measure, we condensed our network structure to minimize poorly defined intermediate steps between obtainable data (Fig. 1A). The condensed network depicts insulin signaling propagating from the IR through the TSC1-TSC2 complex to the mTORC1 complex and includes p70S6K, PRAS40, and Akt. In addition, mTORC1 induction by amino acids was included. At this point, no upstream pathway regulating mTORC2 was assumed. This model formed the starting point for our dynamic study.

Readout selection for mTORC2 activity: Akt-pS^{473} and mTOR-pS^{2481}

Studies suggesting that TSC1-TSC2 regulates mTORC2 commonly used Akt phosphorylated at Ser^{473} (Akt-pS^{473}) as the mTORC2 readout. However, the phosphorylation of Akt depends on PI3K and the phosphatidylinositol 3,4,5-trisphosphate [PtdIns(3,4,5)P_3] generated by PI3K, which binds to Akt and triggers its relocalization to the plasma membrane, where Thr^{308} is phosphorylated by PDK1 and Ser^{473} is phosphorylated by mTORC2 (*27*). Thus, phosphorylation of Akt at either Thr^{308} or Ser^{473} depends on PI3K activity. PI3K and Akt are inhibited in the absence of the inhibitory TSC1-TSC2 complex because of hyperactivation of mTORC1

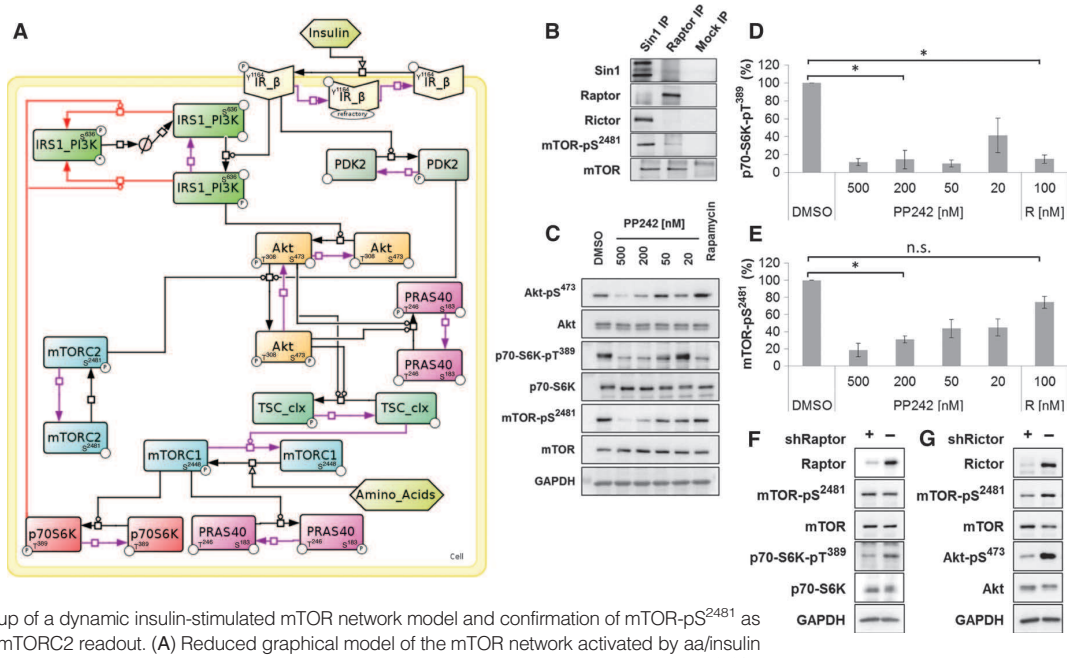

Fig. 1. Setup of a dynamic insulin-stimulated mTOR network model and confirmation of mTOR-pS^{2481} as a specific mTORC2 readout. (**A**) Reduced graphical model of the mTOR network activated by aa/insulin (see fig. S1 for the extended graphical model). (**B**) Coimmunoprecipitation (IP) of mTOR-pS^{2481} with Sin1 (a component of mTORC2) or Raptor (a component of mTORC1); Mock IP, control IP with a nonspecific antibody. Data are representative of three experiments. (**C**) Effect of PP242 or rapamycin on the indicated phosphorylated proteins. Data are representative of three experiments. (**D** and **E**) Quantitation of three experiments similar to the one shown in (C) for mTORC1 readout p70-S6K-pT^{389} (D) and mTORC2 readout mTOR-pS^{2481} (E). R, rapamycin. *$P < 0.05$; n.s., not significant. In (D), PP242 [200 nM, an mTOR-specific standard concentration (*6*)]–treated compared to dimethyl sulfoxide (DMSO)–treated control and rapamycin-treated samples compared to DMSO control were significant. In (E), PP242 (200 nM)–treated compared to DMSO-treated control was significant. Rapamycin (100 nM) compared to DMSO control was not significant. (**F**) Effect of Raptor knockdown on mTOR-pS^{2481}. Data are representative of three experiments. (**G**) Effect of Rictor knockdown on mTOR-pS^{2481}. Data are representative of three experiments.

and the NFL. Consequently, under conditions of TSC1-TSC2 deficiency and NFL activation, monitoring Akt-pS^{473} does not differentiate between PI3K, PDK1, and mTORC2 activity and therefore may not be a suitable readout to investigate the mode of mTORC2 regulation by TSC1-TSC2 (*32*). Other AGC kinases that are targeted by mTORC2 (SGK and PKCα) are not ideal because they have similar issues (*28*, *60*). The rapamycin-insensitive autophosphorylation of Ser^{2481} (mTOR-pS^{2481}) (*61*, *62*) has been described as mTORC2-specific (*63*) and as occuring in both the mTOR complexes (*64*). To determine whether mTOR-pS^{2481} is a better readout for mTORC2 activity than is the phosphorylation of AGC kinases and whether monitoring mTOR-pS^{2481} will distinguish between PI3K and mTORC2 activity, we determined that mTOR-pS^{2481} was a specific readout for mTORC2 activity in HeLa cells. We performed complex-specific immunoprecipitations with antibodies against Sin1 (for mTORC2) or Raptor (for mTORC1) and assessed the amount of mTOR-pS^{2481} that co-immunoprecipitated (Fig. 1B). In HeLa cells, mTOR-pS^{2481} was predominantly associated with mTORC2 and only weakly associated with mTORC1, suggesting that mTOR-pS^{2481} is a suitable readout of mTORC2 activity. Furthermore, whereas the mTORC1-specific readout p70S6K1-pT^{389} was reduced by the mTORC1-specific inhibitor rapamycin (Fig. 1, C and D), in agreement with Copp *et al.* (*63*), mTOR-pS^{2481} was not significantly affected by short-term treatment with the rapamycin (Fig. 1, C and E). In contrast, the TORKinib PP242 (*65*), which inhibits both mTOR complexes, reduced the abundance of mTOR-pS^{2481} in a dose-dependent manner (Fig. 1, C and E), which is consistent with results obtained with Torin1, another TORKinib (*64*, *66*). Therefore, our results suggest that mTOR-pS^{2481} is reduced by mTORC2, but not by mTORC1 inactivation.

Because there are rapamycin-insensitive mTORC1 functions (*67*), we also knocked down specific mTORC1 and mTORC2 components to assess the dependence of mTOR-pS^{2481} on the activity of the two complexes. When the mTORC1-specific component Raptor was knocked down, mTOR-pS^{2481} was unchanged (Fig. 1F), whereas there was a significant reduction in mTOR-pS^{2481} by 67% (three independent experiments, SEM 8%) when the mTORC2-specific component Rictor was knocked down (representative experiment shown in Fig. 1G). Thus, both knockdown and pharmacological experiments indicated that mTOR-pS^{2481} serves as an mTORC2-specific readout in our system.

Parameterization of the network model

To parameterize the static network model, we generated semiquantitative dynamic phosphorylation immunoblot data for network components along the signaling cascade (Fig. 1A). We analyzed HeLa cells under starvation conditions, meaning that they were deprived of amino acids and growth factors for 16 hours to fully inhibit mTOR network activity, and also cells that had been starved and then stimulated with aa/insulin to assure full induction of both mTOR complexes. Dynamics of the mTOR network were monitored from 1 min up to 2 hours after induction with aa/insulin (Fig. 2A). Signals were quantitatively analyzed (see Materials

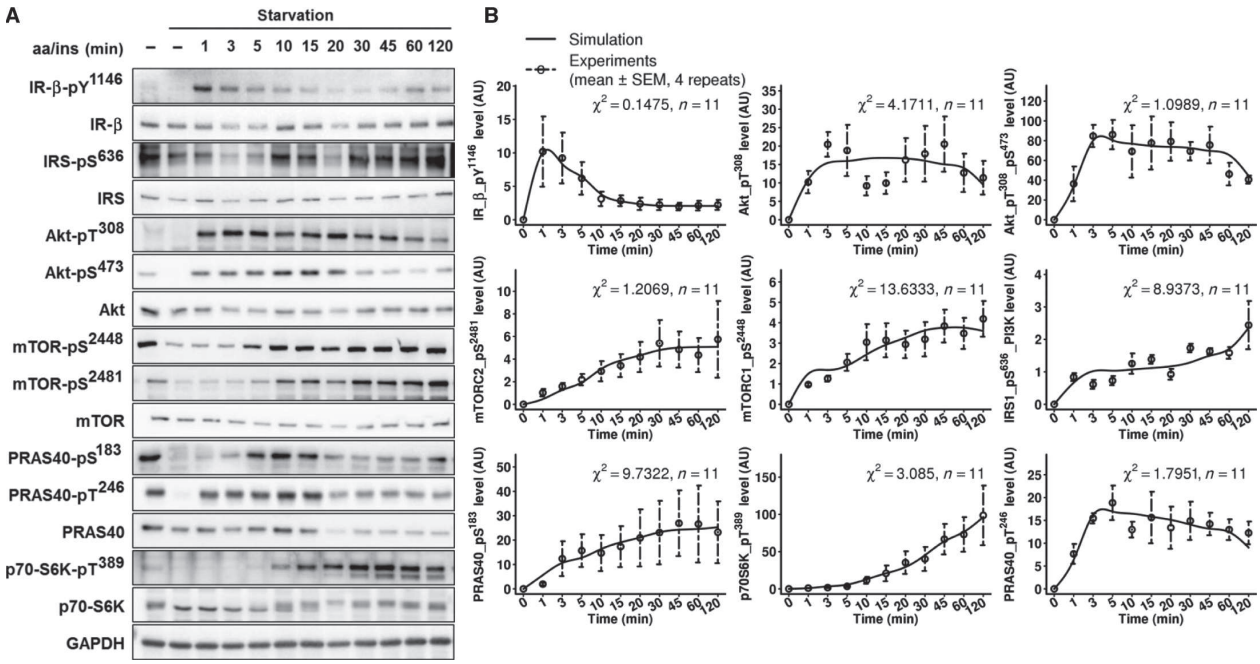

Fig. 2. Setup of a dynamic insulin/mTOR network model. (A) Dynamic quantitative time course acquisition. mTOR pathway activation was followed over time by measuring phosphorylation dynamics of central network components. A representative experiment is shown; signal intensities were quantified and descriptive statistics were computed over four replicates. (B) Comparison between the simulated time courses of the general model (solid lines) and the experimental time courses (points, dotted error bars) within [0, 120] min. For each curve, the χ^2 computed over n time points is reported as goodness-of-fit measure.

and Methods). Because signal linearities are critical for quantitative data generation (*68*), we confirmed the linear signal–to–protein amount relationships by detection of serial dilutions of whole-cell lysates (fig. S2). We calibrated the model parameters by means of the experimental mean time courses (Fig. 2B).

The initial concentrations of the species in their nonphosphorylated state were determined directly from our semiquantitative data (see Materials and Methods). For all other species, the initial concentrations were set to 0. Because it is difficult to fit large numbers of parameters to data to estimate kinetic rate constants (*69*–*71*), which are necessary to calibrate the model, we divided the data fitting into calibration phases and resolved each phase with an iterative procedure (figs. S3 and S4). This procedure is summarized by the following steps: (i) The initial values of the parameters that needed optimization were assigned by random generation. (ii) The calibration was repeated until a set of parameters with consistent values was identified. (iii) This set of parameters was fixed and the remaining free parameters were calibrated again by repeating the process. In phase 1 of the estimation of kinetic rate constants, we sought to identify isolated modules that could be calibrated independently within the network. Because IR regulation was not affected by the rest of the network, this module could be isolated and we could calibrate three parameters at once: the kinetics of IR activation by insulin, dephosphorylation to a refractory state, and transition to a receptive state. We initially generated a model that was independent of the pathway by which mTORC2 was activated. We temporarily modeled the regulation of the mTORC2 substrate Akt-S^{473} and mTORC2 component mTOR-S^{2481} with two autoactivation mechanisms, which were then calibrated with the Akt-pS^{473} and mTOR-pS^{2481} experimental data sets. This enabled us to reproduce Akt-pS^{473} activation while maintaining mTORC2 isolated from the network. During phase 2, a total of 24 reaction rate constants were estimated with eight experimental readouts. Finally, in phase 3, we replaced the autoactivation mechanism of Akt-pS^{473} with a phosphorylation mediated by mTORC2-pS^{2481}. Because the initial induction of Akt-pS^{473} occurred before mTOR-pS^{2481} was induced (Fig. 2, A and B), mTORC2-pS^{2481} alone could not reproduce the dynamics of the experimental data for Akt-pS^{473}. mTORC2 is not the only PDK2 candidate that may phosphorylate Akt-S^{473}; therefore, we introduced an additional PDK2 species and recalibrated the phosphorylation of Akt-S^{473} under the influence of the two kinases. In this phase, three kinetic rate constants were estimated with the Akt-pS^{473} experimental data.

Once this process of parameterization was complete, the experimental and simulated time courses matched well for all the analyzed mTOR network readouts (Fig. 2B). The ordinary differential equations (ODEs) and estimated parameters for the general model are provided in tables S1 and S2. Identifiability analysis, which indicates whether the parameters can be estimated with confidence from the available data, and sensitivity analysis, which indicates how sensitive model behavior is to variation in each parameter, for the general model are shown in figs. S5 and S6. The identifiability analysis does not show high correlation between estimated parameters, indicating that they can be identified.

Validation of the mTORC1 branch: Network perturbation by gradual mTORC1 inhibition

If the parameterized model correctly represents the biological mTOR network dynamics in response to aa/insulin, model simulations must

accurately reflect the dynamics of known network responses to a gradual perturbation. To validate the mTORC1 branch of the model, we perturbed the network by gradually inhibiting mTORC1 first in silico and then experimentally with an inducible Raptor knockdown (shRaptor) cell line. The model was used to simulate the effect of gradual mTORC1 inhibition on the activation dynamics of the direct mTORC1 substrate p70-S6K-pT^{389} at several time points after induction with aa/insulin. The model predicted a constant increase in p70-S6K-pT^{389} signal from 10 min to 2 hours after induction. Furthermore, the model also predicted that p70-S6K-pT^{389} would decrease starting 10 min after induction in a near-linear manner in response to gradual Raptor (mTORC1) inhibition, whereas there should be no detectable increase or Raptor-dependent change in p70-S6K-pT^{389} below 5 min after induction (Fig. 3A). We tested the predicted quantitative p70-S6K-pT^{389} response upon gradual mTORC1 inhibition (Fig. 3B) at specific time points (indicated in the simulation in Fig. 3A by the green lines) and found that the dynamic simulations for p70-S6K-pT^{389} were validated by our experimental data (Fig. 3, C and D). Both the simulations (Fig. 3B) and the experimental results (Fig. 3D) for the change in p70-S6K-pT^{389} in response to gradual Raptor inhibition at 20 and 45 min after induction with aa/insulin matched, showing an overall increase in signal at 45 min after induction and no signal at 3 min after induction.

Hence, we confirmed that the model accurately simulated the dynamic behavior of the mTORC1 substrate p70-S6K-T^{389} in response to aa/insulin and to a network perturbation (Raptor inhibition). This was performed with an experimental perturbation that was not used for parameterization.

Exploration of alternative network structures: Regulation of mTORC2 by the TSC1-TSC2 complex

The mechanism by which TSC1-TSC2 influences mTORC2 activity is currently unclear, with both a direct activation of mTORC2 by TSC1-TSC2 and an indirect effect of the TSC1-TSC2 through mTORC1 and the NFL suggested (*31*, *33*, *35*). The evidence for these mechanisms involves experimental designs that could affect the system in a manner that could complicate the interpretation, for example, overexpression of NFL-independent PI3K versions (*31*) or TSC2 ablation in combination with subsequent in vitro mTOR kinase assays (*33*).

To establish an approach with minimal complicating manipulations, we applied a combined experimental-computational strategy. Because the different suggested molecular mechanisms by which TSC1-TSC2 regulates mTORC2 should result in mechanism-specific changes in the dynamics of the mTORC2 readouts, the response of the readouts to network perturbations should be predictable and distinguishable by our dynamic network model. On the basis of the existing literature, we postulated three different hypotheses for the molecular connection or lack thereof between TSC1-TSC2 and mTORC2 (Fig. 4A). (Hypothesis 1) TSC-dependent: TSC1-TSC2 directly activates mTORC2 in response to insulin and has opposite effects on mTORC1 and mTORC2. (Hypothesis 2) NFL-dependent: mTORC2 is activated by insulin through PI3K, but independently of Akt and TSC1-TSC2; however, mTORC2 activity can be inhibited indirectly by TSC1-TSC2 ablation through NFL-mediated inhibition of PI3K. (Hypothesis 3) PI3K-independent: mTORC2 is activated by insulin in a manner that is independent of both TSC1-TSC2 and PI3K.

We translated these three alternative modes of mTORC2 regulation into the corresponding network structures, reusing the same kinetic parameters of our previous model (Fig. 4B). To keep the hypotheses as comparable as possible, each hypothesis shared the network topology of the general model but assumed a specific mTORC2 upstream regulator (Fig. 4B). We adopted the following rationale: Let M be a model fitting some data and S a species in M. If a modifier (F) directly upstream of S is selected and recalibration solely of the dynamics of S maintains a close fit between the simulated time course for S and the experimental data for S, then all time course curves downstream of S will continue to fit their corresponding data. The model output,

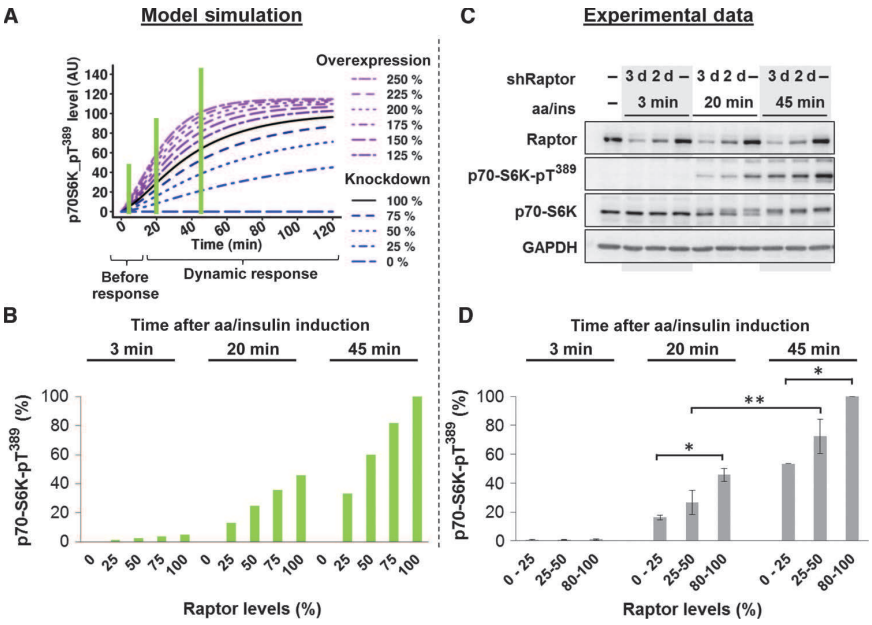

Fig. 3. Validation: dynamic response of p70-S6K-pT^{389} to gradual Raptor inhibition. (**A**) Model predictions for p70-S6K-pT^{389} dynamics in response to a perturbation of mTORC1. The curves show the simulated response to gradual mTORC1 inhibition starting at 5 to 10 min after induction with aa/insulin. The model was simulated with both mTORC1 overexpression and knockdown conditions. Time points for experimental validation are indicated by green lines. (**B**) Simulated and quantified relative amounts of p70-S6K-pT^{389} under conditions of mTORC1 reduction (0, 25, 50, 75, and 100%) at selected time points after induction with aa/insulin. (**C**) Experimental validation of the effect of gradual Raptor knockdown (shRaptor) on p70-S6K phosphorylation in starved cells induced with aa/ins for the indicated times. Data are representative of three experiments. d, days. (**D**) Experimentally determined and quantified p70-S6K-pT^{389} amounts at the indicated times after induction with aa/insulin in cells in which Raptor was knocked down. Data are the average and SEM of three experiments. *P < 0.05; **P < 0.01; low Raptor levels compared to high Raptor levels after 20- and 45-min induction; 20- compared to 45-min induction. Differences in p70-S6K-pT^{389} were significant. aa/ins, aa/insulin.

however, after perturbation of F will not necessarily maintain a fit with the corresponding data when the introduced upstream connection is incorrect.

We defined three new models in which the network and the parameters of our previous model were maintained and only the mTORC2 kinetics were reestimated according to each hypothesis (tables S1 and S3). The

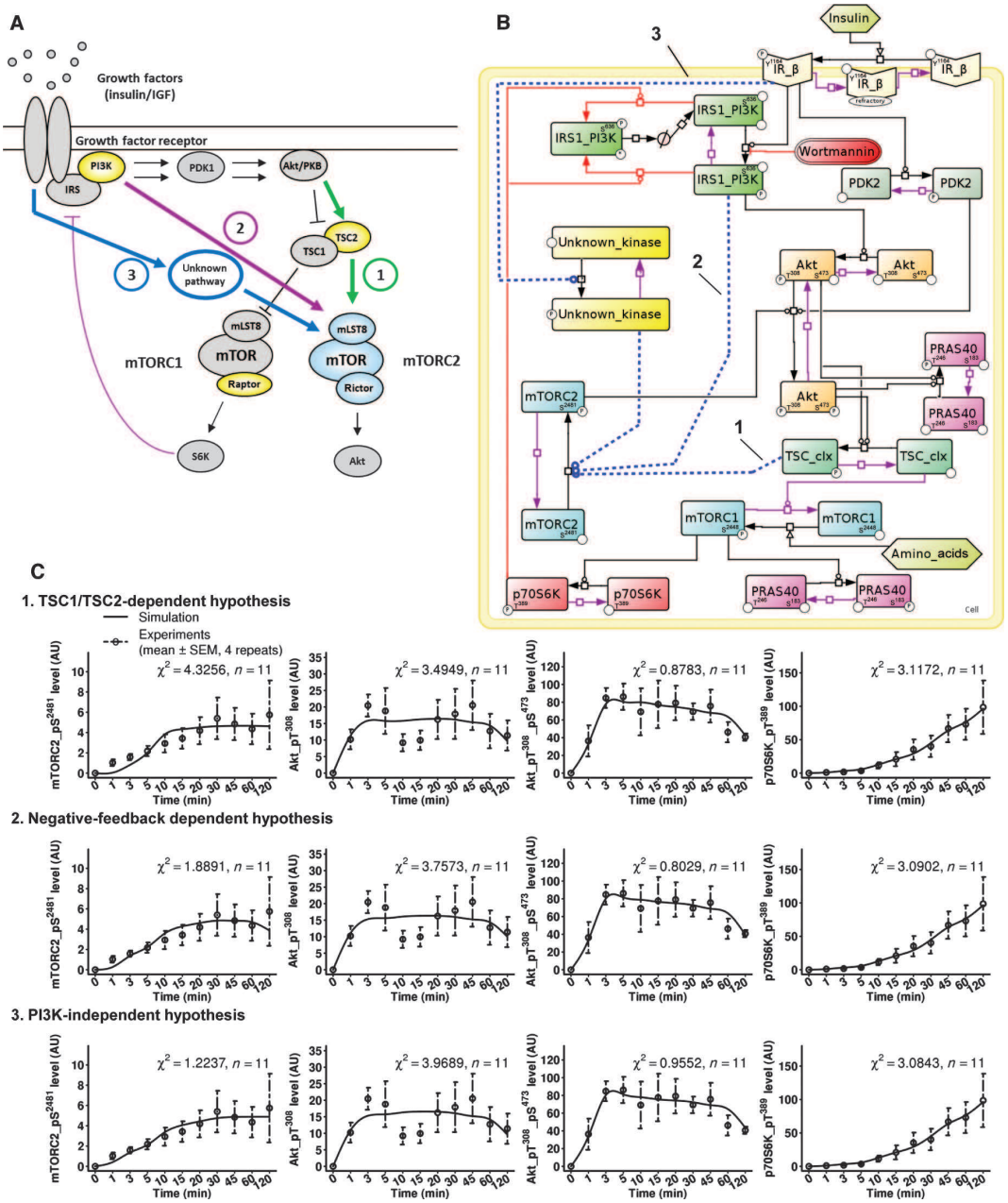

Fig. 4. Three hypotheses for mTORC2 regulation by insulin. (A) Schematic representation of the insulin-induced mTORC1-mTORC2 pathway with three different hypotheses (1, green; 2, purple; 3, dark blue) for mTORC2 activation. Network components that were targeted for perturbations are highlighted in yellow. (B) Reduced graphical network model including the three hypotheses (1, 2, and 3, indicated by the dotted lines), translated into different network structures. (C) Comparisons of simulated time courses, calibrated for each hypothesis, with experimental data. Data are for mTORC2 readouts (mTOR-pS^{2481}, Akt-pS^{473}), the PI3K readout Akt-pT^{308}, and the mTORC1 readout p70-S6K-pT^{389} (see fig. S7 for curves of all other readouts).

total goodness of fit for the general model and each hypothesis showed that no model could be statistically rejected (table S4). For each hypothesis, we performed time course simulations and experimental validation for the mTORC2 readouts mTOR-pS^{2481} and Akt-pS^{473}, the PI3K readout Akt-pT^{308}, and the mTORC1 substrate p70-S6K-pT^{389} (Fig. 4C). The curves for all other analyzed network components are provided in fig. S7. The simulations matched the experimental time courses, indicating that the hypotheses were compatible with the observed dynamics for mTORC2 activation and more generally for the mTOR signaling network. Identifiability and sensitivity analyses for the three models representing each hypothesis are shown in figs. S8 to S13.

We next introduced gradual network perturbations that prevented either TSC1-TSC2 activity (TSC1-TSC2 inhibition), the NFL (mTORC1 inhibition), or insulin activation of the mTOR complexes (PI3K inhibition). For each of the three perturbations and each of the three hypotheses, we modeled the dynamic network response of the readouts of mTORC2 activity (Fig. 5), of mTORC1 activity (fig. S14), and of PI3K activity (fig. S15).

Experimental testing: TSC2-independent mTORC2 induction

From the information obtained from the alternative simulations, we identified experimental setups and time points after induction with aa/insulin for the mTORC2 readouts (mTOR-pS^{2481}, Akt-pS^{473}) that would specifically distinguish among hypotheses 1, 2, and 3 (green lines in Fig. 5). These predictions were then tested experimentally (Figs. 6 to 8).

The models predicted that for gradual TSC1-TSC2 inhibition, if hypothesis 1 was correct, then the abundance of mTOR-pS^{2481} would be affected by TSC1-TSC2 inhibition in a near-linear manner down to minimum levels (Fig. 5A). In contrast, for hypothesis 2, simulated mTOR-pS^{2481} dynamics were only slightly affected by TSC1-TSC2 inhibition, and for hypothesis 3, mTOR-pS^{2481} was not affected (Fig. 5A). For Akt-pS^{473} dynamics, if hypothesis 2 or 3 is correct, then Akt-pS^{473} should only be weakly affected 5 min after induction and should exhibit a gradual decrease starting 10 min after induction for the rest of the time course (Fig. 5B). For hypothesis 1, the model predicted a stronger reduction of Akt-pS^{473} in response to TSC1-TSC2

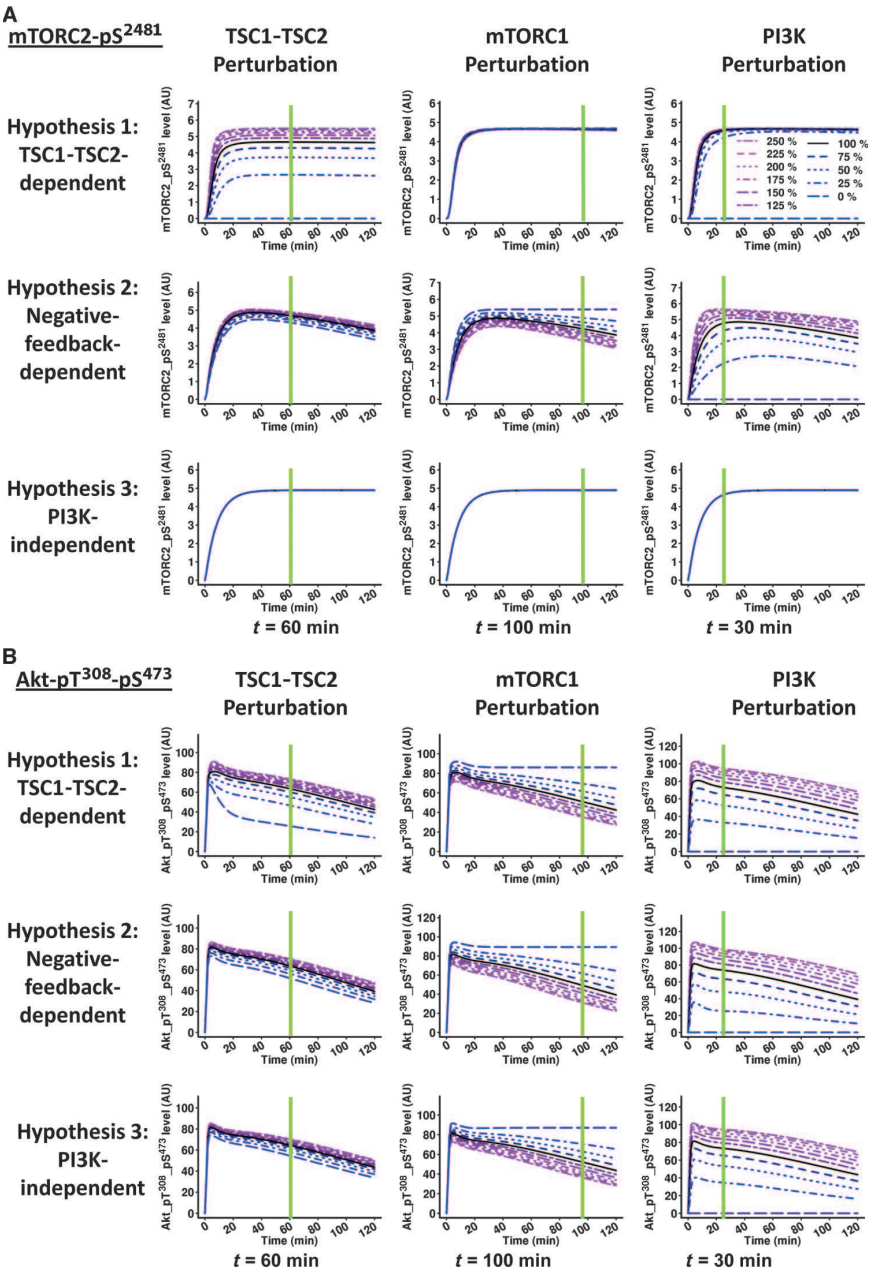

Fig. 5. Simulations of network perturbations at several levels within the network and differential dynamic network responses for the three different hypotheses. (**A**) Simulated mTOR-pS^{2481} response upon aa/insulin induction upon the indicated perturbations: TSC1-TSC2 (experimental equivalent: gradual TSC2 knockdown), mTORC1 (experimental equivalent: gradual Raptor knockdown), and PI3K (experimental equivalent: gradual PI3K inhibition with wortmannin) for hypotheses 1, 2, and 3. The time points that were experimentally tested are indicated with green lines. (**B**) Simulated Akt-pT^{308}-pS^{473} response for each of the three hypotheses upon aa/insulin induction upon perturbations of TSC1-TSC2, mTORC1, and PI3K. The time points that were experimentally tested are indicated with green lines.

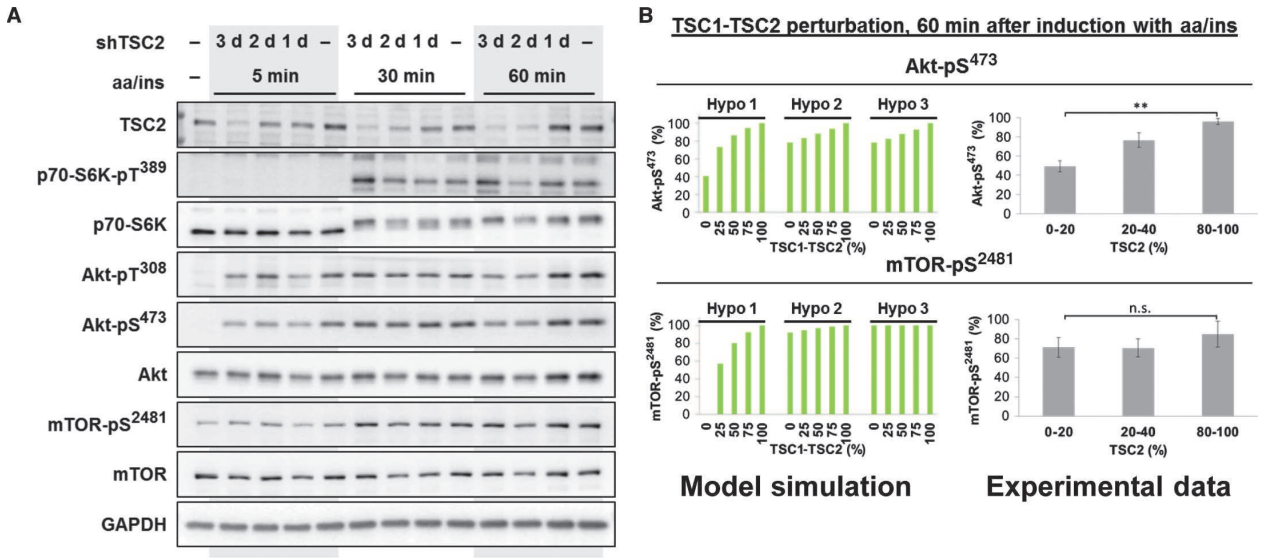

Fig. 6. mTOR-pS^{2481} is not directly activated by TSC1-TSC2. mTOR-pS^{2481} is not directly activated by TSC1-TSC2. (A) Representative immunoblot results of the network response upon mTOR network activation in cells in which TSC2 was knocked down for the indicated amounts of time. Data are representative of three experiments. d, days. (B) Quantitative representations of simulated and experimentally determined Akt-pS^{473} and mTOR-pS^{2481} dynamics 60 min after induction with aa/ins in response to a gradual TSC2 knockdown. (Left) Relative quantitations of the simulated Akt-pS^{473} and mTOR-pS^{2481} behavior for the three hypotheses (Hypo 1, 2, and 3) upon gradual TSC2 knockdown. The amount of TSC1-TSC2 is indicated as a percentage of the total in the control system in the absence of knockdown. (Right) Quantitations of experimental results for 60 min after induction with aa/ins in cells in which TSC2 was reduced to the indicated amounts (percent of total). Values from three independent experiments were merged and grouped according to the amount of TSC2. $^{**}P < 0.01$; n.s., not significant; low TSC2 levels compared to high TSC2 levels. Differences were significant for Akt-pS^{473} and not significant for mTOR-pS^{2481}.

inhibition at all time points after induction, compared to the reduction predicted for hypothesis 2 or 3. Thus, these simulation results indicated that observation of mTOR-pS^{2481} in response to gradual TSC1-TSC2 inhibition should effectively distinguish hypothesis 1 from the other two hypotheses.

For experimental testing, we generated an inducible short hairpin TSC2 (shTSC2) cell line and induced TSC2 knockdown for 0, 1, 2, or 3 days, which resulted in a gradual decline in the amount of TSC2 (Fig. 6A). After starvation, cells were stimulated with aa/insulin for 5, 30, and 60 min. Because TSC1-TSC2 is a negative regulator of mTORC1, p70-S6K-pT^{389} increased as expected with gradual TSC2 inhibition (Fig. 6A). Relative quantitations for Akt-pS^{473} and mTOR-pS^{2481} at 60 min after aa/insulin induction are shown for the simulations of the three hypotheses and for the experimental data (Fig. 6B). Both the time course analysis (Fig. 6A) and the analysis of the effect of increasing knockdown of TSC2 (Fig. 6B) on Akt-pS^{473} suggested that hypothesis 2 or 3 may be correct. Hypothesis 1 of direct TSC1/2 activation of mTORC2 was clearly excluded because mTOR-pS^{2481} was unaffected by TSC2 inhibition at all time points (Fig. 6A) and at all amounts of TSC1-TSC2 inhibition (Fig. 6B). Our experimental data are in line with reported findings, indicating that TSC1-TSC2 does affect Akt-pS^{473} (*31*, *33*, *35*). However, according to our simulations, the regulation of Akt-pS^{473} by TSC1-TSC2 depends on the NFL and PI3K and, thus, in the absence of TSC1-TSC2 mTORC2–mediated phosphorylation of AktS^{473} is indirectly inhibited. Because the direct mTORC2 readout mTOR-pS^{2481} was unchanged in the absence of TSC1-TSC2, we can rule out TSC1-TSC2 as a direct activator of mTORC2.

We followed the same procedure that we used to identify the best experimental condition to assess whether TSC1-TSC2 indirectly controls mTORC2 through the NFL (*35*) (hypothesis 2). For gradual mTORC1 inhibition and consequent NFL inhibition, all three model structures predicted an increase of Akt-pS^{473} with decreasing mTORC1 activity (Fig. 5B). The simulations also predicted that mTOR-pS^{2481}would remain unaffected in hypotheses 1 and 3 and would gradually increase in response to mTORC1 inhibition in hypothesis 2 starting 40 min after induction with aa/insulin. This effect should be clearly experimentally visible at 100 min after induction with aa/insulin, and this paradigm could be used to distinguish hypothesis 2 from the other hypotheses.

For experimental testing, the specific mTORC1 component Raptor was gradually inhibited by knocking down Raptor in an inducible shRaptor cell line for 0, 1, 2, or 3 days. Cells were starved and stimulated with aa/insulin for 45, 100, and 180 min (Fig. 7A). Verification of effective mTORC1 inhibition in this experimental setup was performed by monitoring the abundance of p70-S6K-pT^{389}, which showed the expected reduction in response to decreased Raptor (Fig. 3, B and D). Relative quantitations of Akt-pS^{473} and mTOR-pS^{2481} in response to gradual Raptor inhibition are shown for the simulations of the three hypotheses and for experimental data at 100 min after induction with aa/insulin (Fig. 7B). As predicted for all three hypotheses, Akt-pS^{473} showed a significant increase with declining Raptor levels because the NFL is inhibited (Fig. 7, A and B). The abundance of Akt-pT^{308} also increased as mTORC1 was inhibited (Fig. 7A). In contrast, mTOR-pS^{2481} remained unaffected at all time points after induction with aa/insulin and at all Raptor levels (Fig. 7, A and B), which

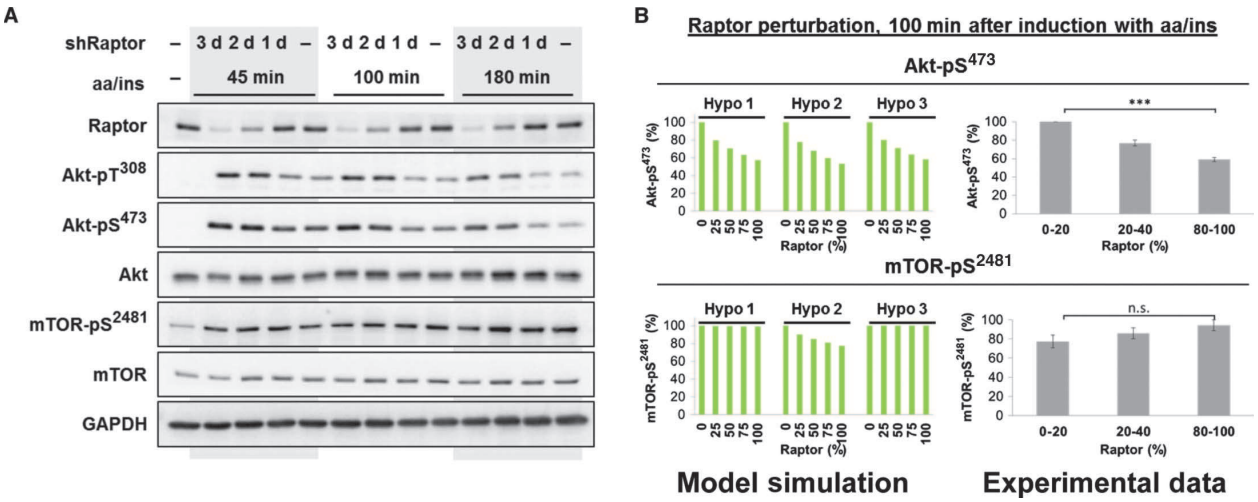

Fig. 7. mTOR-pS^{2481} is not affected by the NFL. (A) Representative immunoblot results of the network response upon mTOR network activation in cells in which Raptor was knocked down for the indicated amounts of time. Data are representative of three experiments. d, days. (B) Quantitative representations of simulated and experimentally determined Akt-pS^{473} and mTOR-pS^{2481} dynamics 100 min after induction with aa/ins in response to knockdown of Raptor to the indicated amounts (percent of total in the absence of knockdown). (Left) Relative quantitations of the simulated Akt-pS^{473} and mTOR-pS^{2481} behavior for the three hypotheses (Hypo 1, 2, 3) upon a gradual Raptor knockdown. (Right) Quantitations of experimental results 100 min after induction with aa/ins in cells in which Raptor was knocked down to the indicated amounts (percent of total). Values from three independent experiments were merged and grouped according to the amount of Raptor. Data are the average and SEM. ***$P < 0.001$; n.s., not significant; low Raptor levels compared to high Raptor levels. Differences were significant for Akt-pS^{473} and not significant for mTOR-pS^{2481}.

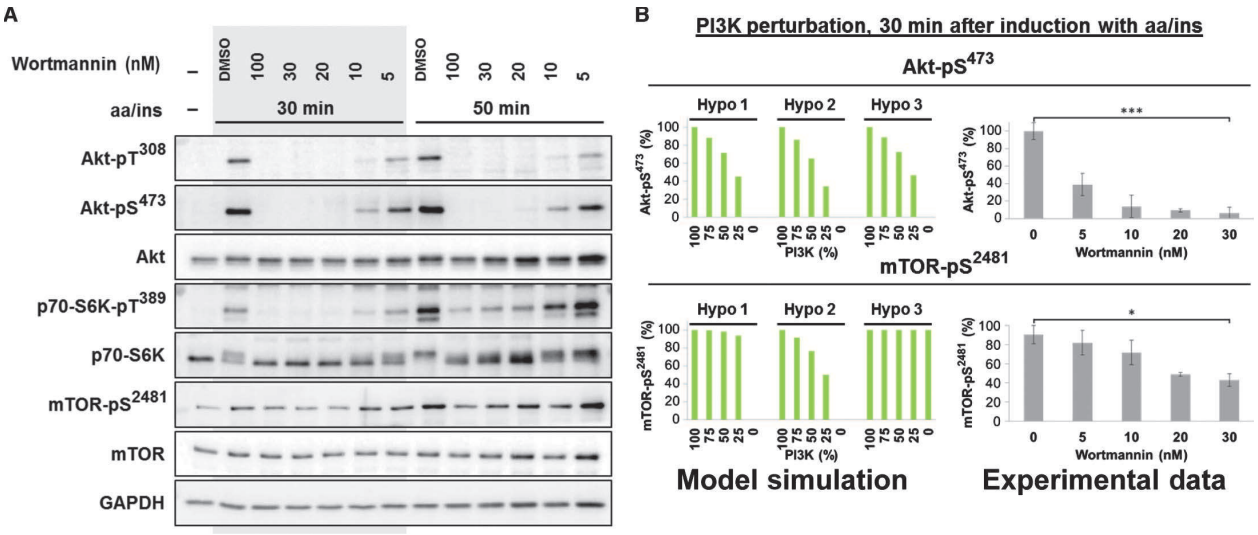

Fig. 8. mTOR-pS^{2481} is sensitive to the PI3K inhibitor wortmannin. (A) Representative immunoblot results of the network response upon mTOR network activation with aa/ins in the presence of wortmannin to inhibit PI3K. Data are representative of three experiments. (B) Quantitative representations of simulated and experimentally determined Akt-pS^{473} and mTOR-pS^{2481} dynamics 30 min after induction with aa/ins in cells in which PI3K activity was inhibited to the indicated amount (percent of total activity). (Left) Relative quantitations of the simulated Akt-pS^{473} and mTOR-pS^{2481} behavior for the three hypotheses (Hypo 1, 2, 3) in response to gradual PI3K inhibition (percent of total activity). (Right) Quantitations of experimental results 30 min after induction with aa/ins in cells in which PI3K was inhibited with the indicated concentrations of wortmannin. Data are the average and SEM of three experiments. *$P < 0.05$; ***$P < 0.001$; 30 nM compared to 0 nM wortmannin. Differences were significant for both Akt-pS^{473} and mTOR-pS^{2481}.

excludes hypothesis 2. Therefore, our model and the experimental testings allowed us to exclude the previously suggested hypothesis of an indirect mTORC2 regulation by TSC1-TSC2 and the NFL. Hence, mTORC2 is neither directly nor indirectly regulated by TSC1-TSC2.

Having excluded both hypotheses 1 and 2 and established that mTORC2 induction was independent of the NFL that inhibits IRS1 and thus PI3K activity, we directly tested whether the model and experimental testing would confirm hypothesis 3, that PI3K inhibition would not affect mTOR-pS^{2481} induction by aa/insulin. For gradual PI3K inhibition, our simulations predicted that Akt-pS^{473} in all three hypotheses would be reduced to a minimum level at all time points after induction with aa/insulin (Fig. 5B). In contrast, the model predicted that mTOR-pS^{2481} (Fig. 5A) would remain either unaffected by PI3K inhibition (hypotheses 1 and 3) or decline with decreasing PI3K starting 20 min after induction (hypothesis 2). Because hypotheses 1 and 2 were already excluded, we expected PI3K inhibition to result in the mTOR-pS^{2481} behavior predicted by hypothesis 3.

To experimentally test the validity of hypothesis 3, we starved cells, gradually inhibited PI3K with increasing wortmannin concentrations, and induced mTOR signaling by aa/insulin for 30 and 50 min (Fig. 8A). We chose a maximal wortmannin concentration of 100 nM, at and below which this inhibitor is specific for class I PI3Ks (*72*). Quantification of simulated and experimentally measured Akt-pS^{473} and mTOR-pS^{2481} in response to gradual PI3K inhibition is shown for 30 min after induction with aa/insulin (Fig. 8B). In agreement with our model, the dynamics of Akt-pS^{473} closely resembled the PDK1 phosphorylation of Akt-T^{308}, decreasing as PI3K was inhibited (Fig. 8A). The mTORC1 target p70-S6K-pT^{389} behaved similarly (Fig. 8A). In line with the literature (*73*) and as predicted by all three hypotheses, Akt-pS^{473} was already inhibited at 5 nM wortmannin and was strongly inhibited by concentrations of 10 nM wortmannin or higher (Fig. 8, A and B). Surprisingly, mTOR-pS^{2481} also was inhibited by wortmannin concentrations of 20 nM or higher (Fig. 8, A and B). Thus, our model and the experimental testing also exclude hypothesis 3 because mTORC2 activation appears to depend on PI3K activity.

A novel network structure integrating PI3K-dependent and NFL-independent activation of mTORC2

Our combined experimental-computational approach showed that insulin regulates mTORC2 through a wortmannin-sensitive enzyme (likely PI3K), and that mTORC2 is affected neither by the NFL nor by TSC1-TSC2. We, therefore, had to postulate a hypothesis 4: There is another kinase, in particular a wortmannin-sensitive but IRS1-independent PI3K species, that is activated by the IR and stimulates mTORC2 in response to insulin (Fig. 9, A and B). The model did not require recalibration because the new branch for mTORC2 activation by insulin was similar to the PI3K-independent hypothesis 3 but contained the new proposed PI3K, which is sensitive to wortmannin and refractory to the NFL.

We experimentally verified that this hypothesis 4 model fitted the data by showing that the simulated time courses matched the experimental readout dynamics [Fig. 9C (mTOR-pS^{2481} and Akt-pS^{473}) and fig. S16A

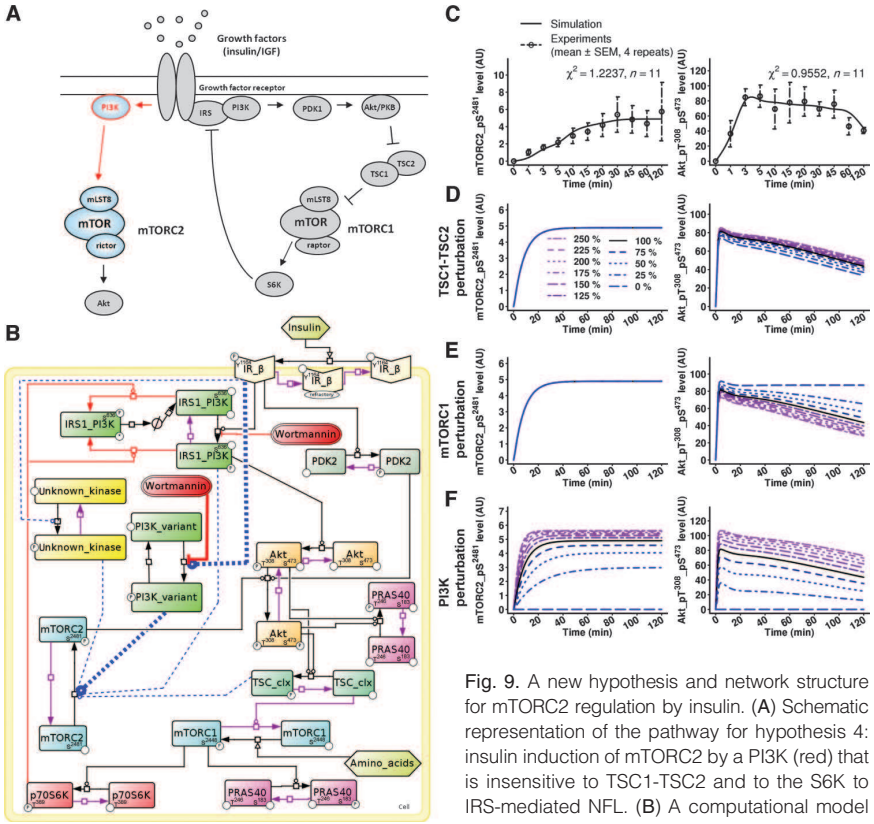

Fig. 9. A new hypothesis and network structure for mTORC2 regulation by insulin. (**A**) Schematic representation of the pathway for hypothesis 4: insulin induction of mTORC2 by a PI3K (red) that is insensitive to TSC1-TSC2 and to the S6K to IRS-mediated NFL. (**B**) A computational model corresponding to hypothesis 4. This hypothesis was equivalent to hypothesis 3 (PI3K and TSC1-TSC2–independent activation), assuming that the mTORC2 activator was sensitive to wortmannin. (**C**) The model simulation data for hypothesis 4 match the experimental dynamic phosphorylation data. The simulated and experimentally measured dynamics are shown for the mTORC2 readouts mTOR-pS^{2481} and Akt-pS^{473} (see fig. S16 for all other readouts). (**D**) Predictions for mTOR-pS^{2481} and Akt-pS^{473} upon gradual TSC1-TSC2 knockdown match the experimental data, which are presented in Fig. 6, A and B (right side). Whereas at 60 min after induction Akt-pS^{473} is gradually reduced by TSC2 inhibition, mTOR-pS^{2481} is TSC2-insensitive. See fig. S16 for Akt-pT^{308} and p70-S6K-pT^{389}. (**E**) Predictions for mTOR-pS^{2481} and Akt-pS^{473} readouts upon gradual Raptor knockdown match the experimental data, which are presented in Fig. 7, A and B (right side). Whereas at 100 min after induction Akt-pS^{473} is gradually induced by Raptor inhibition, mTOR-pS^{2481} is Raptor-insensitive. See fig. S16 for Akt-pT^{308} and p70-S6K-pT^{389}. (**F**) Predictions for mTOR-pS^{2481} and Akt-pS^{473} readouts upon gradual PI3K inhibition match the experimental data, which are presented in Fig. 8, A and B (right side). Both Akt-pS^{473} and mTOR-pS^{2481} are gradually reduced by wortmannin at 30 min after induction. See fig. S16 for Akt-pT^{308} and p70-S6K-pT^{389}.

(curves for all other readouts)]. Next, we modeled the dynamic network response under all previously tested network perturbations (gradual TSC1-TSC2, mTORC1, or PI3K inhibition) and compared the simulations to our experimental data (simulation in Fig. 9, D to F, and fig. S16B; data in Figs. 6 to 8). For each of the three network perturbations, the predictions for all readout dynamics (Fig. 9, D to F) matched the experimental data (Figs. 6 to 8). Identifiability and sensitivity analyses for hypothesis 4 are shown in figs. S17 and S18. The identifiability analysis reports low correlation between the estimated parameters, indicating that the parameters can be identified. Thus, the new network model of a PI3K-species–dependent and NFL-independent mTORC2 induction accurately predicted the responsiveness of mTORC2 to PI3K inhibition, and mTORC2 insensitivity to gradual TSC1-TSC2 or mTORC1 inhibition.

Because a model for mTORC2 activation through an NFL-insensitive PI3K was unexpected, we performed additional experimental testing. To confirm that the reduction of mTOR-pS^{2481} in response to wortmannin was associated with mTORC2, we treated cells with PP242 or wortmannin, or knocked down Raptor and then immunoprecipitated mTORC2 with an antibody recognizing Sin1 (Fig. 10A). We found that both PP242 and wortmannin significantly reduced mTOR-pS^{2481} associated with the immunoprecipitated mTORC2 (Fig. 10B), but that mTORC1 inhibition by shRaptor did not affect mTOR-pS^{2481} associated with the immunoprecipitated mTORC2 (Fig. 10, A and B). These results are consistent with the whole-cell lysate experiments (Figs. 1, E and F, and 8B) and support our previous conclusion that wortmannin inhibits mTORC2.

To verify the PI3K specificity of the wortmannin effect on mTORC2, we inhibited PI3K by two alternative means—with another PI3K inhibitor LY294002 or by overexpression of the PI3K antagonist PTEN (phosphatase and tensin homolog deleted from chromosome 10). We found that mTOR-pS^{2481} was reduced in cells exposed to LY294002 at concentrations as low as 1 μM (Fig. 10C) and in cells overexpressing PTEN (Fig. 10D). Thus, three separate experimental approaches indicated that mTORC2 activation depends on PI3K.

Mechanistic exploration in several cell types: mTORC2 activation independent of Akt

The hypothesis 4 model predicted that the PI3K-dependent, NFL-insensitive activation of mTORC2 should be insensitive to Akt. We overexpressed myristoylated Akt (myr-Akt), which is constitutively recruited to the membrane and constitutively active even without insulin (*74*), or a kinase-dead myr-Akt variant (myr-Akt K179M) in HeLa and C2C12 cells and monitored the activity of mTORC1 and mTORC2 (Fig. 10, E and F). For cells expressing the constitutively active Akt, phosphorylation of the mTORC1 substrate p70-S6K-T^{389} was increased by myr-Akt, whereas it was decreased in the cells expressing the myr-Akt K179M. In contrast, the mTORC2 readout mTOR-pS^{2481} was unchanged in the presence of either of the two myr-Akt constructs. We confirmed that mTOR-pS^{2481} specifically reflected mTORC2 activity in C2C12 cells because the amount of mTOR-pS^{2481} was decreased in response to the mTOR kinase inhibitor PP242, but was unaffected by the mTORC1-specific

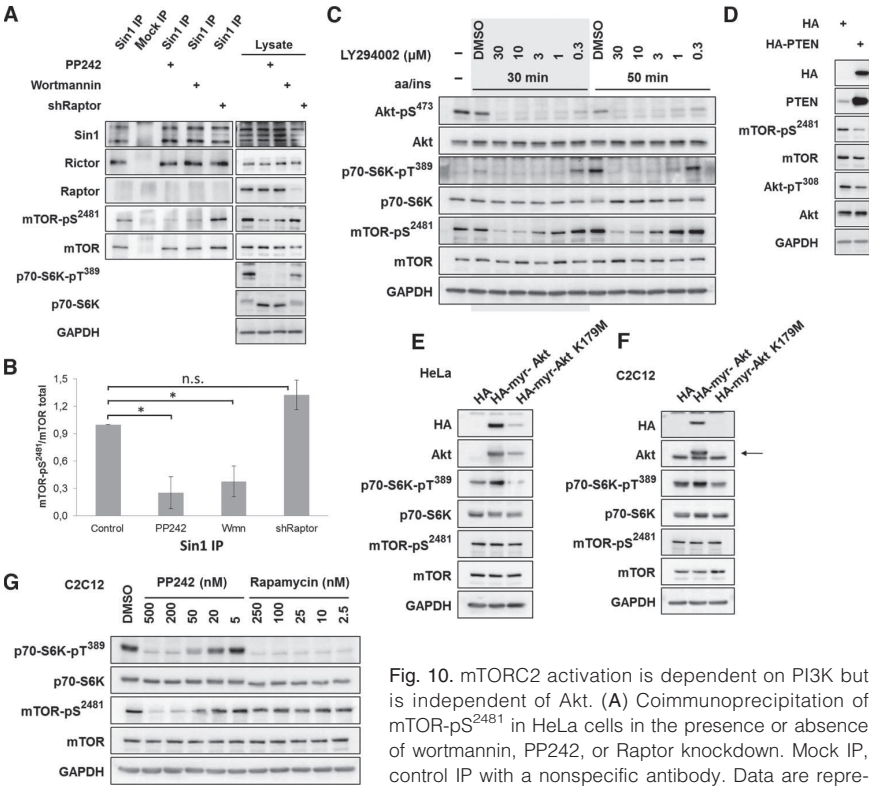

Fig. 10. mTORC2 activation is dependent on PI3K but is independent of Akt. (**A**) Coimmunoprecipitation of mTOR-pS^{2481} in HeLa cells in the presence or absence of wortmannin, PP242, or Raptor knockdown. Mock IP, control IP with a nonspecific antibody. Data are representative of three experiments. (**B**) Quantitation of data from three experiments similar to that shown in (A) for mTOR-pS^{2481} relative to total amount of immunoprecipitated mTOR. *$P < 0.05$; n.s., not significant. For PP242 and wortmannin treatments compared to control, there were significant differences in mTOR-S^{2481} association with Sin1. For the Raptor knockdown compared to control, the differences in mTOR-pS^{2481} association were not significant. (**C**) Effect of the PI3K inhibitor LY294002 on mTOR-pS^{2481} and other components of the mTOR network in HeLa cells. Data are representative of three experiments. (**D**) Effect of HA-tagged PTEN overexpression on mTOR-pS^{2481}. Data are representative of three experiments. HA, HeLa cells transfected with empty vector control. (**E**) Effect of constitutively active (HA–myr-Akt) or kinase-dead (HA–myr-Akt K179M) Akt on mTOR-pS^{2481} and other components of the mTOR network in HeLa cells. Data are representative of three experiments. (**F**) The effect of constitutively active (HA–myr-Akt) or kinase-dead (HA–myr-Akt K179M) Akt on mTOR-pS^{2481} and other components of the mTOR network in C2C12 myoblasts. The specific Akt signal is indicated by an arrow. Data are representative of three experiments. (**G**) Confirmation that mTOR-pS^{2481} is a specific mTORC2 readout in C2C12 myoblasts. The indicated proteins were detected in cells in the presence or absence of the indicated concentrations of PP242 or rapamycin in the continuous presence of aa/insulin. Data are representative of three experiments.

drug rapamycin (Fig. 10G). Thus, mTORC2 activity was not induced by Akt.

DISCUSSION

We present a dynamic mTOR network model, which is based on an integrated experimental-computational approach. We initially postulated three different network structures for mTORC2 induction by insulin, which guided experiments to test the hypotheses. The results of the simulations and experimental data indicated that none of the previously suggested mechanisms of mTORC2 activation were accurate: TSC1-TSC2 is not a direct activator of mTORC2; TSC1-TSC2 does also not indirectly control mTORC2 through inhibition of PI3K by the NFL; and mTORC2 activation depends on PI3K. However, the PI3K-dependent mTORC2 activation is insensitive to the NFL. We, therefore, postulated an activation pathway involving a PI3K variant that is independent of the NFL and we tested this hypothesis by developing a network structure that matched the observed mTOR pathway dynamics, performing simulations, and then experimentally verifying the predictions. Consistent with this model, experimental testing showed that mTORC2 activity was sensitive to different modes of PI3K inhibition but was insensitive to constitutive activation of Akt in several cell types.

Dynamic modeling has been used extensively in the study of cell signaling networks, yielding many important insights related to cellular behavior (*75*). Here, we use dynamic modeling to discriminate among alternative network structures, in particular alternative modes of mTORC2 regulation. Others have used similar approaches to study the possible network structures for the segment polarity gene network (*76*) and the extracellular signal–regulated kinase pathway (*77*). Although network testing can be performed with a Bayesian statistical approach (*77*), we chose to perform experimental testing to distinguish among the proposed network topologies because our simulated conditions and outputs were experimentally tractable.

Because our approach relied on the simulation and experimental testing of differential network dynamics under the assumption of alternative network structures, this may have enabled us to identify a network structure for insulin-regulated mTORC2 activation that is different from any other regulatory mechanism proposed thus far. Our approach enabled exploration of the network dynamics of endogenous proteins, whereas other purely experimental studies have relied on approaches that interfere with the dynamics under investigation, for example, overexpression of mutagenized network components that uncouple upstream cues from feedback inhibition (*31*, *33*). We also confirmed mTOR-pS^{2481} as a specific and direct readout for mTORC2 activity, which unlike other mTORC2 readouts does not require activation by the NFL-dependent PI3K. Because we used changes in network dynamics as a means of testing alternative network structures and we used the phosphorylation status of mTOR Ser^{2481} as the readout of mTORC2 activity, this work is distinguishable from earlier studies (*31*, *33*, *35*), and these differences in the approach may account for the conclusion that mTORC2's induction is independent of TSC1-TSC2 and the NFL.

In addition to revealing a new mechanism of regulation of mTORC2 in response to insulin, our analyses revealed additional complexity in the regulation of Akt. Model parameterization revealed more complex dynamics for mTORC2s target site Ser^{473} in the AGC kinase Akt than for Ser^{2481} in mTOR, and this could not be explained exclusively by mTORC2 activation. To integrate Akt-pS^{473} dynamics into the dynamic network model, we had to estimate a second PDK2 that accounted for the early peak of Akt-pS^{473} at 3 min after induction with aa/insulin (Fig. 2A). In addition to mTORC2, various other PDK2 candidates for Akt have been reported, including DNA-PK (*78*, *79*), ILK (*80*), ATM (*81*), MAPKAPK-2 (*82*), PKC (*83*, *84*), Pak1 (*85*), and even Akt autophosphorylation (*86*), any of which may contribute to Akt-pS^{473} dynamics under different metabolic conditions. Furthermore, we observed that upon network perturbations involving the NFL, the dynamics of mTOR-pS^{2481} were different from those of Akt-pS^{473}, with only the latter resembling the PDK1 phosphorylation on Thr^{308} of Akt (Figs. 6A and 7A). Thus, the AGC kinase targets of mTORC2 were not suitable readouts of mTORC2 activity and could not be used in our system to analyze the dependence of mTORC2 activity on TSC1-TSC2 because TSC1-TSC2 inhibition induces NFL that inhibits PI3K, which in turn can affect AGC kinase phosphorylation by their PDK2s, independently of the actual PDK2 activity. Because of this complexity in Akt phosphorylation dynamics, we chose mTOR-pS^{2481} as the readout of mTORC2 activity. Although mTOR-pS^{2481} has been identified on Raptor-associated mTOR (mTORC1) and is rapamycin-sensitive in 3T3-L1 adipocytes (*62*, *64*), rapamycin did not affect mTOR-pS^{2481} in whole-cell lysates of human embryonic kidney (HEK) 293 cells (*64*) or Tag Jurkat cells (*61*). Soliman *et al.* (*64*) concluded that the rapamycin-insensitive, mTORC2-associated mTOR-pS^{2481} signal predominated over the rapamycin-sensitive, mTORC1-associated mTOR-pS^{2481} signal in HEK293 cells, possibly due to a relatively low abundance of mTORC1 compared to mTORC2. We also found that mTOR-pS^{2481} was predominantly associated with mTORC2 in HeLa cells, which we used for our experimental testing.

Our model assumes that the NFL is exclusively executed by p70-S6K, phosphorylating and thereby inhibiting IRS. GRB10-dependent IR inhibition in response to activated mTORC1 may also contribute to the NFL (*87*, *88*), thus adding more complexity to the NFL mechanism. Although the identification of GRB10 as a contributor to the NFL is mechanistically relevant, the effect is the same, namely, the inhibition of IRS in response to mTORC1 activity, and is readily detected by the reduction of Akt-pT^{308} upon high mTORC1 activity. Given the need to reduce the complexity of our model to enable parameterization, we did not introduce these mechanisms separately into our model, but combined them into one step.

Our data suggested that mTORC2 activity is independent of the NFL, which is consistent with previous studies (*31*, *33*). To ensure that we achieved full activation of both mTOR complexes and thus activation of the NFL, we stimulated the cells with both amino acids and insulin induction. We experimentally observed the activation of the NFL starting 45 min after induction, as measured by IRS1-pS^{636} (Fig. 2, A and B). Thus, under conditions in which the NFL was active, network perturbations inducing or inactivating the NFL did not affect mTORC2 activity as measured by mTOR-pS^{2481}.

Although mTORC2 activity was independent of the NFL, it was dependent on PI3K activity (Fig. 8, A and B). The dynamics of mTOR-pS^{2481} were not affected by inhibition of the TSC1-TSC2 complex or mTORC1, but were inhibited by pharmacological inhibition of PI3K or reduction in its downstream signaling by overexpression of PTEN. Because pharmacological inhibitors can have off-target effects, we used a maximum wortmannin concentration of 100 nM, which has been reported to specifically inhibit only class I PI3Ks (*72*). Although we found that mTOR-pS^{2481} dynamics were less sensitive to wortmannin than were the dynamics of the PDK1-targeted Akt-pT^{308}, mTOR-pS^{2481} inhibition occurred with wortmannin concentrations as low as 20 nM, indicating that mTORC2 inhibition was dependent on class I PI3K activity, which is consistent with previous studies (*61*, *64*). PDK1-deficient cells exhibited a wortmannin-sensitive phosphorylation on Ser^{473} of Akt (*89*), which, although not previously linked to mTORC2 activity, supports our hypothesis of a PI3K-dependent but Akt-independent (and therefore NFL- and TSC1-TSC2–independent) mTORC2 induction. This proposed PI3K regulatory

mechanism was surprising because PI3K induction by insulin is generally thought to be IRS-dependent (*1*), and IRS is inhibited by active p70-S6K and thereby mediates the NFL. Consequently, we propose that mTORC2 is induced by a PI3K species that is different from the PI3K that induces mTORC1, because mTORC1 activity strictly depends on TSC1-TSC2 and the NFL (*1*, *7*).

In our new proposed model for mTOR activation by insulin and amino acids, Akt should activate mTORC1 through the canonical insulin–IRS–PI3K–Akt–TSC1-TSC2 pathway, but should not participate in mTORC2 activation, which is induced by a different PI3K. Indeed, we showed in several cell lines that constitutively active Akt did not induce mTORC2 activity (mTOR-pS^{2481}), although it did activate mTORC1. Two studies have reported mTORC2 regulation downstream of PI3K that differs from the canonical Akt–TSC1-TSC2 signaling axis. Direct PI3K-dependent induction of mTORC2 by PtdIns(3,4,5)P_3 binding (*90*) has been observed, and ribosomal proteins have been described to bind and activate mTORC2 in a PI3K-dependent manner (*91*). Clearly, these mechanisms require further study, which will likely reveal further molecular connectors of PI3K and mTORC2.

What kind of mechanism could account for the observed NFL insensitivity of PI3K for mTORC2 induction? The NFL is mediated by IRS, which activates PI3K downstream of insulin and the IR (*1*). However, PI3K activity has also been observed in cells devoid of IRS protein (*92*, *93*), and the IR may activate PI3K in part by direct binding (*94*). Such IRS-independent PI3K activity might mediate NFL-independent stimulation of mTORC2 activity. For class I PI3Ks, there are at least seven alternative regulatory subunits and four alternative catalytic subunits, and specific combinations of these subunits might mediate different physiologic outputs. Receptor binding and abundance of the isoforms are differentially regulated by metabolic inputs, such as growth factors or amino acids (*95*). We may have detected this apparently IRS-independent PI3K activation because we used simultaneous stimulation with both insulin and amino acids to assure full induction of both mTOR complexes. In contrast, previous studies have mainly tested the effect of a single stimulus on class I PI3K activation. In a physiological environment, cells are confronted with multiple simultaneous inputs, and full activation of some PI3K isoforms can require multiple upstream inputs (*95*). Hence, the existence of an NFL-independent class I PI3K is conceivable and requires further investigation.

In conclusion, the suggested novel network structure, connecting mTORC2 to its upstream inputs, is supported by the existing literature and reveals a need to reevaluate the mTORC2 regulatory mechanisms. The complexity of differential mTORC1 and mTORC2 regulation that we propose highlights the need to apply integrated computational-experimental approaches to understand complex signaling and regulatory networks. Because our dynamic model of mTORC1 and mTORC2 signaling is a mathematical representation of the differential signal transduction toward mTORC1 and mTORC2, it enables simulation of the signaling dynamics that are transmitted through the network under different metabolic conditions. Moreover, despite being a simplification, our model simulations mathematically showed that the simplified system was sufficient to explain the experimental observations. The fully parameterized model provides a resource for future work and other modeling efforts can extend and build upon it, as well as provide a framework on which pharmacological interventions can be tested.

MATERIALS AND METHODS

Lentiviral knockdown cell lines

Experiments were performed in HeLa α Kyoto cells and C2C12 myoblasts. For inducible knockdown of Raptor or TSC2, cells were transduced with lentivirus encoding the tetracycline-sensitive tTR-KRAB repressor and a DsRed reporter (*96*). Cells were subsequently transfected with lentivirus encoding the specific short hairpin RNA (target sequence Raptor: 5′-GGCTAGTCTGTTTCGAAATTT-3′, TSC2: 5′-CGACGAGTCAAACAAGCCAAT-3′), and a green fluorescent protein (GFP) reporter (pLVTH vector), both under the control of tTR-KRAB. For lentivirus-mediated knockdown of Rictor, a pLKO.1-based short hairpin construct specific for Rictor (Addgene plasmid 1853) and a scrambled control sequence (Addgene plasmid 1864) were obtained from Addgene (*21*). HeLa cells were transfected with viral supernatant twice as described previously (*63*) and harvested 60 hours after transfection.

Overexpression of PTEN and myr-Akt variants

Plasmids were ordered from Addgene: N-terminally hemagglutinin (HA)–tagged pSG5L HA PTEN wild type, N-terminally myristoylated and HA-tagged pLNCX.myr.HA.Akt1, and N-terminally myristoylated and HA-tagged, kinase-dead pLNCX.myr.HA.Akt1 K179M. Transfection was performed with 6 μg per 6-cm dish by the use of JetPEI reagent according to the manufacturer's instructions. Cells were harvested 24 hours after transfection.

Antibodies and reagents

The antibody recognizing PRAS40 (Ser^{183} phosphorylated) was purchased from IBL. The polyclonal antibody recognizing PRAS40 (Thr^{246} phosphorylated) was purchased from Biosource. The monoclonal antibody recognizing glyceraldehyde-3-phosphate dehydrogenase (GAPDH) was purchased from Abcam. The antibody recognizing Rictor was purchased from Bethyl. Horseradish peroxidase (HRP)–conjugated goat anti-mouse and goat anti-rabbit immunoglobulin G (IgG) were purchased from Pierce Biotechnology (Thermo Scientific). Antibodies recognizing Akt, phospho-Akt (Thr^{308}), phospho-Akt (Ser^{473}), phospho–IGF-I receptor β (Tyr^{1131})/IRβ (Tyr^{1146}), IRS-1, phospho–IRS-1 (Ser$^{636/639}$), mTOR, phospho-mTOR (Ser^{2448}), phospho-mTOR (Ser^{2481}), PRAS40, p70S6K, phospho-p70S6K (Thr^{389}), and TSC2 were purchased from Cell Signaling Technology. The antibody recognizing IRβ was purchased from Santa Cruz Biotechnology. Rapamycin and LY294002 were purchased from Calbiochem, Merck. PP242 and wortmannin were purchased from Sigma-Aldrich. Chemicals were supplied by Carl Roth if not indicated otherwise.

Immunoprecipitation

Immunoprecipitations were performed as described elsewhere (*13*, *19*). Lysis buffer was complemented with protease inhibitors (Complete; Roche), Phosphatase Inhibitor Cocktail 2, Phosphatase Inhibitor Cocktail 3 (both Sigma-Aldrich), and PP242 to inhibit residual mTOR activity after the time of lysis. Immunoprecipitations were performed with antibody (5 μg/ml) [antibody recognizing Sin1, Raptor, or rabbit IgG (all Bethyl)] and with magnetic Dynabeads Protein G (Invitrogen).

Analysis of whole-cell lysates

For calibration data sets, HeLa cells were starved for serum and amino acids by exchanging standard growth medium for Hank's buffered salt solution (HBSS) (PAN Biotech GmbH) overnight to inhibit mTOR pathway activity. After 16 hours of starvation, mTOR signaling was restimulated with Dulbecco's modified Eagle's medium (DMEM) containing amino acids and supplemented with 100 nM insulin (Sigma-Aldrich).

Gradual knockdowns of Raptor or TSC2 were established by induction with doxycycline (5 μg/ml; Calbiochem, Merck) for 0, 1, 2, or 3 days. Cells were starved for 16 hours in HBSS and mTOR signaling was induced with DMEM (PAA) supplemented with 100 nM insulin. PP242 and rapamycin were added 1 hour before lysis. Wortmannin or LY294002 was

added 30 min before and during the stimulation with DMEM supplemented with 100 nM insulin. Cells were washed once with phosphate-buffered saline (PBS) and lysed with TNE lysis buffer [50 mM tris-HCl (pH 8.0), 150 mM NaCl, 1% (v/v) Triton X-100 (Calbiochem, Merck), Complete (Roche), Phosphatase Inhibitor Cocktail 2, and Phosphatase Inhibitor Cocktail 3 (both Sigma-Aldrich)]. Protein concentrations were measured (Protein Assay Dye Reagent Concentrate, Bio-Rad) according to the manufacturer's protocol. Concentrations were adjusted with lysis buffer. Lysates were diluted in sample buffer [5×: 6 ml glycerol, 0.6 ml β-mercaptoethanol, 1.0 g SDS, 3.75 ml 1 M tris (pH 6.8), 2 mg bromophenol blue, and 2 ml H_2O]. Whole-cell lysates were analyzed with SDS–polyacrylamide gel electrophoresis (SDS-PAGE) gels. Proteins were transferred to polyvinylidene difluoride (PVDF) membranes (Millipore), blocked with 5% bovine serum albumin (BSA) in TBST [8 g NaCl, 0.2 g KCl, 8 g tris (pH 7.4), 0.1% Tween 20] for a minimum of 30 min, and incubated with the primary antibody in 5% BSA in TBST overnight with shaking at 4°C. Blots were washed three times with TBST, incubated with secondary antibodies coupled to HRP, and washed three times with TBST before detection.

Quantitation of immunoblots

HRP was detected with the ECL Western Blotting Substrate or the SuperSignal West Femto reagent (Pierce Biotechnology, Thermo Scientific), and the emitted light was detected and quantified with a chemiluminescence imaging analyzer (LAS 4000 mini; Fujifilm). Obtained images were analyzed with Multi-Gauge version 3.0 software (Fujifilm). Local background was subtracted. All data were normalized against GAPDH. Representative blots were exported as TIF files and processed with Adobe Photoshop.

Modeling

CellDesigner 4.2 (*97*) was used to construct the model network topology in SBGN (*59*). COPASI 4.7.34 (*98*) was used for all deterministic simulations, parameter estimations, parameter scanning, and sensitivity analysis. The deterministic simulation algorithm (LSODA) was configured with the following parameters: duration, 1440; interval size, 1; intervals, 1440; integrate reduced model, 0; relative tolerance, 1×10^{-6}; absolute tolerance, 1×10^{-12}; maximum internal steps, 10,000. The algorithm used for parameter estimation was simulated annealing (*99*, *100*), configured with the following parameters: start temperature, 1; cooling factor, 0.85; tolerance, 1×10^{-6}; random number generator, 1; seed, 0. The parameter estimation weight method was mean square and the experiment type was time course. The initial concentration of the species in nonphosphorylated state was fixed to the maximum intensity of the third quantile time course, computed from the four experimental data sets, of the corresponding experimental phosphorylated protein. This ensured that the modeled kinases did not saturate their substrates and that the concentrations of the substrates remained small. The initial concentration of the species in any other state was fixed to 0. The initial concentration of PDK2 was assumed to be equal to the concentration of the β subunit of the IR because the two species are directly connected in the model. In the absence of experimental data for the TSC complex, the initial concentration was assumed to be 10. The models were formalized with only mass action reactions. For each phase, the kinetic rate constants were estimated by running 350 independent calibrations, each initialized with a random initial configuration of the parameters. The parameter values were constrained within the interval $[1 \times 10^{-4}, 1]$ except for the Akt parameters, which were constrained within the interval $[1 \times 10^{-4}, 10]$. For each calibration phase (F), the solutions of the estimations consistent with the data and achieving the lowest root mean square error (RMSE) were selected as the best solutions set (BS). Among these, the solution closest to the centroid of the BS cluster in the parameter space was selected with the following formula:

$$\arg\min_{S \in \mathrm{BS_F}} \sum_{i=1}^{N} (S(p_i) - \mu_i)^2$$

where $\mathrm{BS_F} = \{x | \forall\, y \in \mathrm{AllSolutions}, \mathrm{RMSE}(\mathrm{Model}(x), \mathrm{Data}) \leq \mathrm{RMSE}(\mathrm{Model}(y), \mathrm{Data})\}$, p_i is the ith estimated parameter in S, μ_i is the ith parameter mean computed from $\mathrm{BS_F}$, and N is the number of estimated parameters.

Model identifiability based on correlation analysis of sensitivity trajectories was calculated with SBToolbox2 and SBPDToolbox (*101*) for MATLAB. SBMLToolbox 4.0.1 (*102*) was used to import our SBML models into SBToolbox2. Identifiability analysis tables for the general model and the four hypotheses models are depicted in figs. S5, S8, S10, S12, and S17.

All parameter values for the final models are given in tables S2 and S3. The sensitivity analysis algorithm was configured for time series with the following parameters: Delta factor, 0.001, and Delta minimum, 1×10^{-12} (figs. S6, S9, S11, S13, and S18). We also used COPASI and CellDesigner to export the models as SBML (*103*) Level 2 Version 4 (models S1 to S5). CellDesigner was used to generate the extended mTOR network model in SBGN (*59*) graphical notation (model S6).

Statistics

The statistical and programming language R version 2.12.1 (*104*) was used to calculate the statistics and generate the plots. The SEM was chosen to estimate the statistical variability of the measured samples of experimental time course. Model goodness of fit was defined by computing Akaike information criterion (*105*) and χ^2 was calculated as follows:

$$\chi^2 = \sum_{i=1}^{N} \left(\frac{y_i - \mu(d_i)}{\sigma(d_i)} \right)^2$$

where N is the number of experimental data points and $y_i - \mu(d_i)$ is the ith residual between the simulated and the experimental mean data point, which is normalized by the SD of the same data point. For the general model and the four hypotheses, χ^2 and Akaike information criterion measures are provided in table S4. Tukey's honest significant differences (HSD) test, in conjunction with one-way analysis of variance (ANOVA), was used as statistical test for multiple comparisons among groups of experimental data.

SUPPLEMENTARY MATERIALS

www.sciencesignaling.org/cgi/content/full/5/217/ra25/DC1

Fig. S1. Extended graphical model of the mammalian TOR network.
Fig. S2. A linear relationship between Western blot signals and protein concentrations.
Fig. S3. Phases of the calibration process.
Fig. S4. Details of a calibration phase.
Fig. S5. Identifiability analysis for the general model.
Fig. S6. Sensitivity analysis for the general model.
Fig. S7. Comparison between the simulated and experimental time courses for hypotheses 1, 2, and 3 for readouts of the mTOR network.
Fig. S8. Identifiability analysis for hypothesis 1: TSC1-TSC2–dependent hypothesis mTORC2 regulation.
Fig. S9. Sensitivity analysis for hypothesis 1: TSC1-TSC2–dependent hypothesis mTORC2 regulation.
Fig. S10. Identifiability analysis for hypothesis 2: NFL-mTORC2 regulation.
Fig. S11. Sensitivity analysis for hypothesis 2: NFL-mTORC2 regulation.
Fig. S12. Identifiability analysis for hypothesis 3: PI3K-independent mTORC2 regulation.

Fig. S13. Sensitivity analysis for hypothesis 3: PI3K-independent mTORC2 regulation.
Fig. S14. The influence of perturbations of TSC1-TSC2, mTORC1, and PI3K on the phosphorylation of Akt-T^{308} for the three hypotheses.
Fig. S15. The influence of perturbations of TSC1-TSC2, mTORC1, and PI3K on the phosphorylation of p70-S6K-T^{389} for the three hypotheses.
Fig. S16. Simulation and perturbations for the new network structure based on hypothesis 4: PI3K-dependent, NFL-independent regulation of mTORC2.
Fig. S17. Identifiability analysis for hypothesis 4: PI3K-dependent, NFL-independent regulation of mTORC2.
Fig. S18. Sensitivity analysis for hypothesis 4: PI3K-dependent, NFL-independent regulation of mTORC2.
Table S1. Ordinary differential equations of the general model and the models representing hypotheses, 1, 2, and 3 for mTORC2 activation.
Table S2. Parameter values of the general model.
Table S3. Parameter values of hypotheses 1, 2, and 3.
Table S4. Summary of model goodness of fit.
Models S1 to S6.

REFERENCES AND NOTES

1. R. Zoncu, A. Efeyan, D. M. Sabatini, mTOR: From growth signal integration to cancer, diabetes and ageing. *Nat. Rev. Mol. Cell Biol.* **12**, 21–35 (2011).
2. J. J. Howell, B. D. Manning, mTOR couples cellular nutrient sensing to organismal metabolic homeostasis. *Trends Endocrinol. Metab.* **22**, 94–102 (2011).
3. C. Garcia-Echeverria, Blocking the mTOR pathway: A drug discovery perspective. *Biochem. Soc. Trans.* **39**, 451–455 (2011).
4. P. Polak, M. N. Hall, mTOR and the control of whole body metabolism. *Curr. Opin. Cell Biol.* **21**, 209–218 (2009).
5. N. Cybulski, M. N. Hall, TOR complex 2: A signaling pathway of its own. *Trends Biochem. Sci.* **34**, 620–627 (2009).
6. M. E. Feldman, K. M. Shokat, New inhibitors of the PI3K-Akt-mTOR pathway: Insights into mTOR signaling from a new generation of Tor kinase domain inhibitors (TORKinibs). *Curr. Top. Microbiol. Immunol.* **347**, 241–262 (2010).
7. S. Sengupta, T. R. Peterson, D. M. Sabatini, Regulation of the mTOR complex 1 pathway by nutrients, growth factors, and stress. *Mol. Cell* **40**, 310–322 (2010).
8. Y. Sancak, L. Bar-Peled, R. Zoncu, A. L. Markhard, S. Nada, D. M. Sabatini, Ragulator-Rag complex targets mTORC1 to the lysosomal surface and is necessary for its activation by amino acids. *Cell* **141**, 290–303 (2010).
9. Y. Sancak, D. M. Sabatini, Rag proteins regulate amino-acid-induced mTORC1 signalling. *Biochem. Soc. Trans.* **37**, 289–290 (2009).
10. J. Avruch, X. Long, Y. Lin, S. Ortiz-Vega, J. Rapley, A. Papageorgiou, N. Oshiro, U. Kikkawa, Activation of mTORC1 in two steps: Rheb-GTP activation of catalytic function and increased binding of substrates to raptor. *Biochem. Soc. Trans.* **37**, 223–226 (2009).
11. K. Thedieck, M. N. Hall, in *The Handbook of Cell Signaling*, R. Bradshaw, E. Dennis, Eds. (Elsevier, San Diego, CA, 2009), vol. 3, chap. 274, pp. 2285–2293.
12. E. Vander Haar, S. I. Lee, S. Bandhakavi, T. J. Griffin, D. H. Kim, Insulin signalling to mTOR mediated by the Akt/PKB substrate PRAS40. *Nat. Cell Biol.* **9**, 316–323 (2007).
13. K. Thedieck, P. Polak, M. L. Kim, K. D. Molle, A. Cohen, P. Jenö, C. Arrieumerlou, M. N. Hall, PRAS40 and PRR5-like protein are new mTOR interactors that regulate apoptosis. *PLoS One* **2**, e1217 (2007).
14. Y. Sancak, C. C. Thoreen, T. R. Peterson, R. A. Lindquist, S. A. Kang, E. Spooner, S. A. Carr, D. M. Sabatini, PRAS40 is an insulin-regulated inhibitor of the mTORC1 protein kinase. *Mol. Cell* **25**, 903–915 (2007).
15. L. Wang, T. E. Harris, R. A. Roth, J. C. Lawrence Jr., PRAS40 regulates mTORC1 kinase activity by functioning as a direct inhibitor of substrate binding. *J. Biol. Chem.* **282**, 20036–20044 (2007).
16. B. D. Fonseca, E. M. Smith, V. H. Lee, C. MacKintosh, C. G. Proud, PRAS40 is a target for mammalian target of rapamycin complex 1 and is required for signaling downstream of this complex. *J. Biol. Chem.* **282**, 24514–24524 (2007).
17. N. Oshiro, R. Takahashi, K. Yoshino, K. Tanimura, A. Nakashima, S. Eguchi, T. Miyamoto, K. Hara, K. Takehana, J. Avruch, U. Kikkawa, K. Yonezawa, The proline-rich Akt substrate of 40 kDa (PRAS40) is a physiological substrate of mammalian target of rapamycin complex 1. *J. Biol. Chem.* **282**, 20329–20339 (2007).
18. L. Wang, T. E. Harris, J. C. Lawrence Jr., Regulation of proline-rich Akt substrate of 40 kDa (PRAS40) function by mammalian target of rapamycin complex 1 (mTORC1)-mediated phosphorylation. *J. Biol. Chem.* **283**, 15619–15627 (2008).
19. E. Jacinto, R. Loewith, A. Schmidt, S. Lin, M. A. Ruegg, A. Hall, M. N. Hall, Mammalian TOR complex 2 controls the actin cytoskeleton and is rapamycin insensitive. *Nat. Cell Biol.* **6**, 1122–1128 (2004).
20. I. Tato, R. Bartrons, F. Ventura, J. L. Rosa, Amino acids activate mammalian target of rapamycin complex 2 (mTORC2) via PI3K/Akt signaling. *J. Biol. Chem.* **286**, 6128–6142 (2011).
21. D. D. Sarbassov, D. A. Guertin, S. M. Ali, D. M. Sabatini, Phosphorylation and regulation of Akt/PKB by the rictor-mTOR complex. *Science* **307**, 1098–1101 (2005).
22. E. Jacinto, V. Facchinetti, D. Liu, N. Soto, S. Wei, S. Y. Jung, Q. Huang, J. Qin, B. Su, SIN1/MIP1 maintains rictor-mTOR complex integrity and regulates Akt phosphorylation and substrate specificity. *Cell* **127**, 125–137 (2006).
23. C. Shiota, J. T. Woo, J. Lindner, K. D. Shelton, M. A. Magnuson, Multiallelic disruption of the *rictor* gene in mice reveals that mTOR complex 2 is essential for fetal growth and viability. *Dev. Cell* **11**, 583–589 (2006).
24. R. C. Hresko, M. Mueckler, mTOR·RICTOR is the Ser^{473} kinase for Akt/protein kinase B in 3T3-L1 adipocytes. *J. Biol. Chem.* **280**, 40406–40416 (2005).
25. J. M. García-Martínez, D. R. Alessi, mTOR complex 2 (mTORC2) controls hydrophobic motif phosphorylation and activation of serum- and glucocorticoid-induced protein kinase 1 (SGK1). *Biochem. J.* **416**, 375–385 (2008).
26. D. D. Sarbassov, S. M. Ali, D. H. Kim, D. A. Guertin, R. R. Latek, H. Erdjument-Bromage, P. Tempst, D. M. Sabatini, Rictor, a novel binding partner of mTOR, defines a rapamycin-insensitive and raptor-independent pathway that regulates the cytoskeleton. *Curr. Biol.* **14**, 1296–1302 (2004).
27. L. R. Pearce, D. Komander, D. R. Alessi, The nuts and bolts of AGC protein kinases. *Nat. Rev. Mol. Cell Biol.* **11**, 9–22 (2010).
28. E. Jacinto, A. Lorberg, TOR regulation of AGC kinases in yeast and mammals. *Biochem. J.* **410**, 19–37 (2008).
29. E. Fayard, G. Xue, A. Parcellier, L. Bozulic, B. A. Hemmings, Protein kinase B (PKB/Akt), a key mediator of the PI3K signaling pathway. *Curr. Top. Microbiol. Immunol.* **346**, 31–56 (2010).
30. K. Inoki, M. N. Corradetti, K. L. Guan, Dysregulation of the TSC-mTOR pathway in human disease. *Nat. Genet.* **37**, 19–24 (2005).
31. J. Huang, C. C. Dibble, M. Matsuzaki, B. D. Manning, The TSC1-TSC2 complex is required for proper activation of mTOR complex 2. *Mol. Cell. Biol.* **28**, 4104–4115 (2008).
32. J. Huang, B. D. Manning, A complex interplay between Akt, TSC2 and the two mTOR complexes. *Biochem. Soc. Trans.* **37**, 217–222 (2009).
33. J. Huang, S. Wu, C. L. Wu, B. D. Manning, Signaling events downstream of mammalian target of rapamycin complex 2 are attenuated in cells and tumors deficient for the tuberous sclerosis complex tumor suppressors. *Cancer Res.* **69**, 6107–6114 (2009).
34. W. van Veelen, S. E. Korsse, L. van de Laar, M. P. Peppelenbosch, The long and winding road to rational treatment of cancer associated with LKB1/AMPK/TSC/mTORC1 signaling. *Oncogene* **30**, 2289–2303 (2011).
35. Q. Yang, K. Inoki, E. Kim, K. L. Guan, TSC1/TSC2 and Rheb have different effects on TORC1 and TORC2 activity. *Proc. Natl. Acad. Sci. U.S.A.* **103**, 6811–6816 (2006).
36. E. A. Goncharova, D. A. Goncharov, H. Li, W. Pimtong, S. Lu, I. Khavin, V. P. Krymskaya, mTORC2 is required for proliferation and survival of TSC2-null cells. *Mol. Cell. Biol.* **31**, 2484–2498 (2011).
37. Y. Kamimura, Y. Xiong, P. A. Iglesias, O. Hoeller, P. Bolourani, P. N. Devreotes, PIP_3-independent activation of TorC2 and PKB at the cell's leading edge mediates chemotaxis. *Curr. Biol.* **18**, 1034–1043 (2008).
38. S. Lee, Z. Shen, D. N. Robinson, S. Briggs, R. A. Firtel, Involvement of the cytoskeleton in controlling leading-edge function during chemotaxis. *Mol. Biol. Cell* **21**, 1810–1824 (2010).
39. P. G. Charest, Z. Shen, A. Lakoduk, A. T. Sasaki, S. P. Briggs, R. A. Firtel, A Ras signaling complex controls the RasC-TORC2 pathway and directed cell migration. *Dev. Cell* **18**, 737–749 (2010).
40. H. Cai, S. Das, Y. Kamimura, Y. Long, C. A. Parent, P. N. Devreotes, Ras-mediated activation of the TORC2–PKB pathway is critical for chemotaxis. *J. Cell Biol.* **190**, 233–245 (2010).
41. G. S. Worthen, N. Avdi, A. M. Buhl, N. Suzuki, G. L. Johnson, FMLP activates Ras and Raf in human neutrophils. Potential role in activation of MAP kinase. *J. Clin. Invest.* **94**, 815–823 (1994).
42. L. Zheng, J. Eckerdal, I. Dimitrijevic, T. Andersson, Chemotactic peptide-induced activation of Ras in human neutrophils is associated with inhibition of p120-GAP activity. *J. Biol. Chem.* **272**, 23448–23454 (1997).
43. Y. Kamada, Y. Fujioka, N. N. Suzuki, F. Inagaki, S. Wullschleger, R. Loewith, M. N. Hall, Y. Ohsumi, Tor2 directly phosphorylates the AGC kinase Ypk2 to regulate actin polarization. *Mol. Cell. Biol.* **25**, 7239–7248 (2005).
44. E. Caron, S. Ghosh, Y. Matsuoka, D. Ashton-Beaucage, M. Therrien, S. Lemieux, C. Perreault, P. P. Roux, H. Kitano, A comprehensive map of the mTOR signaling network. *Mol. Syst. Biol.* **6**, 453 (2010).
45. P. Jain, U. S. Bhalla, Signaling logic of activity-triggered dendritic protein synthesis: An mTOR gate but not a feedback switch. *PLoS Comput. Biol.* **5**, e1000287 (2009).
46. C. Brännmark, R. Palmér, S. T. Glad, G. Cedersund, P. Strålfors, Mass and information feedbacks through receptor endocytosis govern insulin signaling as revealed using a parameter-free modeling framework. *J. Biol. Chem.* **285**, 20171–20179 (2010).
47. D. Ruths, M. Muller, J. T. Tseng, L. Nakhleh, P. T. Ram, The signaling Petri net-based simulator: A non-parametric strategy for characterizing the dynamics of cell-specific signaling networks. *PLoS Comput. Biol.* **4**, e1000005 (2008).

48. N. Borisov, E. Aksamitiene, A. Kiyatkin, S. Legewie, J. Berkhout, T. Maiwald, N. P. Kaimachnikov, J. Timmer, J. B. Hoek, B. N. Kholodenko, Systems-level interactions between insulin-EGF networks amplify mitogenic signaling. *Mol. Syst. Biol.* **5**, 256 (2009).
49. G. Cedersund, J. Roll, E. Ulfhielm, A. Danielsson, H. Tidefelt, P. Strålfors, Model-based hypothesis testing of key mechanisms in initial phase of insulin signaling. *PLoS Comput. Biol.* **4**, e1000096 (2008).
50. V. V. Kiselyov, S. Versteyhe, L. Gauguin, P. De Meyts, Harmonic oscillator model of the insulin and IGF1 receptors' allosteric binding and activation. *Mol. Syst. Biol.* **5**, 243 (2009).
51. D. Faratian, A. Goltsov, G. Lebedeva, A. Sorokin, S. Moodie, P. Mullen, C. Kay, I. H. Um, S. Langdon, I. Goryanin, D. J. Harrison, Systems biology reveals new strategies for personalizing cancer medicine and confirms the role of PTEN in resistance to trastuzumab. *Cancer Res.* **69**, 6713–6720 (2009).
52. L. Kuepfer, M. Peter, U. Sauer, J. Stelling, Ensemble modeling for analysis of cell signaling dynamics. *Nat. Biotechnol.* **25**, 1001–1006 (2007).
53. S. Nelander, W. Wang, B. Nilsson, Q. B. She, C. Pratilas, N. Rosen, P. Gennemark, C. Sander, Models from experiments: Combinatorial drug perturbations of cancer cells. *Mol. Syst. Biol.* **4**, 216 (2008).
54. A. R. Sedaghat, A. Sherman, M. J. Quon, A mathematical model of metabolic insulin signaling pathways. *Am. J. Physiol. Endocrinol. Metab.* **283**, E1084–E1101 (2002).
55. G. Wang, G. R. Krueger, Computational analysis of mTOR signaling pathway: Bifurcation, carcinogenesis, and drug discovery. *Anticancer Res.* **30**, 2683–2688 (2010).
56. P. K. Vinod, K. V. Venkatesh, Quantification of the effect of amino acids on an integrated mTOR and insulin signaling pathway. *Mol. Biosyst.* **5**, 1163–1173 (2009).
57. G. R. Smith, D. P. Shanley, Modelling the response of FOXO transcription factors to multiple post-translational modifications made by ageing-related signalling pathways. *PLoS One* **5**, e11092 (2010).
58. J. A. Papin, T. Hunter, B. O. Palsson, S. Subramaniam, Reconstruction of cellular signalling networks and analysis of their properties. *Nat. Rev. Mol. Cell Biol.* **6**, 99–111 (2005).
59. N. Le Novere, M. Hucka, H. Mi, S. Moodie, F. Schreiber, A. Sorokin, E. Demir, K. Wegner, M. I. Aladjem, S. M. Wimalaratne, F. T. Bergman, R. Gauges, P. Ghazal, H. Kawaji, L. Li, Y. Matsuoka, A. Villeger, S. E. Boyd, L. Calzone, M. Courtot, U. Dogrusoz, T. C. Freeman, A. Funahashi, S. Ghosh, A. Jouraku, S. Kim, F. Kolpakov, A. Luna, S. Sahle, E. Schmidt, S. Watterson, G. Wu, I. Goryanin, D. B. Kell, C. Sander, H. Sauro, J. L. Snoep, K. Kohn, H. Kitano, The Systems Biology Graphical Notation. *Nat. Biotechnol.* **27**, 735–741 (2009).
60. M. A. Bruhn, R. B. Pearson, R. D. Hannan, K. E. Sheppard, Second AKT: The rise of SGK in cancer signalling. *Growth Factors* **28**, 394–408 (2010).
61. R. T. Peterson, P. A. Beal, M. J. Comb, S. L. Schreiber, FKBP12-rapamycin-associated protein (FRAP) autophosphorylates at serine 2481 under translationally repressive conditions. *J. Biol. Chem.* **275**, 7416–7423 (2000).
62. H. A. Acosta-Jaquez, J. A. Keller, K. G. Foster, B. Ekim, G. A. Soliman, E. P. Feener, B. A. Ballif, D. C. Fingar, Site-specific mTOR phosphorylation promotes mTORC1-mediated signaling and cell growth. *Mol. Cell. Biol.* **29**, 4308–4324 (2009).
63. J. Copp, G. Manning, T. Hunter, TORC-specific phosphorylation of mammalian target of rapamycin (mTOR): Phospho-Ser^{2481} is a marker for intact mTOR signaling complex 2. *Cancer Res.* **69**, 1821–1827 (2009).
64. G. A. Soliman, H. A. Acosta-Jaquez, E. A. Dunlop, B. Ekim, N. E. Maj, A. R. Tee, D. C. Fingar, mTOR Ser-2481 autophosphorylation monitors mTORC-specific catalytic activity and clarifies rapamycin mechanism of action. *J. Biol. Chem.* **285**, 7866–7879 (2010).
65. M. E. Feldman, B. Apsel, A. Uotila, R. Loewith, Z. A. Knight, D. Ruggero, K. M. Shokat, Active-site inhibitors of mTOR target rapamycin-resistant outputs of mTORC1 and mTORC2. *PLoS Biol.* **7**, e38 (2009).
66. C. C. Thoreen, S. A. Kang, J. W. Chang, Q. Liu, J. Zhang, Y. Gao, L. J. Reichling, T. Sim, D. M. Sabatini, N. S. Gray, An ATP-competitive mammalian target of rapamycin inhibitor reveals rapamycin-resistant functions of mTORC1. *J. Biol. Chem.* **284**, 8023–8032 (2009).
67. C. C. Thoreen, D. M. Sabatini, Rapamycin inhibits mTORC1, but not completely. *Autophagy* **5**, 725–726 (2009).
68. F. Heidebrecht, A. Heidebrecht, I. Schulz, S. E. Behrens, A. Bader, Improved semi-quantitative Western blot technique with increased quantification range. *J. Immunol. Methods* **345**, 40–48 (2009).
69. W. W. Chen, M. Niepel, P. K. Sorger, Classic and contemporary approaches to modeling biochemical reactions. *Genes Dev.* **24**, 1861–1875 (2010).
70. C. G. Moles, P. Mendes, J. R. Banga, Parameter estimation in biochemical pathways: A comparison of global optimization methods. *Genome Res.* **13**, 2467–2474 (2003).
71. C. Zhan, L. F. Yeung, Parameter estimation in systems biology models using spline approximation. *BMC Syst. Biol.* **5**, 14 (2011).
72. G. J. Brunn, J. Williams, C. Sabers, G. Wiederrecht, J. C. Lawrence Jr., R. T. Abraham, Direct inhibition of the signaling functions of the mammalian target of rapamycin by the phosphoinositide 3-kinase inhibitors, wortmannin and LY294002. *EMBO J.* **15**, 5256–5267 (1996).
73. R. D. Polakiewicz, S. M. Schieferl, A. C. Gingras, N. Sonenberg, M. J. Comb, μ-Opioid receptor activates signaling pathways implicated in cell survival and translational control. *J. Biol. Chem.* **273**, 23534–23541 (1998).
74. A. D. Kohn, F. Takeuchi, R. A. Roth, Akt, a pleckstrin homology domain containing kinase, is activated primarily by phosphorylation. *J. Biol. Chem.* **271**, 21920–21926 (1996).
75. B. N. Kholodenko, Cell-signalling dynamics in time and space. *Nat. Rev. Mol. Cell Biol.* **7**, 165–176 (2006).
76. G. von Dassow, E. Meir, E. M. Munro, G. M. Odell, The segment polarity network is a robust developmental module. *Nature* **406**, 188–192 (2000).
77. T.-R. Xu, V. Vyshemirsky, A. Gormand, A. von Kriegsheim, M. Girolami, G. S. Baillie, D. Ketley, A. J. Dunlop, G. Milligan, M. D. Houslay, W. Kolch, Inferring signaling pathway topologies from multiple perturbation measurements of specific biochemical species. *Sci. Signal.* **3**, ra20 (2010).
78. L. Bozulic, B. Surucu, D. Hynx, B. A. Hemmings, PKBα/Akt1 acts downstream of DNA-PK in the DNA double-strand break response and promotes survival. *Mol. Cell* **30**, 203–213 (2008).
79. J. Feng, J. Park, P. Cron, D. Hess, B. A. Hemmings, Identification of a PKB/Akt hydrophobic motif Ser-473 kinase as DNA-dependent protein kinase. *J. Biol. Chem.* **279**, 41189–41196 (2004).
80. A. A. Troussard, N. M. Mawji, C. Ong, A. Mui, R. St-Arnaud, S. Dedhar, Conditional knock-out of integrin-linked kinase demonstrates an essential role in protein kinase B/Akt activation. *J. Biol. Chem.* **278**, 22374–22378 (2003).
81. J. G. Viniegra, N. Martinez, P. Modirassari, J. H. Losa, C. Parada Cobo, V. J. Lobo, C. I. Luquero, L. Alvarez-Vallina, S. Ramón y Cajal, J. M. Rojas, R. Sánchez-Prieto, Full activation of PKB/Akt in response to insulin or ionizing radiation is mediated through ATM. *J. Biol. Chem.* **280**, 4029–4036 (2005).
82. M. J. Rane, P. Y. Coxon, D. W. Powell, R. Webster, J. B. Klein, W. Pierce, P. Ping, K. R. McLeish, p38 kinase-dependent MAPKAPK-2 activation functions as 3-phosphoinositide-dependent kinase-2 for Akt in human neutrophils. *J. Biol. Chem.* **276**, 3517–3523 (2001).
83. Y. Kawakami, H. Nishimoto, J. Kitaura, M. Maeda-Yamamoto, R. M. Kato, D. R. Littman, M. Leitges, D. J. Rawlings, T. Kawakami, Protein kinase C βII regulates Akt phosphorylation on Ser-473 in a cell type- and stimulus-specific fashion. *J. Biol. Chem.* **279**, 47720–47725 (2004).
84. C. Partovian, M. Simons, Regulation of protein kinase B/Akt activity and Ser^{473} phosphorylation by protein kinase Cα in endothelial cells. *Cell. Signal.* **16**, 951–957 (2004).
85. K. Mao, S. Kobayashi, Z. M. Jaffer, Y. Huang, P. Volden, J. Chernoff, Q. Liang, Regulation of Akt/PKB activity by P21-activated kinase in cardiomyocytes. *J. Mol. Cell. Cardiol.* **44**, 429–434 (2008).
86. A. Toker, A. C. Newton, Akt/protein kinase B is regulated by autophosphorylation at the hypothetical PDK-2 site. *J. Biol. Chem.* **275**, 8271–8274 (2000).
87. Y. Yu, S. O. Yoon, G. Poulogiannis, Q. Yang, X. M. Ma, J. Villén, N. Kubica, G. R. Hoffman, L. C. Cantley, S. P. Gygi, J. Blenis, Phosphoproteomic analysis identifies Grb10 as an mTORC1 substrate that negatively regulates insulin signaling. *Science* **332**, 1322–1326 (2011).
88. P. P. Hsu, S. A. Kang, J. Rameseder, Y. Zhang, K. A. Ottina, D. Lim, T. R. Peterson, Y. Choi, N. S. Gray, M. B. Yaffe, J. A. Marto, D. M. Sabatini, The mTOR-regulated phosphoproteome reveals a mechanism of mTORC1-mediated inhibition of growth factor signaling. *Science* **332**, 1317–1322 (2011).
89. M. R. Williams, J. S. Arthur, A. Balendran, J. van der Kaay, V. Poli, P. Cohen, D. R. Alessi, The role of 3-phosphoinositide-dependent protein kinase 1 in activating AGC kinases defined in embryonic stem cells. *Curr. Biol.* **10**, 439–448 (2000).
90. X. Gan, J. Wang, B. Su, D. Wu, Evidence for direct activation of mTORC2 kinase activity by phosphatidylinositol 3,4,5-trisphosphate. *J. Biol. Chem.* **286**, 10998–11002 (2011).
91. V. Zinzalla, D. Stracka, W. Oppliger, M. N. Hall, Activation of mTORC2 by association with the ribosome. *Cell* **144**, 757–768 (2011).
92. M. G. Myers Jr., T. C. Grammer, L. M. Wang, X. J. Sun, J. H. Pierce, J. Blenis, M. F. White, Insulin receptor substrate-1 mediates phosphatidylinositol 3′-kinase and p70S6k signaling during insulin, insulin-like growth factor-1, and interleukin-4 stimulation. *J. Biol. Chem.* **269**, 28783–28789 (1994).
93. F. Peruzzi, M. Prisco, M. Dews, P. Salomoni, E. Grassilli, G. Romano, B. Calabretta, R. Baserga, Multiple signaling pathways of the insulin-like growth factor 1 receptor in protection from apoptosis. *Mol. Cell. Biol.* **19**, 7203–7215 (1999).
94. D. J. Van Horn, M. G. Myers Jr., J. M. Backer, Direct activation of the phosphatidylinositol 3′-kinase by the insulin receptor. *J. Biol. Chem.* **269**, 29–32 (1994).
95. B. Vanhaesebroeck, J. Guillermet-Guibert, M. Graupera, B. Bilanges, The emerging mechanisms of isoform-specific PI3K signalling. *Nat. Rev. Mol. Cell Biol.* **11**, 329–341 (2010).
96. M. Wiznerowicz, D. Trono, Conditional suppression of cellular genes: Lentivirus vector-mediated drug-inducible RNA interference. *J. Virol.* **77**, 8957–8961 (2003).

97. A. Funahashi, M. Morohashi, H. Kitano, N. Tanimura, CellDesigner: A process diagram editor for gene-regulatory and biochemical networks. *BIOSILICO* **1**, 159–162 (2003).
98. S. Hoops, S. Sahle, R. Gauges, C. Lee, J. Pahle, N. Simus, M. Singhal, L. Xu, P. Mendes, U. Kummer, COPASI—A COmplex PAthway SImulator. *Bioinformatics* **22**, 3067–3074 (2006).
99. A. Corana, M. Marchesi, C. Martini, S. Ridella, Minimizing multimodal functions of continuous variables with the "simulated annealing" algorithm. *ACM Trans. Math. Softw.* **13**, 262–280 (1987).
100. S. Kirkpatrick, C. D. Gelatt Jr., M. P. Vecchi, Optimization by simulated annealing. *Science* **220**, 671–680 (1983).
101. H. Schmidt, M. Jirstrand, Systems Biology Toolbox for MATLAB: A computational platform for research in systems biology. *Bioinformatics* **22**, 514–515 (2006).
102. S. M. Keating, B. J. Bornstein, A. Finney, M. Hucka, SBMLToolbox: An SBML toolbox for MATLAB users. *Bioinformatics* **22**, 1275–1277 (2006).
103. M. Hucka, A. Finney, H. M. Sauro, H. Bolouri, J. C. Doyle, H. Kitano, A. P. Arkin, B. J. Bornstein, D. Bray, A. Cornish-Bowden, A. A. Cuellar, S. Dronov, E. D. Gilles, M. Ginkel, V. Gor, I. I. Goryanin, W. J. Hedley, T. C. Hodgman, J. H. Hofmeyr, P. J. Hunter, N. S. Juty, J. L. Kasberger, A. Kremling, U. Kummer, N. Le Novere, L. M. Loew, D. Lucio, P. Mendes, E. Minch, E. D. Mjolsness, Y. Nakayama, M. R. Nelson, P. F. Nielsen, T. Sakurada, J. C. Schaff, B. E. Shapiro, T. S. Shimizu, H. D. Spence, J. Stelling, K. Takahashi, M. Tomita, J. Wagner, J. Wang; SBML Forum, The systems biology markup language (SBML): A medium for representation and exchange of biochemical network models. *Bioinformatics* **19**, 524–531 (2003).
104. R Development Core Team, *R: A Language and Environment for Statistical Computing* (R Foundation for Statistical Computing, Vienna, Austria, 2005), Version 2.12.1.
105. H. Akaike, A new look at the statistical model identification. *IEEE Trans. Automat. Contr. AC* **19**, 716–723 (1974).

Acknowledgments: We thank P. Polak, T. B. L. Kirkwood, G. Smith, and A. Merz-Biro for critical reading of the manuscript. We thank B. Holzwarth for technical assistance. We also thank our reviewers for critical and constructive input. **Funding:** This work was supported by the European Council 6th FP NoE LifeSpan (LSHG-CT-2007-036894 to D.P.S., K.T., and R.B.), the Schlieben-Lange-Programm (K.T.), the Excellence Initiative of the German Federal and State Governments (EXC 294 to K.T., R.B., and T.B.H.; FRIAS LifeNet to R.B.), Bundesministeriums für Bildung und Forschung GerontoSys II–NephAge (031 5896A) (K.T., T.B.H., and R.B.), and Deutsche Forschungsgemeinschaft grant P7-KFO 201 (T.B.H., R.B., and E.N.-H.). **Author contributions:** K.T., D.P.S., and R.B. planned and guided the project. K.T. and D.P.S. conceived and designed the experiments. P.D.P., A.G.S., S.F., A.T., and M.T.P. performed the experiments. K.T., D.P.S., P.D.P., and A.G.S. analyzed the data. A.T., T.B.H., M.G., and E.N.-H. contributed reagents, materials, and analysis tools. K.T. and D.P.S. wrote the paper. A.G.S. and P.D.P. contributed to manuscript writing. **Competing interests:** The authors declare that they have no competing interests. A part of this work is part of a pending European patent application, which has been filed on 1 June 2011 (application number 11004471.6-1225, Method for modelling, optimizing, parameterizing, testing and/or validating a dynamic network or network perturbation).

Submitted 26 August 2011
Accepted 8 March 2012
Final Publication 27 March 2012
10.1126/scisignal.2002469
Citation: P. Dalle Pezze, A. G. Sonntag, A. Thien, M. T. Prentzell, M. Gödel, S. Fischer, E. Neumann-Haefelin, T. B. Huber, R. Baumeister, D. P. Shanley, K. Thedieck, A dynamic network model of mTOR signaling reveals TSC-independent mTORC2 regulation. *Sci. Signal.* **5**, ra25 (2012).

Appendix B

the FEBS Journal

A modelling–experimental approach reveals insulin receptor substrate (IRS)-dependent regulation of adenosine monosphosphate-dependent kinase (AMPK) by insulin

Annika G. Sonntag[1,*], Piero Dalle Pezze[2,3,*], Daryl P. Shanley[2,3] and Kathrin Thedieck[1,4,5]

1 Bioinformatics and Molecular Genetics (Faculty of Biology), Institute for Biology 3, Albert-Ludwigs-Universität Freiburg, Germany
2 Institute for Ageing and Health, Newcastle University, Campus for Ageing and Vitality, UK
3 Centre for Integrated Systems Biology of Ageing and Nutrition, Institute for Ageing and Health, Newcastle University, UK
4 BIOSS Centre for Biological Signalling Studies, Albert-Ludwigs-Universität Freiburg, Germany
5 Center for Systems Biology (ZBSA), Albert-Ludwigs-Universität Freiburg, Germany

Keywords
adenosine monophosphate-dependent kinase; Akt; dynamic network model; insulin; insulin receptor substrate; mammalian target of rapamycin

Correspondence
K. Thedieck, Department of Bioinformatics and Molecular Genetics (Faculty of Biology), Albert-Ludwigs-Universität Freiburg, Schaenzlestr.1, 79104 Freiburg, Germany
Fax: +49 761 203 8352
Tel: +49 761 203 2725
E-mail: kathrin.thedieck@biologie.uni-freiburg.de
Website: http://www.celegans.de/thedieck
D. P. Shanley, Institute for Ageing and Health, Newcastle University, Campus for Ageing and Vitality, Newcastle upon Tyne NE4 5PL, UK
Fax: +44 191 248 1101
Tel: +44 191 248 1105
E-mail: daryl.shanley@ncl.ac.uk
Website: http://www.ncl.ac.uk/iah/staff/profile/daryl.shanley

*These authors contributed equally to this work

(Received 5 January 2012, revised 28 February 2012, accepted 22 March 2012)

doi:10.1111/j.1742-4658.2012.08582.x

Mammalian target of rapamycin (mTOR) kinase responds to growth factors, nutrients and cellular energy status and is a central controller of cellular growth. mTOR exists in two multiprotein complexes that are embedded into a complex signalling network. Adenosine monophosphate-dependent kinase (AMPK) is activated by energy deprivation and shuts off adenosine 5′-triphosphate (ATP)-consuming anabolic processes, in part via the inactivation of mTORC1. Surprisingly, we observed that AMPK not only responds to energy deprivation but can also be activated by insulin, and is further induced in mTORC1-deficient cells. We have recently modelled the mTOR network, covering both mTOR complexes and their insulin and nutrient inputs. In the present study we extended the network by an AMPK module to generate the to date most comprehensive data-driven dynamic AMPK-mTOR network model. In order to define the intersection via which AMPK is activated by the insulin network, we compared simulations for six different hypothetical model structures to our observed AMPK dynamics. Hypotheses ranking suggested that the most probable intersection between insulin and AMPK was the insulin receptor substrate (IRS) and that the effects of canonical IRS downstream cues on AMPK would be mediated via an mTORC1-driven negative-feedback loop. We tested these predictions experimentally in multiple set-ups, where we inhibited or induced players along the insulin–mTORC1 signalling axis and observed AMPK induction or inhibition. We confirmed the identified model and therefore report a novel connection within the insulin–mTOR–AMPK network: we conclude that AMPK is positively regulated by IRS and can be inhibited via the negative-feedback loop.

Abbreviations
AIC, akaike information criterion; AMP, adenosine monophosphate; AMPK, adenosine monophosphate-dependent kinase; ATM, ataxia-telangiectasia mutated; ATP, adenosine 5′-triphosphate; BIC, Bayesian Information Criterion; CaMKK, Ca^{2+}-sensitive calmodulin-dependent protein kinase kinase; CV, coefficient of variance; GAPDH, glyceraldehyde-3-phosphate dehydrogenase; HA-myr-Akt, myristoylated version of Akt; HRP, horseradish peroxidase; IR, insulin receptor; IRE1, inositol-requiring enzyme 1; IRS, insulin receptor substrate; LKB1, liver kinase B1; MOTA, Mean Optimal Transformation Approach; mTOR, mammalian target of rapamycin; mTORC1, mammalian target of rapamycin complex 1; mTORC2, mammalian target of rapamycin complex 2; NFL, negative-feedback loop; PDK1, phosphoinositide-dependent protein kinase 1; p.i., postinduction; PI3K, phosphatidylinositol 3-kinase; PRAS40, proline-rich Akt substrate of 40 kDa; PTEN, phosphatase and tensin homologue; p70-S6K, S6-kinase; shRaptor, inducible short hairpin Raptor knockdown;TAK1/MAP3K7, transforming growth factor-beta-activated kinase-1; TSC1–TSC2, tuberous sclerosis complex 1/2 dimer; 4E-BP, 4E-binding protein.

Introduction

Mammalian target of rapamycin (mTOR) kinase is a central controller of cellular growth and metabolism and is conserved in all eukaryotes. mTOR controls anabolic and catabolic processes, including translation, ribosome biogenesis and autophagy, in response to nutrients (amino acids), energy and growth factors (insulin). mTOR exists in two multiprotein complexes – mTOR complex 1 (mTORC1) and mTOR complex 2 (mTORC2) – which are functionally and structurally distinct: mTORC1 contains Raptor and proline-rich Akt substrate of 40 kDa (PRAS40) as specific binding partners and controls cellular growth, whereas mTORC2 comprises mammalian stress–activated protein kinase–interacting protein 1 (mSIN1), proline rich protein 5 (PRR5)/PRR5-Like (PRR5L) and Rictor, and controls apoptosis as well as spatial growth via the actin cytoskeleton [1,2].

Being a central growth regulator, mTOR is tightly embedded into a complex signalling network, transducing insulin signals via the insulin receptor (IR), the insulin receptor substrate (IRS), class I phosphatidylinositol 3-kinases (PI3Ks), phosphoinositide-dependent protein kinase 1 (PDK1) and the protein kinase A/protein kinase G/protein kinase C-family (AGC) kinase, Akt (also known as PKB). Akt inhibits the tuberous sclerosis complex 1/2 dimer (TSC1–TSC2), which is the inhibitory GTPase-activating protein for Rheb [1–4]. Via this cascade, Akt induces mTORC1. mTORC1 phosphorylates S6-kinase (p70-S6K), the translation initiation regulator 4E-binding protein (4E-BP) and the mTORC1-inhibitor PRAS40 [5–12]. Whereas PRAS40 inhibits mTORC1 activity, p70-S6K and 4E-BP mediate mTORC1 downstream effects. Furthermore, active p70-S6K phosphorylates and inhibits the IRS, which consequently cannot activate PI3K in response to insulin. This mechanism results in a negative-feedback loop (NFL), which inhibits upstream insulin signalling upon mTORC1 activation [2]. We have recently modelled this network and shown that whereas mTORC1 is induced via the above described signalling cascade, the induction of mTORC2 occurs via a distinct PI3K that is insensitive to the NFL [13].

mTOR not only responds to the insulin network but is also connected to many other signalling cascades, including adenosine monophosphate (AMP)-dependent kinase (AMPK), Wnt signalling and the mitogen-activated protein kinase kinase kinase (MEK)/extracellular signal-regulated kinase (Erk) pathway. To incorporate further kinase inputs into our dynamic network model, we decided to focus on the development of an AMPK module. AMPK turns on catabolic adenosine 5′-triphosphate (ATP)-generating pathways and shuts off ATP-consuming anabolic processes, such as ribosome biogenesis and translation, in part via the inactivation of mTORC1 [14]. AMPK is activated by both energy deprivation and by the liver kinase B1 (LKB1) (or STK11). Inhibition of glycolytic flux leads to a high AMP/ATP ratio, activating AMPK by direct, allosteric AMP binding. LKB1 activates AMPK by phosphorylating AMPK-T172 and thereby negatively regulates mTORC1 [14]. Although LKB1 seems to be the main upstream kinase of AMPK, LKB1 also phosphorylates 12 other kinases [15], termed AMPK-related kinases. The physiological functions of these kinases are still poorly understood. Apart from LKB1, several other kinases can phosphorylate AMPK-T172 independently of the cellular energy status, including Ca^{2+}-sensitive calmodulin-dependent protein kinase kinase (CaMKK) [16–19] and transforming growth factor-beta-activated kinase-1 (TAK1/MAP3K7) [20–22]. Also, ataxia-telangiectasia mutated (ATM) kinase-dependent [23,24] or inositol-requiring enzyme 1 (IRE1)-dependent [25] induction of AMPK have been reported.

To inhibit mTORC1 signalling, AMPK multiply phosphorylates and activates TSC2 when cellular energy is low [26]. In addition, AMPK also directly phosphorylates the essential mTORC1 component Raptor on two serine residues [27]. This phosphorylation induces 14-3-3 to bind to Raptor and is required for mTORC1 inhibition by energy deprivation.

We observed, in the present work, that AMPK not only responds to energy deprivation but is also strongly activated by insulin and is further induced in Raptor-deficient cells. These findings are in line with others [23,28,29]; however, the underlying signalling events have been only poorly investigated to date. In order to define the intersection via which AMPK is activated by the insulin network, we generated a data-driven dynamic AMPK–mTOR network model and used a combined modelling-experimental approach. We compared simulations for different model structures with our observed AMPK dynamics. Hypotheses ranking suggested that the most probable intersection between insulin and AMPK was the IRS, and that the effects of canonical IRS downstream cues on AMPK are mediated via the NFL. We tested and confirmed these predictions experimentally in multiple set-ups. We report here a novel connection within the insulin–mTOR–AMPK network: we conclude that AMPK is positively regulated by IRS and can be inhibited via the NFL.

Results

An insulin–TOR–AMPK model

We recently described the development of a dynamic mTOR network model [13] that covered insulin and amino-acid signalling as mTORC1 regulators. AMPK is another important mTOR regulator that suppresses mTORC1 activity in response to energy deprivation [14] and we decided to add this regulation to our model. We introduced the following novel connection into the existing network structure [13]: AMPK phosphorylation at T172 allows AMPK to phosphorylate the species TSC1_TSC2 at S1387, which leads to the activation of TSC1–TSC2 and the subsequent inhibition of mTORC1. Conversely, the phosphorylation of the species TSC1_TSC2 at T1462 by Akt_pT308 inhibits the TSC1_TSC2 complex, activating mTORC1. Finally, the species Akt_pS473, PRAS40_pT246 and PRAS40_pS183 were defined as supplementary readouts for mTORC2, Akt and mTORC1, respectively.

In order to calibrate the AMPK module and connect it to our existing mTOR model, we acquired AMPK time courses under the same conditions that we had used for calibration of the dynamic mTOR network model [13]. These were starvation of serum and amino acids followed by network induction by insulin and amino acids. AMPK is described to be induced in Raptor-deficient cells [28,29]. Therefore, we also investigated AMPK activity upon gradual knockdown in an inducible short hairpin Raptor knockdown (shRaptor) HeLa cell line. The knockdown was induced by doxycycline treatment for 3, 2 or 0 days. Cells were starved for 16 h and activated with insulin and amino acids from 3 min up to 100 min postinduction (p.i.) (Fig. 1A). As previously described [13], the direct mTORC1 substrate, p70-S6K-pT389, was activated from 20 min onwards and displayed reduced phosphorylation upon induction of Raptor knockdown. AMPK activity was monitored by detecting phosphorylation at T172, reflecting active AMPK [14]. Although AMPK is known to be induced by energy depletion [14], we found, to our surprise, that AMPK-pT172 is also strongly induced by insulin and amino acids, and induction was apparent at only 3 min p.i. Overall, AMPK-pT172 induction decreased with time. As expected, AMPK-pT172 was more strongly induced upon Raptor knockdown, and this was observable from 20 min p.i. onwards (Fig. 1A). Upon activation, AMPK phosphorylates TSC2 at S1387, leading to TSC2 activation and subsequent inhibition of mTORC1 [26,30]. Therefore, we used TSC2-S1387 as a

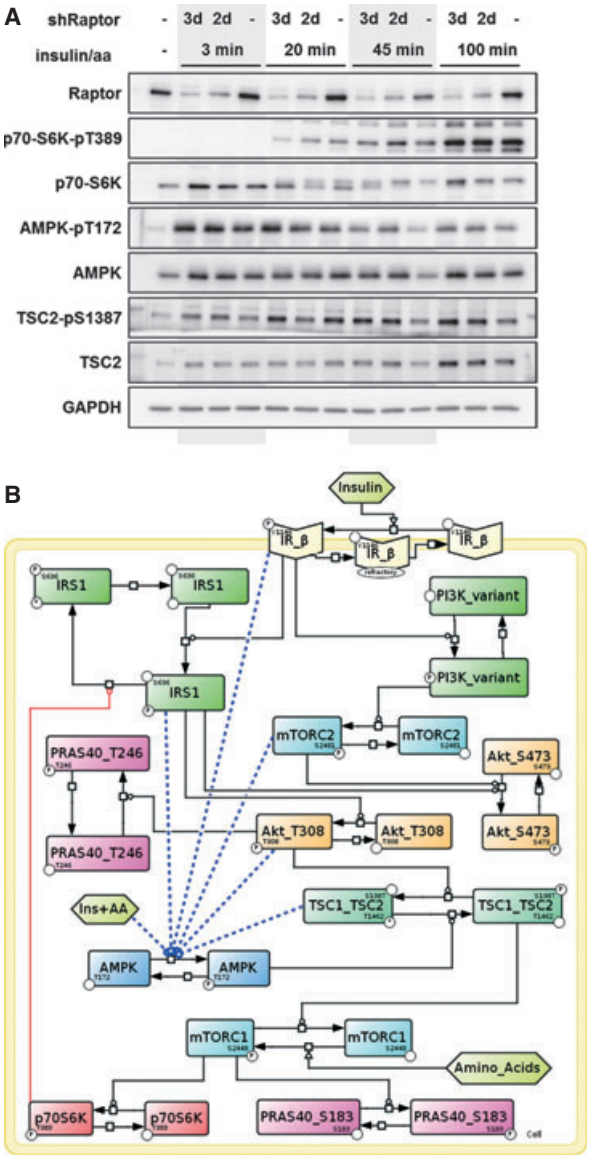

Fig. 1. Set up of an AMPK module. (A) AMPK is induced upon insulin induction. A gradual Raptor knockdown was induced in HeLa cells by doxycyline treatment for the indicated times. Cells were serum/amino acid starved for 16 h and restimulated with amino acids and 100 nM insulin for 3, 20, 45 or 100 min. (B) Insulin–mTOR–AMPK model. This model integrates our previous insulin–mTOR model with AMPK regulation. Six hypotheses of AMPK activation are investigated (blue dotted lines). Except for the insulin- and IR-beta (IR-β)-induced AMPK hypotheses, all others implicitly assume AMPK as being dependent on the p70-S6K NFL. aa or AA, amino acids; Ins, insulin.

second AMPK readout, to confirm our findings on AMPK activation. Indeed, TSC2-pS1387 followed AMPK-pT172 with some delay, starting 20 min p.i. and was induced by insulin and amino acids, and in Raptor knockdown cells. All signal intensities were

quantified, and descriptive statistics were computed over three replicates. The experimental mean time courses were used to calibrate the model parameters.

Although it has been described previously that AMPK is induced by insulin-like growth factor 1 (IGF-1) [23], this signalling connection has been only poorly explored to date. Therefore, in the present study we systematically investigated possible AMPK activators along the insulin–mTORC1 axis. mTORC1 is maximally induced at 30-45 min p.i. [13]. As AMPK induction by insulin peaked as early as 3 min p.i., and AMPK was induced by Raptor knockdown (i.e. mTORC1 inhibition), we selected, as candidate AMPK activators, the species upstream of mTORC1:

1. Insulin, where insulin is considered as constant and direct input to AMPK;
2. IR_beta_pY1146, reflecting IR activation;
3. IRS1_p, reflecting IRS1 activation by the IR;
4. mTORC2_pS2481, reflecting mTORC2 activation by insulin and amino acids [13];
5. Akt_pT308, reflecting Akt activation downstream of PI3K; and
6. TSC1_TSC2_pT1462, reflecting TSC1–TSC2 deactivation by Akt.

A graphical representation of our insulin–mTOR–AMPK model, depicting our six alternative hypotheses of AMPK activation, is provided in Fig. 1B.

Parameter estimation and identifiability

A specific model was instantiated for each hypothesis and calibrated using the same data sets and the Matlab Toolbox PottersWheel [31]. Before calibrating the models, structural identifiability analysis was performed using the software GenSSI [32]. This software calculated the symbolic solution of the problem, computing Lie derivatives for each hypothesis and confirming structural global identifiability for all six models. For the IRS1-induced AMPK model, structural identifiability analysis is reported in Fig. 2A, showing that all the parameters were structurally identified in the first-order (blue circles) or second-order (magenta circles) identifiability tableau.

To calibrate the models, experimental time courses upon insulin/amino acid induction for nine readouts (IR_beta_pY1146, IRS1_pS636, Akt_pT308, Akt_pS473, mTORC1_pS2448, mTORC2_pS2481, p70S6K_pT389, PRAS40_pT246 and PRAS40_pS183; data set 1) in wild-type cells along the insulin–mTOR signalling axis were used in combination with time courses under gradual mTORC1 inhibition (Raptor knockdown; data set 1) in wild-type cells, as measured previously [13]. Furthermore, in order to calibrate the species AMPK_pT172 and TSC1_TSC2_pS1387, the five time points (0, 3, 20, 45 and 100 min p.i.; Fig. 1A) without knockdown induction (i.e. corresponding to wild type), were added as an additional data set (data set 3).

Parameter estimation was executed for each model independently over multiple data sets in order to reduce the bias of the solution and therefore overfitting. However, the addition of data sets used to calibrate a model can lead to a serious increment of variance, particularly because of the increase in intrinsic noise in experimental data, which does not permit to estimate the parameters of the model correctly. Our second data set was characterized by three different levels of Raptor knockdown, obtained by doxycycline treatment for 0, 2 or 3 days, respectively (subsets 1-3). We found a satisfactory bias–variance trade-off by combinatorially and singularly testing these three subsets and eventually selecting only the subset of Raptor knockdown induced by doxycycline treatment for 3 days (subset 3). Subset 3 was selected as it represented the strongest signal reduction and consequently novel information with respect to wild-type time courses (data set 1) for calibrating the model. Moreover, the readouts in our data sets (data set 1, data set 2-subset 3, data set 3) were scaled in order to obtain species time courses of similar intensity. This distributes the cost of the solution equally over the simulated time courses, approximating the data and avoiding an implicit preference ranking of calibration.

For calibrating the models, we only estimated the kinetic rate-constant parameters, whereas the species protein concentrations were determined from our immunoblot time courses by selecting the corresponding readout maximum intensity plus two standard deviations measured at that time point. The addition of two standard deviations to the maximum signal peak guaranteed the avoidance of species protein-saturation conditions. The kinetic rate constants regulating PI3K-variant dynamics were fixed *a priori* assuming a time course similar to the insulin receptor. In fact, no experimental data are available for this PI3K insensitive to the NFL and it is more likely that it follows the IR-beta receptor than other curves. Furthermore, fixing these parameters led us to a full structural identifiability of the model.

A posterior identifiability analysis was performed using the Mean Optimal Transformation Approach (MOTA) plugin [31,33] after selecting the 50% of the best fits (shown in Fig. 2B for the IRS1-induced AMPK model). This analysis revealed that high parameter correlations had a coefficient of variation (CV) lower than 0.05 for all our models except for the

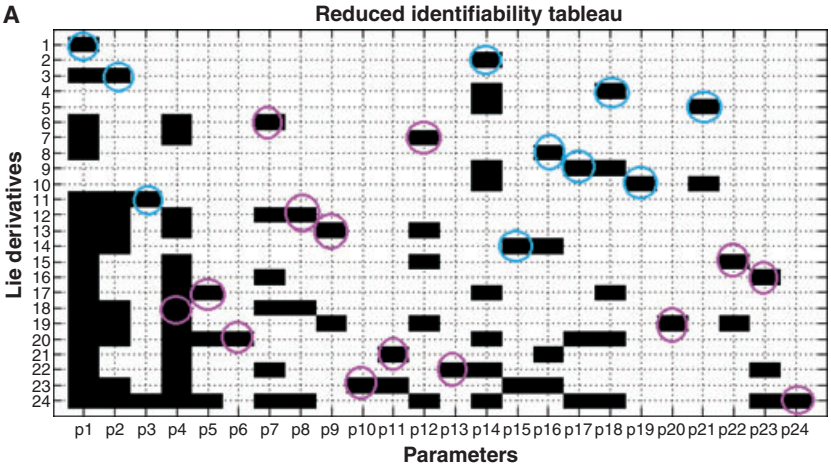

B

Param.	r2	CV	#	Tuples
p1	< 0.793	0.000	1	(p1,p23) >
p2	< 0.997	0.000	2	(p2,p3,p15) >
p3	< 0.999	0.000	2	(p2,p3,p15) >
p4	< 0.997	0.000	1	(p4,p6) >
p5	< 0.998	0.002	1	(p5,p11,p12) >
p6	< 0.998	0.000	1	(p4,p6,p15) >
p7	< 0.999	0.002	2	(p5,p6,p7,p11,p12) >
p8	< 0.966	0.000	1	(p8,p13,p20) >
p9	< 0.929	0.000	1	(p9,p20) >
p10	< 0.938	0.000	1	(p10,p13,p16) >
p11	< 0.999	0.002	1	(p5,p7,p11,p12) >
p12	< 0.999	0.002	2	(p5,p6,p7,p11,p12) >
p13	< 0.998	0.000	2	(p13,p14) >
p14	< 0.998	0.000	2	(p13,p14) >
p15	< 0.997	0.000	1	(p2,p3,p15,p16) >
p16	< 0.975	0.000	1	(p3,p16) >
p17	< 0.967	0.000	2	(p17,p18) >
p18	< 0.967	0.000	2	(p17,p18) >
p19	< 1.000	0.001	2	(p19,p21) >
p20	< 1.000	0.001	1	(p20,p22) >
p21	< 1.000	0.001	2	(p19,p21) >
p22	< 1.000	0.001	1	(p11,p12,p20,p22) >
p23	< 0.998	0.000	1	(p22,p23,p24) >
p24	< 0.997	0.000	1	(p8,p23,p24) >

Parameters Legend:

p1 = IR_beta_phosphorylation_by_Insulin
p2 = IR_beta_pY1146_dephosphorylation
p3 = IR_beta_ready
p4 = IRS1_phosphorylation_by_IR_beta_pY1146
p5 = IRS1_p_phosphorylation_by_p70S6K_pT389
p6 = IRS1_pS636_dephosphorylation
p7 = AMPK_T172_phosphorylation
p8 = AMPK_pT172_dephosphorylation
p9 = Akt_pT308_dephosphorylation
p10 = Akt_pS473_dephosphorylation
p11 = Akt_S473_phosphorylation_by_mTORC2_pS2481_n_IRS1_p
p12 = Akt_T308_phosphorylation_by_IRS1_p
p13 = mTORC1_pS2448_dephosphorylation_by_TSC1_TSC2_pS1387
p14 = mTORC1_S2448_activation_by_Amino_Acids
p15 = mTORC2_pS2481_dephosphorylation
p16 = mTORC2_S2481_phosphorylation_by_PI3K_variant_p
p17 = p70S6K_pT389_dephosphorylation
p18 = p70S6K_T389_phosphorylation_by_mTORC1_pS2448
p19 = PRAS40_pS183_dephosphorylation
p20 = PRAS40_pT246_dephosphorylation
p21 = PRAS40_S183_phosphorylation_by_mTORC1_pS2448
p22 = PRAS40_T246_phosphorylation_by_Akt_pT308
p23 = TSC1_TSC2_S1387_phosphorylation_by_AMPK_pT172
p24 = TSC1_TSC2_T1462_phosphorylation_by_Akt_pT308

Fig. 2. Identifiability analysis for the IRS1-induced AMPK model (hypothesis 3). (A) Structural identifiability analysis was performed using the software GenSSI *a priori*. In the reduced identifiability tableau, blue circles indicate the parameters detected directly as structurally globally identifiable at the first-order tableau, whereas magenta circles highlight the parameters detected as structurally globally identifiable at the second-order tableau after computing the symbolic solution. (B) MOTA identifiability analysis was executed using the 50% of the best fits of the calibration fits sequence. A correlation among a set of parameters is indicated by the tuple of correlated parameters, their correlation coefficient (r2), the CV and the number of times that this correlation was identified by varying the parameters of the tuple (#). Even though high correlations were found among some parameters, the corresponding CV was lower than 0.002, which can be explained as a numeric approximation error in the fit sequence calibration process. (*) $r^2 > 0.9$ and CV > 0.1 (**) $r^2 > 0.9$ and CV > 0.1 and #>1. Param., parameter.

IR-beta-induced AMPK model (hypothesis 2; Fig. S1). For this model, MOTA analysis highlighted high correlation and a high CV for the pair of parameters regulating AMPK dynamics. Model identifiability was obtained after fixing one of the two parameters and recalibrating the other in a second round of calibration. In combination with the previous analysis, we also checked parameter nonidentifiability by directly

analysing the estimated percentage of standard deviations of the parameters, computed over the 50% best fits, and considering nonidentifiable the parameters with a standard deviation percentage higher than a threshold of 5%. Table 1 presents the values for the estimated parameters, with mean, standard deviation and CV values for the IRS1-induced AMPK model showing parameter identifiability. Sensitivity analysis for the same model is provided in Fig. S2, showing a balanced sensitivity among the parameters and that all were required.

In summary, we independently calibrated six models sharing the main network structure and differing in AMPK activation. We were therefore able to investigate our central question, of finding at which level in the network AMPK is induced by insulin.

Intersection level of the signalling from insulin to AMPK: model simulation analyses over AMPK-pT172 and TSC2-pS1387 readouts

Once the parameter estimation was achieved, the simulated time courses for the readouts AMPK_pT172 and TSC1_TSC2_pS1387 of each model were compared with the corresponding experimental time courses (see Fig. 3). Surprisingly, we observed that the readouts AMPK_pT172 and TSC1_TSC2_pS1387 for the IRS1-induced AMPK model (hypothesis 3) fitted the data with high accuracy, whereas the goodness-of-fit decreased for species downstream of IRS1 (Akt and TSC1-TSC2; hypotheses 5 and 6) and upstream of IRS1 (insulin, IR-beta; hypotheses 1 and 2), as indicated by the measure χ^2. Furthermore, the two readouts showed a poorer fit for the mTORC2-induced AMPK model (hypothesis 4). At this point, we questioned whether these local differences could lead to a possible ranking of the overall models. In order to achieve this, several additional likelihood-based statistical criteria, such as the Akaike Information Criterion [34] [AIC, Akaike Information Criterion corrected (AICc)] and the Bayesian Information Criterion [35] (BIC), were used besides the total χ^2, to estimate the goodness-of-fit calculated over the entire models. These estimations allowed us to establish a ranking of the hypotheses in accordance with the goodness-of-fit (Table 2). All values obtained were consistent between these measures and with the above observations in selecting the IRS1-induced AMPK model (hypothesis 3) as the most probable model. The remaining simulated versus experimental time courses for the IRS1-induced AMPK model are reported in Fig. S3. A Systems Biology Markup Language (SBML) model is provided for the IRS1-induced AMPK hypothesis.

In summary, hypotheses ranking suggested that IRS (hypothesis 3) was the most probable inducer of AMPK in response to insulin. This, in turn, suggested that downstream cues of IRS1 could affect AMPK via the NFL, which would be in line with the observed induction of AMPK in mTORC1-deficient cells (Fig. 1A, [28,29]). We then tested this experimentally.

Experimental testing: AMPK activation is IRS dependent and indirectly regulated via the NFL

Hypothesis 3 predicts that IRS will be required for AMPK induction by insulin. We therefore tested first whether IRS hyperactivation alone would result in increased AMPK-T172 phosphorylation. To achieve this we overexpressed wild-type IRS-1 (Myc-IRS-1 WT) or mutagenized IRS-1 variants, resembling either IRS-1 constitutively phosphorylated by S6K (Myc-IRS-1 S636/639 D) or constitutively unphosphorylated on the same sites (Myc-IRS-1 S636/639 A) [36]. The variants are NFL insensitive and whereas the D variant is less active, the A variant will be hyperactive. The constructs were overexpressed in HeLa cells (Fig. 4A). As expected, Myc-IRS-1 WT and Myc-IRS-1 S636/639 A strongly induced Akt-pT308 and mTORC1 activity towards p70-S6K-T389, whereas Myc-IRS-1 S636/639 D did not. Importantly, AMPK-pT172 was induced moderately by Myc-IRS-1 WT and strongly by Myc-IRS-1 S636/639 A, but was refractory to overexpression of Myc-IRS-1 S636/639 D. This finding is in line with hypothesis 3, which suggests the requirement of active IRS for AMPK induction by insulin. To further confirm our finding we also analysed the AMPK target site, TSC2-S1387, upon overexpression of Myc-IRS-1 WT (Fig. 4B). TSC2-pS1387 was strongly induced, again suggesting positive regulation of AMPK by IRS-1.

IRS-1 hyperactivation will strongly induce PI3K activity [36], and we did not differentiate, in our hypothesis 3, between IRS and PI3K activity. We therefore next tested whether PI3K also positively affects AMPK. We inhibited PI3K with wortmannin before induction with insulin/amino acids (Fig. 4C): as expected, wortmannin inhibited Akt-pT308, downstream of PI3K. In contrast, wortmannin induced AMPK-T172 phosphorylation. To confirm this finding in a complementary set-up, we overexpressed the PI3K antagonist phosphatase and tensin homolog (PTEN): PI3K generates phosphatidylinositol (3,4,5)-trisphosphate (PIP3), leading to the induction of PDK1, Akt and their downstream targets; however, PTEN dephosphorylates PIP3, thereby counteracting PI3K activity. As expected, PTEN overexpression strongly

Table 1. Parameter table for the IRS1-induced AMPK model (hypothesis 3). The estimated kinetic rate constants, together with the species concentrations, are provided. The mean, SD and per cent of the SD over the mean, computed over the 50% best fits, are also indicated. These statistics shows that all 24 estimated parameters could be fixed at the first round of calibration. Scaling factor parameters and observable variables are also indicated. The SBML model given in Model S2 (Supporting information) is configured with these parameter values.

Parameter name (AMPK induced by the IRS1 model) [kinetic rate constants (min^{-1})]	Calibration [mean ± SD (%)]	Value
p1 = IR_beta_phosphorylation_by_Insulin	0.124278 ± 1.21324e-05 (0%)	0.124273
p2 = IR_beta_pY1146_dephosphorylation	0.396251 ± 3.02338e-05 (0%)	0.396235
p3 = IR_beta_ready	0.0532808 ± 6.9999e-06 (0%)	0.053277
p4 = IRS1_phosphorylation_by_IR_beta_pY1146	0.00491628 ± 5.46924e-07 (0%)	0.00491599
p5 = IRS1_p_phosphorylation_by_p70S6K_pT389	1681.94 ± 3.80623 (0%)	1682.75
p6 = IRS1_pS636_dephosphorylation	0.0130526 ± 4.45303e-06 (0%)	0.01305
p7 = AMPK_T172_phosphorylation	9.79357 ± 0.0177607 (0%)	9.79766
p8 = AMPK_pT172_dephosphorylation	0.0107217 ± 4.13895e-07 (0%)	0.0107215
p9 = Akt_pT308_dephosphorylation	0.00335553 ± 3.70977e-07 (0%)	0.00335545
p10 = Akt_pS473_dephosphorylation	0.00640225 ± 1.80374e-07 (0%)	0.00640216
p11 = Akt_S473_phosphorylation_by_mTORC2_pS2481_n_IRS1_p	13.1374 ± 0.0302136 (0%)	13.1442
p12 = Akt_T308_phosphorylation_by_IRS1_p	6.9152 ± 0.0123683 (0%)	6.91811
p13 = mTORC1_pS2448_dephosphorylation_by_TSC1_TSC2_pS1387	0.0106657 ± 9.77042e-07 (0%)	0.0106652
p14 = mTORC1_S2448_activation_by_Amino_Acids	0.00438932 ± 3.03977e-07 (0%)	0.00438916
p15 = mTORC2_pS2481_dephosphorylation	0.0183743 ± 1.62188e-06 (0%)	0.0183735
p16 = mTORC2_S2481_phosphorylation_by_PI3K_variant_p	0.375358 ± 1.34923e-05 (0%)	0.375353
p17 = p70S6K_pT389_dephosphorylation	0.0113508 ± 6.03276e-07 (0%)	0.0113512
p18 = p70S6K_T389_phosphorylation_by_mTORC1_pS2448	0.0018404 ± 3.38908e-08 (0%)	0.00184043
p19 = PRAS40_pS183_dephosphorylation	2.33046 ± 0.00198802 (0%)	2.33014
p20 = PRAS40_pT246_dephosphorylation	1.60545 ± 0.00132301 (0%)	1.60513
p21 = PRAS40_S183_phosphorylation_by_mTORC1_pS2448	0.187646 ± 0.000157968 (0%)	0.187621
p22 = PRAS40_T246_phosphorylation_by_Akt_pT308	0.137756 ± 0.000112104 (0%)	0.137729
p23 = TSC1_TSC2_S1387_phosphorylation_by_AMPK_pT172	0.0365597 ± 4.61345e-06 (0%)	0.0365589
p24 = TSC1_TSC2_T1462_phosphorylation_by_Akt_pT308	0.0177568 ± 1.993e-06 (0%)	0.0177562
p25 = PI3K_variant_p_dephosphorylation	Assumed	10
p26 = PI3K_variant_phosphorylation_by_IR_beta_pY1146	Assumed	0.01
Concentrations (AU)		
u1 = Insulin (INPUT)	Fixed	10
u2 = Amino_Acids (INPUT)	Fixed	10
x1 = IR_beta	Determined	16.56070782
x4 = IRS1	Determined	18.93446968
x7 = AMPK	Determined	20.50644836
x9 = Akt_T308	Determined	21.41085271
x11 = Akt_S473	Determined	12.25170805
x13 = mTORC1	Determined	25.14
x15 = mTORC2	Determined	18.79587754
x17 = p70S6K	Determined	14.30096315
x19 = PRAS40_S183	Determined	13.56128255
x21 = PRAS40_T246	Determined	17.55000883
x23 = TSC1_TSC2_pT1462	Determined	14.9175
x25 = PI3K_variant	Determined	18.93446968
x2 = IR_beta_pY1146; x3 = IR_beta_refractory; x5 = IRS1_p; x6 = IRS1_pS636; x8 = AMPK_pT172; x10 = Akt_pT308; x12 = Akt_pS473; x14 = mTORC1_pS2448; x16 = mTORC2_pS2481; x18 = p70S6K_pT389; x20 = PRAS40_pS183; x22 = PRAS40_pT246; x24 = TSC1_TSC2_pS1387; x26 = PI3K_variant_p	Fixed	0
Scaling factors		
s1 = scale_IR_beta_pY1146_obs; s2 = scale_IRS1_pS636_obs; s3 = scale_AMPK_pT172_obs; s4 = scale_Akt_pT308_obs; s5 = scale_Akt_pS473_obs; s6 = scale_TSC1_TSC2_pS1387_obs; s7 = scale_mTOR_pS2448_obs; s8 = scale_mTOR_pS2481_obs; s9 = scale_p70S6K_pT389_obs; s10 = scale_PRAS40_pT246_obs; s11 = scale_PRAS40_pS183_obs	Fixed	1

Table 1. (Continued).

Parameter name (AMPK induced by the IRS1 model) [kinetic rate constants (min^{-1})]	Calibration [mean ± SD (%)]	Value
Observables (AU)		
y1 = IR_beta_pY1146_obs	Assigned	s1*x2
y2 = IRS1_pS636_obs	Assigned	s2*x6
y3 = AMPK_pT172_obs	Assigned	s3*x8
y4 = Akt_pT308_obs	Assigned	s4*x10
y5 = Akt_pS473_obs	Assigned	s5*x12
y6 = TSC1_TSC2_pS1387_obs	Assigned	s6*x14
y7 = mTOR_pS2448_obs	Assigned	s7*x16
y8 = mTOR_pS2481_obs	Assigned	s8*x18
y9 = p70S6K_pT389_obs	Assigned	s9*x20
y10 = PRAS40_pT246_obs	Assigned	s10*x22
y11 = PRAS40_pS183_obs	Assigned	s11*x24
Compartments (AU)		
c1 = Cell	Fixed	1

inhibited mTORC1 activity towards p70-S6K-T389 (Fig. 4D). In agreement with our findings for wortmannin, increased PTEN levels activated AMPK, as evidenced by AMPK-pT172 induction. We conclude that AMPK is induced by IRS, but inhibited by PI3K. The induction of AMPK in response to PI3K inhibition is in line with our own and previous findings on AMPK induction in mTORC1-deficient cells and might be mediated via the NFL. In other words, if IRS is required for AMPK induction, inhibition of the NFL (targeting IRS) should induce AMPK.

If this reasoning and our hypothesis 3 hold true, activation of Akt and subsequent hyperactivation of the NFL should inhibit AMPK. We tested this prediction by overexpressing a myristoylated version of Akt (HA-myr-Akt) [37], which is constitutively localized to the plasma membrane and does not require IRS or PI3K for its activation. As expected for Akt hyperactivation, expression of HA-myr-Akt strongly induced the Akt target site TSC2-pT1462 (Fig. 4E). TSC2-T1462 phosphorylation leads to inhibition of the TSC1-TSC2 complex and hyperactivates mTORC1. Also, mTORC1 activity towards p70-S6K-T389 was expectedly strongly induced by HA-myr-Akt overexpression, and p70-S6K activation induces the NFL. In contrast, AMPK-pT172 was inhibited by HA-myr-Akt and the same could be confirmed for the AMPK target site, TSC2-S1387, which is required for TSC1-TSC2 activation. This result is in agreement with our model 3, predicting a negative effect of Akt on AMPK, via the NFL and IRS. These data also directly exclude hypotheses 5 and 6, which are on ranks 2 and 3 in our hypotheses ranking (Table 2).

In summary, we chose here four independent experimental set-ups to test the predictions of model 3, which was ranked 1 in our hypothesis ranking. All experiments provide strong evidence for model 3, where IRS induces AMPK and exclude the other hypotheses where other insulin downstream cues mediate AMPK activation: we show that IRS-1 strongly induces AMPK, whereas the PI3K-Akt-mTORC1 signalling axis suppresses AMPK (Fig. 5A). This is in line with the NFL (downstream of PI3K, Akt and mTORC1) suppressing AMPK, which is predicted by our model 3. The network structure of our final model is depicted in Fig. 5B.

What are the biological implications of our findings? We and others show that in HeLa cells AMPK is induced by insulin and amino acids (Fig. 1A, [23]). However, HeLa cells are particular in the sense that they do not express the AMPK upstream kinase, LKB1 [23,24]. Therefore, it was important to address whether the induction of AMPK by insulin and amino acids, observed here, is a general feature of AMPK signalling, or whether it remains restricted to LKB1-deficient cells. Hence, we tested the effect of insulin and amino acid induction on AMPK activity in C2C12 myocytes, which are LKB1 positive (Fig. 4F). We observed AMPK induction by insulin and amino acids also in C2C12 cells, underlining the general importance of our findings.

Discussion

In the present study we observed induction of AMPK by insulin and amino acids. Although this has been reported previously [23], ours is the first study to explore systematically the underlying signalling interconnections within the insulin–mTOR network. To achieve this we systematically postulated

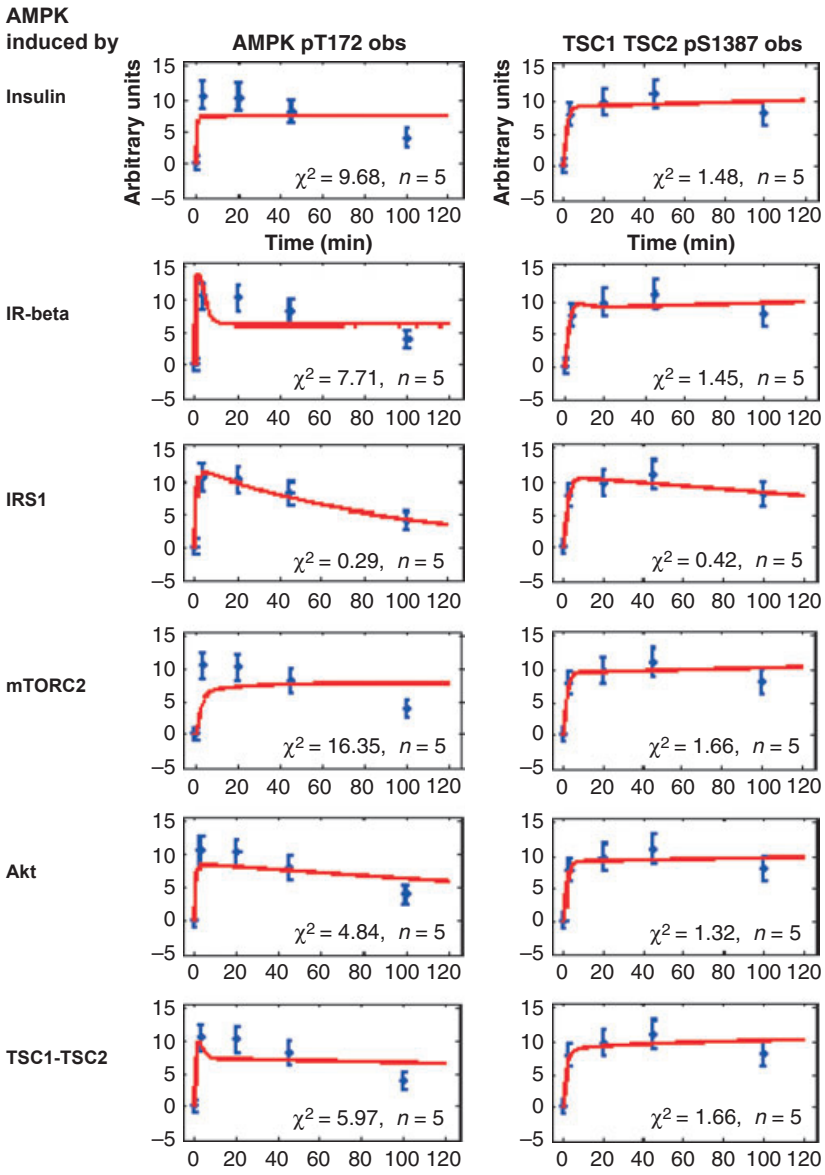

Fig. 3. Prediction: intersection of insulin and AMPK signalling at the level of IRS1. Simulated time courses (red lines) versus experimental data (blue points) for AMPK–pT172 and TSC1–TSC2–pS1387 (columns) for the six hypotheses: insulin-induced AMPK, IR-beta-induced AMPK, IRS-induced AMPK, mTORC2-induced AMPK, Akt-induced AMPK and TSC1–TSC2-induced AMPK (rows). These predictions suggest that AMPK could be regulated by kinases downstream of the IR. The IRS-induced AMPK model showed the best fit to our experimental data. Experimental data error bars indicate the SEM calculated over three repetitions. The SBML model given in Model S2 (Supporting information) reproduces the AMPK induction by IRS1. obs, observable.

Table 2. Statistical ranking of the models. N. Points = 130; K. Parameters = 24. The quality of fitting measures were used to determine a ranking of the investigated models. The IRS1-induced AMPK model showed the lowest χ^2 value, indicating that this model was the most probable (values in bold). AIC, AICc and BIC values are reported as additional measures.

Hypothesis no.	AMPK induction by	χ^2	*P*-value (*N*)	*P*-value (*N* – *p*)	AIC	AICc	BIC	Rank
1	Insulin	80.3086	0.999809	0.970256	367.233	378.66	436.053	5
2	IR-beta	78.1345	0.999908	0.980596	365.058	376.487	433.879	4
3	IRS1	**68.0217**	**0.999999**	**0.998462**	**354.946**	**366.374**	**423.767**	1
4	mTORC2	90.1238	0.99694	0.865145	377.048	388.476	445.869	6
5	Akt	75.5272	0.999964	0.988951	362.451	373.88	431.272	2
6	TSC1–TSC2	76.4666	0.99995	0.986376	363.391	374.819	432.211	3.

molecules along the insulin–mTORC1 signalling axis as putative AMPK activators. Furthermore, we presumed that the putative AMPK inducer would be upstream of mTORC1, first, because AMPK was induced earlier (3 min p.i.) than mTORC1 and its downstream targets and, second, because Raptor

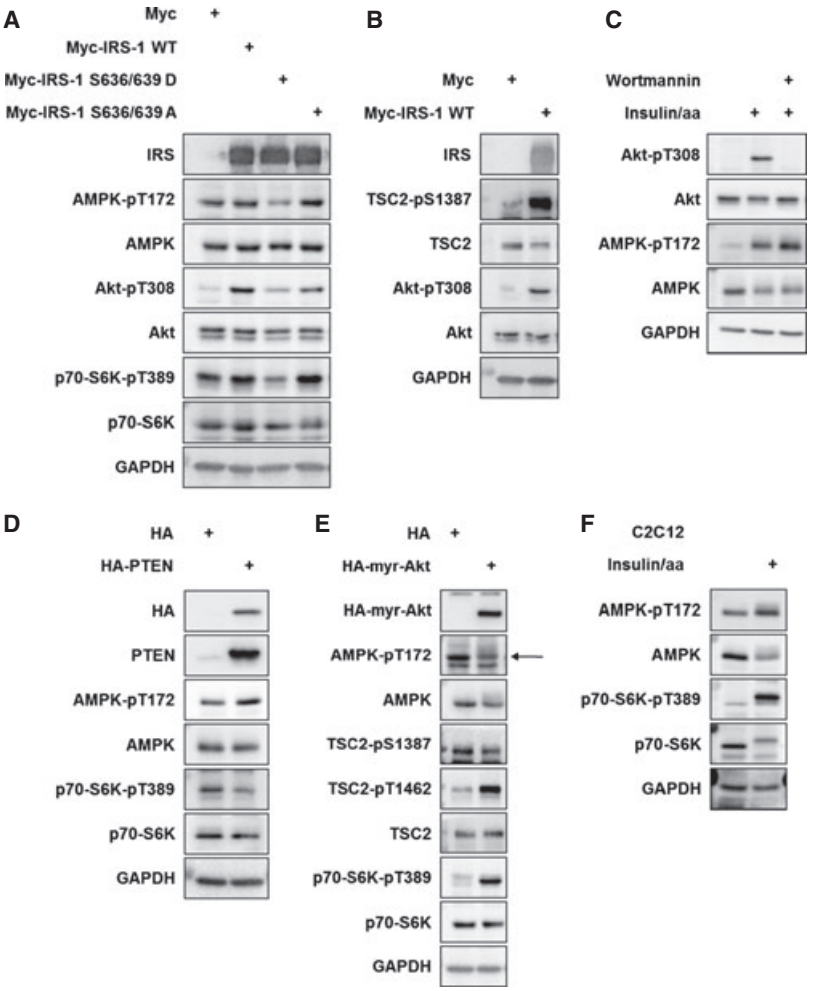

Fig. 4. Experimental testing: IRS induces AMPK. (A) IRS overexpression induces AMPK. HeLa cells were harvested 24 h after transfection with the indicated IRS-1 constructs. The mutagenized Myc-IRS-1 S6367/639 D construct mimics the constitutive phosphorylation by S6K, whereas Myc-IRS-1 S6367/639 A resembles constitutively unphosphorylated IRS and cannot be inhibited by S6K and the NFL. (B) IRS overexpression induces TSC2 phosphorylation by AMPK. HeLa cells were harvested 24 h after transfection with Myc-IRS-1 WT. (C) The PI3K inhibitor wortmannin induces AMPK. HeLa cells were starved and treated with 100 nM wortmannin or carrier before restimulation with insulin/amino acids. (D) Overexpression of the PI3K antagonist, PTEN, induces AMPK. HeLa cells were transfected 24 h before harvesting. Cells were starved of serum/amino acids before restimulation with insulin/amino acids. (E) Constitutively active Akt inhibits AMPK. HeLa cells were harvested 24 h after transfection with myristoylated Akt (HA-myr-Akt). (F) Insulin/amino acids induce AMPK in LKB1-positive C2C12 myocytes. aa, amino acids; WT, wild type.

inhibition induced AMPK (Fig. 1A). Applying a hypothesis ranking approach, we successfully used a dynamic insulin–mTOR–AMPK model for hypothesis prioritization.

In accordance with our hypothesis that best fits the data (hypothesis 3), we confirmed experimentally that IRS activates AMPK. In contrast, all tested IRS downstream cues within the PI3K–mTORC1 axis (PI3K, Akt, mTORC1) inhibited AMPK. This is in line with our prioritized model where the NFL – downstream of mTORC1 and S6K – inactivates IRS for PI3K activation as well as for AMPK induction. AMPK was induced by wild-type IRS and a mutagenized IRS version that cannot be targeted by the NFL, whereas AMPK was refractory to expression of an IRS version that resembles constitutively NFL-targeted IRS (Fig. 4A). Also this finding strongly suggests that indeed the NFL might inactivate IRS, not only for PI3K but also for AMPK induction.

From a modelling point of view, a comprehensive mTOR network has been studied statically, [38] and parts of the mTOR network have been modelled dynamically [13,39–45]. The network presented in this study is

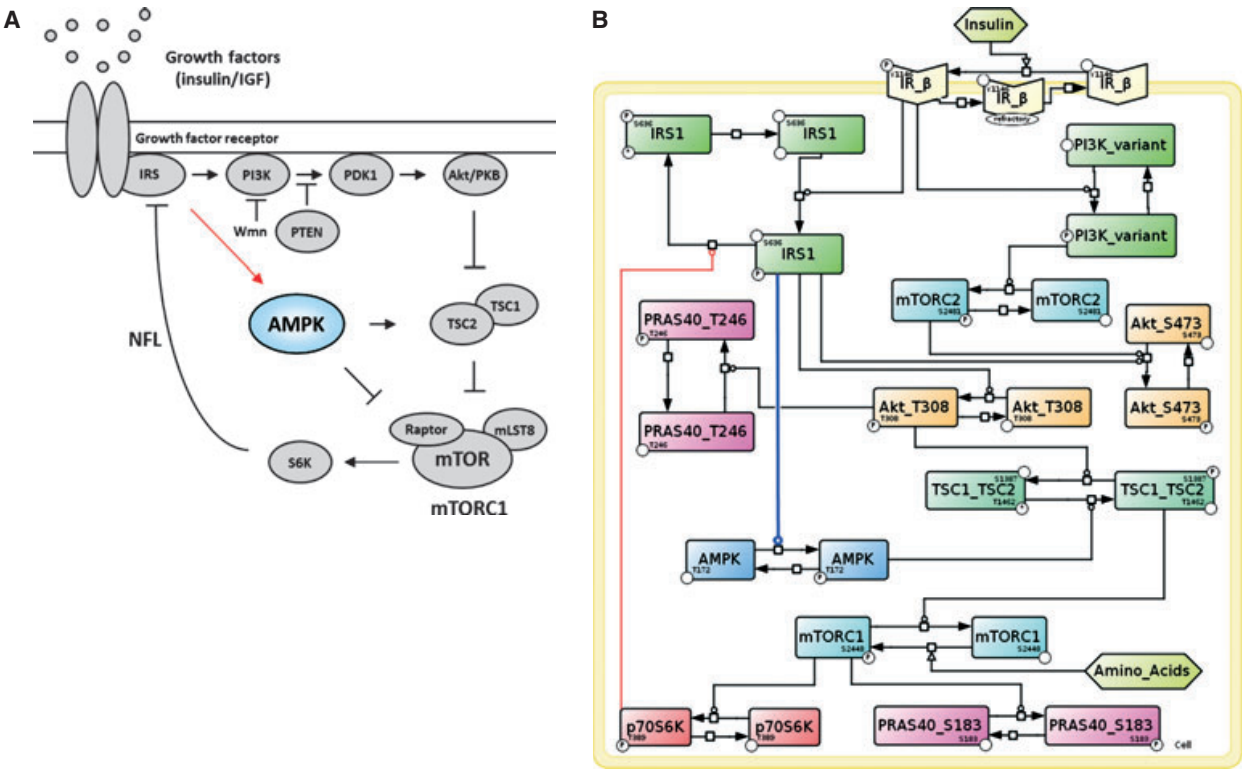

Fig. 5. New model structure: IRS is required for AMPK induction by insulin. (A) Schematic representation of the insulin-induced mTORC1 pathway, including IRS-dependent AMPK induction. Importantly, the NFL via IRS targets not only PI3K but also AMPK. Wmn, wortmannin. (B) Insulin–mTOR–AMPK model describing IRS as a regulator of AMPK.

the most extensive mTOR–AMPK model of which we are aware. Six models were defined and calibrated using our experimental data. The models shared the main network structure, but differed for the AMPK activation mechanism. After repeating cycles of parameter calibration and identifiability for each model, likelihood-based statistical measures were used to estimate a model ranking, based on the goodness-of-fit between each model and the experimental data.

In the present study we observed transient induction of AMPK by insulin and identified active IRS as an AMPK inducer. On the other hand, AMPK inhibits IRS by phosphorylation of IRS-1-S794 [46–48]. Could this mechanism be connected to the AMPK induction by IRS observed here? It is conceivable that two antagonistic mechanisms are mediated by IRS: when IRS is active, it will activate AMPK – and at the same time AMPK could directly, via IRS, contribute to the inhibition of insulin signalling. This putative mechanism clearly deserves further mechanistic investigation.

It is important to note that HeLa cells, which were used in the present study, do not express LKB1. This suggests that AMPK induction by insulin and IRS is LKB1 independent, at least in HeLa cells. Which other kinase could be responsible? AMPK phosphorylation in HeLa (and other) cells is mediated by the kinase ATM [23,24]. Interestingly, AMPK induction by ATM occurs in a tyrosine-kinase dependent, but PI3K-independent, manner [24]. This is consistent with our finding that IRS, but not PI3K, induces AMPK (Fig. 4A–D). Other possible candidates for LKB1-independent AMPK induction are the kinases CaMKK [16–19], TAK1 [20–22] or IRE1 [25].

What is the relevance of the mechanism reported here in LKB1-expressing cells? First, Suzuki *et al.* [23] reported the IGF-1 inducibility of AMPK, not only in LKB1-deficient HeLa cells, but also in LKB1-expressing PANC1 cells. Also, our own data confirm the inducibility of AMPK by insulin and amino acids in LKB1-expressing C2C12 myocytes (Fig. 4F), suggesting that this mechanism may be present in a larger number of cell types. Furthermore, at least two other studies have reported that AMPK is induced by mTORC1 [28] or S6K [29] ablation in mice. This suggests that IRS-dependent AMPK induction might become particularly prominent under conditions when the NFL is inhibited. Hence, IRS-dependent AMPK induction may exert some of the beneficial effects that

have been observed for mTOR-inhibitor treatment of metabolic and tumour diseases [49].

What could be the biological function of a transient induction of AMPK by insulin? First, AMPK inhibits mTORC1 signalling at two levels: TSC1–TSC2 and mTORC1 itself. Therefore, this transient AMPK induction in response to insulin might – in addition to the NFL – serve as a second mechanism to prevent mTORC1 hyperactivation. As an additional benefit, AMPK activation might serve as a protective mechanism to cellular stress under transiently increased metabolic rates in response to insulin.

In conclusion, we present here, to the best of our knowledge, the most comprehensive data-driven dynamic mTOR–AMPK network model. Our combined modelling–experimental approach revealed IRS as a mediator of AMPK induction in response to insulin and strongly suggests an involvement of the mTORC1-dependent NFL in AMPK regulation. The impact of this novel signalling interconnection for AMPK and mTOR biology deserves further exploration. Our findings will be highly relevant to the biomedical field because they can have important implications for administration of drugs targeting mTOR and AMPK, which are commonly used in tumour and metabolic disease treatments.

Materials and methods

Cell lines and lentiviral transduction

Experiments were performed in HeLa α Kyoto cells and C2C12 myocytes. For inducible knockdown of Raptor, HeLa cells were transduced with lentivirus encoding the tetracycline-sensitive tetracycline repressor (tTR)-Krueppel-associated box (protein domain) (KRAB) repressor and a DsRed reporter [50]. Cells were subsequently transfected with lentivirus encoding the Raptor-specific shRNA (target sequence: 5′-GGCTAGTCTGTTTCGAAATTT-3′) and a green fluorescent protein reporter (pLVTH vector), both under the control of tTR-KRAB.

Overexpression of IRS, PTEN and myristoylated Akt variants

N-terminally and hemagglutinin (HA)-tagged pSG5L HA PTEN wt (#10750), N-terminally myristoylated and HA tagged pLNCX.myr.HA.Akt1 (#9005) and N-terminally myristoylated and HA-tagged kinase dead pLNCX.myr.HA.Akt1 K179M (#9006) were ordered from Addgene. IRS1 constructs were a kind gift from A. Tzatsos [36]. Transfection was performed with 6 μg of construct per 6-cm dish using JetPEI reagent according to the manufacturer's instructions. Cells were harvested 24 h after transfection.

Antibodies and reagents

The monoclonal anti-glyceraldehyde-3-phosphate dehydrogenase (GAPDH) IgG1 was purchased from Abcam (Cambridge, UK). The anti-HA IgG 2b k (clone 12CA5) was purchased from Roche. Horseradish peroxidase (HRP)-conjugated goat anti-mouse and goat anti-rabbit IgGs were purchased from Pierce Biotechnology (Thermo Scientific, Rockford, IL USA). All other antibodies were purchased from Cell Signalling Technology (Danvers, MA, USA). Doxycycline for knockdown induction was purchased from Calbiochem, Merck (Darmstadt, Germany). Wortmannin was purchased from Sigma Aldrich (St Louis, MO, USA). Chemicals were supplied by Carl Roth (Karlsruhe, Germany) unless indicated otherwise.

Analysis of cell lysates

Where indicated, HeLa cells were starved for serum and amino acids by exchanging standard growth medium for Hank's balanced salt solution (HBSS) overnight to inhibit mTOR pathway activity. After 16 h of starvation, mTOR signalling was restimulated for 30 min with DMEM containing amino acids and supplemented with 100 nM insulin (Sigma Aldrich).

Gradual knockdown of Raptor was established by induction with 5 μg mL^{-1} of doxycycline (Calbiochem, Merck) for 0, 2 or 3 days. Wortmannin treatment: Wortmannin was added to HBSS 30 min before restimulation for 30 min with Dulbecco's modified Eagle's medium (DMEM), which was supplemented with 100 nM insulin and wortmannin. Cells were washed once with $NaCl/P_i$ and lysed with TNE lysis buffer [50 mM Tris/HCl, pH 8.0, 150 mM NaCl, 1% (v/v) Triton X-100 (Calbiochem, Merck), Complete (Roche, Mannheim, Germany), Phosphatase Inhibitor Cocktail 2 and Phosphatase Inhibitor Cocktail 3 (both Sigma Aldrich)]. Protein concentrations were measured using the Protein Assay Dye Reagent Concentrate (Bio-Rad, Hercules, CA, USA) according to the manufacturer's protocol. Concentrations were adjusted with lysis buffer. Lysates were diluted in sample buffer (5×: 6 mL of glycerol, 0.6 mL of beta-mercaptoethanol, 1.0 g of SDS, 3.75 mL of 1 M Tris, pH 6.8, 2 mg of Bromophenol Blue and 2 mL of H_2O). Whole-cell lysates were analysed using SDS/PAGE. Proteins were transferred to poly(vinylidene difluoride) membranes (Millipore, Billerica, MA, USA), blocked with 5% BSA in TBST (8 g of NaCl, 0.2 g of KCl, 8 g of Tris, pH 7.4, 0.1% Tween 20) for a minimum of 30 min and incubated with the primary antibody in 5% BSA in TBST overnight with shaking at 4°C. Blots were washed 3× with TBST, incubated with secondary antibodies coupled to HRP and washed 3× with TBST before detection.

Modelling

The illustrated graphical model in SBGN graphical notation [51] was designed using CellDesigner 4.2 [52]. The Matlab Toolbox PottersWheel [31] was used for designing and calibrating the models. The parameters for each of the models were estimated by 1000 fits with a parameter disturbance noise of 0.4 using the best fit as the starting value. For each fit a maximum of 250 iterations with χ^2 and parameter tolerances of 1e−07 were run using the optimization algorithm, TrustRegion. To reduce the computation time, cvodes integrator was selected and configured with the following parameters: maximum number of steps = 1500, relative tolerance = 1e−06 and absolute tolerance = 1e−08.

The reactions representing the dynamics of the models were described by mass action laws. Only the kinetic rate constants were estimated, and the interval [1e−06, 1e+04] was selected as constraint for each parameter. The protein initial concentrations were directly determined from our experimental data and scaled to distribute the fitting quality over the model. Experimental error bars indicate SEM. The dynamics for the species PI3K-variant were assumed by reproducing the dynamics of the insulin receptor, whereas its initial concentration was the same of the IRS1 species.

Structural identifiability was calculated *a priori* using GenSSI [32]. The model in Potterswheel format was exported in SBML and converted to Octave format using The System Biology Format Converter (SBFC) (available from sourseforge.net). Then, the model in Octave format was adapted for the software GenSSI. Symbolic solutions for each model were computed, setting 10 as the maximum number of iterations.

After executing each sequence fits, parameters were considered as nonidentifiable when their CV, measured in the best 50% fits of the calibration sequence, were higher than 5%. In combination with this preliminary analysis, the PottersWheel plugin MOTA was used to confirm the parameter nonidentifiability and to assess the relations between the target parameter and the others.

3D sensitivity analysis was performed using PottersWheel and is provided in Fig. S2. We also used PottersWheel to export the models as SBML [53] Level 2 Version 4.

Statistics

The goodness-of-fit statistical measures χ^2 [31], AIC, AICc [34] and BIC [35] were used in order to rank the hypotheses. All these measures were directly computed using PottersWheel Toolbox.

The statistical and programming language R v. 2.13.1 [54] was selected for the graphic representation of the identifiability matrix computed with MOTA.

Acknowledgements

This study was supported by the EC 6th FP NoE LifeSpan (LSHG-CT-2007-036894), the Schlieben-Lange-Programm (K.T.), the Excellence Initiative of the German Federal and State Governments (EXC 294) and the BMBF Gerontosys II – NephAge (031 5896A) (K.T.). We thank A. Tzatsos for kindly providing the IRS1 plasmids. Some of this work is part of a pending European patent application that was filed on 1 June 2011 (Application no. 11004471.6 – 1225). An International Patent Application was filed on 21 March 2012 (number to be assigned).

References

1 Zoncu R, Efeyan A & Sabatini DM (2011) mTOR: from growth signal integration to cancer, diabetes and ageing. *Nat Rev Mol Cell Biol* **12**, 21–35.
2 Polak P & Hall MN (2009) mTOR and the control of whole body metabolism. *Curr Opin Cell Biol* **21**, 209–218.
3 Sengupta S, Peterson TR & Sabatini DM (2010) Regulation of the mTOR complex 1 pathway by nutrients, growth factors, and stress. *Mol Cell* **40**, 310–322.
4 Howell JJ & Manning BD (2011) mTOR couples cellular nutrient sensing to organismal metabolic homeostasis. *Trends Endocrinol Metab* **22**, 94–102.
5 Thedieck K & Hall MN (2009) Translational control by amino acids and energy. In *The Handbook of Cell Signaling* (Bradshaw R & Dennis E eds), pp. 2285–2293. Elsevier, Academic Press, Amsterdam.
6 Thedieck K, Polak P, Kim ML, Molle KD, Cohen A, Jeno P, Arrieumerlou C & Hall MN (2007) PRAS40 and PRR5-like protein are new mTOR interactors that regulate apoptosis. *PLoS One* **2**, e1217.
7 Vander Haar E, Lee SI, Bandhakavi S, Griffin TJ & Kim DH (2007) Insulin signalling to mTOR mediated by the Akt/PKB substrate PRAS40. *Nat Cell Biol* **9**, 316–323.
8 Sancak Y, Thoreen CC, Peterson TR, Lindquist RA, Kang SA, Spooner E, Carr SA & Sabatini DM (2007) PRAS40 is an insulin-regulated inhibitor of the mTORC1 protein kinase. *Mol Cell* **25**, 903–915.
9 Wang L, Harris TE, Roth RA & Lawrence JC Jr (2007) PRAS40 regulates mTORC1 kinase activity by functioning as a direct inhibitor of substrate binding. *J Biol Chem* **282**, 20036–20044.
10 Fonseca BD, Smith EM, Lee VH, MacKintosh C & Proud CG (2007) PRAS40 is a target for mammalian target of rapamycin complex 1 and is required for signaling downstream of this complex. *J Biol Chem* **282**, 24514–24524.

11 Oshiro N, Takahashi R, Yoshino K, Tanimura K, Nakashima A, Eguchi S, Miyamoto T, Hara K, Takehana K, Avruch J *et al.* (2007) The proline-rich Akt substrate of 40 kDa (PRAS40) is a physiological substrate of mammalian target of rapamycin complex 1. *J Biol Chem* **282**, 20329–20339.
12 Wang L, Harris TE & Lawrence JC Jr (2008) Regulation of proline-rich Akt substrate of 40 kDa (PRAS40) function by mammalian target of rapamycin complex 1 (mTORC1)-mediated phosphorylation. *J Biol Chem* **283**, 15619–15627.
13 Dalle Pezze P, Sonntag AG, Thien A, Prentzell MT, Gödel M, Fischer S, Neumann-Haefelin E, Huber TB, Baumeister R, Shanley DP *et al.* (2012) A dynamic network model of mTOR signalling reveals TSC-independent mTORC2 regulation. *Sci Signal* **5**, ra25. doi:10.1126/scisignal.2002469.
14 Mihaylova MM & Shaw RJ (2011) The AMPK signalling pathway coordinates cell growth, autophagy and metabolism. *Nat Cell Biol* **13**, 1016–1023.
15 Lizcano JM, Goransson O, Toth R, Deak M, Morrice NA, Boudeau J, Hawley SA, Udd L, Makela TP, Hardie DG *et al.* (2004) LKB1 is a master kinase that activates 13 kinases of the AMPK subfamily, including MARK/PAR-1. *EMBO J* **23**, 833–843.
16 Hawley SA, Pan DA, Mustard KJ, Ross L, Bain J, Edelman AM, Frenguelli BG & Hardie DG (2005) Calmodulin-dependent protein kinase kinase-beta is an alternative upstream kinase for AMP-activated protein kinase. *Cell Metab* **2**, 9–19.
17 Fogarty S, Hawley SA, Green KA, Saner N, Mustard KJ & Hardie DG (2010) Calmodulin-dependent protein kinase kinase-beta activates AMPK without forming a stable complex: synergistic effects of Ca2+ and AMP. *Biochem J* **426**, 109–118.
18 Hurley RL, Anderson KA, Franzone JM, Kemp BE, Means AR & Witters LA (2005) The Ca2+/calmodulin-dependent protein kinase kinases are AMP-activated protein kinase kinases. *J Biol Chem* **280**, 29060–29066.
19 Woods A, Dickerson K, Heath R, Hong SP, Momcilovic M, Johnstone SR, Carlson M & Carling D (2005) Ca2+/calmodulin-dependent protein kinase kinase-beta acts upstream of AMP-activated protein kinase in mammalian cells. *Cell Metab* **2**, 21–33.
20 Xie M, Zhang D, Dyck JR, Li Y, Zhang H, Morishima M, Mann DL, Taffet GE, Baldini A, Khoury DS *et al.* (2006) A pivotal role for endogenous TGF-beta-activated kinase-1 in the LKB1/AMP-activated protein kinase energy-sensor pathway. *Proc Natl Acad Sci USA* **103**, 17378–17383.
21 Herrero-Martin G, Hoyer-Hansen M, Garcia-Garcia C, Fumarola C, Farkas T, Lopez-Rivas A & Jaattela M (2009) TAK1 activates AMPK-dependent cytoprotective autophagy in TRAIL-treated epithelial cells. *EMBO J* **28**, 677–685.
22 Momcilovic M, Hong SP & Carlson M (2006) Mammalian TAK1 activates Snf1 protein kinase in yeast and phosphorylates AMP-activated protein kinase in vitro. *J Biol Chem* **281**, 25336–25343.
23 Suzuki A, Kusakai G, Kishimoto A, Shimojo Y, Ogura T, Lavin MF & Esumi H (2004) IGF-1 phosphorylates AMPK-alpha subunit in ATM-dependent and LKB1-independent manner. *Biochem Biophys Res Commun* **324**, 986–992.
24 Sun Y, Connors KE & Yang DQ (2007) AICAR induces phosphorylation of AMPK in an ATM-dependent, LKB1-independent manner. *Mol Cell Biochem* **306**, 239–245.
25 Meares GP, Hughes KJ, Naatz A, Papa FR, Urano F, Hansen PA, Benveniste EN & Corbett JA (2011) IRE1-dependent activation of AMPK in response to nitric oxide. *Mol Cell Biol* **31**, 4286–4297.
26 Inoki K, Zhu T & Guan KL (2003) TSC2 mediates cellular energy response to control cell growth and survival. *Cell* **115**, 577–590.
27 Gwinn DM, Shackelford DB, Egan DF, Mihaylova MM, Mery A, Vasquez DS, Turk BE & Shaw RJ (2008) AMPK phosphorylation of raptor mediates a metabolic checkpoint. *Mol Cell* **30**, 214–226.
28 Polak P, Cybulski N, Feige JN, Auwerx J, Ruegg MA & Hall MN (2008) Adipose-specific knockout of raptor results in lean mice with enhanced mitochondrial respiration. *Cell Metab* **8**, 399–410.
29 Aguilar V, Alliouachene S, Sotiropoulos A, Sobering A, Athea Y, Djouadi F, Miraux S, Thiaudiere E, Foretz M, Viollet B *et al.* (2007) S6 kinase deletion suppresses muscle growth adaptations to nutrient availability by activating AMP kinase. *Cell Metab* **5**, 476–487.
30 Inoki K, Ouyang H, Li Y & Guan KL (2005) Signaling by target of rapamycin proteins in cell growth control. *Microbiol Mol Biol Rev* **69**, 79–100.
31 Maiwald T & Timmer J (2008) Dynamical modeling and multi-experiment fitting with PottersWheel. *Bioinformatics* **24**, 2037–2043.
32 Chis O, Banga JR & Balsa-Canto E (2011) GenSSI: a software toolbox for structural identifiability analysis of biological models. *Bioinformatics* **27**, 2610–2611.
33 Hengl S, Kreutz C, Timmer J & Maiwald T (2007) Data-based identifiability analysis of non-linear dynamical models. *Bioinformatics* **23**, 2612–2618.
34 Akaike H (1974) A new look at the statistical model identification. *IEEE Trans Automat Contr* **19**, 716–723.
35 Schwarz G (1978) Estimating the dimension of a model. *Ann Stat* **6**, 461–464.
36 Tzatsos A & Kandror KV (2006) Nutrients suppress phosphatidylinositol 3-kinase/Akt signaling via raptor-dependent mTOR-mediated insulin receptor substrate 1 phosphorylation. *Mol Cell Biol* **26**, 63–76.
37 Kohn AD, Takeuchi F & Roth RA (1996) Akt, a pleckstrin homology domain containing kinase, is activated

primarily by phosphorylation. *J Biol Chem* **271**, 21920–21926.
38 Caron E, Ghosh S, Matsuoka Y, Ashton-Beaucage D, Therrien M, Lemieux S, Perreault C, Roux PP & \Kitano H (2010) A comprehensive map of the mTOR signaling network. *Mol Syst Biol* **6**, 453.
39 Sedaghat AR, Sherman A & Quon MJ (2002) A mathematical model of metabolic insulin signaling pathways. *Am J Physiol Endocrinol Metab* **283**, E1084–E1101.
40 Jain P & Bhalla US (2009) Signaling logic of activity-triggered dendritic protein synthesis: an mTOR gate but not a feedback switch. *PLoS Comput Biol* **5**, e1000287.
41 Faratian D, Goltsov A, Lebedeva G, Sorokin A, Moodie S, Mullen P, Kay C, Um IH, Langdon S, Goryanin I *et al*. (2009) Systems biology reveals new strategies for personalizing cancer medicine and confirms the role of PTEN in resistance to trastuzumab. *Cancer Res* **69**, 6713–6720.
42 Vinod PK & Venkatesh KV (2009) Quantification of the effect of amino acids on an integrated mTOR and insulin signaling pathway. *Mol BioSyst* **5**, 1163–1173.
43 Borisov N, Aksamitiene E, Kiyatkin A, Legewie S, Berkhout J, Maiwald T, Kaimachnikov NP, Timmer J, Hoek JB & Kholodenko BN (2009) Systems-level interactions between insulin-EGF networks amplify mitogenic signaling. *Mol Syst Biol* **5**, 256.
44 Kuepfer L, Peter M, Sauer U & Stelling J (2007) Ensemble modeling for analysis of cell signaling dynamics. *Nat Biotechnol* **25**, 1001–1006.
45 Kiselyov VV, Versteyhe S, Gauguin L & De Meyts P (2009) Harmonic oscillator model of the insulin and IGF1 receptors' allosteric binding and activation. *Mol Syst Biol* **5**, 243.
46 Ning J & Clemmons DR (2010) AMP-activated protein kinase inhibits IGF-I signaling and protein synthesis in vascular smooth muscle cells via stimulation of insulin receptor substrate 1 S794 and tuberous sclerosis 2 S1345 phosphorylation. *Mol Endocrinol* **24**, 1218–1229.
47 Tzatsos A & Tsichlis PN (2007) Energy depletion inhibits phosphatidylinositol 3-kinase/Akt signaling and induces apoptosis via AMP-activated protein kinase-dependent phosphorylation of IRS-1 at Ser-794. *J Biol Chem* **282**, 18069–18082.
48 Jakobsen SN, Hardie DG, Morrice N & Tornqvist HE (2001) 5′-AMP-activated protein kinase phosphorylates IRS-1 on Ser-789 in mouse C2C12 myotubes in response to 5-aminoimidazole-4-carboxamide riboside. *J Biol Chem* **276**, 46912–46916.
49 Garcia-Echeverria C (2011) Blocking the mTOR pathway: a drug discovery perspective. *Biochem Soc Trans* **39**, 451–455.
50 Wiznerowicz M & Trono D (2003) Conditional suppression of cellular genes: lentivirus vector-mediated drug-inducible RNA interference. *J Virol* **77**, 8957–8961.
51 Le Novere N, Hucka M, Mi H, Moodie S, Schreiber F, Sorokin A, Demir E, Wegner K, Aladjem MI, Wimalaratne SM *et al*. (2009) The Systems Biology Graphical Notation. *Nat Biotechnol* **27**, 735–741.
52 Funahashi A, Morohashi M, Kitano H & Tanimura N (2003) CellDesigner: a process diagram editor for gene-regulatory and biochemical networks. *BIOSILICO* **1**, 159–162.
53 Hucka M, Finney A, Sauro HM, Bolouri H, Doyle JC, Kitano H, Arkin AP, Bornstein BJ, Bray D, Cornish-Bowden A *et al*. (2003) The systems biology markup language (SBML): a medium for representation and exchange of biochemical network models. *Bioinformatics* **19**, 524–531.
54 R Development Core Team (2005) *A Language and Environment for Statistical Computing*. R Foundation for Statistical Computing, Vienna, Austria.

Supporting information

The following supplementary material is available:
Fig. S1. Identifiability and parameter estimation for the IR-beta-induced AMPK model (hypothesis No.2).
Fig. S2. Sensitivity analysis for the IRS1-induced AMPK model (hypothesis No.3).
Fig. S3. Additional simulated versus experimental time courses for the IRS1-induced AMPK model (hypothesis No.3).
Model S1. febs_mtor_model_ampk_by_irs1_pottersWheel.m (PottersWheel format).
Model S2. febs_mtor_model_ampk_by_irs1_sbml.xml (SBML format).

This supplementary material can be found in the online version of this article.

Please note: As a service to our authors and readers, this journal provides supporting information supplied by the authors. Such materials are peer-reviewed and may be reorganized for online delivery, but are not copy-edited or typeset. Technical support issues arising from supporting information (other than missing files) should be addressed to the authors.

References

Aguilar, V., Alliouachene, S., Sotiropoulos, A., Sobering, A., Athea, Y., Djouadi, F., Miraux, S., Thiaudière, E., Foretz, M., Viollet, B., Diolez, P., Bastin, J., Benit, P., Rustin, P., Carling, D., Sandri, M., Ventura-Clapier, R., and Pende, M. (2007). S6 kinase deletion suppresses muscle growth adaptations to nutrient availability by activating AMP kinase. *Cell Metabolism*, **5**(6):476–87.

Akaike, H. (1973). Information theory and an extension of the maximum likelihood principle. In Proceedings of the Second International Symposium on Information Theory, pages 267–281, Petrov, B. N. and Caski, F. (Eds.), Akademiai Kiado, Budapest.

Aldridge, B. B., Burke, J. M., Lauffenburger, D. A., and Sorger, P. K. (2006). Physicochemical modelling of cell signalling pathways. *Nature Cell Biology*, **8**(11):1195–1203.

Alvers, A. L., Wood, M. S., Hu, D., Kaywell, A. C., Dunn, W. A., and Aris, J. P. (2009). Autophagy is required for extension of yeast chronological life span by rapamycin. *Autophagy*, **5**(6):847–9.

Amato, R., D'Antona, L., Porciatti, G., Agosti, V., Menniti, M., Rinaldo, C., Costa, N., Bellacchio, E., Mattarocci, S., Fuiano, G., Soddu, S., Paggi, M. G., Lang, F., and Perrotti, N. (2009). Sgk1 activates MDM2-dependent p53 degradation and affects cell proliferation, survival, and differentiation. *Journal of Molecular Medicine*, **87**(12):1221–39.

Anisimov, V. N., Zabezhinski, M. A., Popovich, I. G., Piskunova, T. S., Semenchenko, A. V., Tyndyk, M. L., Yurova, M. N., Antoch, M. P., and Blagosklonny, M. V. (2010). Rapamycin extends maximal lifespan in cancer-prone mice. *American Journal of Pathology*, **176**(5):2092–7.

Araujo, R. P., Liotta, L. A., and Petricoin, E. F. (2007). Proteins, drug targets and the mechanisms they control: the simple truth about complex networks. *Nature Reviews Drug Discovery*, **6**(11):871–80.

Ay, F., Xu, F., and Kahveci, T. (2009). Scalable steady state analysis of boolean biological regulatory networks. *PLOS ONE*, **4**(12):e7992.

Bach, D., Pich, S., Soriano, F., Vega, N., Baumgartner, B., Oriola, J., Daugaard, J. L. M. C. J. Z. J., Rabasa-Lhoret, R., Wallberg-Henriksson, M. L. H., Palacín, M., Vidal, F. R. H., and Brand, A. Z. M. (2003). Mitofusin-2 determines mitochondrial network architecture and mitochondrial metabolism. A novel regulatory mechanism altered in obesity. *The Journal of Biological Chemistry*, **278**(19):17190–7.

Bäck, T., Fogel, D. B., and Michalewicz, Z. (1997). *Handbook of evolutionary computation*. Taylor and Francis (Eds.), IOP Publishing Ltd., Bristol, UK, 1st edition.

Bäck, T. and Schwefel, H. P. (1993). An overview of evolutionary algorithms for parameter optimization. *Evolutionary Computation*, **1**(1):1–23.

Bahar, R., Hartmann, C. H., Rodriguez, K. A., Denny, A. D., Busuttil, R. A., Dollé, M. E., Calder, R. B., Chisholm, G. B., Pollock, B. H., Klein, C. A., and Vijg, J. (2006). Increased cell-to-cell variation in gene expression in ageing mouse heart. *Nature*, **441**(7096):1011–4.

Bai, X., Ma, D., Liu, A., Shen, X., Wang, Q. J., Liu, Y., and Jiang, Y. (2007). Rheb activates mTOR by antagonizing its endogenous inhibitor, FKBP38. *Science*, **318**(5852):977–80.

Balsa-Canto, E., Alonso, A. A., and Banga, J. R. (2010). An iterative identification procedure for dynamic modeling of biochemical networks. *BMC Systems Biology*, **4**(11).

Bass, T., Weinkove, D., Houthoofd, K., Gems, D., and Partridge, L. (2007). Effects of resveratrol on lifespan in Drosophila melanogaster and Caenorhabditis elegans. *Mechanisms of Ageing and Development*, **128**(10):546–52.

Beggs, A., Latchford, A., Vasen, H., Moslein, G., Alonso, A., Aretz, S., Bertario, L., Blanco, I., Bülow, S., Burn, J., Capella, G., Colas, C., Friedl, W., Møller, P., Hes, F., Järvinen, H., Mecklin, J., Nagengast, F., Parc, Y., Phillips, R., Hyer, W., Ponz de Leon, M., Renkonen-Sinisalo, L., Sampson, J., Stormorken, A., Tejpar, S., Thomas, H., Wijnen, J., Clark, S., and Hodgson, S. (2010). Peutz-Jeghers syndrome: a systematic review and recommendations for management. *Gut*, **59**(7):975–86.

Bellot, G., Garcia-Medina, R., Gounon, P., Chiche, J., Roux, D., Pouysségur, J., and Mazure, N. M. (2009). Hypoxia-induced autophagy is mediated through hypoxia-

inducible factor induction of BNIP3 and BNIP3L via their BH3 domains. *Molecular and Cellular Biology*, **29**(10):2570–2581.

Bellu, G., Saccomani, M. P., Audoly, S., and D'Angiò, L. (2007). DAISY: a new software tool to test global identifiability of biological and physiological systems. *Computer Methods and Programs in Biomedicine*, **88**(1):52–61.

Biondi, R. M. (2004). Phosphoinositide-dependent protein kinase 1, a sensor of protein conformation. *Trends in Biochemical Sciences*, **29**(3):136–42.

Bjornsti, M.-A. and Houghton, P. J. (2004). The tor pathway: a target for cancer therapy. *Nature Reviews Cancer*, **4**(5):335–348.

Blagosklonny, M. V. (2010). Linking calorie restriction to longevity through sirtuins and autophagy: any role for TOR. *Cell Death and Disease*, **1**(1):e12.

Blagosklonny, M. V. and Hall, M. N. (2009). Growth and aging: a common molecular mechanism. *Aging*, **1**(4):357–62.

Borisov, N., Aksamitiene, E., Kiyatkin, A., Legewie, S., Berkhout, J., Maiwald, T., Kaimachnikov, N. P., Timmer, J., Hoek, J. B., and Kholodenko, B. N. (2009). Systems-level interactions between insulin-EGF networks amplify mitogenic signaling. *Molecular Systems Biology*, **5**(256).

Borisuk, M. T. (1997). *Bifurcation analysis of a model of the frog egg cell cycle*. PhD thesis. Digital Library and Archives, University Library, Virginia Tech, USA.

Borisuk, M. T. and Tyson, J. J. (1998). Bifurcation analysis of a model of mitotic control in frog eggs. *Journal of Theoretical Biology*, **195**(1):69–85.

Boulbes, D., Chen, C. H., Shaikenov, T., Agarwal, N. K., Peterson, T. R., Addona, T. A., Keshishian, H., Carr, S. A., Magnuson, M. A., and Sabatini, D. M. (2010). Rictor phosphorylation on the Thr-1135 site does not require mammalian target of rapamycin complex 2. *Molecular Cancer Research*, **8**(6):896–906.

Bozulic, L., Surucu, B., Hynx, D., and Hemmings, B. A. (2008). PKBα/Akt1 acts downstream of DNA-PK in the DNA double-strand break response and promotes survival. *Molecular Cell*, **30**(2):203–13.

Brännmark, C., Palmér, R., Glad, S. T., Cedersund, G., and Strålfors, P. (2010). Mass and information feedbacks through receptor endocytosis govern insulin signaling as revealed using a parameter-free modeling framework. *The Journal of Biological Chemistry*, **285**(26):20171–9.

Brugarolas, J., Lei, K., Hurley, R. L., Manning, B. D., Reiling, J. H., Hafen, E., Witters, L. A., Ellisen, L. W., and Kaelin, W. G. (2004). Regulation of mTOR function in response to hypoxia by REDD1 and the TSC1/TSC2 tumor suppressor complex. *Genes and Development*, **18**(23):2893–904.

Bruhn, M. A., Pearson, R. B., Hannan, R. D., and Sheppard, K. E. (2010). Second AKT: the rise of SGK in cancer signalling. *Growth Factors*, **28**(6):394–408.

Brunet, A., Park, J., Tran H, Hu, L., Hemmings, B., and Greenberg, M. (2001). Protein kinase SGK mediates survival signals by phosphorylating the forkhead transcription factor FKHRL1 (FOXO3a). *Molecular and Cellular Biology*, **21**(3):952–965.

Brunet, A., Sweeney, L. B., Sturgill, J. F., Chua, K. F., Greer, P. L., Lin, Y., Tran, H., Ross, S. E., Mostoslavsky, R., Cohen, H. Y., Hu, L. S., Cheng, H. L., Jedrychowski, M. P., Gygi, S. P., Sinclair, D. A., Alt, F. W., and Greenberg, M. E. (2004). Stress-dependent regulation of FOXO transcription factors by the SIRT1 deacetylase. *Science*, **303**(5666):2011–5.

Brunn, G. J., Williams, J., Sabers, C., Wiederrecht, G., Lawrence Jr., J. C., and Abraham, R. T. (1996). Direct inhibition of the signaling functions of the mammalian target of rapamycin by the phosphoinositide 3-kinase inhibitors, wortmannin and LY294002. *EMBO Journal*, **15**(19):5256–67.

Byrd, R. H., Schnabel, R. B., and Schultz, G. A. (1987). A trust region algorithm for nonlinearly constrained optimization. *SIAM Journal on Numerical Analysis*, **24**:1152–1170.

Cai, H., Das, S., Kamimura, Y., Long, Y., Parent, C. A., and Devreotes, P. N. (2010). Ras-mediated activation of the TORC2–PKB pathway is critical for chemotaxis. *The Journal of Cell Biology*, **190**(2):233.

Cantó, C., Gerhart-Hines, Z., Feige, J., Lagouge, M., Noriega, L., Milne, J., Elliot, P., Puigserver, P., and Auwerx, J. (2009). AMPK regulates energy expenditure by modulating NAD+ metabolism and SIRT1 activity. *Nature*, **458**(7241):1056–60.

Caron, E., Ghosh, S., Matsuoka, Y., Ashton-Beaucage, D., Therrien, M., Lemieux, S., Perreault, C., Roux, P. P., and Kitano, H. (2010). A comprehensive map of the mTOR signaling network. *Molecular Systems Biology*, **6**(453).

Celis, M., Dennis, J. E., and Tapia, R. A. (1984). A trust region strategy for nonlinear equality constrained optimization. In Proceedings of the SIAM Conference on Numerical Optimization, pages 71–82, Boggs, P., Byrd, R. and Schnabel, R. (Eds.), Philadelphia, USA.

Chaanine, A. H., Jeong, D., Liang, L., Chemaly, E. R., Fish, K., Gordon, R. E., and Hajjar, R. J. (2012). JNK modulates FOXO3a for the expression of the mitochondrial death and mitophagy marker BNIP3 in pathological hypertrophy and in heart failure. *Cell Death and Disease*, **3**(2):265.

Charest, P. G., Shen, Z., Lakoduk, A., Sasaki, A. T., Briggs, S. P., and Firtel, R. A. (2010). A Ras signaling complex controls the RasC-TORC2 pathway and directed cell migration. *Developmental Cell*, **18**(5):737–749.

Chen, W. W., Niepel, M., and Sorger, P. K. (2010). Classic and contemporary approaches to modeling biochemical reactions. *Genes and Development*, **24**(17):1861–1875.

Chiş, O., Banga, J. R., and Balsa-Canto, E. (2011). GenSSI: a software toolbox for structural identifiability analysis of biological models. *Bioinformatics*, **27**(18):2010–1.

Cho, K. H., Shin, S. Y., Kolch, W., and Wolkenhauer, O. (2003). Experimental design in systems biology, based on parameter sensitivity analysis using a Monte Carlo method: a case study for the TNFα-mediated NF-κB signal transduction pathway. *SIMULATION*, **79**(12):726–739.

Choi, J., Chen, J., Schreiber, S. L., and Clardy, J. (1996). Structure of the FKBP 12-rapamycin complex interacting with the binding domain of human FRAP. *Science*, **273**(5272):239–239.

Christie, G. R., Hajduch, E., Hundal, H. S., Proud, C. G., and Taylor, P. M. (2002). Intracellular sensing of amino acids in Xenopus laevis oocytes stimulates p70 S6 kinase in a target of rapamycin-dependent manner. *The Journal of Biological Chemistry*, **277**(12):9952–7.

Colman, R. J., Anderson, R. M., Johnson, S. C., Kastman, E. K., Kosmatka, K. J., Beasley, T. M., Allison, D. B., Cruzen, C., Simmons, H. A., Kemnitz, J. W., and Weindruch, R. (2009). Caloric restriction delays disease onset and mortality in rhesus monkeys. *Science*, **325**(5937):201–4.

Copp, J., Manning, G., and Hunter, T. (2009). TORC-specific phosphorylation of mammalian target of rapamycin (mTOR): phospho-Ser2481 is a marker for intact mTOR signaling complex 2. *Cancer Research*, **69**(5):1821.

Corana, A., Marchesi, M., Martini, C., and Ridella, S. (1987). Minimizing multimodal functions of continuous variables with the "simulated annealing" algorithm. *ACM Transactions on Mathematical Software*, **13**(3):262–280.

Cormen, T. H., Leiserson, C. E., Rivest, R. L., and Stein, C. (2009). *Introduction to algorithms*. MIT Press, USA, 3rd edition.

Cuervo, A. M. (2008). Autophagy and aging. *Trends in Genetics*, **24**(12):604–612.

Cybulski, N. and Hall, M. N. (2009). TOR complex 2: a signaling pathway of its own. *Trends in Biochemical Sciences*, **34**(12):620–7.

Dalle Pezze, P., Sonntag, A. G., Thien, A., Prentzell, M. T., Gödel, M., Fischer, S., Neumann-Haefelin, E., Huber, T. B., Baumeister, R., Shanley, D. P., and Thedieck, K. (2012a). A dynamic network model of mTOR signaling reveals TSC-independent mTORC2 regulation. *Science Signaling*, **5**(217):ra25.

Dalle Pezze, P., Sonntag, A. G., Shanley, D. P., and Thedieck, K. (2012b). Response to Comment on "A Dynamic Network Model of mTOR Signaling Reveals TSC-Independent mTORC2 Regulation": Building a Model of the mTOR Signaling Network with a Potentially Faulty Tool. *Science Signaling*, **5**(232):lc4.

Dann, S. G., Selvaraj, A., and Thomas, G. (2007). mTOR Complex1-S6K1 signaling: at the crossroads of obesity, diabetes and cancer. *Trends in Molecular Medicine*, **13**(6):252–9.

Dann, S. G. and Thomas, G. (2006). The amino acid sensitive TOR pathway from yeast to mammals. *FEBS Letters*, **580**(12):2821–9.

Déry, M. A., Michaud, M. D., and Richard, D. E. (2005). Hypoxia-inducible factor 1: regulation by hypoxic and non-hypoxic activators. *The International Journal of Biochemistry and Cell Biology*, **37**(3):535–40.

deVente, J. E., Carey, J. O., Bryant, W. O., Pettit, G. J., and Ways, D. K. (1996). Transcriptional regulation of insulin receptor substrate 1 by protein kinase C. *The Journal of Biological Chemistry*, **271**(50):32276–80.

Drummond, M. J., Bell, J. A., Fujita, S., Dreyer, H. C., Glynn, E. L., Volpi, E., and Rasmussen, B. B. (2008). Amino acids are necessary for the insulin-induced activation of mTOR/S6K1 signaling and protein synthesis in healthy and insulin resistant human skeletal muscle. *Clinical Nutrition*, **27**(3):447–56.

Dunlop, E. A. and Tee, A. R. (2009). Mammalian target of rapamycin complex 1: signalling inputs, substrates and feedback mechanisms. *Cellular Signalling*, **21**(6):827–835.

Durán, R. V., Oppliger, W., Robitaille, A. M., Heiserich, L., Skendaj, R., Gottlieb, E., and Hall, M. N. (2012). Glutaminolysis activates Rag-mTORC1 signaling. *Molecular Cell*, **47**(3):1–10.

Embi, N., Rylatt, D. B., and Cohen, P. (1980). Glycogen synthase kinase-3 from rabbit skeletal muscle. Separation from cyclic-AMP-dependent protein kinase and phosphorylase kinase. *European Journal of Biochemistry*, **107**(2):519–27.

Evans, D. S., Kapahi, P., Hsueh, W.-C., and Kockel, L. (2010). TOR signaling never gets old: aging, longevity and TORC1 activity. *Ageing Research Reviews*, **10**(2):225–37.

Faratian, D., Goltsov, A., Lebedeva, G., Sorokin, A., Moodie, S., Mullen, P., Kay, C., Um, I. H., Langdon, S., Goryanin, I., and Harrison, D. J. (2009). Systems biology reveals new strategies for personalizing cancer medicine and confirms the role of PTEN in resistance to trastuzumab. *Cancer Research*, **69**(16):6713–20.

Feldman, M. E., Apsel, B., Uotila, A., Loewith, R., Knight, Z. A., Ruggero, D., and Shokat, K. M. (2009). Active-site inhibitors of mTOR target rapamycin-resistant outputs of mTORC1 and mTORC2. *PLOS Biology*, **7**(2):e1000038.

Feldman, M. E. and Shokat, K. M. (2010). New inhibitors of the PI3K-Akt-mTOR pathway: insights into mTOR signaling from a new generation of Tor kinase domain inhibitors (TORKinibs). *Current Topics in Microbiology and Immunology*, **347**:241–62.

Feng, J., Park, J., Cron, P., Hess, D., and Hemmings, B. A. (2004). Identification of a PKB/Akt hydrophobic motif Ser-473 kinase as DNA-dependent protein kinase. *The Journal of Biological Chemistry*, **279**(39):41189–41196.

Finch, C. E. and Kirkwood, T. B. L. (2000). *Chance, development and aging*. Oxford University Press, USA.

Finkel, T. and Holbrook, N. (2000). Oxidants, oxidative stress and the biology of ageing. *Nature*, **408**(6809):239–47.

Finley, L. W. S. and Haigis, M. C. (2009). The coordination of nuclear and mitochondrial communication during aging and calorie restriction. *Ageing Research Reviews*, **8**(3):173–88.

Fogel, D. B., Fogel, L. J., and Atmar, J. W. (1991). Meta-evolutionary programming. In Proceedings of the 25th Annual Asilomar Conference on Signals, Systems and Computers, pages 540–545, Chen, R. R. (Eds.), Pacific Grove, California, USA.

Foster, K. G. and Fingar, D. C. (2010). Mammalian target of rapamycin (mTOR): conducting the cellular signaling symphony. *The Journal of Biological Chemistry*, **285**(19):14071–7.

Frias, M. A., Thoreen, C. C., Jaffe, J. D., Schroder, W., Sculley, T., Carr, S. A., and Sabatini, D. M. (2006). mSin1 is necessary for Akt/PKB phosphorylation, and its isoforms define three distinct mTORC2s. *Current Biology*, **16**(18):1865–70.

Funahashi, A., Matsuoka, Y., Jouraku, A., Morohashi, M., Kikuchi, N., and Kitano, H. (2008). CellDesigner 3.5: a versatile modeling tool for biochemical networks. *Proceedings of the IEEE*, **96**(8):1254–1265.

Funahashi, A., Tanimura, N., Morohashi, M., and Kitano, H. (2003). CellDesigner: a process diagram editor for gene-regulatory and biochemical networks. *BIOSILICO*, **1**(5):159–162.

Garcia-Echeverria, C. (2011). Blocking the mTOR pathway: a drug discovery perspective. *Biochemical Society Transactions*, **39**(part 2):451–455.

Garcia-Martinez, J. M. and Alessi, D. R. (2008). mTOR complex 2 (mTORC2) controls hydrophobic motif phosphorylation and activation of serum- and glucocorticoid-induced protein kinase 1 (SGK1). *Biochemical Journal*, **416**(3):375–85.

Garg, A., Xenarios, I., Mendoza, L., and De Micheli, G. (2007). An efficient method for dynamic analysis of gene regulatory networks and in silico gene perturbation experiments. In Proceedings of the 11th Annunal International Conference on Research in Computational Molecular Biology (RECOMB), pages 62–76, Speed, T. and Huang, H. (Eds.), Springer-Verlag, Berlin.

Geva-Zatorsky, N., Rosenfeld, N., Itzkovitz, S., Milo, R., Sigal, A., Dekel, E., Yarnitzky, T., Liron, Y., Polak, P., Lahav, G., and Alon, U. (2006). Oscillations and variability in the p53 system. *Molecular Systems Biology*, **2**(2006.0033).

Gibson, M. A. and Bruck, J. (2000). Efficient exact stochastic simulation of chemical systems with many species and many channels. *Journal of Physical Chemistry A*, **104**(9):1876–1889.

Gill, P. E., Murray, W., and Wright, M. H. (1981). *Practical optimization*. Academic Press, London.

Gillespie, D. T. (1976). A general method for numerically simulating the stochastic time evolution of coupled chemical reactions. *Journal of Computational Physics*, **22**(4):403–434.

Gingras, A. C., Raught, B., and Sonenberg, N. (1999). eIF4 initiation factors: effectors of mRNA recruitment to ribosomes and regulators of translation. *Annual Review of Biochemistry*, **68**:913–63.

Giri, L., Mutalik, V. K., and Ventakesh, K. V. (2004). A steady state analysis indicates that negative feedback regulation of PTP1B by Akt elicits bistability in insulin-stimulated GLUT4 translocation. *Theoretical Biology and Medical Modelling*, **1**(2).

Glick, D., Barth, S., and Macleod, K. F. (2010). Autophagy: cellular and molecular mechanisms. *Journal of Pathology*, **221**(1):3–12.

Gomez, M. R., Sampson, J. R., and Whittemore, V. H. (1999). *Tuberous Sclerosis Complex (Developmental Perspectives in Psychiatry)*. Oxford University Press, USA, 3rd edition.

Goncharova, E. A., Goncharov, D. A., Li, H., Pimtong, W., Lu, S., Khavin, I., and Krymskaya, V. P. (2011). mTORC2 is required for proliferation and survival of TSC2-null cells. *Molecular and Cellular Biology*, **31**(12):2484–2498.

Gray, M. J., Zhang, J., Ellis, L. M., Semenza, G. L., Evans, D. B., Watowich, S. S., and Gallick, G. E. (2005). HIF-1α, STAT3, CBP/p300 and Ref-1/APE are components of a transcriptional complex that regulates Src-dependent hypoxia-induced expression of VEGF in pancreatic and prostate carcinomas. *Oncogene*, **24**(19):3110–20.

Gredilla, R. and Barja, G. (2005). Minireview: the role of oxidative stress in relation to caloric restriction and longevity. *Endocrinology*, **146**(9):3713–7.

Greer, E. L. and Brunet, A. (2005). FOXO transcription factors at the interface between longevity and tumor suppression. *Oncogene*, **24**(50):7410–7425.

Greer, E. L. and Brunet, A. (2008). FOXO transcription factors in ageing and cancer. *Acta Physiologica*, **192**(1):19–28.

Griner, E. M. and Kazanietz, M. G. (2007). Protein kinase C and other diacylglycerol effectors in cancer. *Nature Reviews Cancer*, **7**(4):281–94.

Gual, P., Le Marchand-Brustel, Y., and Tanti, J. (2005). Positive and negative regulation of insulin signaling through IRS-1 phosphorylation. *Biochimie*, **87**(1):99–109.

Gwinn, D. M., Shackelford, D. B., Egan, D. F., Mihaylova, M. M., Mery, A., Vasquez, D. S., Turk, B. E., and Shaw, R. J. (2008). AMPK phosphorylation of raptor mediates a metabolic checkpoint. *Molecular Cell*, **30**(2):214–26.

Hansen, M., Chandra, A., Mitic, L. L., Onken, B., Driscoll, M., and Kenyon, C. (2008). A role for autophagy in the extension of lifespan by dietary restriction in C. elegans. *PLOS Genetics*, **4**(2):e24.

Hara, S., Oya, M., Mizuno, R., Horiguchi, A., Marumo, K., and Murai, M. (2005). Akt activation in renal cell carcinoma: contribution of a decreased PTEN expression and the induction of apoptosis by an Akt inhibitor. *Annals of Oncology*, **16**(6):928–33.

Hara, T., Nakamura, K., Matsui, M., Yamamoto, A., Nakahara, Y., Suzuki-Migishima, R., Yokoyama, M., Mishima, K., Saito, I., Okano, H., and Mizushima, N. (2006). Suppression of basal autophagy in neural cells causes neurodegenerative disease in mice. *Nature*, **441**(7095):885–9.

Harper, J. M., Leathers, C. W., and Austad, S. N. (2006). Does caloric restriction extend life in wild mice? *Aging Cell*, **5**(6):441–449.

Harrington, L. S., Findlay, G. M., Gray, A., Tolkacheva, T., Wigfield, S., Rebholz, H., Barnett, J., Leslie, N. R., Cheng, S., Shepherd, P. R., Gout, I., Downes, C. P., and Lamb, R. F. (2004). The TSC1-2 tumor suppressor controls insulin-PI3K signaling via regulation of IRS proteins. *The Journal of Cell Biology*, **166**(2):213–223.

Harrison, D. E., Strong, R., Sharp, Z. D., Nelson, J. F., Astle, C. M., Flurkey, K., Nadon, N. L., Wilkinson, J. E., Frenkel, K., Carter, C. S., Pahor, M., Javors, M. A., Fernandez, E., and Miller, R. A. (2009). Rapamycin fed late in life extends lifespan in genetically heterogeneous mice. *Nature*, **460**(7253):392–5.

Hauge, C., Antal, T. L., Hirschberg, D., Doehn, U., Thorup, K., Idrissova, L., Hansen, K., Jensen, O. N., Jørgensen, T. J., Biondi, R. M., and Frödin, M. (2007). Mechanism for activation of the growth factor-activated AGC kinases by turn motif phosphorylation. *EMBO Journal*, **263**(9):2251–2261.

Hay, N. and Sonenberg, N. (2004). Upstream and downstream of mTOR. *Genes and Development*, **18**:1926–1945.

Heinonen, H., Nieminen, A., Saarela, M., Kallioniemi, A., Klefstrom, J., Hautaniemi, S., and Monni, O. (2008). Deciphering downstream gene targets of PI3K/mTOR/p70S6K pathway in breast cancer. *BMC Genomics*, **9**(348).

Heitman, J., Movva, N. R., and Hall, M. N. (1991). Targets for cell cycle arrest by the immunosuppressant rapamycin in yeast. *Science*, **253**(5022):905–9.

Hengl, S., Kreutz, C., Timmer, J., and Maiwald, T. (2007). Data-based identifiability analysis of non-linear dynamical models. *Bioinformatics*, **23**(19):2612.

Hindmarsh, A. C. (1983). ODEPACK, a systematized collection of ODE solvers. In IMACS Transactions on Scientific Computation, Stepleman, volume 1, pages 55–64, R. S. et al. (Eds.), North-Holland, Amsterdam.

Hirsch, M. W., Smale, S., and Devaney, R. L. (2004). *Differential equations, dynamical systems, and an introduction to chaos*. Elsevier Academic Press, USA, 2nd edition.

Hock, M. and Kralli, A. (2009). Transcriptional control of mitochondrial biogenesis and function. *Annual Review of Physiology*, **71**:177–203.

Holzenberger, M., Hamard, G., Zaoui, R., Leneuve, P., Ducos, B., Beccavin, C., Périn, L., and Le Bouc, Y. (2001). Experimental IGF-I receptor deficiency generates a sexually dimorphic pattern of organ-specific growth deficits in mice, affecting fat tissue in particular. *Endocrinology*, **142**(10):4469–4478.

Hoops, S., Sahle, S., Gauges, R., Lee, C., Pahle, J., Simus, N., Singhal, M., Xu, L., Mendes, P., and Kummer, U. (2006). COPASI - a COmplex PAthway SImulator. *Bioinformatics*, **22**(24):3067.

Horn, D. J. V., Myers Jr., M. G., and Backer, J. M. (1994). Direct activation of the phosphatidylinositol 3'-kinase by the insulin receptor. *The Journal of Biological Chemistry*, **269**(1):29–32.

Hornbeck, P. V., Kornhauser, J. M., Tkachev, S., Zhang, B., Skrzypek, E., Murray, B., Latham, V., and Sullivan, M. (2012). PhosphoSitePlus: a comprehensive resource for investigating the structure and function of experimentally determined post-translational modifications in man and mouse. *Nucleic Acids Research*, **40**(Database issue):D261–70.

Howell, J. J. and Manning, B. D. (2011). mTOR couples cellular nutrient sensing to organismal metabolic homeostasis. *Trends in Endocrinology and Metabolism*, **22**(3):94–102.

Hsu, P. P., Kang, S. A., Rameseder, J., Zhang, Y., Ottina, K. A., Lim, D., Peterson, T. R., Choi, Y., Gray, N. S., Yaffe, M. B., Marto, J. A., and Sabatini, D. M. (2011). The mTOR-regulated phosphoproteome reveals a mechanism of mTORC1-mediated inhibition of growth factor signaling. *Science*, **332**(6035):1317–1322.

Huang, J., Dibble, C. C., Matsuzaki, M., and Manning, B. D. (2008). The TSC1-TSC2 complex is required for proper activation of mTOR complex 2. *Molecular and Cellular Biology*, **28**(12):4104–15.

Huang, J. and Manning, B. D. (2008). The TSC1-TSC2 complex: a molecular switchboard controlling cell growth. *Biochemical Journal*, **412**(2):179–90.

Huang, J. and Manning, B. D. (2009). A complex interplay between Akt, TSC2, and the two mTOR complexes. *Biochemical Society Transactions*, **37**(Pt 1):217.

Huang, J., Wu, S., Wu, C. L., and Manning, B. D. (2009). Signaling events downstream of mammalian target of rapamycin complex 2 are attenuated in cells and tumors deficient for the tuberous sclerosis complex tumor suppressors. *Cancer Research*, **69**(15):6107.

Huang, Y., Hickey, R. P., Yeh, J. L., Liu, D., Dadak, A., Young, L. H., Johnson, R. S., and Giordano, F. J. (2004). Cardiac myocyte-specific HIF-1α deletion alters vascularization, energy availability, calcium flux, and contractility in the normoxic heart. *FASEB Journal*, **18**(10):1138–40.

Hucka, M., Finney, A., Sauro, H. M., Bolouri, H., Doyle, J. C., Kitano, H., Arkin, A. P., Bornstein, B. J., Bray, D., and Cornish-Bowden, A. (2003). The systems biology markup language (SBML): a medium for representation and exchange of biochemical network models. *Bioinformatics*, **19**(4):524–531.

Hughey, J. J., Lee, T. K., and Covert, M. W. (2010). Computational modeling of mammalian signaling networks. *WIREs Systems Biology and Medicine*, **2**(2):194–209.

Ihekwaba, A. E., Broomhead, D. S., Grimley, R. L., Benson, N., and Kell, D. B. (2004). Sensitivity analysis of parameters controlling oscillatory signalling in the NF-κB pathway: the roles of IKK and IκBα. *Systems Biology (Stevenage)*, **1**(1):93–103.

Ikenoue, T., Inoki, K., Yang, Q., Zhou, X., and Guan, K. L. (2008). Essential function of TORC2 in PKC and Akt turn motif phosphorylation, maturation and signalling. *EMBO Journal*, **27**(14):1919–31.

Inoki, K., Corradetti, M. N., and Guan, K. L. (2005). Dysregulation of the TSC-mTOR pathway in human disease. *Nature Genetics*, **37**(1):19–24.

Inoki, K. and Guan, K. (2006). Complexity of the TOR signaling network. *Trends In Cell Biology*, **16**(4):206–212.

Inoki, K., Li, Y., Zhu, T., Wu, J., and Guan, K.-L. (2002). TSC2 is phosphorylated and inhibited by Akt and suppresses mTOR signalling. *Nature Cell Biology*, **4**(9):648–57.

Inoki, K., Ouyang, H., Zhu, T., Lindvall, C., Wang, Y., Zhang, X., Yang, Q., Bennett, C., Harada, Y., Stankunas, K., Wang, C. Y., He, X., MacDougald, O. A., You, M., Williams, B. O., and Guan, K. L. (2006). TSC2 integrates Wnt and energy signals via a coordinated phosphorylation by AMPK and GSK3 to regulate cell growth. *Cell*, **126**(5):955–68.

Inoki, K., Zhu, T., and Guan, K. L. (2003). TSC2 mediates cellular energy response to control cell growth and survival. *Cell*, **115**(5):577–90.

Jacinto, E., Facchinetti, V., Liu, D., Soto, N., Wei, S., Jung, S. Y., Huang, Q., Qin, J., and Su, B. (2006). SIN1/MIP1 maintains rictor-mTOR complex integrity and regulates Akt phosphorylation and substrate specificity. *Cell*, **127**(1):125–37.

Jacinto, E., Loewith, R., Schmidt, A., Lin, S., Rüegg, M. A., Hall, A., and Hall, M. N. (2004). Mammalian TOR complex 2 controls the actin cytoskeleton and is rapamycin insensitive. *Nature Cell Biology*, **6**(11):1122–8.

Jacinto, E. and Lorberg, A. (2008). TOR regulation of AGC kinases in yeast and mammals. *Biochemical Journal*, **410**(1):19–37.

Jain, P. and Bhalla, U. S. (2009). Signaling logic of activity-triggered dendritic protein synthesis: an mTOR gate but not a feedback switch. *PLOS Computational Biology*, **5**(2):e1000287.

Jakobsen, S. N., Hardie, D. G., Morrice, N., and Tornqvist, H. E. (2001). 5'-AMP-activated protein kinase phosphorylates IRS-1 on Ser-789 in mouse C2C12 myotubes in response to 5-aminoimidazole-4-carboxamide riboside. *The Journal of Biological Chemistry*, **276**(50):46912–6.

Janes, M. R. and Fruman, D. A. (2010). Targeting TOR dependence in cancer. *Oncotarget*, **1**(1):69–76.

Jia, J. F. and Yue, H. (2008). Model reduction of a signalling transduction pathway based on global sensitivity analysis. *Journal of Communications of SWIN*, **3**:102–106.

Jiang, W., Zhu, Z., and Thompson, H. J. (2008). Dietary energy restriction modulates the activity of AMPK, Akt, and mTOR in mammary carcinomas, mammary gland, and liver. *Cancer Research*, **68**(13):5492–5499.

Julien, L.-A., Carriere, A., Moreau, J., and Roux, P. P. (2010). mTORC1-activated S6K1 phosphorylates Rictor on threonine 1135 and regulates mTORC2 signaling. *Molecular and Cellular Biology*, **30**(4):908–21.

Kaeberlein, M. (2010). Lessons on longevity from budding yeast. *Nature*, **464**(7288):513–9.

Kaeberlein, M., Burtner, C. R., and Kennedy, B. K. (2007). Recent developments in yeast aging. *PLOS Genetics*, **3**(5):e84.

Kaeberlein, M. and Kapahi, P. (2009). Cell signaling. Aging is RSKy business. *Science*, **326**(5949):55–6.

Kalender, A., Selvaraj, A., Kim, S. Y., Gulati, P., Brule, S., Viollet, B., Kemp, B. E., Bardeesy, N., Dennis, P., Schlager, J. J., Marette, A., Kozma, S. C., and Thomas, G. (2010). Metformin, independent of AMPK, inhibits mTORC1 in a rag GTPase-dependent manner. *Cell Metabolism*, **11**(5):390–401.

Kamada, Y., Fujioka, Y., Suzuki, N. N., Inagaki, F., Wullschleger, S., Loewith, R., Hall, M. N., and Ohsumi, Y. (2005). Tor2 directly phosphorylates the AGC kinase Ypk2 to regulate actin polarization. *Molecular and Cellular Biology*, **25**(16):7239–48.

Kamimura, Y., Xiong, Y., Iglesias, P. A., Hoeller, O., Bolourani, P., and Devreotes, P. N. (2008). PIP3-independent activation of TorC2 and PKB at the cell's leading edge mediates chemotaxis. *Current Biology*, **18**(14):1034–1043.

Kapahi, P., Chen, D., Rogers, A. N., Katewa, S. D., Li, P. W., Thomas, E. L., and Kockel, L. (2010). With TOR, less is more: a key role for the conserved nutrient-sensing TOR pathway in aging. *Cell Metabolism*, **11**(6):453–65.

Kapahi, P., Zid, B. M., Harper, T., Koslover, D., Sapin, V., and Benzer, S. (2004). Regulation of lifespan in Drosophila by modulation of genes in the TOR signaling pathway. *Current Biology*, **14**(10):885–90.

Kawakami, Y., Nishimoto, H., Kitaura, J., Maeda-Yamamoto, M., Kato, R. M., Littman, D. R., Rawlings, D. J., and Kawakami, T. (2004). Protein kinase C βII regulates Akt phosphorylation on Ser-473 in a cell type- and stimulus-specific fashion. *The Journal of Biological Chemistry*, **279**(46):47720–47725.

Ke, Q. and Costa, M. (2006). Hypoxia-inducible factor-1 (HIF-1). *Molecular Pharmacology*, **70**(5):1469.

Keating, S. M., Bornstein, B. J., Finney, A., and Hucka, M. (2006). SBMLToolbox: an SBML toolbox for MATLAB users. *Bioinformatics*, **22**(10):1275–1277.

Kenyon, C. (2011). The first long-lived mutants: discovery of the insulin/IGF-1 pathway for ageing. *Philosophical Transactions of the Royal Society B*, **366**(1561):9–16.

Kenyon, C. J. (2010). The genetics of ageing. *Nature*, **464**(7288):504–12.

Kholodenko, B. N. (2006). Cell-signalling dynamics in time and space. *Nature Reviews Molecular Cell Biology*, **7**(3):165–76.

Kim, E., Goraksha-Hicks, P., Li, L., Neufeld, T. P., and Guan, K.-L. (2008). Regulation of TORC1 by Rag GTPases in nutrient response. *Nature Cell Biology*, **10**(8):935–45.

Kim, J., Kundu, M., Viollet, B., and Guan, K.-L. (2011). AMPK and mTOR regulate autophagy through direct phosphorylation of Ulk1. *Nature Cell Biology*, **13**(2):132–141.

Kim, Y. M., Stone, M., Hwang, T. H., Kim, Y. G., Dunlevy, J. R., Griffin, T. J., and Kim, D. H. (2012). SH3BP4 Is a negative regulator of amino acid-rag GTPase-mTORC1 signaling. *Molecular Cell*, **46**(6):833–46.

Kirkpatrick, S., Gelatt, C. D. J., and Vecchi, M. P. (1983). Optimization by simulated annealing. *Science*, **220**(4598):671–680.

Kirkwood, T. B. L. (1977). Evolution of ageing. *Nature*, **170**(5635):201–4.

Kirkwood, T. B. L. (1981). *Repair and its evolution: survival versus reproduction*, pages 165–189. In Physiological evology: an evolutionary approach to resource use. Townsend, C. R. and Calow, P. (Eds.), Oxford: Blackwell Scientific Publications.

Kirkwood, T. B. L. (2008). Understanding ageing from an evolutionary perspective. *Journal of Internal Medicine*, **263**(2):117–27.

Kirkwood, T. B. L. and Rose, M. R. (1991). Evolution of senescence: late survival sacrificed for reproduction. *Philosophical Transactions of the Royal Society B*, **332**(1262):15–24.

Kiselyov, V. V., Versteyhe, S., Gauguin, L., and De Meyts, P. (2009). Harmonic oscillator model of the insulin and IGF1 receptors' allosteric binding and activation. *Molecular Systems Biology*, **5**(243).

Klimova, T. and Chandel, N. S. (2008). Mitochondrial complex III regulates hypoxic activation of HIF. *Cell Death and Differentiation*, **15**(4):660–666.

Kloeden, P. E. and Platen, E. (1999). *Numerical solution of stochastic differential equations*. Spinger-Verlag, Berlin.

Kobayashi, T. and Cohen, P. (1999). Activation of serum- and glucocorticoid-regulated protein kinase by agonists that activate phosphatidylinositide 3-kinase is mediated by 3-phosphoinositide-dependent protein kinase-1 (PDK1) and PDK2. *Biochemical Journal*, **339**(Pt 2):319–28.

Kolch, W., Calder, M., and Gilbert, D. (2005). When kinases meet mathematics: the systems biology of MAPK signalling. *FEBS Letters*, **579**(8):1891–5.

Komatsu, M., Waguri, S., Chiba, T., Murata, S., Iwata, J.-i., Tanida, I., Ueno, T., Koike, M., Uchiyama, Y., Kominami, E., and Tanaka, K. (2006). Loss of autophagy in the central nervous system causes neurodegeneration in mice. *Nature*, **441**(7095):880–4.

Koren, I., Reem, E., and Kimchi, A. (2010). DAP1, a novel substrate of mTOR, negatively regulates autophagy. *Current Biology*, **20**(12):1093–8.

Koshiba, T., Detmer, S. A., Kaiser, J. T., Chen, H., McCaffery, J. M., and Chan, D. C. (2004). Structural basis of mitochondrial tethering by mitofusin complexes. *Science*, **305**(5685):858–62.

Kreutz, C., Raue, A., and Timmer, J. (2012). Likelihood based observability analysis and confidence intervals for predictions of dynamic models. *BMC Systems Biology*, **6**(1):120.

Krymskaya, V. P. and Goncharova, E. A. (2009). PI3K/mTORC1 activation in hamartoma syndromes: therapeutic prospects. *Cell Cycle*, **8**(3):403–13.

Kuepfer, L., Peter, M., Sauer, U., and Stelling, J. (2007). Ensemble modeling for analysis of cell signaling dynamics. *Nature Biotechnology*, **25**(9):1001–6.

Kuznetsov, N. V. (2008). *Stability and oscillations of dynamical systems: theory and applications*. PhD thesis. Jyväskylä University Printing House, Finland.

Lagouge, M., Argmann, C., Gerhart-Hines, Z., Meziane, H., Lerin, C., Daussin, F., Messadeq, N., Milne, J., Lambert, P., Elliott, P., Geny, B., Laakso, M., Puigserver, P., and Auwerx, J. (2006). Resveratrol improves mitochondrial function and protects against metabolic disease by activating SIRT1 and PGC-1alpha. *Cell*, **127**(6):1109–22.

Laplante, M. and Sabatini, D. (2012). mTOR signaling in growth control and disease. *Cell*, **149**(2):274–93.

Le Novère, N., Hucka, M., Mi, H., Moodie, S., Schreiber, F., Sorokin, A., Demir, E., Wegner, K., Aladjem, M. I., and Wimalaratne, S. M. (2009). The systems biology graphical notation. *Nature Biotechnology*, **27**(8):735–741.

Lee, J., Giordano, S., and Zhang, J. (2012). Autophagy, mitochondria and oxidative stress: cross-talk and redox signalling. *Biochemical Journal*, **441**(2):523–40.

Lee, J. W., Park, S., Takahashi, Y., and Wang, H.-G. (2010a). The Association of AMPK with ULK1 Regulates Autophagy. *PLOS ONE*, **5**(11):e15394.

Lee, S., Shen, Z., Robinson, D. N., Briggs, S., and Firtel, R. A. (2010b). Involvement of the cytoskeleton in controlling leading-edge function during chemotaxis. *Molecular Biology of the Cell*, **21**(11):1810–24.

Lee, S. S., Kennedy, S., Tolonen, A. C., and Ruvkun, G. (2003). DAF-16 target genes that control C. elegans life-span and metabolism. *Science*, **300**(5619):644–7.

Lehtinen, M. K., Yuan, Z., Boag, P. R., Yang, Y., Villén, J., Becker, E. B., DiBacco, S., de la Iglesia, N., Gygi, S., Blackwell, T. K., and Bonni, A. (2006). A conserved MST-FOXO signaling pathway mediates oxidative-stress responses and extends life span. *Cell*, **125**(5):987–1001.

Lehuen, A., Diana, J., Zaccone, P., and Cooke, A. (2010). Immune cell crosstalk in type 1 diabetes. *Nature Reviews Immunology*, **10**(7):501–513.

Leonov, G. A. and Kuznetsov, N. V. (2007). Time-varying linearization and the Perron effects. *International Journal of Bifurcation and Chaos*, **17**(4):1079–1107.

Levenberg, K. (1944). A method for the solution of certain nonlinear problems in least squares. *Quarterly of Applied Mathematics*, **2**:164–168.

Levine, B. and Kroemer, G. (2008). Autophagy in the pathogenesis of disease. *Cell*, **132**(1):27–42.

Libina, N., Berman, J. R., and Kenyon, C. (2003). Tissue-specific activities of C. elegans DAF-16 in the regulation of lifespan. *Cell*, **115**(4):489–502.

Liesa, M., Borda-d'Água, B., Medina-Gómez, G., Lelliott, C. J., and Paz, J. C. (2008). Mitochondrial fusion is increased by the Nuclear Coactivator PGC-1β. *PLOS ONE*, **3**(10):e3613.

Lin, K., Hsin, H., Libina, N., and Kenyon, C. (2001). Regulation of the Caenorhabditis elegans longevity protein DAF-16 by insulin/IGF-1 and germline signaling. *Nature Genetics*, **28**(2):139–45.

Liu, Q., Wang, J., Kang, S., Thoreen, C., Hur, W., Ahmed, T., Sabatini, D., and Gray, N. (2011). Discovery of 9-(6-aminopyridin-3-yl)-1-(3-(trifluoromethyl)phenyl)benzo[h][1,6]naphthyridin-2(1H)-one (Torin2) as a potent, selective, and orally available mammalian target of rapamycin (mTOR) inhibitor for treatment of cancer. *Journal of Medicinal Chemistry (ACS Publications)*, **54**(5):1473–80.

Lyapunov, A. M. (1992). *The General problem of the Stability of Motion*. Taylor and Francis (Eds.), London (translated by A. T Fuller).

MacLean, M., Harris, N., and Piper, P. W. (2001). Chronological lifespan of stationary phase yeast cells; a model for investigating the factors that might influence the ageing of postmitotic tissues in higher organisms. *Yeast*, **18**(6):499–509.

Mahdavi, A., Davey, R. E., Bhola, P., Yin, T., and Zandstra, P. W. (2007). Sensitivity analysis of intracellular signaling pathway kinetics predicts targets for stem cell fate control. *PLOS Computational Biology*, **3**(7):e130.

Maiwald, T. and Timmer, J. (2008). Dynamical modeling and multi-experiment fitting with PottersWheel. *Bioinformatics*, **24**(18):2037–2043.

Malesani, P. (2004). *Ricerca operativa*. Edizioni Libreria Progetto, Padova, Italy.

Mao, K., Kobayashi, S., Jaffer, Z. M., Huang, Y., Volden, P., Chernoff, J., and Liang, Q. (2008a). Regulation of Akt/PKB activity by P21-activated kinase in cardiomyocytes. *Journal of Molecular and Cellular Cardiology*, **44**(2):429–34.

Mao, K., Kobayashi, S., Jaffer, Z. M., Huang, Y., Volden, P., Chernoff, J., and Liang, Q. (2008b). Regulation of Akt/PKB activity by P21-activated kinase in cardiomyocytes. *Journal of Molecular and Cellular Cardiology*, **44**(2):429–34.

Marino, S., Hogue, I. B., Ray, C. J., and Kirschner, D. E. (2008). A methodology for performing global uncertainty and sensitivity analysis in systems biology. *Journal of Theoretical Biology*, **254**(1):178–96.

Marquardt, D. W. (1963). An algorithm for least squares estimation of nonlinear parameters. *SIAM Journal on Applied Mathematics*, **11**(2):431–441.

Mattison, J., Roth, G., Beasley, T., Tilmont, E., Handy, A., Herbert, R., Longo, D., Allison, D., Young, J., Bryant, M., Barnard, D., Ward, W., Qi, W., Ingram, D., and de Cabo, R. (2012). Impact of caloric restriction on health and survival in rhesus monkeys from the NIA study. *Nature*, **489**(7415):318–21.

Maxwell, P. H. (2005). Hypoxia-inducible factor as a physiological regulator. *Experimental Physiology*, **90**(6):791–797.

McCarthy, N. (2004). Protein kinases: REDD or dead? *Nature Reviews Cancer*, **4**(12):925–925.

McInnes, K. J., Brown, K. A., Hunger, N. I., and Simpson, E. R. (2012). Regulation of LKB1 expression by sex hormones in adipocytes. *International Journal of Obesity*, **36**(7):982–5.

McManus, E. J., Collins, B. J., Ashby, P. R., Prescott, A. R., Murray-Tait, V., Armit, L. J., Arthur, J. S. C., and Alessi, D. R. (2004). The in vivo role of PtdIns(3,4,5)P3 binding to PDK1 PH domain defined by knockin mutation. *EMBO Journal*, **23**(10):2071–82.

Michalewicz, Z. (1994). *Genetic algorithms + data structures = evolution programs*. Springer-Verlag, Berlin, 3rd edition.

Mihaylova, M. M. and Shaw, R. J. (2011). The AMPK signalling pathway coordinates cell growth, autophagy and metabolism. *Nature Cell Biology*, **13**(9):1016–23.

Mitchell, M. (1998). *An introduction to genetic algorithms*. MIT Press, Boston, USA.

Moles, C. G., Mendez, P., and Banga, J. R. (2003). Parameter estimation in biochemical pathways: a comparison of global optimization methods. *Genome Research*, **13**(11):2467–2474.

Mora, A., Komander, D., van Aalten, D. M. F., and Alessi, D. R. (2004). PDK1, the master regulator of AGC kinase signal transduction. *Seminars in Cell and Developmental Biology*, **15**(2):161–70.

Mortimer, R. K. and Johnston, J. R. (1959). Life span of individual yeast cells. *Nature*, **183**(4677):1751–2.

Motwani, R. and Raghavan, P. (1995). *Randomized algorithms*. Cambridge University Press, Cambridge, UK.

Murphy, C. T., McCarroll, S. A., Bargmann, C. I., Fraser, A., Kamath, R. S., Ahringer, J., Li, H., and Kenyon, C. (2003). Genes that act downstream of DAF-16 to influence the lifespan of Caenorhabditis elegans. *Nature*, **424**(6946):277–83.

Murphy, M. P. (2009). How mitochondria produce reactive oxygen species. *Biochemical Journal*, **417**(Pt 1):1–13.

Myers, Jr, M. G., Grammer, T. C., Wang, L. M., Sun, X. J., Pierce, J. H., Blenis, J., and White, M. F. (1994). Insulin receptor substrate-1 mediates phosphatidylinositol 3'-kinase and p70S6k signaling during insulin, insulin-like growth factor-1, and interleukin-4 stimulation. *The Journal of Biological Chemistry*, **269**(46):28783–28789.

Nascimento, E. B. M. and Ouwens, D. M. (2009). PRAS40: target or modulator of mTORC1 signalling and insulin action? *Archives of Physiology and Biochemistry*, **115**(4):163–75.

Nascimento, E. B. M., Snel, M., Guigas, B., van der Zon, G. C. M., Kriek, J., Maassen, J. A., Jazet, I. M., Diamant, M., and Ouwens, D. M. (2010). Phosphorylation of PRAS40 on THR246 by PKB/AKT facilitates efficient phosphorylation of Ser183 by mTORC1. *Cell Signaling*, **22**(6):961–7.

Nash, S. G. (1984). Newton-type minimization via the Lanczos method. *SIAM Journal of Numerical Analysis*, **21**(4):770–788.

Newton, A. C. (2003). Regulation of the ABC kinases by phosphorylation: protein kinase C as a paradigm. *Biochemical Journal*, **370**(Pt 2):361–71.

Ning, J. and Clemmons, D. R. (2010). AMP-activated protein kinase inhibits IGF-I signaling and protein synthesis in vascular smooth muscle cells via stimulation of insulin receptor substrate 1 S794 and tuberous sclerosis 2 S1345 phosphorylation. *Molecular Endocrinology*, **24**(6):1218–29.

Nyman, E., Fagerholm, S., Jullesson, D., Strålfors, P., and Cedersund, G. (2012). Mechanistic explanations for counter-intuitive phosphorylation dynamics of the insulin receptor and insulin receptor substrate-1 in response to insulin in murine adipocytes. *FEBS Journal*, **279**(6):987–999.

Papin, J. A., Hunter, T., Palsson, B. O., and Subramariam, S. (2005). Reconstruction of cellular signalling networks and analysis of their properties. *Nature Reviews Molecular Cell Biology*, **6**(2):99–11.

Parks, P. C. (1992). A.M. Lyapunov's stability theory - 100 years on. *IMA Journal of Mathematical Control and Information*, **9**(4):275–303.

Partovian, C. and Simons, M. (2004). Regulation of protein kinase B/Akt activity and Ser473 phosphorylation by protein kinase Cα in endothelial cells. *Cell Signaling*, **16**(8):951–7.

Passos, J. F., Nelson, G., Wang, C., Richter, T., Simillion, C., Proctor, C. J., Miwa, S., Olijslagers, S., Hallinan, J., Wipat, A., Saretzki, G., Rudolph, K. L., Kirkwood, T. B. L., and von Zglinicki, T. (2010). Feedback between p21 and reactive oxygen production is necessary for cell senescence. *Molecular Systems Biology*, **6**(347):347.

Passos, J. F., Saretzki, G., and von Zglinicki, T. (2007). DNA damage in telomeres and mitochondria during cellular senescence: is there a connection? *Nucleic Acids Research*, **35**(22):7505–7513.

Pearce, L. R., Komander, D., and Alessi, D. R. (2010). The nuts and bolts of AGC protein kinases. *Nature Reviews Molecular Cell Biology*, **11**(1):9–22.

Perron, O. (1930). Die stabilitatsfrage bei differentialgleichungen. *Mathematische Zeitschrift*, **bd. 32**(5):702–728.

Peruzzi, F., Prisco, M., Dews, M., Salomoni, P., Grassilli, E., Romano, G., Calabretta, B., and Baserga, R. (1999). Multiple signaling pathways of the insulin-like growth factor 1 receptor in protection from apoptosis. *Molecular and Cellular Biology*, **19**(10):7203–15.

Peterson, R. T., Beal, P. A., Comb, M. J., and Schreiber, S. L. (2000). FKBP12-rapamycin-associated protein (FRAP) autophosphorylates at serine 2481 under translationally repressive conditions. *The Journal of Biological Chemistry*, **275**(10):7416–7423.

Peterson, T. R., Laplante, M., Thoreen, C. C., Sancak, Y., Kang, S. A., Kuehl, W. M., Gray, N. S., and Sabatini, D. M. (2009). DEPTOR is an mTOR inhibitor frequently overexpressed in multiple myeloma cells and required for their survival. *Cell*, **137**(5):873–86.

Peterson, T. R., Sengupta, S. S., Harris, T. E., Carmack, A. E., Kang, S. A., Balderas, E., Guertin, D. A., Madden, K. L., Carpenter, A. E., Finck, B. N., and Sabatini, D. M. (2011). mTOR Complex 1 regulates Lipin 1 localization to control the SREBP pathway. *Cell*, **146**(3):408–420.

Petzold, L. (1983). Automatic selection of methods for solving stiff and nonstiff systems of ordinary differential equations. *SIAM Journal on Scientific and Statistical Computing*, **4**(1):136–148.

Pilarski, R. (2009). Cowden syndrome: a critical review of the clinical literature. *Journal of Genetic Counseling*, **18**(1):13–27.

Polak, P., Cybulski, N., Feige, J. N., Auwerx, J., Rüegg, M. A., and Hall, M. N. (2008). Adipose-specific knockout of raptor results in lean mice with enhanced mitochondrial respiration. *Cell Metabolism*, **8**(5):399–410.

Polak, P. and Hall, M. N. (2009). mTOR and the control of whole body metabolism. *Current Opinion in Cell Biology*, **21**(2):209–18.

Potter, C. J., Pedraza, L. G., and Xu, T. (2002). Akt regulates growth by directly phosphorylating Tsc2. *Nature Cell Biology*, **4**(9):658–65.

Proctor, C. J. and Gray, D. A. (2008). Explaining oscillations and variability in the p53-Mdm2 system. *BMC Systems Biology*, **2**:75.

R Development Core Team (2010). *R: a language and environment for statistical computing*. R Foundation for Statistical Computing, Vienna, Austria.

Rane, M. J., Coxon, P. Y., Powell, D. W., Webster, R., Klein, J. B., Pierce, W., Ping, P., and McLeish, K. R. (2000). p38 kinase-dependent MAPKAPK-2 activation functions as 3-phosphoinositide-dependent kinase-2 for Akt in human neutrophils. *The Journal of Biological Chemistry*, **276**(5):3517–3523.

Rao, R. D., Buckner, J. C., and Sarkaria, J. N. (2004). Mammalian target of rapamycin (mTOR) inhibitors as anti-cancer agents. *Current Cancer Drug Targets*, **4**(8):621–35.

Rathinam, M., Petzold, L. R., Cao, Y., and Gillespie, D. T. (2003). Stiffness in stochastic chemically reacting systems: The implicit tau-leaping method. *Journal of Chemical Physics*, **119**(24):12784–12794.

Raue, A., Becker, V., Klingmüller, U., and Timmer, J. (2010). Identifiability and observability analysis for experimental design in non-linear dynamical models. *Chaos*, **20**(4):045105.

Raue, A., Kreutz, C., Maiwald, T., Bachmann, J., Schilling, M., Klingmüller, U., and Timmer, J. (2009). Structural and practical identifiability analysis of partially observed dynamical models by exploiting the profile likelihood. *Bioinformatics*, **25**(15):1923–1929.

Raue, A. and Timmer, J. (2011). *Model identification by utilizing likelihood-based methods*, pages 395–416. In Handbook of Statistical Systems Biology, Stumpf, M., Balding, D., and Girolami, M. (Eds.), John Wiley and Sons, Chichester, UK.

Ravikumar, B., Sarkar, S., Davies, J. E., Futter, M., Garcia-Arencibia, M., Green-Thompson, Z. W., Jimenez-Sanchez, M., Korolchuk, V. I., Lichtenberg, M., Luo, S., Massey, D. C., Menzies, F. M., Moreau, K., Narayanan, U., Renna, M., Siddiqi, F. H., Underwood, B. R., Winslow, A. R., and Rubinsztein, D. C. (2010). Regulation of mammalian autophagy in physiology and pathophysiology. *Physiological Reviews*, **90**(4):1383–435.

Rodgers, J., Lerin, C., Haas, W., Gygi, S., Spiegelman, B., and Puigserver, P. (2005). Nutrient control of glucose homeostasis through a complex of PGC-1alpha and SIRT1. *Nature*, **434**(7029):113–8.

Rosner, M., Hanneder, M., Siegel, N., Valli, A., Fuchs, C., and Hengstschlager, M. (2008). The mTOR pathway and its role in human genetic diseases. *Mutatation Research*, **659**(3):284–92.

Russell, R. C., Fang, C., and Guan, K.-L. (2011). An emerging role for TOR signaling in mammalian tissue and stem cell physiology. *Development*, **138**(16):3343–3356.

Sahin, E., Colla, S., Liesa, M., Moslehi, J., Müller, F., Guo, M., Cooper, M., Kotton, D., Fabian, A., Walkey, C., Maser, R., Tonon, G., Foerster, F., Xiong, R., Wang, Y., Shukla, S., Jaskelioff, M., Martin, E., Heffernan, T., Protopopov, A., Ivanova, E., Mahoney, J., Kost-Alimova, M., Perry, S., Bronson, R., Liao, R., Mulligan, R., Shirihai, O., Chin, L., and DePinho, R. (2011). Telomere dysfunction induces metabolic and mitochondrial compromise. *Nature*, **470**(7334):359–65.

Saltelli, A., Ratto, M., Andres, T., Campolongo, F., Cariboni, J., Gatelli, D., Saisana, M., and Tarantola, S. (2008). *Global sensitivity analysis. The primer*. John Wiley and Sons.

Saltelli, A., Ratto, M., Tarantola, S., and Campolongo, F. (2005). Sensitivity analysis for chemical models. *Chemical Reviews*, **105**(7):2811–2828.

Sancak, Y., Bar-Peled, L., Zoncu, R., Markhard, A. L., Nada, S., and Sabatini, D. M. (2010). Ragulator-Rag complex targets mTORC1 to the lysosomal surface and is necessary for its activation by amino acids. *Cell*, **141**(2):290–303.

Sancak, Y., Peterson, T. R., Shaul, Y. D., Lindquist, R. A., Thoreen, C. C., Bar-Peled, L., and Sabatini, D. M. (2008). The Rag GTPases bind raptor and mediate amino acid signaling to mTORC1. *Science*, **320**(5882):1496–501.

Sarbassov, D. D., Ali, S. M., Kim, D.-H., Guertin, D. A., Latek, R. R., Erdjument-Bromage, H., Tempst, P., and Sabatini, D. M. (2004). Rictor, a novel binding partner of mTOR, defines a rapamycin-insensitive and raptor-independent pathway that regulates the cytoskeleton. *Current Biology*, **14**(14):1296–302.

Sarbassov, D. D., Ali, S. M., Sengupta, S., Sheen, J.-H., Hsu, P. P., Bagley, A. F., Markhard, A. L., and Sabatini, D. M. (2006). Prolonged rapamycin treatment inhibits mTORC2 assembly and Akt/PKB. *Molecular Cell*, **22**(2):159–68.

Sarbassov, D. D., Guertin, D. A., Ali, S. M., and Sabatini, D. M. (2005). Phosphorylation and regulation of Akt/PKB by the rictor-mTOR complex. *Science*, **307**(5712):1098–101.

Saunders, R. N., Metcalfe, M. S., and Nicholson, M. L. (2001). Rapamycin in transplantation: a review of the evidence. *Kidney International*, **59**(1):3–16.

Schilling, M., Maiwald, T., Hengl, S., Winter, D., Kreutz, C., Kolch, W., Lehmann, W. D., Timmer, J., and Klingmüller, U. (2009). Theoretical and experimental analysis links isoform-specific ERK signalling to cell fate decisions. *Molecular Systems Biology*, **5**(334).

Schmidt, H. and Jirstrand, M. (2006). Systems Biology Toolbox for MATLAB: a computational platform for research in systems biology. *Bioinformatics*, **22**(4):514–515. `http://www.sbtoolbox2.org`.

Schwarz, G. (1978). Estimating the dimension of a model. *Annals of Statistics*, **6**(2):461–464.

Sedaghat, A. R., Sherman, A., and Quon, M. J. (2002). A mathematical model of metabolic insulin signaling pathways. *American Journal of Physiology - Endocrinology and Metabolism*, **283**(5):E1084–101.

Selman, C., Tullet, J. M. A., Wieser, D., Irvine, E., Lingard, S. J., Choudhury, A. I., Claret, M., Al-Qassab, H., Carmignac, D., Ramadani, F., Woods, A., Robinson, I. C. A., Schuster, E., Batterham, R. L., Kozma, S. C., Thomas, G., Carling, D., Okkenhaug, K., Thornton, J. M., Partridge, L., Gems, D., and Withers, D. J. (2009). Ribosomal protein S6 kinase 1 signaling regulates mammalian life span. *Science*, **326**(5949):140–4.

Sengupta, A., Molkentin, J., and Yutzey, K. (2009). FoxO transcription factors promote autophagy in cardiomyocytes. *The Journal of Biological Chemistry*, **284**(41):28319–31.

Sengupta, S., Peterson, T. R., and Sabatini, D. M. (2010). Regulation of the mTOR complex 1 pathway by nutrients, growth factors, and stress. *Molecular Cell*, **40**(2):310–322.

Seoane, J., Le, H. V., Shen, L., Anderson, S. A., and Massagué, J. (2004). Integration of Smad and forkhead pathways in the control of neuroepithelial and glioblastoma cell proliferation. *Cell*, **117**(2):211–23.

Shackelford, D. B. and Shaw, R. J. (2009). The LKB1-AMPK pathway: metabolism and growth control in tumour suppression. *Nature Reviews Cancer*, **9**(8):563–75.

Shah, O., Wang, Z., and Hunter, T. (2004). Inappropriate activation of the TSC/Rheb/mTOR/S6K cassette induces IRS1/2 depletion, insulin resistance, and cell survival deficiencies. *Current Biology*, **14**(18):1650–6.

Shanley, D. P. and Kirkwood, T. B. L. (2000). Calorie restriction and aging: a life-history analysis. *Evolution*, **54**(3):740–50.

Shokolenko, I., Venediktova, N., Bochkareva, A., Wilson, G. L., and Alexeyev, M. F. (2009). Oxidative stress induces degradation of mitochondrial DNA. *Nucleic Acids Research*, **37**(8):2539–2548.

Smith, G. R. and Shanley, D. P. (2010). Modelling the response of FOXO transcription factors to multiple post-translational modifications made by ageing-related signalling pathways. *PLOS ONE*, **5**(6):e11092.

Soliman, G. A., Acosta-Jaquez, H. A., Dunlop, E. A., Ekim, B., Maj, N. E., Tee, A. R., and Fingar, D. C. (2010). mTOR Ser-2481 autophosphorylation monitors mTORC-specific catalytic activity and clarifies rapamycin mechanism of action. *The Journal of Biological Chemistry*, **285**(11):7866–7879.

Sonntag, A. G., Dalle Pezze, P., Shanley, D. P., and Thedieck, K. (2012). A modelling-experimental approach reveals insulin receptor substrate (IRS)-dependent regulation of adenosine monosphosphate-dependent kinase (AMPK) by insulin. *FEBS Journal*, **279**(18):3314–3328.

Soriano, F. X., Liesa, M., Bach, D., Chen, D. C., Palacin, M., and Zorzano, A. (2006). Evidence for a mitochondrial regulatory pathway defined by Peroxisome Proliferator–Activated Receptor-γ Coactivator-1α, Estrogen-Related Receptor-α, and Mitofusin 2. *Diabetes*, **55**(6):1783–1791.

Sparks, C. A. and Guertin, D. A. (2010). Targeting mTOR: prospects for mTOR complex 2 inhibitors in cancer therapy. *Oncogene*, **29**(26):3733–44.

Stanfel, M. N., Shamieh, L. S., Kaeberlein, M., and Kennedy, B. K. (2009). The TOR pathway comes of age. *Biochimica et Biophysica Acta*, **1790**(10):1067–74.

Stocker, H., Radimerski, T., Schindelholz, B., Wittwer, F., Belawat, P., Daram, P., Breuer, S., Thomas, G., and Hafen, E. (2003). Rheb is an essential regulator of S6K in controlling cell growth in Drosophila. *Nature Cell Biology*, **5**(6):559–65.

Sun, Y., Connors, K. E., and Yang, D. Q. (2007). AICAR induces phosphorylation of AMPK in an ATM-dependent, LKB1-independent manner. *Molecular and Cellular Biochemistry*, **306**(1-2):239–45.

Suresh-Babu, C. V., Yoon, S., Nam, H. S., and Yoo, Y. S. (2004). Simulation and sensitivity analysis of phosphorylation of EGFR signal transduction pathway in PC12 cell model. *Systems Biology (Stevenage)*, **1**(2):213–21.

Suzuki, A., Kusakai, G., Kishimoto, A., Shimojo, Y., Ogura, T., Lavin, M. F., and Esumi, H. (2004). IGF-1 phosphorylates AMPK-α subunit in ATM-dependent and LKB1-independent manner. *Biochemical et Biophysical Research Communications*, **324**(3):986–92.

Tato, I., Bartrons, R., Ventura, F., and Rosa, J. L. (2011). Amino acids activate mammalian target of rapamycin complex 2 (mTORC2) via PI3K/Akt signaling. *The Journal of Biological Chemistry*, **286**(8):6128–42.

Taylor, P. M. (2009). Amino acid transporters: eminences grises of nutrient signalling mechanisms? *Biochemical Society Transactions*, **37**(Pt 1):237–41.

Tee, A. R., Anjum, R., and Blenis, J. (2003). Inactivation of the tuberous sclerosis complex-1 and -2 gene products occurs by phosphoinositide 3-kinase/Akt-dependent and -independent phosphorylation of tuberin. *The Journal of Biological Chemistry*, **278**(39):37288–96.

Tee, A. R., Fingar, D. C., Manning, B. D., Kwiatkowski, D. J., Cantley, L. C., and Blenis, J. (2002). Tuberous sclerosis complex-1 and -2 gene products function together to inhibit mammalian target of rapamycin (mTOR)-mediated downstream signaling. *Proceedings of the National Academy of Sciences*, **99**(21):13571–13576.

Thedieck, K. and Hall, M. N. (2009). *Translational control by amino acids and energy*, pages 2285–2293. In Handbook of Cell Signaling. Bradshaw, R. and Dennis, E. (Eds.), Elsevier Inc., San Diego, California.

Thedieck, K., Polak, P., Kim, M. L., Molle, K. D., Cohen, A., Jeno, P., Arrieumerlou, C., and Hall, M. N. (2007). PRAS40 and PRR5-like protein are new mTOR interactors that regulate apoptosis. *PLOS ONE*, **2**(e1217).

Thomson, M. and Gunawardena, J. (2009). Unlimited multistability in multisite phosphorylation system. *Nature*, **460**(7252):274–277.

Toker, A. and Newton, A. C. (2000). Cellular signaling: pivoting around PDK-1. *Cell*, **103**(2):185–8.

Treins, C., Giorgetti-Peraldi, S., Murdaca, J., Semenza, G. L., and Van Obberghen, E. (2002). Insulin Stimulates Hypoxia-inducible Factor 1 through a Phosphatidylinositol 3-kinase/target of rapamycin-dependent signaling pathway. *The Journal of Biological Chemistry*, **277**(31):27975–27981.

Treins, C., Warne, P. H., Magnuson, M. A., Pende, M., and Downward, J. (2010). Rictor is a novel target of p70 S6 kinase-1. *Oncogene*, **29**(7):1003–16.

Tremblay, F., Brule, S., Hee Um, S., Li, Y., Masuda, K., Roden, M., Sun, X. J., Krebs, M., Polakiewicz, R. D., Thomas, G., and Marette, A. (2007). Identification of IRS-1 Ser-1101 as a target of S6K1 in nutrient- and obesity-induced insulin resistance. *Proceedings of the National Academy of Sciences*, **104**(35):14056–61.

Troussard, A. A., Mawji, N. M., Ong, C., Mui, A., St. Arnaud, R., and Dedhar, S. (2003). Conditional knock-out of integrin-linked kinase demonstrates an essential role in protein kinase B/Akt activation. *The Journal of Biological Chemistry*, **278**(25):22374–22378.

Tsutsui, H., Kinugawa, S., and Matsushima, S. (2009). Mitochondrial oxidative stress and dysfunction in myocardial remodelling. *Cardiovascular Research*, **81**(3):449–56.

Turrens, J. (2003). Mitochondrial formation of reactive oxygen species. *The Journal of Physiology*, **552**(Pt 2):335–44.

Tyson, J. J., Chen, K. C., and Novak, B. (2003). Sniffers, buzzers, toggles and blinkers: dynamics of regulatory and signaling pathways in the cell. *Current Opinion in Cell Biology*, **15**(2):221–231.

Tzatsos, A. and Tsichlis, P. N. (2007). Energy depletion inhibits phosphatidylinositol 3-kinase/Akt signaling and induces apoptosis via AMP-activated protein kinase-dependent phosphorylation of IRS-1 at Ser-794. *The Journal of Biological Chemistry*, **282**(25):18069–82.

Umeoka, S., Koyama, T., Miki, Y., Akai, M., Tsutsui, K., and Togashi, K. (2008). Pictorial review of tuberous sclerosis in various organs. *Radiographics*, **28**(7):e32.

van der Vos, K. E., Eliasson, P., Proikas-Cezanne, T., Vervoort, S. J., van Boxtel, R., Putker, M., van Zutphen, I., Mauthe, M., Zellmer, S., Pals, C., Verhagen, L. P., Groot Koerkamp, M. J., Braat, A. K., Dansen, T. B., Holstege, F. C., Gebhardt, R., Burgering, B. M., and Coffer, P. J. (2012). Modulation of glutamine metabolism by the PI(3)K-PKB-FOXO network regulates autophagy. *Nature Cell Biology*, **14**(8):829–37.

van Veelen, W., Korsse, S. E., van de Laar, L., and Peppelenbosch, M. P. (2011). The long and winding road to rational treatment of cancer associated with LKB1/AMPK/TSC/mTORC1 signaling. *Oncogene*, **30**(20):2289–2303.

Vaziri, H., Dessain, S., Ng Eaton, E., Imai, S., Frye, R., Pandita, T., Guarente, L., and Weinberg, R. (2001). hSIR2(SIRT1) functions as an NAD-dependent p53 deacetylase. *Cell*, **107**(2):149–59.

Vignot, S., Faivre, S., Aguirre, D., and Raymond, E. (2005). mTOR-targeted therapy of cancer with rapamycin derivatives. *Annals of Oncology*, **16**(4):525–37.

Viniegra, J. G., Martinez, N., Modirassari, P., Losa, J. H., Cobo, C. P., Lobo, V. J. S., Luquero, C. I. A., Álvarez-Vallina, L., y Cajal, S. R., Rojas, J. M., and Sánchez-Prieto, R. (2004). Full activation of PKB/Akt in response to insulin or ionizing radiation is mediated through ATM. *The Journal of Biological Chemistry*, **280**(6):4029–4036.

Vinod, P. K. U. and Venkatesh, K. V. (2009). Quantification of the effect of amino acids on an integrated mTOR and insulin signaling pathway. *Molecular BioSystems*, **5**(10):1163–73.

Volarevic, S. and Thomas, G. (2001). Role of S6 phosphorylation and S6 kinase in cell growth. *Progress in Nucleic Acid Research and Molecular Biology*, **65**:101–27.

von Dassow, G., Meir, E., Munro, E. M., and Odell, G. M. (2000). The segment polarity network is a robust developmental module. *Nature*, **406**(6792):188–92.

Walker, G., Houthoofd, K., Vanfleteren, J. R., and Gems, D. (2005). Dietary restriction in C. elegans: From rate-of-living effects to nutrient sensing pathways. *Mechanisms of Ageing and Development*, **126**(9):929–937.

Wang, D. Y. Q., Cardelli, L., Phillips, A., Piterman, N., and Fisher, J. (2009). Computational modeling of the EGFR network elucidates control mechanisms regulating signal dynamics. *BMC Systems Biology*, **3**(118).

Wang, G. and Krueger, G. R. F. (2010). Computational analysis of mTOR signaling pathway: bifurcation, carcinogenesis, and drug discovery. *Anticancer Research*, **30**(7):2683.

Wang, L., Harris, T. E., Roth, R. A., and Lawrence, J. C. (2007). PRAS40 regulates mTORC1 kinase activity by functioning as a direct inhibitor of substrate binding. *The Journal of Biological Chemistry*, **282**(27):20036–44.

Wanke, V., Cameroni, E., Uotila, A., Piccolis, M., Urban, J., Loewith, R., and De Virgilio, C. (2008). Caffeine extends yeast lifespan by targeting TORC1. *Molecular Microbiology*, **69**(1):277–85.

Wilkinson, D. J. (2006). *Stochastic modelling for systems biology*. Mathematical and Computational Biology Series. Chapman and Hall/CRC (Eds.), CRC Press, 1st edition.

Willcox, B. J., Donlon, T. A., He, Q., Chen, R., Grove, J. S., Yano, K., Masaki, K. H., Willcox, D. C., Rodriguez, B., and Curb, J. D. (2008). FOXO3A genotype is strongly associated with human longevity. *Proceedings of the National Academy of Sciences*, **105**(37):13987–13992.

Williams, M. R., Arthur, J. S. C., Balendran, A., van der Kaay, J., Poli, V., Cohen, P., and Alessi, D. R. (2000). The role of 3-phosphoinositide-dependent protein kinase 1 in activating AGC kinases defined in embryonic stem cells. *Current Biology*, **10**(8):439–448.

Wolf, A., Swift, J. B., Swinney, H., and Vastano, J. A. (1985). Determining Lyapunov exponents from a time series. *Physica*, **16D**:285–317.

Woo, S. Y., Kim, D. H., Jun, C. B., Kim, Y. M., Haar, E. V., Lee, S. I., Hegg, J. W., Bandhakavi, S., Griffin, T. J., and Kim, D. H. (2007). PRR5, a novel component of mTOR complex 2, regulates platelet-derived growth factor receptor beta expression and signaling. *The Journal of Biological Chemistry*, **282**(35):25604–12.

Worthen, G. S., Avdi, N., Buhl, A. M., Suzuki, N., and Johnson, G. L. (1994). FMLP activates Ras and Raf in human neutrophils. Potential role in activation of MAP kinase. *Journal of Clinical Investigation*, **94**(2):815–23.

Wouters, B. G. and Koritzinsky, M. (2008). Hypoxia signalling through mTOR and the unfolded protein response in cancer. *Nature Reviews Cancer*, **8**(11):851–64.

Wullschleger, S., Loewith, R., and Hall, M. N. (2006). TOR signaling in growth and metabolism. *Cell*, **124**(3):471–84.

Xu, T. R., Vyshemirsky, V., Gormand, A., von Kriegsheim, A., Girolami, M., Braillie, G. S., Ketley, D., Dunlop, A. J., Milligan, G., Houslay, M. D., and Kolch, W. (2010). Inferring signaling pathway topologies from multiple perturbation measurements of specific biochemical species. *Science Signaling*, **3**(134):ra20.

Yamamoto, T., Watanabe, K., Inoue, N., Nakagawa, Y., Ishigaki, N., Matsuzaka, T., Takeuchi, Y., Kobayashi, K., Yatoh, S., Takahashi, A., Suzuki, H., Yahagi, N., Gotoda, T., Yamada, N., and Shimano, H. (2010). Protein kinase Cβ mediates hepatic induction of sterol-regulatory element binding protein-1c by insulin. *Journal of Lipid Research*, **51**(7):1859–70.

Yang, Q. and Guan, K.-L. (2007). Expanding mTOR signaling. *Cell Research*, **17**(8):666–681.

Yang, Q., Inoki, K., Kim, E., and Guan, K. L. (2006). TSC1/TSC2 and Rheb have different effects on TORC1 and TORC2 activity. *Proceedings of the National Academy of Sciences*, **103**(18):6811–6816.

Yu, L., McPhee, C. K., Zheng, L., Mardones, G. A., Rong, Y., Peng, J., Mi, N., Zhao, Y., Liu, Z., Wan, F., Hailey, D. W., Oorschot, V., Klumperman, J., Baehrecke, E. H.,

and Lenardo, M. J. (2010). Termination of autophagy and reformation of lysosomes regulated by mTOR. *Nature*, **465**(7300):942–946.

Yu, Y., Yoon, S., Poulogiannis, G., Yang, Q., Ma, X. M., Villén, J., Kubica, N., Hoffman, G. R., Cantley, L. C., Gygi, S. P., and Blenis, J. (2011). Phosphoproteomic analysis identifies Grb10 as an mTORC1 substrate that negatively regulates insulin signaling. *Science*, **332**(6035):1322–1326.

Yuan, Y. (2000). A review of trust region algorithms for optimization. In Proceedings of the 4th International Congress on Industrial and Applied Mathematics (ICIAM99), pages 271–282, Ball, J. M. and Hunt, J. C. R. (Eds.), Edinburgh, UK.

Zhan, C. and Yeung, L. F. (2011). Parameter estimation in systems biology models using spline approximation. *BMC Systems Biology*, **5**:14.

Zheng, L., Eckerdal, J., Dimitrijevic, I., and Anderson, T. (1997). Chemotactic peptide-induced activation of Ras in human neutrophils is associated with inhibition of p120-GAP activity. *The Journal of Biological Chemistry*, **12**(272):23448–54.

Zid, B. M., Rogers, A. N., Katewa, S. D., Vargas, M. A., Kolipinski, M. C., Lu, T. A., Benzer, S., and Kapahi, P. (2009). 4E-BP extends lifespan upon dietary restriction by enhancing mitochondrial activity in Drosophila. *Cell*, **139**(1):149–60.

Zoncu, R., Efeyan, A., and Sabatini, D. M. (2011). mTOR: from growth signal integration to cancer, diabetes and ageing. *Nature Reviews Molecular Cell Biology*, **12**(1):21–35.